A search for massive top quark resonances with the ATLAS detector at the Large Hadron Collider

Sarah S. A. Livermore

Exeter College

University of Oxford

Thesis submitted in partial fulfilment of the requirements
for the degree of Doctor of Philosophy

Michaelmas term 2012

A search for massive top quark resonances with the ATLAS detector at the Large Hadron Collider

Sarah S. A. Livermore, Exeter College, University of Oxford

Thesis submitted in partial fulfilment of the requirements
for the degree of Doctor of Philosophy, Michaelmas term 2012

Abstract

This thesis presents a search for resonant production of top-antitop quark pairs in final states containing at least one electron or muon. A number of beyond the standard model (BSM) theories incorporate a specific role for the top quark, resulting in resonances that preferentially decay to $t\bar{t}$ pairs. The data sample analysed corresponds to an integrated luminosity of $2.05\ \mathrm{fb}^{-1}$ recorded during 2011 using the ATLAS detector at the Large Hadron Collider. The proton-proton centre-of-mass energy was $7\ \mathrm{TeV}$.

The search is tailored towards heavy resonances at the TeV-scale which therefore decay to top quarks with high transverse momentum. Large hadronic jets are used to reconstruct the energy carried by the hadrons and the substructure of these jets is studied in order to identify hadronically decaying top quarks. The reconstruction can therefore proceed even if the decay products of the top quark are highly collimated. This study represents the first use of jet substructure techniques in a search for $t\bar{t}$ resonances using hadron-hadron collision data.

The invariant mass of the reconstructed $t\bar{t}$ pair is used to test compatibility of the data with the standard model prediction. No evidence for $t\bar{t}$ resonances is found. Upper limits are derived on the production cross-section times branching ratio for narrow and wide resonant states, at the $95\ \%$ credibility level. An upper limit of 0.61 (0.65) pb is set for a narrow (wide) resonance with a mass of $1\ \mathrm{TeV}$. Two specific BSM models are excluded within certain mass ranges: the narrow leptophobic Z' boson with mass 600 – $1150\ \mathrm{GeV}$ and the wide Kaluza-Klein gluon with a mass below $1.5\ \mathrm{TeV}$. These results represent a significant improvement on those of previous searches performed at the ATLAS experiment, which did not use jet substructure techniques.

In addition, the possibility of using jets which decrease in size as their transverse momentum increases is investigated using simulated data. The yield of events due to resonant $t\bar{t}$ production increases by approximately $20\ \%$ compared to when using jets of fixed size. Furthermore, the resolution of the invariant mass of the reconstructed $t\bar{t}$ pair is found to improve by almost one fifth. It is recommended that a calibration scheme be developed for these variable-sized jets, so that their potential to improve the sensitivity to $t\bar{t}$ resonances can be investigated further.

Dedicated to the one and only, Linda Livermore.

Acknowledgements

I must first thank the Science and Technology Facilities Council (STFC) for providing the financial support for my doctoral studies, including additional funding for a two year placement at CERN. The opportunity to work closely with many brilliant physicists at the epicentre of particle physics was tremendously beneficial and something that I shall never forget. I'm also very grateful to Exeter College and the Institute of Physics for help with meeting costs to attend conferences.

When I began my D.Phil. I held the innocent belief that an inquisitive mind combined with a weighty number of hours in the lab would keep me afloat. How wrong I was! I rapidly learnt that the key to successful (and enjoyable) studies was held by those around me. For that reason I owe a debt of gratitude to a number of people, particularly the postdocs I worked with at Oxford, James Ferrando and Jiahang Zhong. I was constantly struck by their patience and willingness to help me, not to mention their fierce intellect combined with a calm, pragmatic approach. James also provided the initial idea for the application of variable-R jets and gave vital ongoing advice. I hope that the STFC continue to understand that postdocs are crucial to the development of doctoral students.

I would also like to thank Elin Bergeås Kuutmann and Marcel Vos, the editors of the boosted $t\bar{t}$ resonances search paper. They were always available to help me understand the details of the analysis and provided many helpful comments on my thesis drafts. It was really a pleasure to work with them.

I owe the greatest thanks to my supervisor Dr. Çiğdem İşsever. It is no exaggeration to say that the completion of my D.Phil. would not have been possible without her, particularly the vital encouragement in the first stages of my studies. I valued her keen instinct for realising worthwhile projects to pursue and the extremely high standards that she expects; the experience of working with her has endowed me with skills that will be useful throughout my life.

A number of people also helped me a great deal along the way, with both technical and moral support. Bertrand Chapleau wrote our indispensable ntuple-production software and provided continual assistance. Esteban Fullana Torregrosa was always available to share his expertise on jet calibration and calorimetry. Thanks to Alison Lister for her help with collating top group information. Averil MacDonald provided some crucial and gratefully received moral support and guidance during the early stages, through the MentorSET scheme. The l'Athénée-Skype-chat gang for truly being quicker-off-the-mark than any search engine and providing humorous chat on all manner of subjects (mainly cats). All my colleagues at Oxford for being a most friendly bunch of physicists, and particularly the group head Tony Weidberg, the director of graduate Studies Todd Huffman and my "physics-uncle" Farrukh Azfar for their support. Many thanks also to Sue Geddes, Kim Proudfoot, Laura Nevay and Daniella Ellis for guiding me through the maze of Oxford University and CERN administration (a tricky combination). Also to the computing team, Ewan MacMahon, Sean Brisbane and Pete Gronbech, for their invaluable expertise.

I was fortunate enough to make many wonderful friends during the course of my studies at Oxford and CERN. In addition to those mentioned above, I'd like to thank the following people for sharing laughs along the way: the macaron-makers (Caterina, Andrée, Emily), my $t\bar{t}$ resonances compadres Chris and Luz, my Exeter college buddies (particularly Therese, Alistair, Simon, Katherine, and Chris and Paul in the lodge) and Alice, Chris, Nick and Tim on DWB L6.

I'd also like to thank Abi and Will for always being happy to listen and for the top D.Phil. tips. Finally thank you to Giacomo for being an undeniable smarty-pants and for always finding the right words, whatever the situation. When dealing with someone who's writing a thesis, that is no small feat.

Preface

The hardware and software of the ATLAS experiment has been developed by many thousands of physicists, engineers, technicians and software developers; the current membership stands at around 3,000. It is natural, therefore, that the foundations of the work documented in this thesis contain significant contributions from past and present colleagues in the collaboration. However, there are a number of sections to which the author of this thesis has made a leading contribution; these are listed below.

The search for $t\bar{t}$ resonances included in this thesis has been published in the Journal of High Energy Physics [1] with additional material contained in an ATLAS collaboration internal document [2]. Any figures in this thesis labelled with “ATLAS”, “ATLAS simulation”, “ATLAS preliminary” or “ATLAS internal” have been produced by the collaboration as a whole. Figures in the first two categories have featured in a refereed publication; those labelled with preliminary have been approved by the collaboration but did not feature in a refereed publication. “Internal” figures have been circulated to the collaboration but have not been presented to a public audience. Any figure without one of these labels has been produced by the author of this thesis.

- The author co-ordinated the production of all ntuples needed for the search; this included over 100 datasets of simulated data and over 300 of collision data. Significant preparatory work had to be carried out for this, including adaption of the ntuple-production software to make it compatible with the infrastructure of the LHC computing grid. The output of the software also had to be validated to ensure that it was consistent with the software that produces the ATLAS top group’s ntuples.

- The author was one of three people in the analysis team to write their own software for the selection of potential signal events and for the $t\bar{t}$ reconstruction. Hence, the graph of signal selection efficiency (Figure 4.8) included in [1] was produced by the author and the histograms comparing the data with the background prediction (Chapters 4 and 6) are equivalent to those presented in [1] and [2].

- The author carried out all studies into the effect of raising the transverse momentum threshold on the hadronic top candidate (Chapter 4).

- The impact of systematic uncertainties, related to muons, on the final result of Chapter 6 was determined by the author.

- W+jets background: the data-driven normalisation of the estimation using Monte Carlo (MC) simulation was performed by the author. The uncertainty on the shape of the $t\bar{t}$ invariant mass distribution due to systematics associated with the W+jets prediction was also estimated by the author.

- The studies of variable-R jets of Chapter 7 are entirely the author’s own work.

Contents

List of Figures

List of Tables

Introduction

The field of particle physics has an incredibly successful history. Through the work of scientists and engineers around the world, we have the standard model which encompasses all known fundamental particles and the interactions between them. It has survived rigorous testing to an extremely high degree of precision. However, a number of observations indicate that it fails to provide a complete description of the universe. In parallel with the development of the standard model, additional theories have been proposed to explain these observations, collectively known as beyond the standard model (BSM) theories. A succession of increasingly energetic particle colliders has been built in order to test the standard model and to gain evidence of the validity of BSM theories. The Tevatron at Fermilab was the first to operate with a centre-of-mass energy of the colliding particles at the TeV-scale[1] and enabled a multitude of searches for BSM phenomena to be carried out. Despite this, the proposed new particles remain elusive.

This thesis describes work carried out to search for BSM phenomena using data from CERN's Large Hadron Collider, collected by the ATLAS detector. These impressive machines represent some of the greatest technological prowess ever known. The centre-of-mass energy of LHC collisions will eventually be over seven times that achieved at the Tevatron; the integrated luminosity in the first phase of data-taking will be a factor of thirty greater. Chapter 2 contains a concise description of the collider followed by an account of the ATLAS detector. Chapter 3 then goes on to discuss the processes used to reconstruct detector signals into objects that can be associated with subatomic particles,

[1]Natural units are used throughout this thesis i.e. $\hbar = c = 1$.

which form the basic components of the search.

A huge plethora of final states are predicted in the various BSM scenarios; this study concentrates on that composed of a top and an antitop quark. The driving motivation is that the standard model does not explain why the top mass is so extreme, at a level of two orders of magnitude greater than the next heaviest quark. The void caused by the absence of explanation has naturally been filled with a number of BSM theories in which the top quark has a prominent role. Two specific theories are explored further in Chapter 1, which both encompass heavy resonant states predominantly decaying to a $t\bar{t}$ pair. Focus is placed on these two models in order to aid comparison with previous similar searches. However, a major principle of this, and similar, BSM searches is to maintain a generalist strategy and avoid over-emphasis on one particular theory. BSM theories provide inspiration and motivation to the experimental community but should not lead to a single-minded approach whilst they remain unproven.

The topology of the top quark decay is naturally dependent on the transverse momentum, or boost, of the parent particle. Top quarks produced at rest will have well-separated or easily "resolved" decay products. As the level of boost increases, these decay products become increasingly more collimated until they occupy the same region of the detector. Previous top quark reconstruction strategies were only applicable to the resolved case and therefore incapable of handling any significant degree of merging of the decay products. There was no great drive for a solution to this issue at the Tevatron, which had a relatively low centre-of-mass energy compared to the LHC. However, the lack of a boosted strategy at the LHC would severely limit the sensitivity to heavy resonances at the TeV-scale and above.

This thesis details the development of two substantially different strategies to reconstruct boosted top quarks at the ATLAS experiment. The first involves reconstruction of the hadronically decaying top quark as a single hadronic jet and the use of substructure techniques to preferentially identify jets containing top quark decays. Furthermore, this strategy is then applied for the first time to a $t\bar{t}$ resonance search using data collected by the ATLAS detector. Chapter 4 details these techniques for reconstructing boosted top quark decays using jet substructure methods. Chapter 5 discusses the methods used to estimate the backgrounds to this search, with a particular focus on W boson production in association with jets. The final result of the search is presented in Chapter 6.

The second technique for the reconstruction of boosted top quarks proposes an inherently different approach. All published $t\bar{t}$ searches to date have employed jets of fixed size. In Chapter 7, "variable-R" jets are used in the reconstruction, which shrink in size as the boost of the parent top increases. The aim is to maintain the resolved topology by allowing these variable-R jets to become closer together before merging into a single jet. This thesis details the first application of variable-R jets to $t\bar{t}$ resonance searches. It is shown that the resolution of the reconstructed $t\bar{t}$ invariant mass distribution can be improved when using variable-R jets as opposed to conventional jets of fixed size.

Chapter 1

Theoretical background and motivation for this search

1.1 A summarised history of particle physics

At the start of the 20^{th} century, the subatomic world was unexplored territory. John Dalton had proposed an atomic theory to explain the ability of evaporated water to exist within air as early as 1803 [3]. However, the theory did not seek to explain what the atoms might be composed of, nor why different elements contained different types of atoms. The first valid explanation of atomic structure, as a minute positively charged nucleus surrounded by electrons, was proposed by Rutherford in 1909 [4]. Bohr revised this model in 1913 to include the necessary idea of quantised energy levels for the electrons [5].

A great deal of activity then ensued in the field of quantum mechanics and the newly created field of elementary particle physics. By the outbreak of the second world war, the grounding principles of the former were essentially laid out, although relativistic quantum field theories would be required to explain the non-conservation of particle number, for instance. Searches for fundamental particles had also borne many fruits: the positron was discovered in 1931 [6] and the neutron soon after, in 1932 [7]. The positron discovery was a fine example of an improbable, but highly motivated, particle proposed by an eloquent hypothesis: Dirac's formulation of relativistic quantum mechanics [8]. The genius of both Dirac and Fermi led to the development of Fermi's golden rule [9], which enables calculation of the transition rate between states, given the matrix element for the interaction and the density of final states.

Although much light had been shed on atomic structure and quantum behaviour at the femtoscopic scale, there were a number of observations whose explanation lay unexposed to the light of scientific investigation. In particular, Fermi's theory of beta decay successfully predicted the lifetime of the decay and the energy spectrum of the resulting electrons. However, in this theory unitarity is violated when the centre-of-mass energy exceeds ≈ 300 GeV[10].

Suspicions that all pieces of the jigsaw were not yet in place were soon confirmed when the neutral kaon was discovered in 1947 by Rochester and Butler [11]. In the subsequent ten years, a slew of new particles was discovered in cosmic rays and then studied in detail at the first man-made particle accelerator at the GeV-scale: Brookhaven's cosmotron [12]. Their discovery was unexpected and threw up surprising observations: many of the new particles had a decay time that was thirteen orders of magnitude greater than their production time, leading to the collective classification of *strange*.

A key idea which helped tremendously in categorising the components of the new "particle zoo" was that of quarks [13, 14, 15]. These were proposed to be fundamental particles which, when combined with two other quarks or an antiquark, made up all the baryons and mesons discovered in the previous decades. A discussion of quarks is left until the following section, however it is important to note that the collection of observed hadrons is perfectly described by this initial model of three quarks and three antiquarks, with no discrepancy observed to date.

1.2 The standard model of Particle Physics

The standard model (SM) is a quantum field theory concerning all known fundamental particles and three of the four interactions between them; an introductory review is presented in [16]. The first stage of its development can be considered to be the unification of the electromagnetic and weak forces by Glashow, Salam and Weinberg [17, 18, 19]. This required the existence of intermediate spin-1 bosons to propagate the weak force. Weinberg further predicted their masses to be at least 40 GeV and 80 GeV. The success of this unified theory was confirmed in 1983 with the discovery of the $W^{\pm}$ and Z bosons, by the UA1 and UA2 experiments at CERN [20, 21, 22, 23].

A mechanism for generating the masses of not only these electroweak bosons, but *all* known particles, was proposed in 1964 by Brout and Englert [24], Higgs [25, 26], and Guralnik, Hagen and Kibble [27]. This involved the introduction of a complex doublet of scalar fields, resulting in a Lagrangian where the electroweak interaction remains invariant under $SU(2) \times U(1)$ gauge symmetry but the ground state described by the Lagrangian loses its invariance. That is, the field acquires a vacuum expectation value (VEV), equal to 246 GeV. This is known as *spontaneous* symmetry breaking because there is no external force causing the symmetry to be broken. The result is a massive gauge field (the Higgs field) and a single massive scalar: the Higgs boson. A full description of the Higgs mechanism of electroweak symmetry breaking is presented in [28].

On 4 July 2012, the ATLAS and CMS experiments at CERN announced the results of independent searches for this particle. Both found evidence for the production of a neutral boson with a mass of around 126 GeV. The first publications [29, 30] after this date demonstrated a significance of at least 5.9 and 5.0 standard deviations respectively. As of December 2012, the ATLAS experiment has measured the mass of this "Higgs-like" boson to be 125.2 ± 0.3 (stat.) $\pm\, 0.6$ (sys.) GeV [31]. Furthermore, no significant deviations have been found in the couplings of this boson to the standard model particles [32]. Many more detailed studies, such as measurements of the spin, parity and couplings to SM particles, will be required to confirm if this is indeed the standard model Higgs boson.

The SM as it stands today incorporates five spin-1 bosons which propagate three forces: the W^+, W^- and Z bosons of the weak force; the massless photon γ of the electromagnetic force; and an octet of massless coloured gluons which propagate the strong force.

The constituents of matter are the twelve fundamental spin-$1/2$ fermions, categorised by the forces through which they interact. There are six leptons, divided into three generations, which are subject to the weak force, but not the strong force. These include the electron e, muon μ and tau τ lepton which all have charge -1, together with their corresponding neutrinos (ν_e, ν_μ and ν_τ). The neutrinos are chargeless and have a very small but, crucially, non-zero mass [33, 34]. Like the electron-positron pairing, all leptons have an antimatter partner of opposite charge but equal mass. There are also six quarks, similarly divided: up, charm, top, down, strange and bottom (u, c, t, d, s, b). The first three have charge $+\ 2/3$ and are referred to as *up-type*; the latter three are *down-type* with charge $-\ 1/3$. The non-zero electromagnetic charge means that quarks experience the electromagnetic force. However, they also carry a *colour* charge and are therefore subject to the strong force. Each (anti)quark can have one of three types of colour: (anti)red, (anti)blue or (anti)green.

When the quark model was formulated, only the up, down and strange quarks were proposed, along with the antiquarks $\bar{u}$, $\bar{d}$ and $\bar{s}$. The fourth quark to be discovered, charm, was proposed by Glashow, Iliopolous and Maiani in 1970 [35] as a means of suppressing flavour-changing neutral currents such as that involved in the decay $K^0 \rightarrow \mu^+\mu^-$. Evidence for charm was subsequently provided in 1974 by means of the observation of the $c\bar{c}$ bound state, J/ψ [36, 37]. This was another striking example, similar to the positron discovery, of theory providing a strong argument for a particle, followed by its subsequent discovery. Two quark generations were expanded to three in 1977, with the first observation of the bottom quark in a $b\bar{b}$ bound state, known as the upsilon [38].

Figure 1.1 lists all the fundamental particles of the SM, including their masses; a key

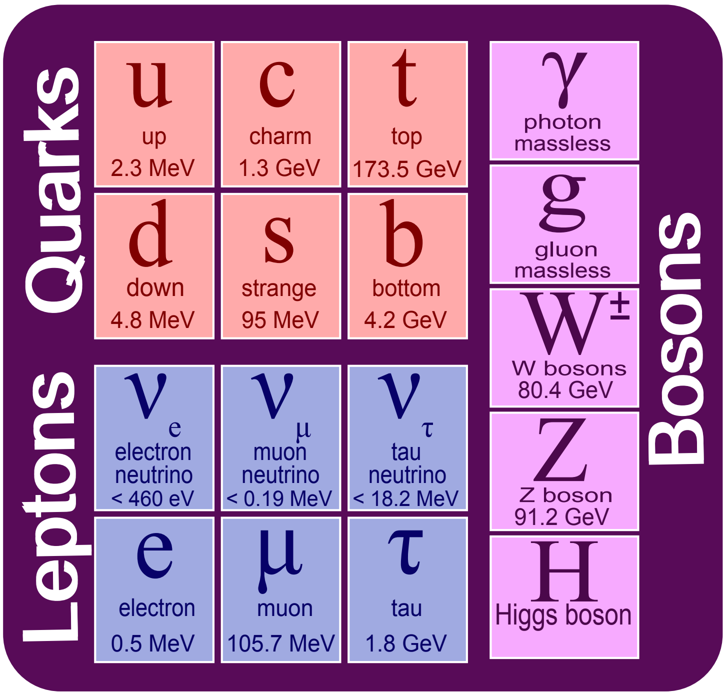

Figure 1.1: Constituent particles of the standard model: quarks, leptons and gauge bosons. The masses of the particles are also shown, taken from [39]. The existence of the SM Higgs boson is yet to be confirmed (see text).

feature is the extremely wide range of fermion masses. This situation was made even more extreme in 1995, when the top quark was discovered at the Tevatron $p\bar{p}$ collider [40, 41]. The current value of its mass stands at $173.5 \pm 0.6 \pm 0.8$ GeV [39], almost equal to that of heavy metal nuclei such as gold and platinum.

The mass of each fermion is generated via its specific coupling to the Higgs field. This *Yukawa coupling* is quantified as follows:

$$m_f = y_i \frac{v}{\sqrt{2}} \tag{1.1}$$

where m_f is the mass of the fermion in question, y_i is the Yukawa coupling constant for quark i, and v is the VEV of the Higgs field.

Figure 1.2 displays the Yukawa couplings for the quarks and the charged leptons; the top quark has a coupling that is almost six orders of magnitude greater than that for the electron. This striking observation of diverse couplings *has no explanation within the standard model*.

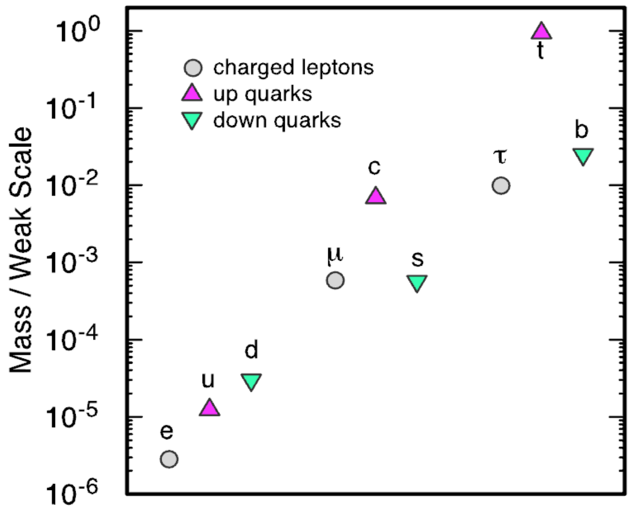

Figure 1.2: Yukawa couplings of the quarks and charged leptons, taken from [42]. This hierarchy of couplings, dominated by the top quark, has no explanation within the standard model.

A viewpoint which is of utmost relevance to the top quark was put forward by Quigg [42]: "The Yukawa couplings that produce the observed quark and charged-lepton masses range over many orders of magnitude. Their origin is unknown. In an important sense, therefore, *all fermion masses involve physics beyond the standard model*.[1]" As a natural extension of this position, a key method for searching for such *beyond the standard model (BSM) phenomena* would be via their coupling to the top quark. This idea forms the driving motivation for this search for heavy resonances resulting from BSM processes, which decay to pairs of top quarks. Prior to a detailed discussion of BSM phenomena, the production and decay of top quarks within the standard model will first be described.

1.2.1 Pair production of top quarks

Pairs of top and antitop quarks ($t\bar{t}$) can be produced copiously at the LHC via the strong interaction. For example, when the centre-of-mass energy is $7\ \mathrm{TeV}$, a pair is produced approximately every second. The top quark width, $\Gamma_t = 2.0\ ^{+0.7}_{-0.6}\ \mathrm{GeV}$ [39], is far in excess of the parameter $\Lambda_{QCD} = 261\ (17)\ (26)\ \mathrm{MeV}$, where the first number in brackets is the statistical error and the second is due to systematic uncertainties [43]. The dynamics

[1]The italics are part of the original quote, taken from [42].

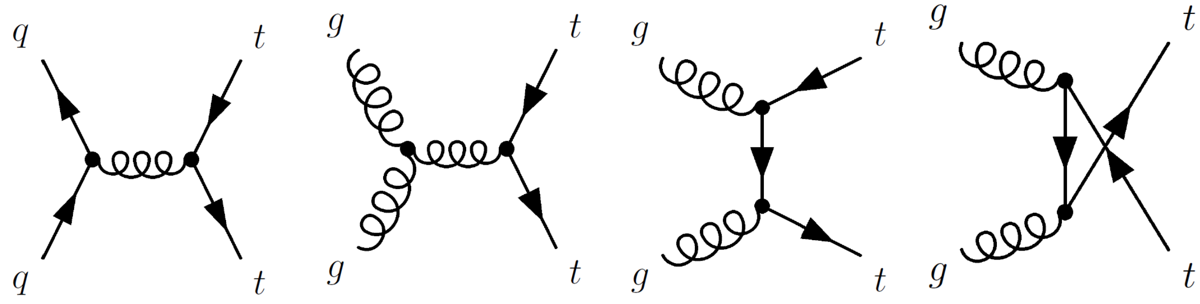

(a) $q\bar{q} \rightarrow t\bar{t}$ (b) Three subprocesses for $gg \rightarrow t\bar{t}$

Figure 1.3: Feynman diagrams for leading order standard model $t\bar{t}$ production processes, via (a) quark and antiquark annihilation ($q\bar{q} \rightarrow t\bar{t}$) and (b) gluon-gluon fusion ($gg \rightarrow t\bar{t}$).

of the top quark can therefore be described by perturbative quantum chromodynamics (QCD) [44]. Specifically, the cross-section is calculable as a perturbation series in the QCD coupling constant α_s, evaluated at the mass of the quark. At leading order, i.e. including $\mathcal{O}(\alpha_S^2)$ terms, there are two possible production processes whose corresponding Feynman diagrams are shown in Figure 1.3.

The dominant process depends on the types of colliding hadrons and the centre-of-mass energy $\sqrt{s}$ at which the collider operates. These two factors crucially determine the probability of finding a parton i carrying a fraction x of its parent hadron's momentum p. This probability is also known as the parton distribution function (PDF). PDFs are extracted from data and evolved to other kinematic scales using the DGLAP equations; a comprehensive description of this procedure can be found in [45]. The PDFs at a momentum transfer scale Q^2 relevant to the top quark mass of 173.5 GeV, are shown in Figure 1.4(a).

In order to determine the x values pertaining to $t\bar{t}$ production, it is illuminating to refer to a plot of the *parton kinematics*, such as that displayed in Figure 1.4(b) for $\sqrt{s} = 7$ TeV at the LHC [47]. Production of a $t\bar{t}$ pair at rest at a central rapidity,[2] for example, requires two colliding partons with x values of ≈ 0.06. This is denoted by the red dotted lines on the figure. Referring back to the PDFs, one can see that the probability of finding

[2]The rapidity is defined as $y = \frac{1}{2}\ln\left(\frac{E+p_z}{E-pz}\right)$, where p_z is the momentum of the outgoing particle in the direction of the colliding particles and E is the energy of the particle [39]. A discussion of rapidity and the related quantity pseudorapidity, can be found in Section 2.2.1.

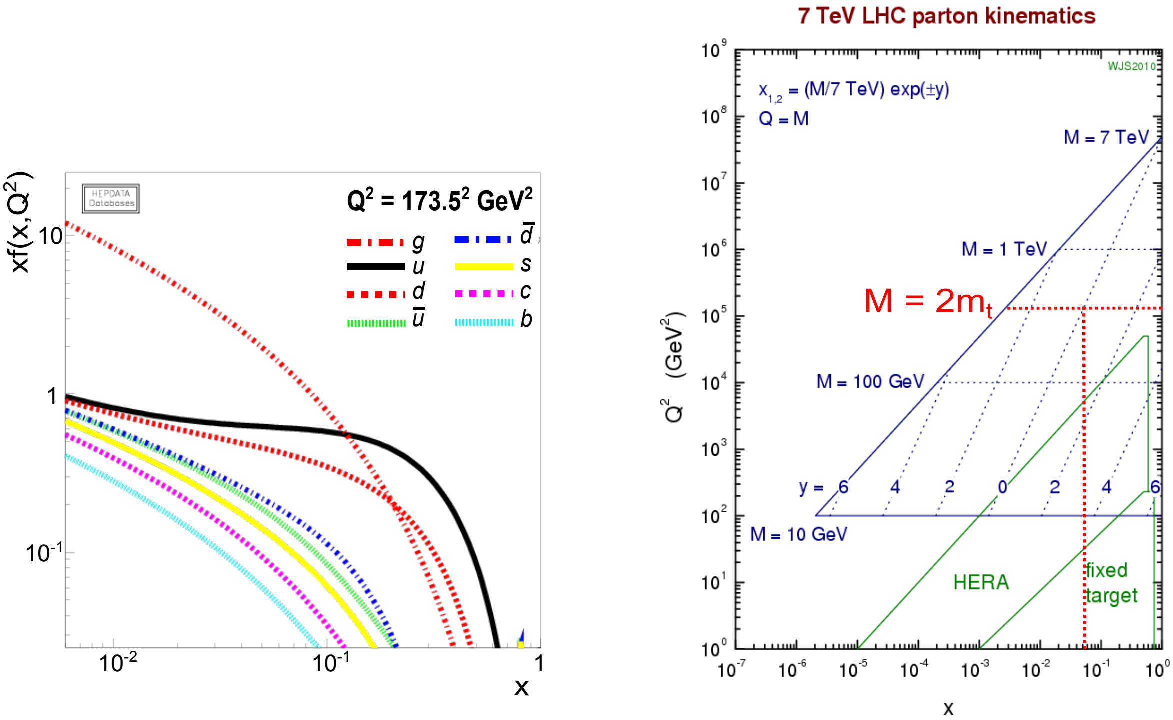

(a) (b)

Figure 1.4: Parton distribution functions (a), from the MSTW 2008 NNLO set, at a momentum transfer scale Q^2 consistent with the threshold for $t\bar{t}$ production. The fraction x of the parent hadron's momentum carried by a particular parton is displayed on the x-axis, with the probability density multiplied by x on the y-axis. The PDF for the gluons dominates over that for the (anti)quarks for all x values below ≈ 0.1. Produced courtesy of [46]. Parton kinematics for the $\sqrt{s} = 7$ TeV LHC (b), which indicates the x values of the two colliding hadrons required for production of states of mass M (thin blue horizontal dashed lines) at a rapidity y (thin blue diagonal dashed lines). The thick red dotted lines represent the production of a $t\bar{t}$ at rest. Courtesy of W. J. Stirling [47].

gluons with these x values dominates more than tenfold over the probability of finding a $\bar{u}$ quark or a $\bar{d}$ quark, required for $q\bar{q}$ annihilation. This results in approximately $80\ \%$ of SM $t\bar{t}$ production arising from gg fusion at $\sqrt{s} = 7$ TeV.

A theoretical calculation of the cross-section for $t\bar{t}$ production at next-to-leading order (NLO), that is, including radiative corrections and hence with terms of order $\mathcal{O}(\alpha_S^3)$, was first carried out thirty years ago [48]. However, cross-section measurements at the ATLAS and CMS experiments [49] have been achieved with an extremely high degree of precision ($\approx 6\ \%$) and are predicted to fall to below $5\ \%$ [50]. Therefore a next-to-next-to-leading order (NNLO, including $\mathcal{O}(\alpha_S^4)$ terms) calculation is necessary in order to reduce the theoretical uncertainties. Furthermore, as will be discussed in subsequent sections, BSM searches have a very small cross-section relative to SM processes; the SM cross-sections must therefore be estimated with a high degree of precision. This is particularly true for $t\bar{t}$ production which is the dominant background process in the search detailed in this thesis. The impact of the current level of the SM $t\bar{t}$ cross-section uncertainty on the final result of this search is investigated in Section 6.2.

The cross-section for the interaction between two hadrons h_1 and h_2 producing a $t\bar{t}$ pair is obtained from the convolution of the parton-level cross-section $\hat{\sigma}_{ij}$ with the *parton luminosities* $\mathcal{L}_{ij}$:

$$\sigma_{h_1 h_2 \to t\bar{t}}(S, m_t) = \sum_{i,j} \int_{4m_t^2}^{S} ds\, \mathcal{L}_{ij}(s, S, \mu_f)\, \hat{\sigma}_{ij}(s, m_t, \alpha_s(\mu_r), \mu_f), \tag{1.2a}$$

where

$$\mathcal{L}_{ij}(s, S, \mu_f) = \frac{1}{S} \int_{s}^{S} \frac{d\hat{s}}{\hat{s}}\, f_{\frac{i}{h_1}}\left(\frac{\hat{s}}{S}, \mu_f\right) f_{\frac{j}{h_2}}\left(\frac{\hat{s}}{S}, \mu_f\right). \tag{1.2b}$$

In the above equations, taken from [51], S denotes the (hadron-level) centre-of-mass energy squared, $\hat{s}$ is the square of the centre-of-mass energy of the colliding partons, m_t is the top quark mass, $\mu_r(\mu_f)$ denotes the renormalisation (factorisation) scale,[3] and $f_{\frac{i}{h_k}}(x, \mu_f)$ are the PDFs for the parton i in the hadron h_k. HATHOR, the HAdronic Top and Heavy quarks crOss section calculatoR [51], is used to calculate the value of the total NNLO cross-section, $\sigma = 165$ pb, used in this thesis.

The factorisation of the expression for the hadron-level cross-section in order to have a separate parton luminosity function is useful because the latter contains all the dependence on energy. The result is that $\hat{\sigma}$ is a dimensionless factor which approximately depends solely on the couplings between the partons. The rapidly falling parton luminosities for gg and $q\bar{q}$ pairs, as a function of the mass of the intermediate state M_X, is illustrated in Figure 1.2.1. The tenfold dominance of gluon pairs at the energy scale relevant

[3]The renormalisation scale (μ_r) is the energy scale at which renormalisation takes place, that is, the procedure to handle ultraviolet divergences in the calculation of amplitudes. The factorisation scale (μ_f) determines whether gluon radiation in the initial state is incorporated in the calculation of the parton distribution functions or the parton-level cross-section. For further details, see [52].

for $t\bar{t}$ production, discussed above, is demonstrated again here.

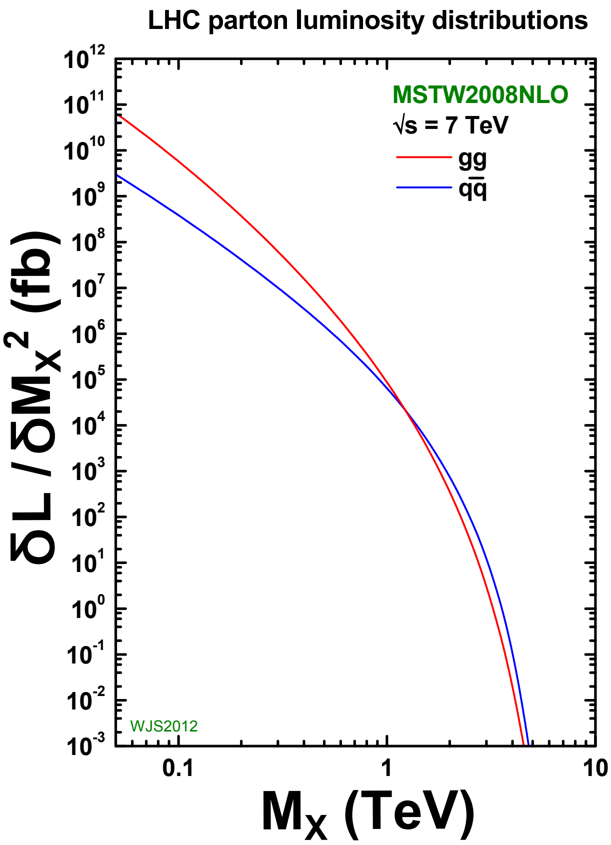

Figure 1.5: Absolute parton luminosities for gg and $q\bar{q}$ pairs at $\sqrt{s} = 7$ TeV, as a function of the mass of the intermediate state M_X. Gluon pairs are dominant for the production of all states with masses below ≈ 1 TeV, including $t\bar{t}$ pairs. Courtesy of W. J. Stirling [47].

1.2.2 Single production of top quarks

Top quarks can also be produced singly within the standard model; this process is commonly referred to as *single top production*. It proceeds via the weak rather than the strong interaction, resulting in a production cross-section that is one to two orders of magnitude less than that for $t\bar{t}$ pair production, depending on the channel. Figure 1.6 displays Feynman diagrams for all the LO subprocesses. Production in the t-channel has the largest cross-section, followed by associated-W production. The cross-section values can be found in Section 2.4.2.

The study of single top production can also be used to search for BSM processes; the interested reader is referred to [53]. However, it has a much smaller contribution to the total background for this search, compared to pair production. Therefore single top production will not be discussed in detail here.

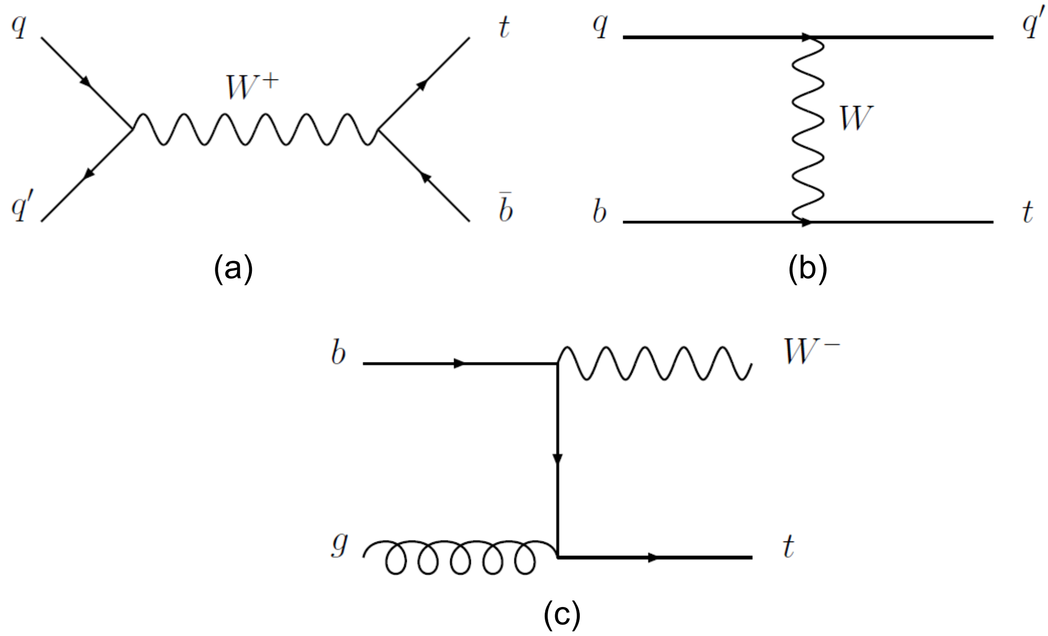

Figure 1.6: Representative Feynman diagrams for single top production at leading order: (a) s-channel, (b) t-channel, (c) associated-W production.

1.2.3 Top quark decay channels

Of all the quarks, the top quark is unique in that it decays before hadronising due to its extremely short lifetime of $\approx 10^{-25}$ s. The reason for this can be seen in Equation 1.3 taken from [54], which shows that the top quark decay width Γ_t, including first order QCD radiative corrections, is proportional to its mass raised to the third power:

$$\Gamma_t = \frac{G_F m_t^3}{8\pi\sqrt{2}} |V_{tb}|^2 \, (1-x)^2 \, (1+2x) \left[1 - \frac{2\alpha_s}{3\pi} \cdot f(x)\right] \tag{1.3}$$

where $x = (M_W/m_t)^2$ and $f(x) = 2\pi^2/3 - 2.5 - 3x + 4.5x^2 - 3x^2 \ln(x)$.

The decay $t \to b + W^+$ dominates over both $t \to d + W^+$ and $t \to s + W^+$ due to the relative magnitudes of the complex terms V_{tb}, V_{td} and V_{ts} in the CKM matrix [39], displayed in Equation 1.4. All three decays are possible because the weak interaction couples not to the quark mass eigenstates (e.g. d, s, b) but to linear combinations of them. The decays involving d and s quarks have a much smaller probability than that involving the d quark, therefore only the V_{tb} term features in the calculation of Γ_t. Indeed, the ratio of the partial width $\Gamma(t \to b + W)$ and the full width Γ_t, known as the branching ratio, is 0.91 ± 0.04 [39]. As a corollary, the decay $\bar{t} \to \bar{b} + W^-$ also dominates for antitops.

$$\begin{pmatrix} \mid V_{ud} \mid = 0.97425 \pm 0.00022 & \mid V_{us} \mid = 0.2252 \pm 0.0009 & \mid V_{ub} \mid = (4.15 \pm 0.49) \times 10^{-3} \\ \mid V_{cd} \mid = 0.230 \pm 0.011 & \mid V_{cs} \mid = 1.006 \pm 0.023 & \mid V_{cb} \mid = (40.9 \pm 1.1) \times 10^{-3} \\ \mid V_{td} \mid = (8.4 \pm 0.6) \times 10^{-3} & \mid V_{ts} \mid = (42.9 \pm 2.6) \times 10^{-3} & \mid V_{tb} \mid = 0.89 \pm 0.07 \end{pmatrix} \tag{1.4}$$

The W bosons produced in the decays are real because the top quark mass m_t exceeds the combined masses of the b-quark and the W boson. Both W bosons subsequently decay to a fermion and an antifermion, which will then hadronise in the case of quarks. The specific decay mode characterises the final state of the $t\bar{t}$ system as *fully hadronic*, *lepton+jets* or *dileptonic*. The full process in each case is as follows:

1. $t\bar{t} \to W^+b\, W^-\bar{b} \to q\bar{q}'b\, q''\bar{q}'''\bar{b}$
2. $t\bar{t} \to W^+b\, W^-\bar{b} \to q\bar{q}'b\, l\bar{\nu}_l\bar{b}$ or $\bar{l}\nu_l b\, q\bar{q}'\bar{b}$
3. $t\bar{t} \to W^+b\, W^-\bar{b} \to \bar{l}\nu_l b\, l'\bar{\nu}_{l'}\bar{b}$

The fully hadronic and lepton+jets channels dominate more than fourfold over the dileptonic channel as can be seen from the branching ratios (BR) for the W boson decay channels, taken from [39]:

- $BR\,(W \to e\nu_e) = 10.75 \pm 0.13$
- $BR\,(W \to \mu\nu_\mu) = 10.57 \pm 0.15$
- $BR\,(W \to \tau\nu_\tau) = 11.25 \pm 0.20$
- $BR\,(W \to$ hadrons$) = 67.60 \pm 0.27$

The reason for this dominance becomes apparent when considering two facts. First, the hadronic final states are made up of the following six pairs of quarks: $u\bar{d}$, $u\bar{s}$, $u\bar{b}$, $c\bar{d}$, $c\bar{s}$, $c\bar{b}$ (the top quark is absent since $m_t > m_W$). Secondly, each quark can exist in one of three coloured states, resulting in an enhanced decay width by a factor of three compared to the leptonic channels.

The relatively large τ-lepton mass of 1.78 GeV [39] enables a decay into a final state containing hadrons as well as solely leptons. This presents experimental challenges to their identification and hence this decay channel is not specifically accounted for in the analysis presented here, as explained in Chapter 3.

The momentum with which the top quarks are produced will have a significant effect on the relative separations of their decay products. It is vital to adapt existing experimental techniques in order to handle the decays of tops quarks with a large momentum relative to their mass. The development and application of these techniques is a major component of this thesis and is discussed in detail in Chapter 4.

1.3 Beyond the standard model and the role of the top quark

The standard model is an extremely successful theory concerning the interactions between the fundamental particles; indeed between *all* fundamental particles that compose the entirety of the matter observed in the universe. It has a number of triumphs to its name, including a prediction of the top quark mass consistent with observation [42], shortly prior to its discovery. This was possible because the top quark dominates loop diagrams which contribute to electroweak precision observables. There is also a high degree of internal consistency between the measured and predicted values of some twenty parameters [55].

However, the theory does not incorporate gravity and fails to explain a number of key observations. First, there is an inconsistency between the amount of matter which interacts electromagnetically and that which exerts large scale gravitational effects as observed in galactic rotation curves [56] and cluster mergers [57]. This leads to the proposition of dark matter which experiences gravity but not the electromagnetic force or strong forces. The candidates for dark matter must lie beyond the standard model; the only viable SM candidate are the neutrinos, but these are ruled out by being insufficiently abundant and the fact of being relativistic particles [58].

There is also a preponderance of matter over antimatter in all regions of the *observed* universe, implying that when the temperature of the universe exceeded $(O)(\mathrm{GeV})$, the level of asymmetry between baryons and antibaryons was $\approx 10^{-8}$ [59]. In 1967, Sakharov proposed that a mechanism for CP violation is required to explain this observation [60]. There is indeed a complex phase incorporated into the CKM matrix of the standard model, however, the resulting effect is far too small to explain the observed matter-antimatter asymmetry. Therefore it is believed that an additional mechanism for CP violation lies outside of the SM [59]. Finally, a relatively recent measurement was made at CERN's LEP collider of the forward-backward asymmetry of b-quark production at a centre-of-mass energy equivalent to the pole mass of the Z boson. The measurement was found to deviate from the SM prediction by $2.8\ \sigma$ [61].

These observations indicate that the standard model does not provide a complete explanation of the universe. The top quark may provide a window onto possible BSM processes due to the large and unexplained value of its mass. It is therefore vital to perform precision measurements of the top quark's properties. An excellent review of these measurements performed at the Tevatron is provided in [62], and results from the LHC are available in [63, 64].

In essence, the measurements of *almost* all of the top quark's properties have been found to be consistent with their SM prediction. The exception to this is the forward-backward asymmetry in $t\bar{t}$ pair production via $q\bar{q}$ annihilation. This describes the directions with which the top and antitop quarks emerge from the production process, relative to the directions of the initial quark and antiquark. There is no asymmetry predicted within QCD at leading order. However, at next-to-leading order, an asymmetry is predicted due to radiative corrections to quark and antiquark annihilation processes [65]. Perturbative QCD predicts that the top quark is preferentially emitted in the direction of the incoming quark and the antitop quark in the direction of the incoming antiquark [65]. Both CDF and D0 produced measurements which exceeded the SM prediction at NLO by approximately $2\,\sigma$ [66, 67].

The initial state at the LHC pp collider is symmetric and therefore the above asymmetry, in terms of the directions of the initial quark and antiquark, cannot be assessed. However, an alternative measure of asymmetry can be used, the source of which is still $q\bar{q}$ annihilation. In this case, it arises because the valence quarks carry, on average, a larger momentum than the antiquarks in the sea. The top quarks, which are preferentially emitted in the same direction as the incoming quark, are therefore boosted into either the forward or backward directions while the antiquarks are emitted more centrally. The most recent measurements from both ATLAS and CMS disfavour large deviations from the SM prediction [68, 69]. However, this asymmetry effect is predicted to be around an order of magnitude smaller at the LHC than at the Tevatron because of the dominance of the gg production mode over $q\bar{q}$ annihilation. A larger dataset will therefore need to be analysed in order to exclude specific BSM scenarios.

Evidence of BSM processes connected to top quarks can be searched for in another key way, besides measurement of the quark's properties. Namely, by identification of resonant production of heavy particles which predominantly decay to pairs of top quarks. The search for such $t\bar{t}$ *resonances* is the subject of this thesis. This search is motivated by *any* BSM theory with an enhanced coupling to top quarks; it is not tailored to any particular model or subsequent decay signature. That is, the search is designed to be *model-independent* to as great an extent as possible. However, *benchmark models* are used to quantify the sensitivity of such searches and facilitate comparison between them. Two models are used due to their very different widths (Γ/m); they are discussed in turn below.

1.3.1 Benchmark model A: the leptophobic topcolor Z' boson

The model of a leptophobic topcolor Z' boson is chosen primarily because it has a narrow width, much smaller than the experimental resolution.[4] The specific width chosen for the search discussed in this thesis, and at all searches by the ATLAS, CDF and D0 collaborations to date (see, for example, [71, 72, 73]), is $1.2\ \%$ of the Z' mass.[5]

The topcolor Z' boson arises from a mechanism for EWSB via a strong interaction, known as topcolor-assisted technicolor (TC2) [75]. The original manifestation of technicolor was proposed over 30 years ago by Weinberg [76] and Susskind [77]. It involved a new gauge theory incorporating gluons, which provided the longitudinal modes of the W and Z bosons, thereby endowing them with mass. TC2 was developed because the original technicolor predicted massless quarks.

The recent compelling evidence for the Higgs boson indicates that EWSB is explained not by technicolor but by the Higgs mechanism. Although it has recently been proposed that a model similar to technicolor could underlie the Higgs mechanism [78]. The use of this topcolor Z' boson as a benchmark model continues regardless of the validity, or otherwise, of technicolor. It is pursued specifically because it is a very narrow resonance, meaning that the upper limits which are determined on its production cross-section times branching ratio to $t\bar{t}$ ($\sigma \times BR(\rightarrow t\bar{t})$) are valid for *any* resonance whose width is narrower than the experimental resolution.

There are four variants of the topcolor Z', discussed in [79]. The benchmark chosen in this search is *Model IV*, a leptophobic, topophyllic boson. This specific Z' model would therefore be first observed via its decay to top quarks rather than via the dileptonic decay mode, which has fewer background processes and is usually the favoured search channel for similar BSM resonances. The specific form of the Lagrangian and the partial width for the decays to $t\bar{t}$, $u\bar{u}$ and $d\bar{d}$ are stated in Section 3(B) of [79].

[4] The measurement of the experimental resolution depends on the method of reconstructing the $t\bar{t}$ system. However, it is considered to be approximately 6 – $12\ \%$ of the resonance mass [70].

[5] The CMS collaboration use an alternative width, of $10\ \%$ [74]. Such a large width is not precluded, however it can then no longer then be used as a benchmark *narrow* resonance.

1.3.2 Benchmark model B: the Kaluza-Klein gluon

The second benchmark model, the Kaluza-Klein gluon (KK-gluon or g_{KK}), arises from a theory of extra dimensions. This particular model has a relatively large width, $\Gamma/m = 15.3$ %. Theories of extra dimensions were first proposed by Arkani, Dimopoulos and Dvali in 1998 [80] to solve the hierarchy problem. That is, the fact that the energy scale of weak interactions is around 10^{33} times higher than that for gravitational interactions. In this "ADD model", the observed weakness of gravity is proposed to be due to there being n additional dimensions to the four common space-time ones; only the propagators of gravity being permitted to enter this "bulk". With a suitable choice for n, such as 2, the gravitational scale can be permitted to be of the order of the weak scale at distances smaller than those yet probed, without affecting the observed gravitational interaction in everyday phenomena.

The specific Kaluza-Klein gluon considered here is part of the set of Randall-Sundrum theories of extra dimensions [81, 82]. These were proposed in response to a problem in the ADD theory: the relatively large volume of the bulk (V_n) led to a hierarchy between the weak scale and the compactification scale, $1/V_n^{1/n}$. The RS scenario explains the hierarchy between the weak and gravitational interactions by means of a single, warped extra dimension which is much smaller than the ADD extra dimensions. The particular RS scenario (RS2) [83] which gives rise to this benchmark model allows all SM fermions and gauge bosons to propagate in the bulk. Notably, this scenario can explain the hierarchy of fermion masses.

A consequence of particles being located in a dimension of finite size is that they take on a spectrum of mass states, known as a Kaluza-Klein tower. The size of the warped extra dimension is sufficiently small that the states are of discrete mass. This is not the case for the ADD scenario, in which the extra dimensions are large enough that the mass states are effectively continuous.

The KK-gluon is the most strongly coupled of all the KK-states and would therefore provide the first evidence for this theory of extra dimensions. Implications for top quark physics come to the fore because the wavefunction of the KK-gluon is predicted to have the largest degree of overlap with the top quark, compared to other SM particles. Hence, the search for $t\bar{t}$ resonances becomes a key method for exploring evidence of extra dimensions. Furthermore, being a coloured resonance there is no decay via leptonic channels and therefore the $t\bar{t}$ decay channel would be central to the discovery of any such resonant state.

There are however a number of challenges to the detection of the KK-gluon via its decay to $t\bar{t}$, which were previously identified in [84]. First, as noted above, its width is significantly larger than the experimental resolution. This necessitates an increase in the sensitivity of the search compared to that for a narrow resonance. Secondly, the feature of being a coloured resonance results in significant interference with SM $t\bar{t}$ production. For the couplings of the light quarks to the particular g_{KK} model considered here, the overall effect of the interference is to cause a narrowing of the peak for a resonance with mass around the TeV-scale. This is demonstrated in Figure 1.7. These two factors somewhat reduce the claim of model-independence in the case of a wide resonance, although the extent of the effect is not investigated here.

1.3.3 Existing constraints from hadron-hadron collider experiments

A consistent choice of benchmark model(s) across experiments allows for a comparison of current results and a study of their evolution with time. During the formulation of the search detailed in this thesis, another ATLAS search [71] in the lepton+jets channel for the same models was carried out using the same $2\ \mathrm{fb}^{-1}$ of data to be analysed in this thesis. The observed upper limit on $\sigma \times BR(\rightarrow t\bar{t})$ for the Z' (g_{KK}) with a mass of $0.5\ \mathrm{TeV}$ was 9.3 (10.1) pb. For a heavier resonance with a mass of $1.3\ \mathrm{TeV}$, the observed upper limits were 0.95 and $1.6\ \mathrm{pb}$ for the Z' and g_{KK} respectively. This led to the exclusion of the leptophobic Z' boson with $500 < m_{Z'} < 880\ \mathrm{GeV}$ and of the g_{KK} with mass between $500\ \mathrm{GeV}$ and $1.130\ \mathrm{TeV}$, both with the widths stated above. All results are at the $95\ \%$

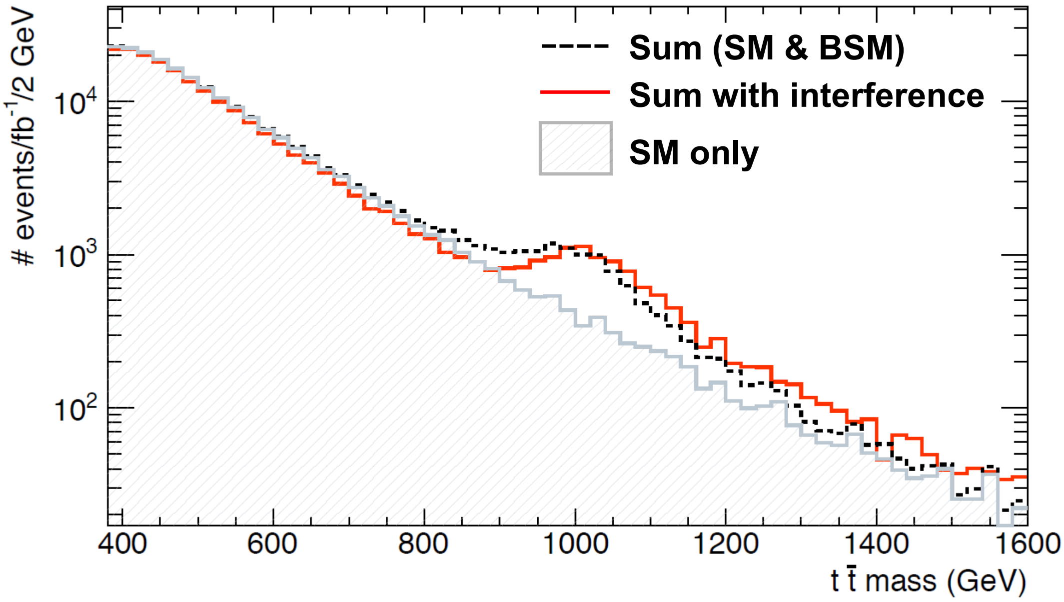

Figure 1.7: The $t\bar{t}$ invariant mass distribution, showing the effects of interference, for a generic spin-1 colour octet with a mass of 1 TeV and the couplings of the Kaluza-Klein gluon (g_{KK}) implemented in MadGraph [85]. The SM $t\bar{t}$ continuum is represented by the shaded histogram (*SM only*); the sum of SM $t\bar{t}$ and resonant g_{KK} production, by the dashed black line (*Sum (SM & BSM)*). The same sum, *with* interference effects between SM and resonant production taken into account, is represented by the continuous red line (*Sum with interference*). For the case of the g_{KK} considered here, the peak due to resonant production becomes narrower if interference is considered. Taken from [84].

credibility level.

The derivation of these limits can be repeated using the SM prediction instead of the data actually observed. These *expected* limits can be used to compare methodologies between different searches since they are less dependent on the nature of the observed dataset. For this search, the expected upper limit for the Z' (g_{KK}) with a mass of 0.5 TeV was 8.5 (10.3) pb. With a mass of 1.3 TeV, the expected upper limits were 0.62 and 0.90 pb for the Z' and g_{KK} respectively. The expected mass exclusion for the leptophobic Z' boson was $500 < m < 1010$ GeV and $500 < m < 1360$ GeV for the g_{KK}. The expected upper limits on $\sigma \times BR(\rightarrow t\bar{t})$ from other experiments, released during the development of the search presented in this thesis, are as follows:

- From the CDF experiment at the Tevatron, using 4.8 fb^{-1} of data: 0.4 (0.104) pb for a Z' with mass 0.5 (1.3) TeV, leading to an exclusion of $m_{Z'} < 900$ GeV [86].

- From the D0 experiment at the Tevatron, using $5.3\ \mathrm{fb}^{-1}$ of data: 0.62 (0.07) pb for mass 0.5 (1.2) TeV, allowing exclusion of the Z' with mass below $835\ \mathrm{GeV}$ [73]. Neither of the Tevatron experiments choose to set limits on the KK-gluon.

- The CMS experiment at the LHC, using $4.7\ \mathrm{fb}^{-1}$ of data, excluded the leptophobic Z' boson with $m < 1.3\ \mathrm{TeV}$ and the KK-gluon with $m < 1.4\ \mathrm{TeV}$. Specific limits on $\sigma \times BR(\rightarrow t\bar{t})$ were not stated [87].

Therefore, the over-riding aim of the search presented in this thesis is to significantly improve the sensitivity to $t\bar{t}$ resonances with masses of $1\ \mathrm{TeV}$ and above.[6]

1.4 The use of jets in searches for $t\bar{t}$ resonances

Top quarks with a large momentum in the plane transverse to the directions of the colliding particles[7], relative to the top quark mass will result from the decay of particularly massive resonances. This causes the final decay products to be highly collimated, increasingly so as the momentum, or *boost*, of the top quark increases. The challenge that this thesis aims to confront is the adaption of conventional $t\bar{t}$ resonance search techniques to handle highly boosted top quarks. A range of novel techniques is available for the *hadronic* side of the $t\bar{t}$ decay and therefore a preliminary discussion of jets is required.

1.4.1 Jet definitions and jet algorithms

Collimated beams of particles result from proton-proton collisions. The partons in these beams are subject to the strong force, which has the associated coupling constant α_s. The strength of this coupling is a function of the momentum transfer scale of the interaction Q. As this scale decreases (or, equivalently, as the length scale increases), α_s tends towards

[6] It should be noted that, since the results of this search have been published, the upper limits on the production cross-section times branching ratio to $t\bar{t}$ have been greatly improved. The latest results from the LHC experiments are listed in Section 6.2.

[7] This definition of momentum is also known as the *transverse momentum*. The rationale for using quantities defined in the transverse plane is presented in Section 2.2.1.

infinity. This "running" of α_s is illustrated in Figure 1.8. The result is that colour-singlet hadrons form from the partons emerging from the collision as they become increasingly spatially separated, in a process known as *hadronisation*.

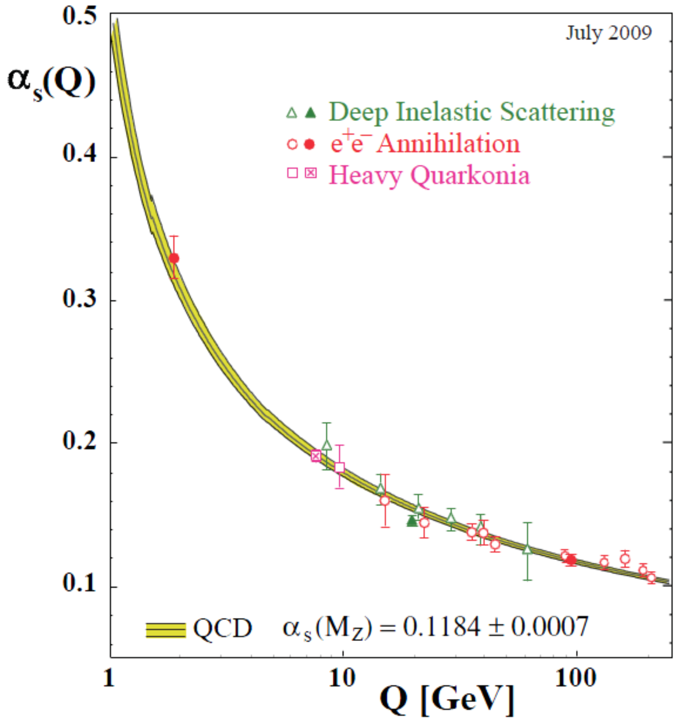

Figure 1.8: The dependence of the strong force coupling constant α_s on the momentum transfer scale Q. α_s increases asymptotically as Q decreases, leading to the hadronisation of partons emerging from pp collisions. The symbols represent the summary of experimental measurements and the curves result from QCD predictions for the combined world average value of α_s calculated for $Q = M_Z$. Details in [88].

It is the hadrons rather than the partons which interact with the detector material. However, the short-distance collision, which produces the partons, is the process of interest. A strategy for collecting the experimentally-observed hadrons into groups is therefore required, and furthermore, one that will yield similar results when applied to a theoretical calculation with partons. These grouping of particles are known as *jets* and are formed using a *jet algorithm*.

The jets often correspond to the *individual* partons from the hard-scattering process but this need not always be the case. Indeed, the algorithm itself, the algorithm's parameters, and the recombination scheme,[8] define the nature of the resulting jets and are therefore

[8] A set of rules for obtaining the four-momentum of the jet.

intrinsic to their description. These three elements are together known as the *jet definition*.

The "Snowmass accord" of 1990 [89] aimed to facilitate the comparison of jet cross-section measurements from different experiments, by providing "several important properties that should be met by a jet definition":

1. Simple to implement in an experimental analysis.
2. Simple to implement in the theoretical calculation.
3. Defined at any order of perturbation theory.
4. Yields finite cross-sections at any order of perturbation theory.
5. Yields a cross-section that is relatively insensitive to hadronisation.

The theorists and experimentalists at Snowmass proposed an actual jet definition, however many other definitions have been suggested in the intervening period. An excellent review is provided in [90], in which the jet *algorithms* are separated into two broad categories:

1. **Cone algorithms**, which were the first algorithms to be developed. They aim to find the direction(s) of dominant energy flow in an event, and around them place a cone of a certain radius in y-ϕ space, where y is the rapidity and ϕ is the azimuthal angle.[9]
2. **Sequential recombination algorithms**, which provide much more of a "bottom-up" approach, by taking a collection of energy deposits and combining them to produce jets.

Sequential recombination algorithms will be expounded below. First, however, it is necessary to introduce the concepts of infrared (IR) and collinear safety. IR-safe means that the output of the algorithm is insensitive to the presence or absence of additional soft particles radiated by the primary partons. A simple illustration of the output from

[9] ϕ is defined in Section 2.2.1.

IR-safe and IR-unsafe algorithms can be seen in Figure 1.9, in which two hard partons are produced in an event, with, for example, a W boson to balance momentum. In subfigure (a), the algorithm results in one jet being formed around each parton. A soft gluon is radiated from one of the partons in subfigures (b) and (c). The first case demonstrates the resulting behaviour of an IR-*unsafe* algorithm, since only one jet is formed around all three partons. However in subfigure (c), the chosen algorithm is IR-*safe*; the same two jets are formed as for the situation without soft gluon radiation in subfigure (a).

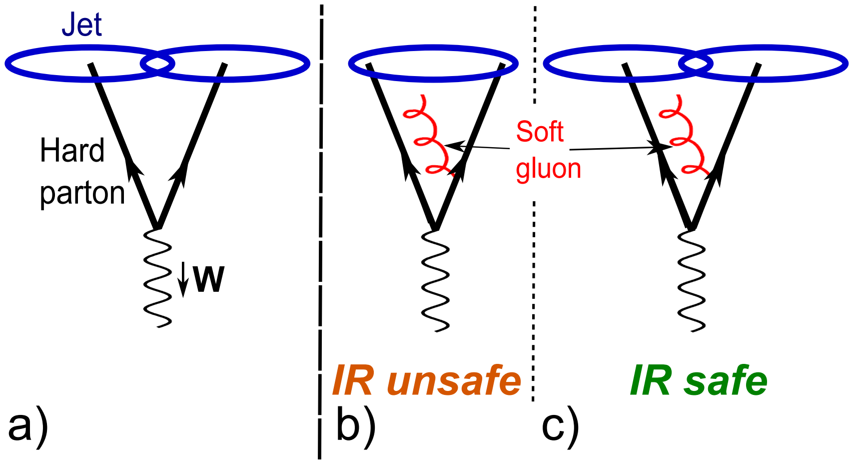

Figure 1.9: A demonstration of infrared safety. Subfigure (a) displays an event in which two hard partons and a W boson are produced back-to-back; the jet algorithm forms a jet around *each* parton. In (b) and (c), an additional soft gluon is now present, which is radiated from one of the partons. An IR-unsafe algorithm is demonstrated in (b), since now just one jet is formed around all three partons. However, in (c), the jet multiplicity is unaffected by the presence of the gluon and hence the algorithm used here is IR-safe.

Collinear safety means that the output is unaffected by the radiation of partons at very small angles with respect to the original one. These are known as collinear splittings since they result when a hard parton splits into two softer partons. Other partons may then be ranked as the hardest in the event, leading to the algorithm forming a different set of jets. The situation is demonstrated in Figure 1.10: in (a) there are three partons and the jet algorithm forms a single jet centered on the hardest parton. The collinear unsafe algorithm is illustrated in (b), where the hardest parton splits into two partons, which are then ranked as the softest in the event. Two jets are formed, centered on the two partons now newly ranked as the hardest. In (c), the algorithm is collinear safe since its output is unaffected by the splitting.

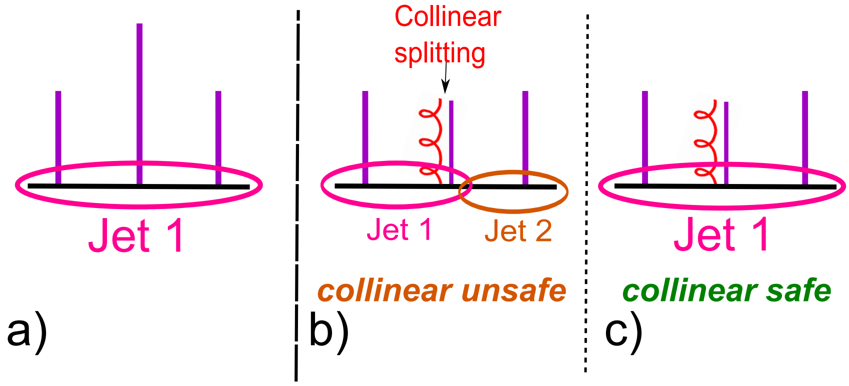

Figure 1.10: A demonstration of collinear safety. In (a), an event containing three partons (purple vertical lines) is displayed, which results in the recombination of a single jet by a jet algorithm. The collinear splitting of (b) results in a different configuration of final jets and hence the jet algorithm is collinear unsafe. However in (c), the algorithm is collinear safe because the final configuration of jets is the same as in (a). The lines representing the partons have a height which is proportional to their momentum. The horizontal axis indicates the rapidity.

The adherence to the concepts of IR and collinear safety is crucial for a jet definition since collinear splittings and soft emissions both involve non-perturbative effects making them difficult to predict, even at the level of their average effect on the resulting final state. Therefore the resulting jets should be insensitive to this additional radiation. Many cone algorithms were found to be IR and collinear unsafe and were therefore rarely used for data analysis. The seedless, infrared-safe cone (`SISCone`) algorithm [91] encompassed a solution to this problem, however it did not become the algorithm of choice in ATLAS, for reasons outlined in the next section.

Sequential recombination algorithms are all IR and collinear safe and are therefore widely used at hadron-hadron collider experiments. The recombination process is most clearly illustrated with the aid of an example such as in Figure 1.11, which displays the case of three input objects.[10] A distance measure, d_{ij}, between each pair of input objects is defined in Equation 1.5a. For each pair, this is compared to a second distance measure d_{iX} defined in Equation 1.5b. d_{iX} includes the user-defined *jet radius parameter* R which controls the size of the resultant jets. If $d_{ij} < d_{iX}$, then i and j are combined into a single intermediate jet. However, if $d_{ij} > d_{iX}$, the i^{th} object is set aside as a final jet.

[10]These input objects are groupings of energy deposits recorded by the calorimeter, described in Section 3.3.

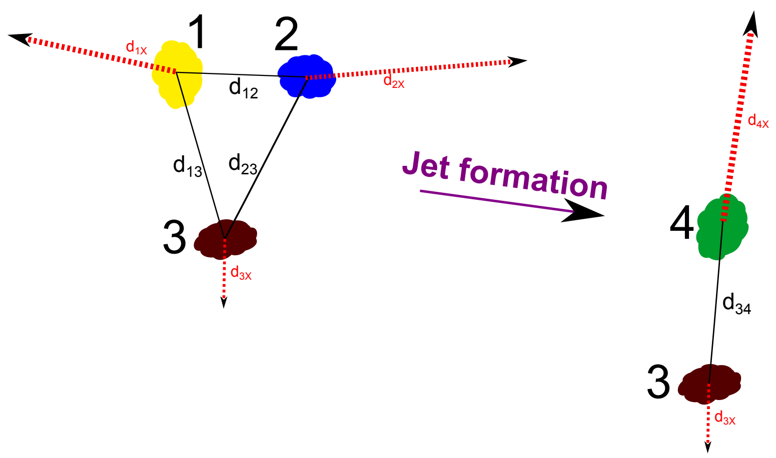

Figure 1.11: A simple illustration of jet formation using a jet algorithm. The upper left of the diagram contains three input objects which are supplied to the algorithm. The values of the relative distance measures d_{ij} and the distance measure d_{iX}, which depends on the jet radius parameter, determine whether the objects will be combined into jets. In this case, a jet (4) is formed from objects 1 and 2 and object 3 forms a jet in its own right.

In this simple case with three objects, the first stage of the recombination combines objects 1 and 2 into a single intermediate jet (labelled 4), since d_{12} is smaller than both d_{1X} and d_{2X}. Object 3 is then set aside as a final jet because $d_{3X} < d_{34}$. Object 4 will also therefore become a jet in its own right since there are no other objects with which it can combine.

$$d_{ij} = \min[p_{Ti}^{2n}, p_{Tj}^{2n}]\, \Delta R_{ij}^2 \tag{1.5a}$$

$$d_{iX} = p_{Ti}^{2n}\, R^2 \tag{1.5b}$$

where the separation of objects i and j in y-ϕ space is given by:

$$\Delta R_{ij}^2 = (y_i - y_j)^2 + (\phi_i - \phi_j)^2 \tag{1.5c}$$

n is an integer which takes the value -1, 0 or $+1$, defined by the user. The choice for this value may appear inconspicuous at first sight, but actually has a rather pronounced effect on the properties of the final jets. A value of $+1$ is used for the k_T algorithm.

Through inspection of Equation 1.5a, one can see that this algorithm will combine *soft* objects first and produce rather irregularly-shaped jets, as shown in Figure 1.12(a). If $n = 0$, the jet recombination will not depend on the kinematics of the input objects and therefore only an angular-ordering is used, with the closest objects being recombined first. The resulting *Cambridge-Aachen* (C/A) jets are also rather variant in size as seen in Figure 1.12(c). The anti-k_T algorithm [92] ($n = -1$) produces jets which are seeded by the hardest input objects. It was motivated by a desire to have jets which are more resilient with respect to soft radiation. They are therefore approximately conical in y-ϕ space, demonstrated in Figure 1.12(b). This uniform shape also makes the energy of these jets easier to calibrate [93].[11]

The radius parameter should not generally be considered as a measure of the jet size, since it is used *during* the reconstruction of the jets and the resulting jets are usually irregularly shaped. However, for the more regularly-shaped anti-k_T jets, R can be used as an approximation of the base radius of the jet "cone". In the vast majority of cases, including for the main body of this thesis, R usually takes a fixed value. However the novel use of a *variable* value for R in $t\bar{t}$ resonance searches is explored in Chapter 7.

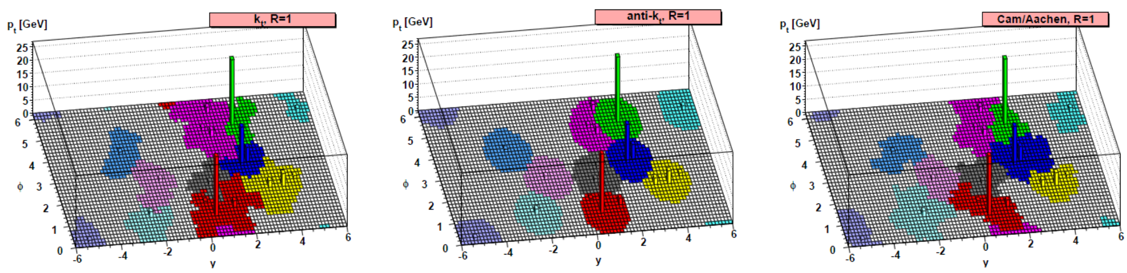

(a) (b) (c)

Figure 1.12: Exemplary jets reconstructed with the following algorithms: (a) k_T, (b) anti-k_T and (c) Cambridge-Aachen. Anti-k_T jets are noticeably the most regular in shape. The events are sample parton-level events, generated with HERWIG, taken from [90].

In 2010, ATLAS systematically compared the anti-k_T, k_T and `SISCone` algorithms [94]. A number of measures were used, including: CPU time and memory consumption; jet reconstruction efficiency and purity; trigger efficiency; sensitivity to the underlying event

[11] Jet energy calibration is described in Section 3.3.2.

(UE) and to noise; and the top quark reconstruction efficiency. Anti-k_T was found to be the most performant in the majority of measures. The exceptions to this were: (1) for noise suppression, where the performance was equal *if* noise is suppressed in the formation of the jet constituents; (2) for UE sensitivity, where anti-k_T was of intermediate performance due to the jets being of intermediate average size between the `SISCone` and the k_T jets. Hence anti-k_T was adopted as the default jet algorithm for all analyses at ATLAS and is the primary jet algorithm used in the studies described in this thesis. The practicalities of reconstructing anti-k_T jets are briefly discussed in Section 2.3.

The four-vector of the jet formed during recombination is obtained by addition of the four-vectors of the jet constituents. The global properties of the jet, such as its mass m_j, therefore correspond to the properties of this jet four-vector.

1.4.2 Substructure of jets

The above discussion of the algorithms relates to the reconstruction of jets as whole objects. However, the advantages of using jet *substructure* for improving the identification of boosted top quarks have been highlighted for some time. Examples of such methods are discussed in [95, 96, 97, 98].

Figure 1.13 illustrates typical pattern of energy deposits resulting from a hadronically decaying top quark[12] and from the hadronisation of light quarks or gluons. The events were generated using the PYTHIA v6.4 generator[13] and an idealised finely-grained calorimeter is used in the detector simulation, with a cell size of $\Delta\eta \times \Delta\phi = 0.1 \times 0.1$[14] The z-axis represents the transverse energy recorded in each cell. Jets have been formed from these deposits, using the Cambridge-Aachen algorithm with $R = 0.6$. The different colours are used to rank the p_T of the jets: red for hardest, green for second hardest and blue for third hardest.

[12] Also known as simply a hadronic top quark.
[13] Event generation is described in Section 2.4.
[14] Pseudorapidity η is an alternative variable to the rapidity y and is defined in Section 2.2.1.

Three jets are reconstructed in the case of the top quark (a), and each jet contains energy deposits with roughly equivalent energy. However, for the light quark / gluon cases there are different numbers of energy deposits: n distinct deposits are produced, with a probability $\mathcal{O}(10^{1-n})$ [99]. Therefore, there is a small probability that light quarks and gluons can result in a pattern of jets similar to that due to a top quark. Crucially, however, the relative values of the energies of the jets in one of the light quark / gluon cases (Figure 1.13(c)) are very different compared to those in the case of the top quark.

The search presented in this thesis exploits the ability to decompose a large jet with a value of R of the order of unity, into subjets and study the relative energies of these subjets. This enables one to determine if the jet contains the decay products of a top quark as opposed to a light quark or gluon. In this way, the contribution of events due to standard model processes, such as a W boson produced in association with jets, can be substantially reduced. This strategy was proposed in [100, 101] and first applied to an ATLAS Monte Carlo study on top quarks [102].

In practice, the decomposition is performed on jets which have been reconstructed using the anti-k_T algorithm, to exploit its previously discussed advantages such as producing regularly-shaped jets. The topo-clusters which make up a particular anti-k_T jet are then fed to the k_T algorithm for recombination. The k_T algorithm is used because of the particular order in which it performs the clustering: if a jet contains the products of a two-body decay of a heavy particle, the final clustering step will usually be to combine these two decay products [103]. This final clustering step has an associated variable obtained from Equation 1.5a, called the first splitting scale, or $\sqrt{d_{12}}$:

$$\sqrt{d_{12}} = \min[(p_{T_1}, p_{T_2})] \times \Delta R_{12} \tag{1.6}$$

where 1 and 2 represents the two subjets that are present just before the final recombination into a single jet, p_{T_i} is the transverse momentum of the i^{th} subjet and ΔR_{12} is their separation in y-ϕ space. The typical values of $\sqrt{d_{12}}$ for jets containing the decay products of heavy particles corresponds to approximately half the parent particle's mass. Jets initi-

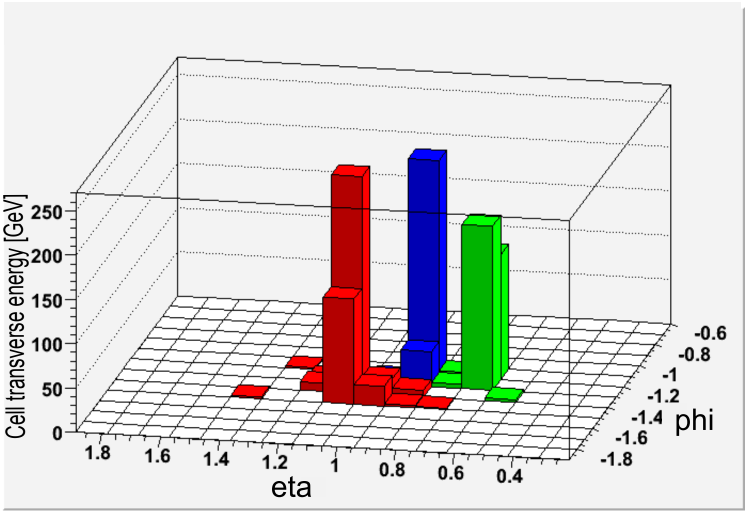

(a) Top quark

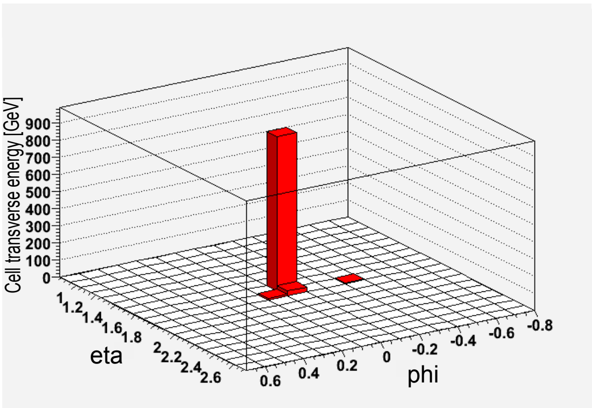

(b) Light quark or gluon

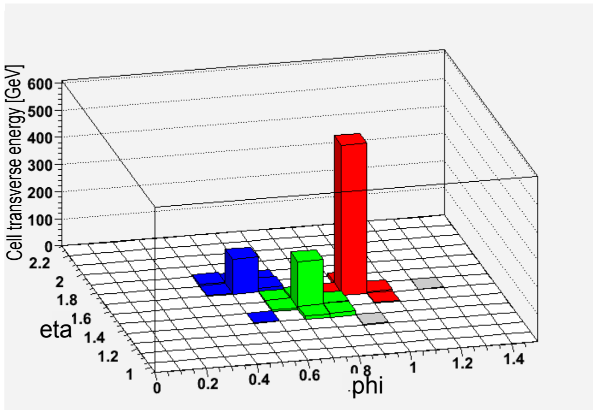

(c) Light quark or gluon

Figure 1.13: Patterns of energy deposits in an idealised calorimeter having cell size $\Delta\eta \times \Delta\phi = 0.1 \times 0.1$. The deposits have been recombined into jets using the Cambridge-Aachen algorithm with $R = 0.6$ and the different colours represent the different jets (red is hardest, green is 2^{nd} hardest, blue is 3^{rd} hardest). Any deposits coloured grey were not recombined. The particle inducing the deposits is either (a) a top quark or ((b) and (c)) a gluon / light quark. There are three distinct regions of energy deposits in the case of the top quark. However, the light quark or gluon can result in various patterns of energy deposit, including one similar to that from the top quark with a probability $\mathcal{O}(0.01)$. The use of large jets ($R \approx 1$) with an analysis of their substructure can be employed to discriminate between cases (a) and (c) by studying the relative transverse momenta of its subjets.

ated by light quarks and gluons are expected to have values of $\sqrt{d_{12}}$ below ≈ 20 GeV [104]. This features provides a method to distinguish between different types of initiating particle. The specific application of this method to searches for $t\bar{t}$ resonances is detailed in Section 4.1.4.

1.5 Summary

The top quark is integral to searches for phenomena which cannot be explained within the standard model. This thesis is dedicated to the search for resonant production of top-antitop pairs, particularly those with a mass of at least $1\ \mathrm{TeV}$. Two particular theories which give rise to these $t\bar{t}$ resonances have been outlined in this chapter. However, the use of these models is solely to aid comparison with results from similar searches and this particular search strives to be model-independent. Resonances at the TeV-scale produce top quarks with a very high transverse momentum which can be identified through the use of jet substructure techniques. The first application of these techniques in a search for $t\bar{t}$ resonant production using ATLAS data is one of the major aims of this work.

Chapter 2

Data collection and Monte Carlo simulation

2.1 The Large Hadron Collider

The LHC at CERN is by far the most powerful collider of subatomic particles built to date. The aims of the main associated experiments (ALICE, ATLAS, CMS and LHCb) are to test the standard model to unprecedented levels of precision and search for evidence of BSM phenomena.

Two counter rotating beams of protons or heavy ions are collided at four interaction points around the $27\ \mathrm{km}$ circumference. Figure 2.1 shows the accelerator chain: the particles are accelerated to full energy via the LINAC2, booster, proton synchrotron (PS), super PS (SPS) and finally within the LHC. They are grouped into bunches in order to be accelerated by the oscillating RF field. The bunch interval is designed to be $25\ \mathrm{ns}$, although this was held at a maximum of $50\ \mathrm{ns}$ for the data collected for this study, limiting the number of bunches per beam to 1380 [105].

Circulation of proton beams deemed sufficiently stable for physics analysis was first achieved in December 2009. The design energy is $7\ \mathrm{TeV}$ per beam, although this is not

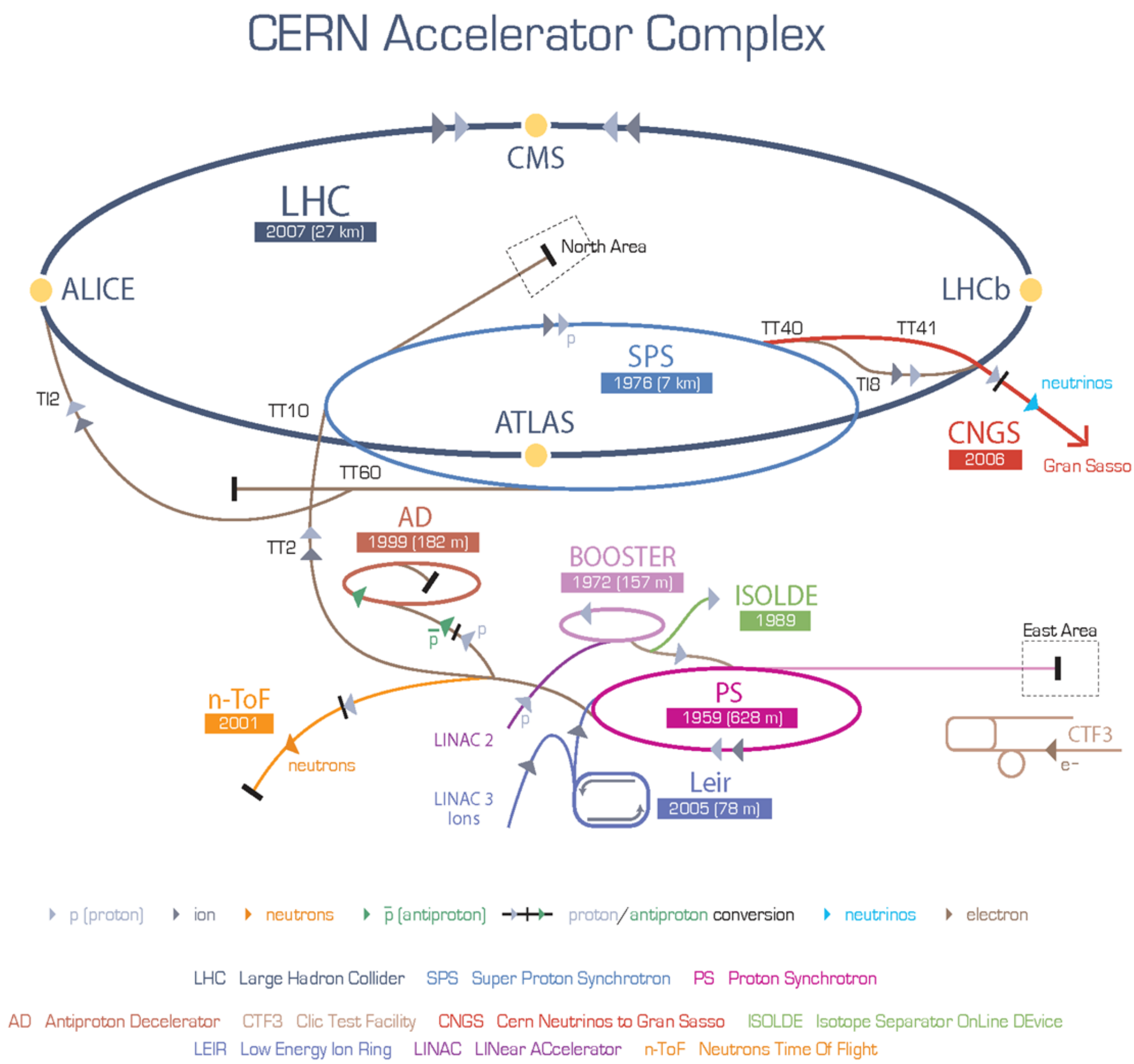

Figure 2.1: The CERN accelerator complex. The relevant systems for pp collisions are the LINAC2, booster, proton synchrotron (PS), super PS (SPS) and LHC. The four main experiments are also shown, at roughly equidistant points around the LHC's ring.

foreseen until at least 2014 due to constraints imposed by the magnet system. A reduced beam energy of 3.5 TeV was achieved in 2010, continued in 2011 and subsequently increased to 4 TeV for the 2012 programme. The data analysed in this thesis were all collected at a beam energy of 3.5 TeV.

The maximum instantaneous luminosity to date is currently lower than the design value of 10^{34} cm^{-2} s^{-1} [106],[1] although a record of 7.73×10^{33} cm^{-2} s^{-1} was achieved during August 2012. This contributed to a total integrated luminosity, recorded by ATLAS by the end of 2012, of 5.25 fb^{-1} at a 7 TeV centre-of-mass energy, and 21.7 fb^{-1} at $\sqrt{s} = 8$ TeV [107]. Figure 2.2(a) displays the maximum instantaneous luminosity versus day delivered to ATLAS during 2011; it increased by an order of magnitude whilst the data used in this thesis were collected. Figure 2.2(b) then shows the cumulative luminosity versus day recorded by ATLAS, the rate of which was ≈ 1 fb^{-1} per month. Finally, Figure 2.2(c) illustrates the maximum value, for each day of data-taking, of the number of interactions per bunch crossing averaged across all bunch crossings in a discrete time period[2] $\langle\mu\rangle$.

The maximum $\langle\mu\rangle$ is a measure of the amount of *pile-up* present in a particular event. That is, energy deposits resulting from events other than the one under consideration which caused the trigger to fire.[3] There are two types: *in-time*, arising from other pp interactions in the same bunch crossing; and *out-of-time*, where the deposits result from either preceding or subsequent bunch crossings. At a temporal bunch spacing of 50 ns, effects due to both types of pile-up are present in the events of interest. Techniques used to mitigate or account for these effects are discussed throughout this thesis.

[1]With a bunch interval of 25 ns.
[2]This time period is known as a luminosity block and is defined in Section 2.2.5.
[3]An explanation of trigger terminology is provided in Section 2.2.5

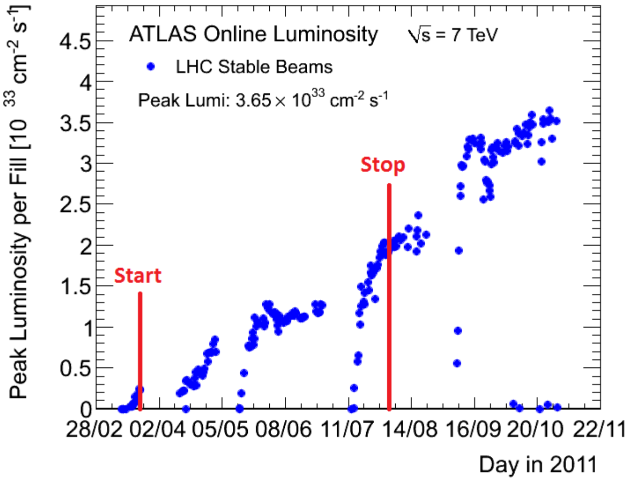

(a) Maximum instantaneous luminosity versus day delivered to ATLAS in 2011.

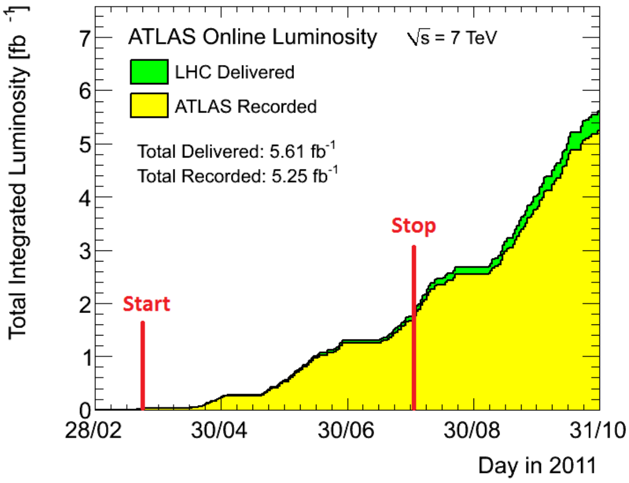

(b) Cumulative luminosity versus day.

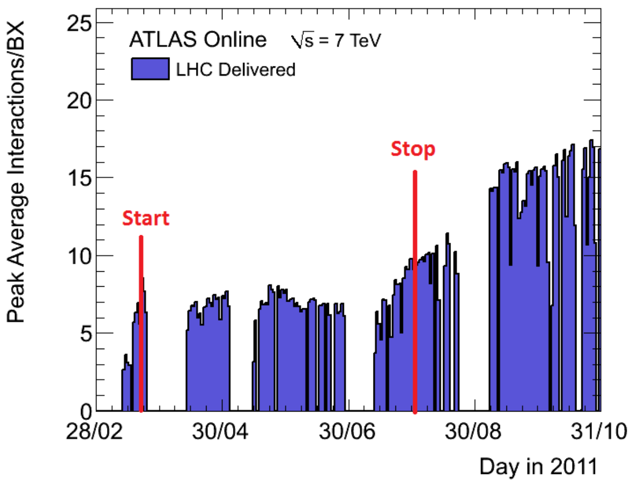

(c) Mean maximum number of events per beam crossing, which remained relatively low and stable for the data analysed in this thesis.

Figure 2.2: Instantaneous and integrated luminosity, together with the peak average interactions per bunch crossing, during 2011. *Start* and *Stop* indicate the boundaries of the data-collection period relevant to this thesis.

2.2 The ATLAS detector

ATLAS[4] is one of seven experiments located around the LHC ring. The detector has been designed to search for a wide variety of signatures, including that of the Higgs boson and of postulated BSM phenomena. For this reason it is often described as a general-purpose detector with a balance in performance between all sub-detectors; the purpose and specifications of each are described below. A complete account of the detector can be found in [108] and a diagram of its entirety is shown in Figure 2.3.

2.2.1 Co-ordinate system and kinematic terminology

The co-ordinate system is right-handed, with the x-axis pointing towards the centre of the LHC ring and the y-axis pointing upwards. The azimuthal angle ϕ is defined in the x-y plane, with $\phi = 0$ lying along the positive x-axis and increasing clockwise when looking in the positive z direction. Pseudorapidity η is used to describe the direction of a particle relative to the beam axis and is therefore also used to describe the layout of the detector. It is defined as:

$$\eta = -\ln\left[\tan\left(\frac{\theta}{2}\right)\right] \tag{2.1}$$

where θ is the polar angle, measured from the z-axis. In the central region of the detector perpendicular to the beam, $\theta = \pi/2$ and $\eta = 0$, whereas in the forward direction close to the beam line, θ tends to zero and η tends to infinity. In this analysis, no physics objects are reconstructed beyond $|\eta| = 3$ and therefore complications arising from η tending to infinity are not encountered.

As seen in Chapter 1, *rapidity* is the variable used to describe the directions of particles when the detector is not being taken into account. For example, for the purposes of determining parton distribution functions and for jet recombination. This is because

[4] A Toroidal LHC Apparatus.

it is invariant under boosts along the z-axis, which is a particularly important feature at hadron-hadron colliders where the p_z of the colliding partons cannot be determined. Rapidity depends on the kinematics of the particles whereas pseudorapidity is a purely geometrical quantity. The latter is therefore favoured when describing the detector and the location of signals within it. Pseudorapidity is approximately equal to the rapidity for particles which have $p \gg m$ and the two are equivalent for massless particles.

Although the longitudinal momentum p_z of the partons in the initial state are unknown, their momentum perpendicular, or transverse, to the beam-line is zero to a good approximation. Therefore one can deduce the *transverse* momenta p_T of particles which evade direct detection, such as neutrinos, through the requirement of momentum balance in the x-y plane. The p_T of *charged* particles is measured using the inner detector and the muon system, as discussed below. For all other detectable particles, it is not measured directly. Instead, deposits of energy in the calorimeters are projected onto the transverse plane. This quantity is known as the transverse energy, E_T, and is equal to $E \sin\theta$.

The transverse momenta (or transverse energies) of all the detected particles are then summed vectorially. The negative value of this sum is termed the missing transverse momentum and usually denoted (albeit somewhat inaccurately) as E_T^{miss}. The reconstruction of E_T^{miss} is described in Section 3.4.

2.2.2 Inner detector

The inner detector (ID) is located at the core of ATLAS and records the tracks and vertices left by charged particles, with $p_T > 0.5$ GeV, from the LHC beam-pipe to the calorimeter system. The coverage in η extends to 2.5 in both the forward and backward directions. A solenoid envelopes this entire region, to bend the tracks of the particles by means of a 2 T magnetic field.

It is imperative for measurements to be made with an intrinsic accuracy at the sub-millimetre scale, in order to identify the decay vertices of short-lived particles such as τ-

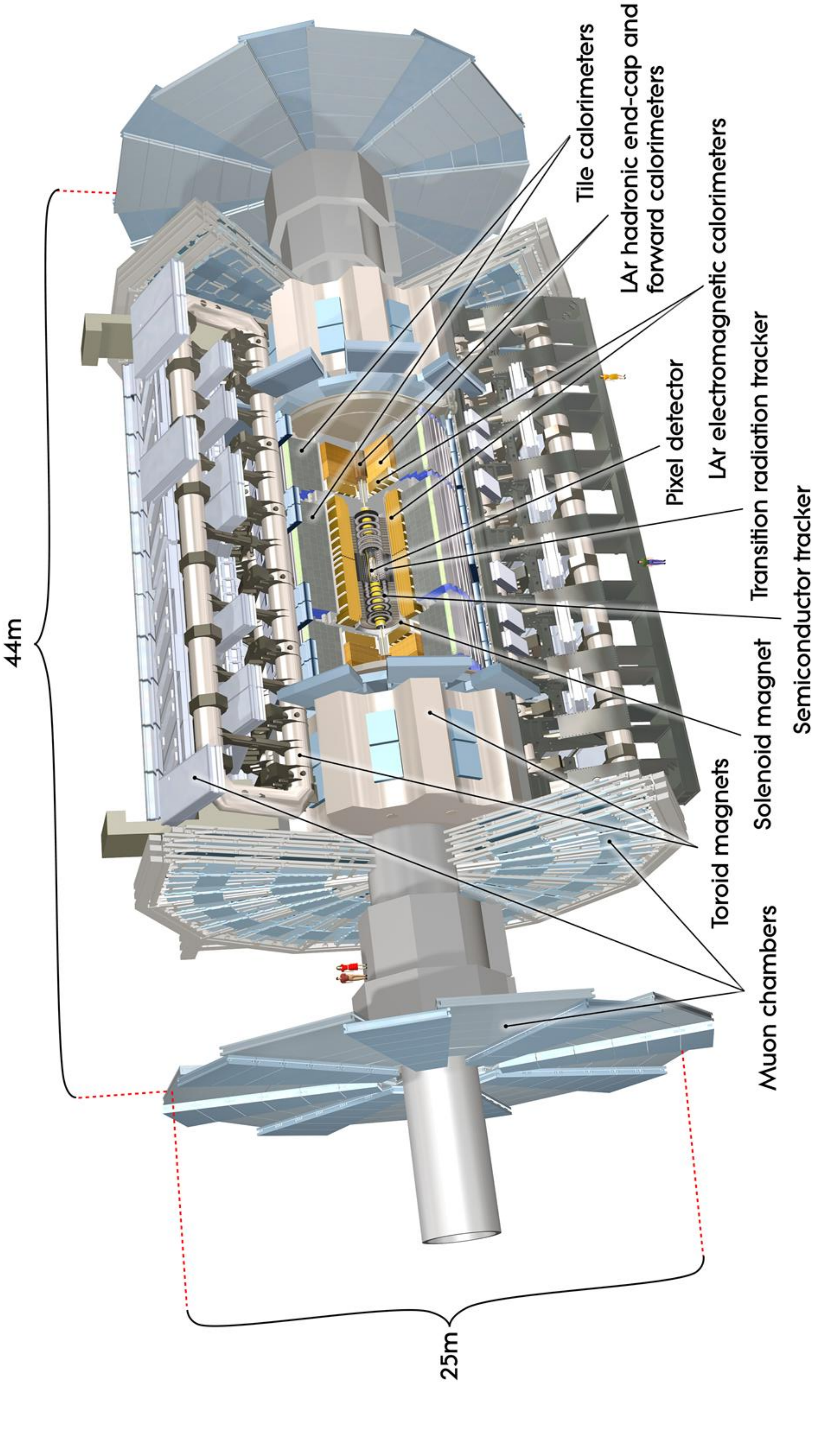

Figure 2.3: The ATLAS detector, with individual sub-systems labelled. The inner detector is located at the core, surrounded by the calorimetry system and then the muon chambers.

leptons and hadrons containing a bottom quark (B-hadrons). Identification of the latter is a particularly useful technique in the selection of events involving top quark production, whose final state involves such B-hadrons. This is known as *b-tagging*, and is described in Section 3.3.4.

There are three ID components, which successively enclose each other: the pixel detector; the semiconductor tracker (SCT); and the transition radiation tracker (TRT). The design of each element is tailored to its specific environment and provides a complementary whole for the ID. Figure 2.4(a) displays a semi-cylindrical view of its interior.

The pixel detector has the highest granularity of all of the sub-detectors since it is located closest to the beam pipe and therefore closest to the decay vertices of the aforementioned short-lived particles.[5] It utilises silicon sensors with read-out across 80 million channels. The resulting intrinsic accuracies in the barrel section are $104\ \mu\mathrm{m}$ (in the R-ϕ plane) and $115\ \mu\mathrm{m}$ in the z-direction. The SCT also employs silicon technology in the form of four (eight) layers of microstrip detectors in the barrel (end-caps). The design ensures four precision measurements per track, giving a resolution in the barrel of $17\ \mu\mathrm{m}$ (in the R-ϕ plane) and $580\ \mu\mathrm{m}$ in z. There are 6.3 million read-out channels.

The TRT is composed of straw tubes, each $4\ \mathrm{mm}$ in diameter, aligned with the beam axis in the barrel section and radially in the two end-caps. It provides, typically, 36 hits per track in the region to $|\eta| = 2.5$, which enables tracks that have been reconstructed from hits in the silicon systems to be connected with TRT hits. However, the achievable accuracy is limited to $130\ \mu\mathrm{m}$ per straw, and measurements are possible in the R-ϕ direction only. The TRT makes a significant contribution to electron identification by means of transition radiation produced as charged particles pass through the xenon-based mixture of gases in the tubes. A threshold of $5\ \mathrm{keV}$ is applied to the output signal to identify highly energetic photons resulting from this transition radiation.

[5] The most central layer of pixels is at a radius of $51\ \mathrm{mm}$ from the nominal interaction point.

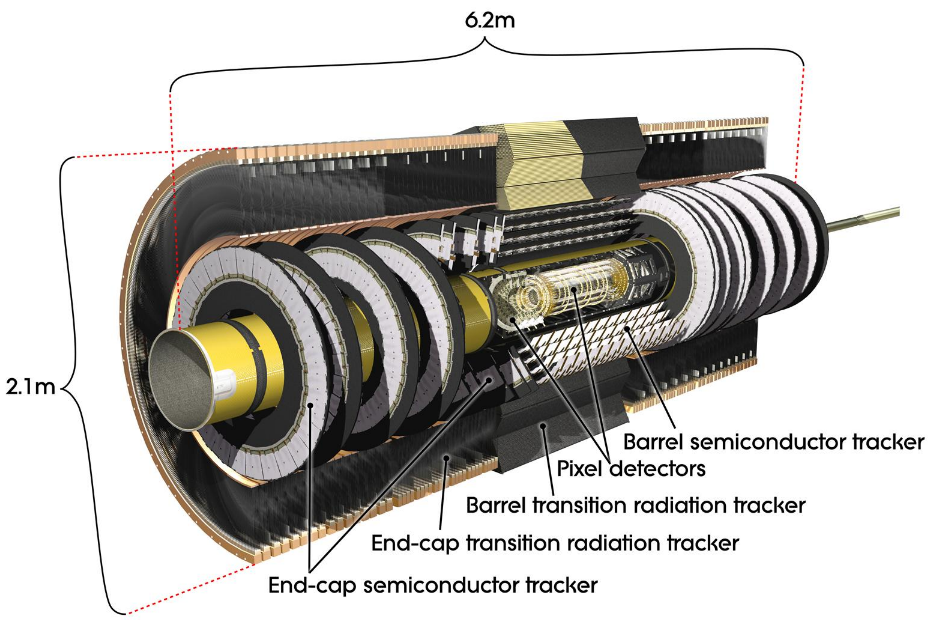

(a) The inner detector, with the three sub-detectors identified.

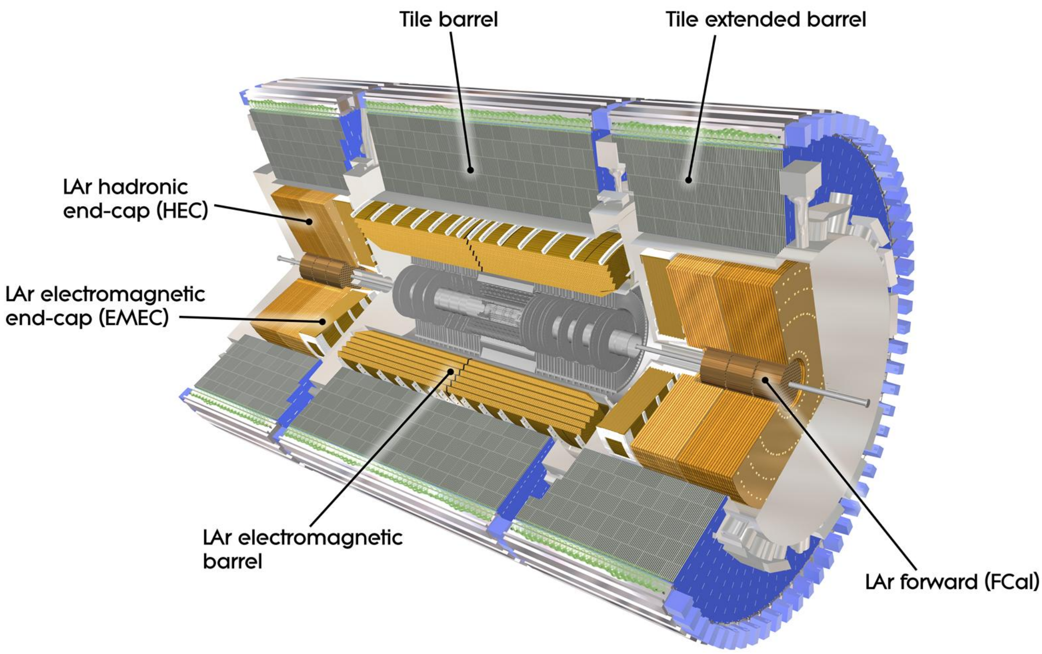

(b) The calorimeter system, with the inner detector at the centre. *Tile* is the main hadronic calorimeter, detailed in the text.

Figure 2.4: Detailed layout of two ATLAS sub-systems: the inner detector and calorimeters.

2.2.3 Calorimeter system

Separate electromagnetic and hadronic calorimeters constitute the ATLAS calorimetry, which measures the energy of particles interacting via the electromagnetic and/or strong forces. This energy measurement is obtained at the *electromagnetic scale* (EM-scale), which correctly accounts for the energy deposited by EM showers. It was derived using test-beam measurements of electrons interacting with the calorimeter material, in a process described in section five of [109].

The electromagnetic (EM) calorimeter extends to $|\eta| = 3.2$. Lead and stainless steel are used as the absorbing materials; liquid argon (LAr) was chosen for the sampling due to its radiation hardness and read-out speed. The absorber plates have an accordion geometry, for complete ϕ symmetry without gaps.

Very precise measurements of the EM shower position are achievable due to the fine granularity, having a maximum of $\Delta\eta \times \Delta\phi = 0.025 \times 0.025$ at the depth at which the largest number of secondary particles are produced. Front-end boards (FEBs) contain the electronics for amplifying, shaping and digitising the signals. Various operational problems were encountered during the period in which data for this study were collected: several FEBs were inactive between 30 April and 13 July 2011 in the region $0.0 < \eta < 1.5$ and $-0.8 < \phi < -0.6$;[6] there were interruptions to localised regions of the high-voltage supply across the active medium; and noise was encountered in many of the cells. The necessary treatment of such problems during data analysis is described in Chapters 3 and 4.

The hadronic system surrounds the EM calorimeter. Iron absorber plates with plastic scintillating tiles are used in the central region ($|\eta| < 1.7$), hence the common name of *tile* calorimeter. In the forward region, $1.7 < |\eta| < 3.2$, parallel copper plates, with LAr as the active medium, are used due to the greater radiation resistance required. The granularity is somewhat coarser than in the EM calorimeter, generally being $\Delta\eta \times \Delta\phi =$

[6] Henceforth known as the "LAr hole" problem

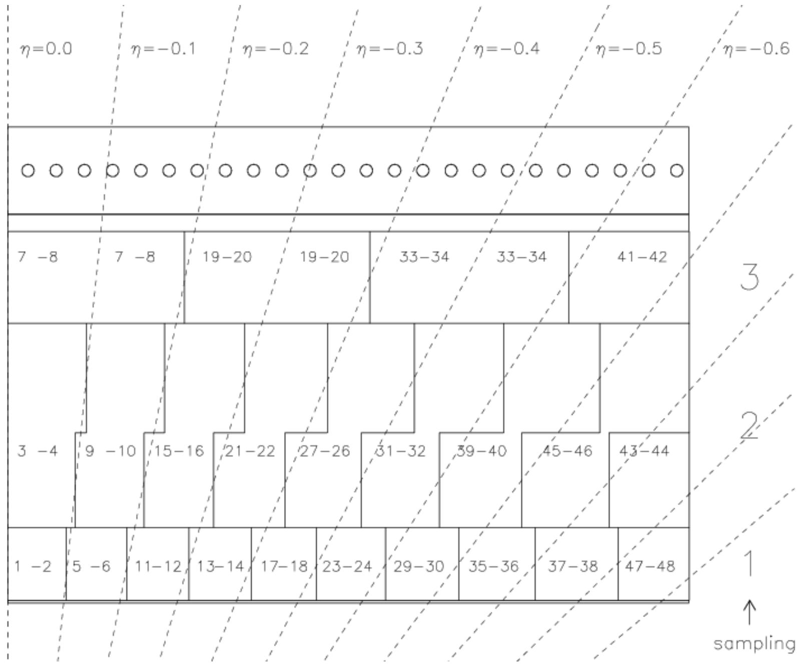

Figure 2.5: An R-z section of a test module of the hadronic tile calorimeter. The three depth segmentations (samplings) are shown, the third sampling having the coarsest granularity of $\Delta\eta \times \Delta\phi = 0.2 \times 0.1$. The numbers in the blocks refer to the read-out channels. Taken from [110].

0.1×0.1 for $|\eta| < 2.5$. The exception to this is in the third longitudinal segment (*sampling*) of the central region, where a coarser granularity of $\Delta\eta \times \Delta\phi = 0.2 \times 0.1$ is used as shown in Figure 2.5.

The calorimetry is completed by LAr technology in the radiation-dense forward region, $3.1 < |\eta| < 4.9$. Three separate cylindrical sections are positioned consecutively along the beam pipe. The first, `FCal1`, is an EM calorimeter with copper chosen as the absorbing material in order to optimise the resolution of the energy measurements. `FCal2` and `FCal3` are hadronic calorimeters with a tungsten absorber to minimise the lateral spread of the hadronic showers. The "crack" between the barrel and end-cap sections of the calorimetry system is within $1.37 < |\eta| < 1.45$ and contains many services for the ID and central EM calorimeter.

The energy resolution of jets has a significant contribution to the total systematic uncertainty associated with the result of this analysis, as discussed in Section 6.3. This is due to the fact that hadrons incident on the ATLAS calorimeters will be measured with a lower energy than for particles which interact only electromagnetically. In other words, the *response* to hadrons is lower than that for electrons or photons. A combination of factors causes this reduced response. First, the energy deposited in the calorimeters is detected by means of *photons* that are collected in scintillating material. Secondly, around 20 – 35 %[7] of the average energy dissipated by hadrons is in fact non-electromagnetic or non-ionising in nature and therefore essentially invisible [111, 112]. Instead, it is dissipated via nuclear-recoil, nuclear break-up and neutrons which gradually lose energy on the timescale of nanoseconds. It is the *fluctuation* of this invisible fraction which adversely affects the jet energy resolution, together with, to a lesser extent, inactive material in the calorimeters [113].

Procedures to make the response to hadrons equal to that of electrons or photons can be implemented in the detector hardware and/or the analysis software. This is known as *compensation*. A common detector-compensation procedure is to insert depleted uranium-238 absorber plates in the calorimeter [114]. The nuclear fission processes induced by incident hadrons in such a material yield additional, soft photons which are collected by the scintillating material. Therefore some of the energy arising from nuclear excitations/break-up is recovered, which would otherwise go undetected.

The strategy of detector-compensation was considered in the design of the ATLAS hadronic calorimeter, since it has the potential to significantly improve the resolution of the measurements provided by the calorimeter. The fractional jet transverse momentum resolution can be parameterised as:

$$\frac{\sigma_{p_T}}{p_T} = \frac{S}{\sqrt{p_T}} \oplus \frac{N}{p_T} \oplus C \tag{2.2}$$

N parameterises fluctuations due to noise and due to energy deposits from multiple proton-proton interactions; C encompasses any fluctuations that are a constant fraction of the energy deposited; S parameterises stochastic fluctuations in the amount of energy

[7] This fraction decreases with the energy of the incident hadron [111] and is also highly dependent on the calorimeter's absorbing material.

sampled from the jet hadron shower [113]. Compensation through the use of depleted uranium can reduce the value of S from $50\ \%$ to $30\ \%$ [115]. However, the benefits of a compensating hadronic calorimeter are severely limited if the EM calorimeter remains non-compensating. The presence of compensating material in the latter is detrimental for the measurement of the energy and direction of hard photons emerging from physics processes of great interest, such as a Higgs boson decaying to two photons. This, combined with the fact that safety precautions are required for the handling of depleted uranium [116], resulted in the choice to maintain a strategy of non-compensation in the detector hardware. However, the ATLAS collaboration has developed sophisticated software-compensation techniques to recover the energy of incident hadrons; these are discussed in Section 3.3.2.

2.2.4 Muon system

The muon spectrometer (MS) completes the detector composition. It is designed to provide a stand-alone measurement of muon momentum, with a resolution of around $4\ (12)\ \%$ for muons with a p_T of $100\ (1000)\ \mathrm{GeV}$. Superconducting toroid magnets, operating with a nominal current of $20.4\ \mathrm{kA}$ and a field of approximately $0.5\ \mathrm{T}$, deflect the muon trajectories predominantely in the η-direction. The magnetic field has roughly constant $\oint B.dl$ in the region $|\eta| < 2.7$, although there is a significant drop at $1.4 < |\eta| < 1.6$ due to the transition between the barrel and the end-caps.

The muon trajectory is measured in the η-direction at three stations, the vast majority of which are filled with monitored drift tubes (MDTs) up to $|\eta| = 2$. At $\eta \approx 0$ and at $|\eta| \approx 1.2$, there are a reduced number of muon chambers due to, respectively, gaps for detector services and the transition region between the barrel and end-cap chambers. The precision with which the η co-ordinate can be measured is typically better than $100\ \mu\mathrm{m}$. Cathode strip chambers (CSCs) are used in the forward region ($2 < |\eta| < 2.7$) due to their enhanced counting rate of $1\ \mathrm{kHz/m^2}$. They additionally provide a coarse measurement of the ϕ co-ordinate, with a resolution of $1\ \mathrm{cm}$. The entire MS is illustrated in Figure 2.6(a) and with detail in Figure 2.6(b).

The trigger system for muons is made up of resistive plate chambers (RPCs) in the barrel ($|\eta| < 1.05$) and thin gap chambers (TGCs) in the end-caps ($1.05 < |\eta| < 2.4$). It measures the muon tracks in two orthogonal projections with a spatial resolution of around 1 cm and temporal resolution of 1 ns. The RPCs and TGCs can be seen in Figure 2.6(b), lying on both sides of the blocks of MDTs. The spatial coverage of the trigger system is about 99 % in the end-cap regions and 80 % in the barrel region. The reduced value in the barrel region is mainly due to a gap at $\eta = 0$ to provide spaces for services of the ID and calorimeters and for the support feet, also visible in Figure 2.6(a).

2.2.5 Trigger and data acquisition systems

The ATLAS trigger faces an unprecedented challenge. Rare events must be selected from amongst background processes occurring at a much higher rate, thereby reducing a bunch crossing rate as high as 40 MHz to a maximum event storage rate of ≈ 400 Hz. This is achieved by three successive levels: level 1 (L1), level 2 (L2) and event filter (EF). The latter two are together known as the high-level trigger (HLT).

The L1 trigger is hardware-based, enabling each event to be processed in as little as 2.5 μs. There are up to 256 different configurations, or *items*, at any one time and events can independently pass or fail each item simultaneously. If the event passes an item, it is said to have *fired* the trigger. The L1 trigger is divided into two systems, `L1Calo` and `L1Muon`, based on the sub-detector providing the information.

`L1Muon` uses the measurement of trajectories in the muon trigger detectors. The η-ϕ co-ordinates are measured by the RPCs (in the barrel) and the R-ϕ co-ordinates are measured by the TGCs (in the end-caps). This enables the trigger to estimate the muon p_T, which is passed to the HLT together with the spatial co-ordinates. Essentially, the trigger searches for patterns of hits consistent with high p_T muons originating from the interaction region; the temporal resolution is sufficiently high that it can unambiguously identify

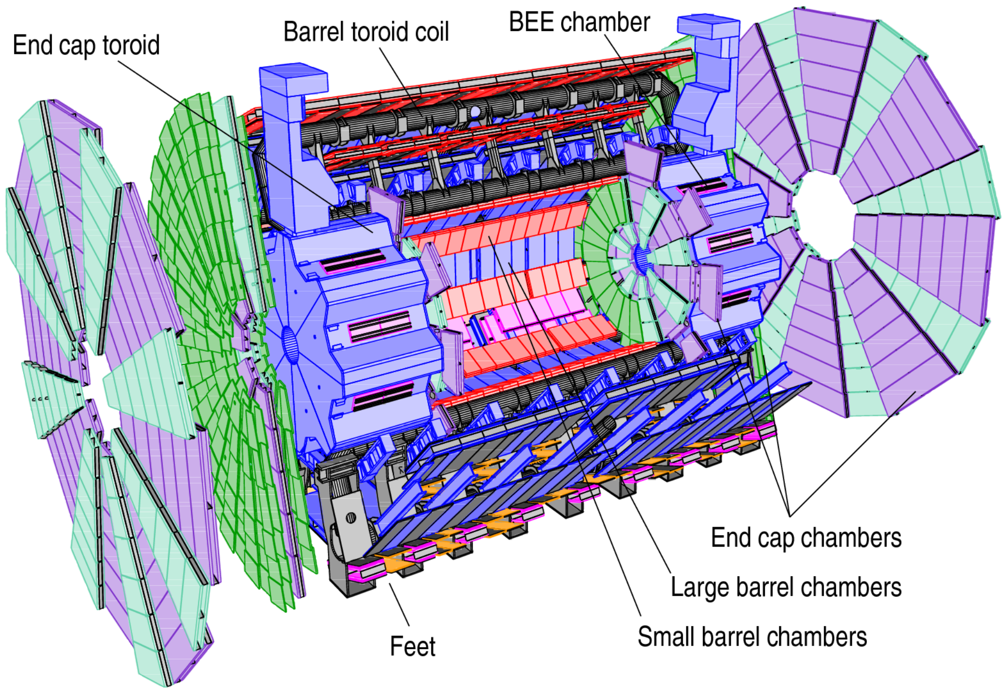

(a)

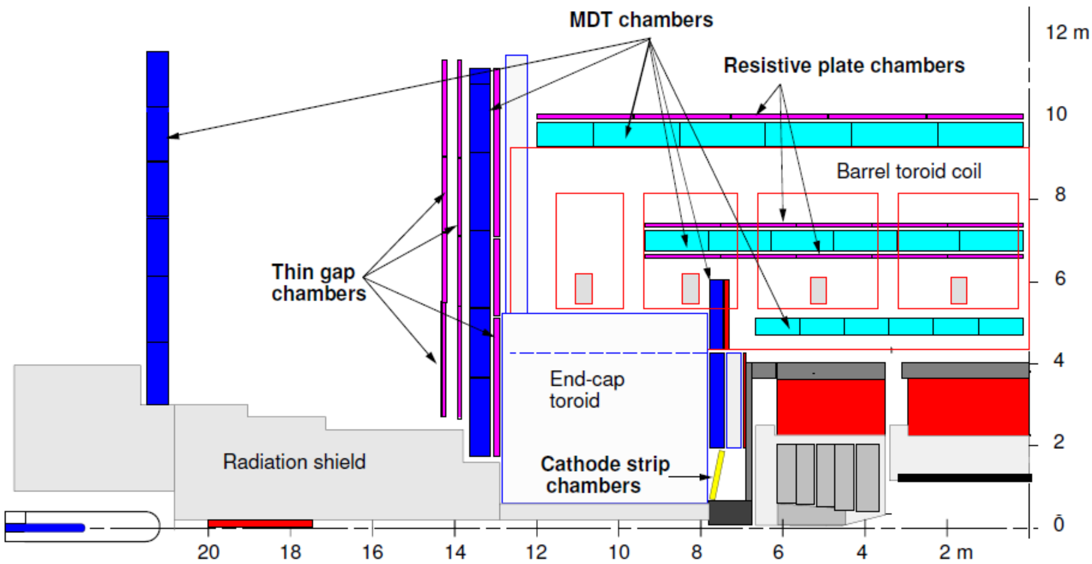

(b)

Figure 2.6: Schematic drawings of the muon spectrometer, (a) whole and (b) a section in detail, with distances in the R-z plane shown. The MDT and cathode strip chambers provide precision measurements of the muon trajectory. The thin gap and resistive plate chambers are part of the trigger system. BEE stands for "barrel end-cap extra", which are additional MDT chambers to provide measurements of tracks passing from the barrel to the end-caps. Bending of the muons in the η direction is produced by the toroid magnets. The feet provide support.

the bunch crossing from which the candidate muon originated.

`L1Calo` aims to identify signatures from high p_T electrons, photons, hadrons and τ-leptons decaying hadronically. Coverage is within the region $|\eta| < 2.5$ which corresponds to the extent of fine-granularity cells in the EM calorimeter. The E_T is measured in approximately 7200 *trigger towers* of size $\Delta\eta \times \Delta\phi = 0.1 \times 0.1$, which receive signals from both the EM and hadronic calorimeters. Clusters of energy are formed if the total E_T in a window of 4×4 towers passes a certain threshold. They may also have an isolation requirement placed on them, which is the total E_T in the 12 surrounding towers. However, this is *not* the case for any of the trigger items used to collect the data analysed in this study. Additionally, the clusters are classified as EM or hadronic. The former simply consider towers in the EM calorimeter. The latter combine towers in both the EM and hadronic calorimeters.

`L1Calo` also includes a jet trigger. The associated algorithm sums the E_T in overlapping windows of 2×2, 3×3 or 4×4 trigger towers. This sum must pass a pre-defined threshold. Multiple-counting of candidates is avoided by requiring the window to surround 2×2 trigger towers which contain a local maximum of the contained summed E_T. The location of this 2×2 local maximum also defines the coordinates of a so-called jet *region of interest* (RoI). The jet trigger extends to $|\eta| = 3.2$, corresponding to the limit of the EM calorimeter acceptance. The following event-level trigger items are also constructed: the scalar sum of the E_T of each jet element, and the E_T^{miss} when considering all jet elements in the event.

Overall, the L1 trigger bases its decision on the multiplicity of trigger objects passing various thresholds and/or whether an event-level item passes a certain threshold. Events which are determined by the trigger to contain interesting physics processes are assigned into data *streams* depending which items allow it to pass. There are three streams and each event can be directed to more than one stream.

L1 reduces the L2 input rate to a maximum of 75 kHz, thereby permitting the use of more refined software algorithms with a maximum processing time of 10 µs per event.

Every L1 item that passes an event provides a seed position for L2. The L2 algorithms use calorimeter and muon system information at full granularity in the RoI around the seed, to assess whether it is a valid object. This is combined with information from the ID to provide detailed trigger objects to the EF. The L2 output rate was kept below $5\ \mathrm{kHz}$ during 2011 [117].

The EF is the final, and most detailed, step in the trigger chain. Like L2, it operates with a seed strategy, but also has access to the full detector information and the offline reconstruction algorithms used, for example, in the jet calibration process. The EF trigger items used to collect the data analysed in this study are *single lepton triggers*, described in Section 4.1. The data was hence taken from the `physics_Egamma` and `physics_Muons` streams.

Each chain of L1+HLT items can have its final output rate reduced by a factor N. This procedure, known as *prescaling*, allows the rate to remain at its maximum permitted value of $5\ \mathrm{kHz}$ during a data collection interval by successively decreasing N as the instantaneous luminosity falls. These intervals are known as *runs*. Each run is subdivided into time intervals of approximately one minute, called *luminosity blocks* (LBs). This enables data quality and detector condition information to be applied to the data at sufficiently fine temporal granularity. A consequence for the trigger is that the prescale factor can only be changed at LB boundaries. The concept of *data periods* is also used to collect together a series of runs with similar configurations of the LHC beam and of the ATLAS detector and trigger. Periods are labelled with a letter and sub-periods with an additional number.

A handful of events (typically ≈ 1000 per fb of data) may render the trigger unable to make a decision within the required time. They are assigned to the *debug stream* for reprocessing. These events may subsequently be passed or rejected by the trigger, or fail to be recovered at all. However, any passed events are not retrospectively inserted into the main datasets and must therefore be specifically included if analysis of them is required. The treatment of debug stream events in this analysis is discussed in Section 4.1.4.

2.2.6 Data quality

Quality requirements are applied to all data by the ATLAS data quality group. At the primary level, these ensure that the LHC was in stable beam mode during the period of data collection, that the ATLAS magnets were operating at their nominal current levels, and that all sub-detectors were switched on. There are further requirements resulting from the operation of each sub-detector. These requirements are amalgamated into good run lists which detail the LBs that contain data suitable for a particular analysis.

2.2.7 Data sample used in this thesis

The data used for the search presented here were collected by ATLAS between 21 March and 4 August 2011 and is contained in the periods B to K. The centre-of-mass energy of the collisions was $7\ \mathrm{TeV}$. Following the application of data quality requirements discussed previously, the number of events in the dataset corresponded to an integrated luminosity of $2.05 \pm 0.08\ \mathrm{fb}^{-1}$. Of this, $0.87\ \mathrm{fb}^{-1}$ were affected by the LAr hole.

The luminosity is determined by measuring the observed interaction rate per bunch crossing, with a variety of independent detectors. The calibration of all luminosity detectors is obtained using beam-separation, or *van der Meer*, scans [118]. A description of the entire procedure is given in [119].

2.3 The ATLAS data management and analysis model

The raw data from events that pass through the entire trigger chain are recorded at a rate of over $500\ \mathrm{MB/s}$. This is transferred to CERN's Tier-0 computing centre for reconstruction of physics objects which are then stored in event summary data files. The detector-level information is subsequently removed for storage, in analysis object data (AOD) files. This reduces the size per event by a factor of five, to approximately $100\ \mathrm{kB}$ [120].

A further reduction is achieved by retaining (or *skimming*) only those events which are deemed necessary for a particular analysis. These events are further filtered by removing non-essential information for each event, such as that not relevant to the analysis in question. The resulting format is known as derived-AOD (dAOD). The following skimming, defined by the ATLAS top working group, was applied to the data used in this thesis. For the `physics_Egamma` (`physics_Muons`) stream, each event must have:

- At least one electron (muon) with $p_T > 20$ GeV $(18$ GeV$)$, or;
- At least one electron (muon) with $p_T > 13$ GeV, and *either* $E_T^{miss} > 20$ GeV *or* at least two leptons (electron or muon) with $p_T > 13$ GeV.

The processing of all data to (d)AOD level is performed centrally by the ATLAS data production team. This is done in ATHENA: a C++ framework based on the GAUDI framework developed by the LHCb collaboration [121]. A further layer of the data format hierarchy is produced which enables the user to carry out analysis within the ROOT data analysis framework [122]. Files in this format are known as D3PDs (for Derived Physics Dataset at the third level) or NTUPs, due to their ntuple structure.

The NTUP contents are tailored to the needs of each analysis group, the format used in this thesis being NTUP_BOOST. Their production is also *usually* handled by the data production team. However, this was not possible for NTUP_BOOST since the related software was relatively novel and, at the time of production, not yet located in the central software repository. They were therefore produced outside of the central framework but their contents were validated against similar NTUPs used by the top working group. The author of this thesis had a leading role in the specification and validation of the contents, and co-ordinated the production of *all* 400 individual NTUP_BOOST datasets used for this analysis, containing both real and simulated data.

The data are stored and processed by the distributed data management (DDM) system [123] at more than a hundred individual sites, which are part of the *worldwide LHC computing grid* (WLCG) [124]. The DDM aggregates datafiles into datasets, the unit for transferal and replication on the WLCG; there is a one-to-one correspondence between datasets and run number. For centrally-produced datasets, the replication is an automatic process done in bulk. In this case, the replication had to be individually requested for each dataset.

Reconstruction of jets is performed with the `FastJet` software package [125, 126]. This provides implementations of the anti-k_T and k_T sequential recombination algorithms required to build the two jet collections used in this search, together with the variable-R adaption (or *plug-in*) to the anti-k_T algorithm, required for the study in Chapter 7. `FastJet` is usually run during the NTUP production stage. However, for technical reasons the reconstruction of variable-R jets used in this study was performed using the NTUP as an *input*.

2.4 Monte Carlo simulation of physics processes

It is vital for any particle physics analysis to have a precise, accurate and robust representation of all processes resulting from the *pp* collisions, and the subsequent passage of particles through the detector. Poor modelling of any associated process could mask a potential BSM signal or even lead to a false discovery being claimed. In this analysis, the following standard model processes are modelled *entirely* using Monte Carlo (MC) methods [127, 128]:

- Production of $t\bar{t}$ pairs.
- Electroweak production of single top quarks.
- Z boson production in association with jets (Z+jets).
- Production of diboson pairs.

Furthermore, production of both benchmark signal models is also simulated using MC techniques. Details of the resulting samples are described in the following sections.[8]

Despite the predictive power of MC simulation, it is preferable to estimate backgrounds from data, where possible, since the dependence on knowledge of both the detector simulation and the nature of the initial processes is vastly reduced. For the analysis presented here, a fully data-driven estimation is provided for the production of multiple jets entirely by QCD processes (*QCD multijet production*). The production of W bosons in association with jets (W+jets) is predicted using MC simulation and then *normalised* using data. These procedures are described in Chapter 5. MC modelling of W+jets production is described below.

Following event generation, the GEANT4 software toolkit [129] is used to simulate the passage of the resulting particles through the detector material. The subsequent energy deposits are digitised into voltages and currents so that the output matches the format of real detector data, and both can be passed through the same reconstruction software. The entire simulation framework is described in [130], which includes details of the models used for the particles' interactions with the detector material and the validation of this modelling.

The effects of both in-time and out-of-time pile-up are simulated by overlaying various numbers of minimum-bias events onto the hard process of interest. However, the resulting MC simulated samples were produced before the configuration of the LHC had been finalised for the 2011 collisions and therefore the amount of pile-up does not match that in the subsequently collected data. To resolve this, the simulated events are reweighted so that the samples' $\langle \mu \rangle$ distribution, defined in Section 2.1, matches that in the data.

[8] In this thesis, when reference is made to "simulated samples", it is implicit that these samples were produced using MC techniques.

2.4.1 Benchmark signal models

The production and decay of the leptophobic topcolor Z' boson described in Section 1.3.1 is simulated using the leading order generator PYTHIA v6.421 [131], with the CTEQ6L1 PDF set [132]. The production cross-section is evaluated using the method described in [133] and a K-factor of 1.3 is applied to account for NLO effects in QCD [134]. The specific couplings used in the generation are pertinent to the sequential standard model (SSM) Z' boson which has the same couplings to fermions as the Z boson. The cross-section times branching ratio to $t\bar{t}$ pairs ($\sigma \times BR$) is then rescaled to that of the leptophobic topcolor Z' boson. The resulting values are shown in Table 2.1.

The second signal model is that of the Kaluza-Klein gluon g_{KK} which is also generated at LO, using MADGRAPH v4.4.51 [85]. Hadronisation and showering is done using PYTHIA v6.421 and the PDF set is CTEQ6L1, as above. The production cross-section is determined using PYTHIA v8.1 [135]. No K-factor is applied due to there being no published cross-section calculation at higher orders. The resulting values are again shown in Table 2.1. It is important to note that $\sigma \times BR(\rightarrow t\bar{t})$ for the KK-gluon is almost four times greater than for a leptophobic Z' of equivalent mass.

For both cases of generation, all decay channels of the $t\bar{t}$ pair are allowed: fully hadronic, lepton+jets and dileptonic.

Table 2.1: Production cross-section times branching ratio to $t\bar{t}$ pairs ($\sigma \times BR$) for the benchmark signal models: the leptophobic Z' boson and the Kaluza-Klein gluon g_{KK}. A K-factor of 1.3 has been applied to the Z' cross-sections, to account for NLO effects. The g_{KK} cross-sections are at LO; no K-factor is available.

Mass [GeV]	600	700	800	900	1000	1200	1300	1400	1600	1800	2000
$\sigma_{Z'} \times BR$ [pb]	10.3	5.6	3.2	1.9	1.2	0.46	0.30	0.19	0.068	0.039	0.018
$\sigma_{g_{KK}} \times BR$ [pb]	39.4	20.8	11.6	6.8	4.1	1.7	1.1	0.73	0.35	0.18	0.095

2.4.2 Single and pair production of top quarks in the standard model

The SM production of $t\bar{t}$ pairs is simulated using MC@NLO v3.41 [136, 137, 138] and includes spin-correlation effects between the top and antitop quarks. Showering is performed using HERWIG [139, 140], with JIMMY [141] to model the effects due to the underlying event and multiple parton scattering. The CTEQ6.6 PDF set [142] is used. For these samples, only the lepton+jets and dileptonic decay channels were permitted during the event generation. A K-factor of 1.11 is applied to normalise the sample to the approximate NNLO cross-section of 165 pb. This cross-section is obtained using HATHOR which implements the calculation of Moch and Uwer [143, 144]. The impact on the sensitivity of this search due to the cross-section uncertainties is discussed in Section 6.3.2.

Production of single top quarks via the electroweak interaction is simulated using the same programs as for $t\bar{t}$ production above. For the s-channel and t-channel processes, the W boson from the top quark decays leptonically only. For the Wt-channel process, all decay channels were open. The resulting cross-sections were 1.4 pb for the s-channel, 21.5 pb for the t-channel and 14.6 pb for the Wt-channel processes respectively, obtained directly from MC@NLO. No K-factor is applied. The theoretical uncertainty on the cross-sections is $\pm\ 10\ \%$ [145].

2.4.3 W boson production in association with jets

W+jets events in which the jets arising in the matrix element process are from gluons and from up, down, strange and charm quarks are referred to as W+*light-jets* events. All quarks in these events are treated as massless, including the charm quarks. ALPGEN v2.13 [146], a leading order generator, is used to simulate the matrix element process. HERWIG is used to simulate the fragmentation and parton shower and JIMMY is used for the underlying event. The "MLM"[9] matching method [147] is used to avoid double-counting of events with $(n+1)$-jets, resulting from either an $(n+1)$-parton final state or

[9]This acronym represents the initials of its author.

an n-parton final state where the extra jet is created during the parton shower. The cross-sections for the samples are listed in Table 2.2. These samples are subdivided according to the number of partons generated in each event. There are separate samples for each parton multiplicity lower than five, and a single sample if there are five partons or more.

Any bottom quarks in the above light-jets samples are produced only in the parton shower and are considered to be massless. Separate $W + b\bar{b} +$ jets samples are generated for events with massive bottom quarks, produced in the matrix element process. They are also subdivided depending on the parton multiplicity, as listed in Table 2.3. Although charm quarks in the $W+$light-jets samples *are* produced in the matrix element process, they are treated as massless. Samples with *massive* charm quarks produced in the matrix element process ($W+c+$jets, $W+\bar{c}+$jets and $W+c\bar{c}+$jets), are generated separately. These are collectively referred to as $W+$*heavy-jets* samples and the corresponding cross-sections are listed in Table 2.3.

Table 2.2: Leading order cross-sections for $W+$light-jets sub-samples generated using ALPGEN+HERWIG+JIMMY. A K-factor of 1.20 is applied to each one, to reproduce the NNLO cross-section. A data-driven normalisation and associated systematic uncertainty is derived for these samples. "Np" refers to the number of partons generated.

Sub-sample	Cross-section [pb]
$W \to e\nu$ + Np0	6921.60
$W \to e\nu$ + Np1	1304.30
$W \to e\nu$ + Np2	378.29
$W \to e\nu$ + Np3	101.43
$W \to e\nu$ + Np4	25.87
$W \to e\nu$ + Np5	7.00
$W \to \mu\nu$ + Np0	6919.60
$W \to \mu\nu$ + Np1	1304.20
$W \to \mu\nu$ + Np2	377.83
$W \to \mu\nu$ + Np3	101.88
$W \to \mu\nu$ + Np4	25.75
$W \to \mu\nu$ + Np5	6.92
$W \to \tau\nu$ + Np0	6918.60
$W \to \tau\nu$ + Np1	1303.20
$W \to \tau\nu$ + Np2	378.18
$W \to \tau\nu$ + Np3	101.51
$W \to \tau\nu$ + Np4	25.64
$W \to \tau\nu$ + Np5	7.04

Both light-jets and heavy-jets samples are used because they have complementary strengths. The light-jets samples provide a more accurate simulation of the collinear gluon splitting, whereas the heavy-jets samples better describe the large opening angles between the heavy quarks [128]. However, one must take care to avoid double counting of the same heavy-flavour final states when these sets of samples are combined. Certain classes of events are vetoed in each of the samples, by determining the distance in η-ϕ space between the heavy-flavour quarks and the reconstructed jets, in a procedure described in section 4 of [128].

A K-factor of 1.20 is applied to all of the above W+jets samples, to reproduce the NNLO cross-section as calculated with FEWZ [148]. These samples have a data-driven normalisation applied which has an associated systematic uncertainty; the normalisation procedure is discussed in Section 5.1.1. The theoretical uncertainties on the cross-sections are not considered.

Table 2.3: Leading order cross-sections for W+heavy-jets. Additional details as for Table 2.2.

Sub-sample	Cross-section [pb]
$W + b\bar{b}$ + Np0	47.32
$W + b\bar{b}$ + Np1	35.77
$W + b\bar{b}$ + Np2	17.34
$W + b\bar{b}$ + Np3	6.63
$W + c\bar{c}$ + Np0	127.53
$W + c\bar{c}$ + Np1	104.68
$W + c\bar{c}$ + Np2	52.08
$W + c\bar{c}$ + Np3	16.96
$W + c$ or $(\bar{c})$ + Np0	644.4
$W + c$ or $(\bar{c})$ + Np1	205.0
$W + c$ or $(\bar{c})$ + Np2	50.8
$W + c$ or $(\bar{c})$ + Np3	11.4
$W + c$ or $(\bar{c})$ + Np4	2.8

2.4.4 Z boson production in association with jets

Z+jets production is also generated using ALPGEN and the parton shower is simulated with HERWIG. JIMMY is used for the underlying event. As for W+jets, the samples are subdivided into exclusive bins of parton multiplicity for multiplicities lower than five, and inclusively above that. Double-counting of events with the same number of jets is again avoided by applying the MLM method. Photon interference effects ($\gamma* \rightarrow ll +$ jets) are included, although the dilepton invariant mass has to satisfy $40 < m_{ll} < 2000$ GeV. The lower threshold serves to remove the large contribution of events from photon interference, which have a small probability of passing the analysis event selection criteria. Events with a dilepton mass larger than 2 TeV have a negligible cross-section [149]. K-factors of 1.25 are applied to all samples in order to reproduce the NNLO cross-section, once again calculated with FEWZ. The cross-sections for the samples are listed in Table 2.4 and the theoretical uncertainties on these cross-sections are $\pm$ 48 % [150].

Events with heavy quarks produced in the matrix element process are *not* generated separately. This is because Z+jets' events comprise only around 5 % of the total background.

2.4.5 Diboson production

These events were generated using HERWIG with JIMMY. A filter to require the presence of one lepton with $p_T > 10$ GeV and $|\eta| < 2.8$ was applied. The corresponding cross-sections were 11.50 pb for WW production, 3.46 pb for WZ production and 0.97 pb for ZZ production. K-factors of (respectively) 1.48, 1.60 and 1.30 were applied in order to reproduce the NLO results obtained [151] using the MCFM generator. The theoretical uncertainty on each cross-section is $\pm$ 5 % [145].

Table 2.4: Leading order cross-sections for Z+light-jets sub-samples generated using ALPGEN+HERWIG+JIMMY. The K-factor to reproduce the NNLO cross-sections is 1.25. The theoretical uncertainty on each cross-section is $\pm$ 48 $\%$. "Np" refers to the number of partons generated.

Sub-sample	Cross-section [pb]
$Z \rightarrow ee$ + Np0	668.32
$Z \rightarrow ee$ + Np1	134.36
$Z \rightarrow ee$ + Np2	40.54
$Z \rightarrow ee$ + Np3	11.16
$Z \rightarrow ee$ + Np4	2.88
$Z \rightarrow ee$ + Np5	0.83
$Z \rightarrow \mu\mu$ + Np0	668.68
$Z \rightarrow \mu\mu$ + Np1	134.14
$Z \rightarrow \mu\mu$ + Np2	40.33
$Z \rightarrow \mu\mu$ + Np3	11.19
$Z \rightarrow \mu\mu$ + Np4	2.75
$Z \rightarrow \mu\mu$ + Np5	0.77
$Z \rightarrow \tau\tau$ + Np0	668.40
$Z \rightarrow \tau\tau$ + Np1	134.81
$Z \rightarrow \tau\tau$ + Np2	40.36
$Z \rightarrow \tau\tau$ + Np3	11.25
$Z \rightarrow \tau\tau$ + Np4	2.79
$Z \rightarrow \tau\tau$ + Np5	0.77

2.5 Summary

The ATLAS detector incorporates a silicon tracking detector, calorimeters and muon chambers which provide kinematic and spatial measurements with high resolution. This makes the detector ideally suited to the detection of top quarks with a range of transverse momenta. A description of all sub-detectors has been provided in this chapter, together with details of the data sample to be analysed. Monte Carlo simulation is vital in order to estimate the yields and distributions from processes which form a background to the search for $t\bar{t}$ resonances. The MC simulation samples used in this thesis are comprehensively detailed in this chapter.

Chapter 3

Particle identification and reconstruction

This search for new phenomena is carried out in the lepton+jets final state of the $t\bar{t}$ decay, the lepton being an electron or a muon. Intermediate processes are the decays of the top and antitop quarks to a W^+ and a W^- boson respectively. One of these W bosons then decays to a pair of quarks, which subsequently hadronise, and the other decays to a pair of leptons. τ-leptons are not directly identified in this search. For the final state containing a τ-lepton and a ν_τ to contribute to this search, the decay chain resulting from the τ-lepton must contain either a muon or an electron. τ-leptons which decay solely to hadrons are not separately identified in this analysis.

The final decay products therefore include hadrons, a neutrino, and an electron or a muon with large transverse momentum. The physical manifestation of these particles is through detector signals which are reconstructed into *physics objects*; these objects are hence defined at the *reconstruction level*. Note that the directions of the physics objects are described by pseudorapidity rather than rapidity since it is necessary to know their position in the detector.

Following reconstruction, identification criteria are imposed. The reconstruction and identification methods are laid out below, since they can have a large impact on the properties of the objects. Indeed, if the criteria are not well chosen, a particle of possible interest may fail to be identified or even reconstructed. The ATLAS combined performance groups carry out detailed studies of these objects, on both real and simulated data, and produce recommendations on the precise definitions to be used in analyses of ATLAS data, including this one.

3.1 Electrons

3.1.1 Reconstruction, identification and isolation

Candidates for electrons are reconstructed from clusters of cells in the EM calorimeter which have recorded $E_T > 2.5$ GeV and have at least one associated track reconstructed by the ID. Clusters up to an $|\eta|$ of 2.47 are considered, but the "crack" located at $1.37 < |\eta| < 1.52$ is excluded since the large amount of un-instrumented material can significantly degrade the resolution of the electron energy measurement. The reconstruction efficiency in MC simulation is 100 % for electrons with $E_T > 15$ GeV from W and Z boson decays [109]. The cluster energy is determined by summing four different contributions: (1) the estimated energy deposited in material in front of the EM calorimeter; (2) the measured energy deposited in the cluster; (3) the estimated energy deposited outside of the cluster (*lateral leakage*); and (4), the estimated energy deposited beyond the EM calorimeter (*longitudinal leakage*).

The EM-scale is the scale at which the energy of *electrons* is correctly measured in the calorimeters. The total uncertainty on this scale in the central region is 3 % which is dominated by the transfer of test-beam results to the actual environment of the calorimeter. An in-situ calibration of the electron energy scale can be performed using $Z \to ee$ decays, as described in [109], and is indeed carried out for the data used in this analysis. Specifically, the energy of all electrons with $E_T > 10$ GeV, is corrected so that the reconstructed Z boson mass peak is centered on its known mass. The energy measured in simulated events is also corrected so that the *width* of this reconstructed mass peak matches that in data. The energy resolution of calibrated electrons having $E_T > 25$ GeV is better than 2 %

in the most central region. It exceeds $3\,\%$ only for electrons which enter the crack region.

Identification requirements are further imposed, to give a high efficiency for selecting *prompt* electrons; that is, those resulting directly from the decay of a W or Z boson, which themselves were produced in the proton-proton hard-scatter or, for the W boson, in the decay of a top quark. Strong suppression of non-prompt electrons must be achieved; the sources of these electrons are:

- Semileptonic heavy-flavour decays (of B- or D-hadrons).
- The decay-in-flight of charged pions.
- Photon conversions to electron-positron pairs.

Furthermore, the process $\pi^0 \rightarrow \gamma\gamma$ produces photons which may be mistakenly reconstructed as one or more electrons, if there is at least one nearby reconstructed track. This source of "fake" electrons must also be suppressed. Figure 3.1 provides a basic illustration of some of these processes, occurring within a spray of hadrons.

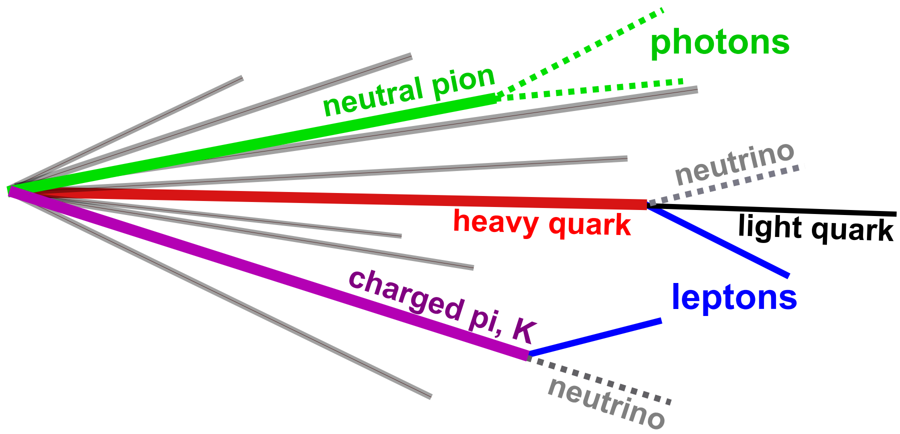

Figure 3.1: Processes resulting in the production of non-prompt leptons and "fake" electrons. From top to bottom: $\pi_0 \rightarrow \gamma\gamma$, where one of the photons may be reconstructed as an electron due to nearby charged tracks; a heavy quark decaying semileptonically; a $\pi^{\pm}$ or $K^{\pm}$ decaying leptonically, predominantly in the muon channel due to angular momentum conservation requirements.

Identification is a criteria (or *cut*)-based selection involving variables measured either separately in the calorimeter and the ID, or in both combined. The criteria define three classifications, *loose*, *medium* and *tight*, giving an increasingly strong rejection power[1] of 500, 5000 and $50,000$ respectively. Each classification builds on the previous one, hence loose is a subset of medium and medium is a subset of tight. A broad description of the criteria used are listed below (*for each classification*).

- A shower shape resembling that of an EM shower in the EM calorimeter, based on expectations from simulation, test beam and reconstructed $Z \to ee$ events (*loose, with additional variables for medium*).
- Minimal energy deposits in the hadronic calorimeter (*loose*).
- A high multiplicity of ID hits and the matching of an ID track to the cluster (*loose, with additional variables for medium*).
- At least one hit in the pixel B-layer [152] to discriminate against photon conversions (*tight*).
- A ratio of measured cluster energy to track momentum consistent with an electron rather than a charged hadron (*tight*).
- A sufficiently high multiplicity of hits in the TRT and, of these, a certain fraction being above the high-threshold which was defined in Section 2.2.2) (*tight*).

The values associated with the criteria placed on each variable are optimised in 10 bins of cluster η and 11 bins of cluster E_T from 5 GeV to above 80 GeV; this optimisation is described in [109] and [153]. The distribution of one of these variables, the fraction of high-threshold TRT hits, is provided in Figure 3.2 as an example of the discrimination power between electrons and hadrons.

An isolation requirement is imposed to reduce the contribution from non-prompt electrons. That is, the sum of the transverse energy recorded in all EM and hadronic calorimeter cells within a cone of 0.2 and centred on the electron, must not total more than 3.5 GeV.

[1] The reciprocal of the fraction of electrons that is incorrectly labeled as jets, based on studies of simulated data.

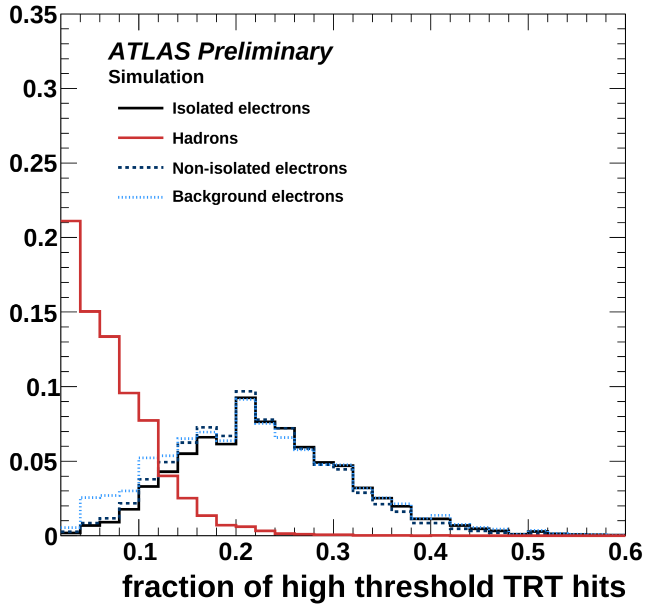

Figure 3.2: Distribution of the fraction of high-threshold TRT hits, a discriminant used to determine the electron identification classification via simulated data. *Background electrons* are those referred to as non-prompt in the main text. Good discrimination between electrons and hadrons is possible using this variable.

A central core of 5×7 cells is excluded from this cone in order to reduce the dependence of the isolation energy on the electron E_T. Figure 3.3 provides an illustration of this layout. A correction is made for the contribution due to soft energy deposits from pile-up interactions and leakage of the electron out of the central core; details can be found in [154].

The reconstruction, identification and isolation procedures have associated efficiencies ε whose values differ between data and simulated events. These efficiencies, and their associated uncertainties, are derived in bins of electron η using the *tag-and-probe* technique [155]. This essentially involves collecting a sample of $Z \rightarrow ll$ events, in which one of the leptons (the "tag") must satisfy tight selection criteria and the other (the "probe") has looser criteria applied. The specific criteria are described in [156].

The efficiencies are measured in both data and MC simulation using the same type of events, such as $Z \rightarrow ll$. The resulting ratio $\varepsilon_{data}/\varepsilon_{MC}$ is known as a *scale factor* (SF). This is applied to simulated events to correct the predicted efficiency values and bring them in

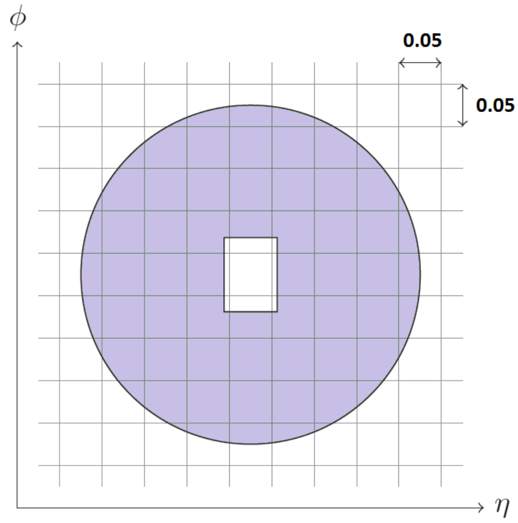

Figure 3.3: A map in η-ϕ space of the calorimeter cells (lilac) used in the calculation of the degree of electron isolation. All cells within a cone of radius 0.2 are used, although a central core of 5×7 cells is subtracted.

line with those measured in data. In practice, this is achieved via the application of this multiplicative SF to the weight of the simulated event.

The combined SFs for the electron identification and isolation procedures are shown in Table 3.1, and for the reconstruction procedure in Table 3.2. The SFs are measured in bins of the electron E_T and/or the electron cluster η. They are not measured beyond an $|\eta|$ of 2.47 nor in the "crack" region ($1.37 \leq |\eta| \leq 1.52$). In these regions, a SF of unity is used. The divergence of the identification and isolation SF from unity is due to differences in the distributions of TRT-related variables in data and in MC simulation [109]. The reconstruction SF is consistent with unity in the central region and within $1.5\ \sigma$ of unity for $|\eta| > 0.8$.

Problematic regions of the LAr calorimeter, discussed in Section 2.2.3, are avoided through the use of a quality flag applied to each electron. The loss of the FEBs affected approximately $40\ \%$ of the total dataset and occurred *after* the simulated datasets were produced. To avoid significant discrepancies when comparing to data, this quality flag is only applied to the corresponding fraction of simulated events.

	Electron η_{cl}				
E_T [GeV]	[−2.47, −2.37]	[−2.37, −2.01]	[−2.01, −1.81]	[−1.81, −1.37]	[−1.37, −1.15]
[25,30]	0.972 ± 0.038	0.964 ± 0.029	1.007 ± 0.037	1.016 ± 0.027	1.071 ± 0.029
[30,35]	1.003 ± 0.037	0.996 ± 0.028	1.040 ± 0.036	1.049 ± 0.026	1.106 ± 0.028
[35,40]	1.013 ± 0.035	1.005 ± 0.025	1.050 ± 0.034	1.059 ± 0.023	1.117 ± 0.026
[40,45]	1.012 ± 0.035	1.005 ± 0.025	1.049 ± 0.034	1.059 ± 0.023	1.116 ± 0.026
[45,50]	1.015 ± 0.037	1.008 ± 0.027	1.053 ± 0.036	1.062 ± 0.025	1.120 ± 0.028

E_T [GeV]	[−1.15, −0.8]	[−0.8, −0.6]	[−0.6, −0.1]	[−0.1, 0]	[0, 0.1]
[25,30]	1.007 ± 0.027	0.967 ± 0.027	0.957 ± 0.026	0.979 ± 0.030	0.963 ± 0.027
[30,35]	1.039 ± 0.026	0.998 ± 0.025	0.988 ± 0.025	1.010 ± 0.028	0.994 ± 0.026
[35,40]	1.050 ± 0.023	1.008 ± 0.023	0.998 ± 0.022	1.020 ± 0.026	1.004 ± 0.023
[40,45]	1.049 ± 0.023	1.007 ± 0.023	0.997 ± 0.022	1.019 ± 0.026	1.003 ± 0.023
[45,50]	1.052 ± 0.025	1.010 ± 0.025	1.000 ± 0.024	1.023 ± 0.028	1.006 ± 0.025

E_T [GeV]	[0.1, 0.6]	[0.6, 0.8]	[0.8, 1.15]	[1.15, 1.52]	[1.52, 1.81]
[25,30]	0.953 ± 0.026	0.975 ± 0.027	0.999 ± 0.027	1.057 ± 0.033	1.024 ± 0.028
[30,35]	0.984 ± 0.025	1.006 ± 0.026	1.031 ± 0.026	1.091 ± 0.032	1.057 ± 0.026
[35,40]	0.993 ± 0.022	1.016 ± 0.023	1.041 ± 0.023	1.102 ± 0.029	1.068 ± 0.023
[40,45]	0.993 ± 0.022	1.015 ± 0.023	1.041 ± 0.023	1.101 ± 0.029	1.067 ± 0.023
[45,50]	0.996 ± 0.024	1.019 ± 0.025	1.044 ± 0.025	1.105 ± 0.031	1.070 ± 0.025

E_T [GeV]	[1.81, 2.01]	[2.01, 2.37]	[2.37, 2.47]
[25,30]	1.007 ± 0.035	0.957 ± 0.028	0.993 ± 0.033
[30,35]	1.039 ± 0.034	0.988 ± 0.026	1.025 ± 0.032
[35,40]	1.050 ± 0.031	0.997 ± 0.024	1.035 ± 0.030
[40,45]	1.049 ± 0.032	0.997 ± 0.024	1.034 ± 0.030
[45,50]	1.052 ± 0.033	1.000 ± 0.025	1.037 ± 0.031

Table 3.1: Combined scale factors for the electron identification and isolation procedures, in 5 bins of electron E_T and 18 bins of the electron cluster η. Divergences from unity, particularly in the region at $|\eta| \approx 1.15$, are due to the mis-modelling of TRT variables.

Electron $\|\eta_{cl}\|$		
[0, 0.8]	[0.8, 2.37]	[2.37, 2.47]
0.9984 ± 0.0066	1.0091 ± 0.0070	0.9759 ± 0.0184

Table 3.2: Electron reconstruction SFs, in three bins of the electron cluster η. It is within $1.5\ \sigma$ of unity in all regions. The combined statistical and systematic uncertainties are displayed.

3.1.2 Electron trigger

Two triggers were used for electrons in this study. This is because the instantaneous luminosity increased during the data-taking period, hence the minimum E_T of the electrons which could fire the trigger was raised to avoid prescaling.[2] Specifically, the electron trigger item requires an EM cluster with $E_T > 20$ GeV[3] in the first $1.6\ \mathrm{fb}^{-1}$ of the dataset, and $E_T > 22$ GeV in the latter part.

The efficiency of the triggers is measured using tag-and-probe on a sample of $Z \rightarrow ee$ and $W \rightarrow e\nu$ events [156]. The efficiency for the first trigger, with the lower E_T threshold, is displayed in Figure 3.4 for both data and MC simulation as a function of the electron E_T and electron cluster η. When measuring versus one variable, the SF is integrated over the other so that η_{cl} and E_T are treated as uncorrelated. The results for both medium and tight electrons are shown; the latter electrons are used in this thesis. The efficiencies measured in both data and MC simulation are above $97\ \%$ for tight electrons with an $E_T > 25$ GeV or with $|\eta_{cl}| < 1.5$ (subfigures (a) and (b)). The SFs are above $98\ \%$ for all tight electrons within these regions of phase-space (subfigures (c) and (d)). The drop in efficiency at $|\eta_{cl}| \approx 1.4$ is due to the "crack" region.

3.2 Muons

3.2.1 Reconstruction, identification and isolation

The reconstruction and identification of muons used in this study involves information from both the ID and the MS. An MS track must be associated to an ID track, and the latter must have a certain multiplicity of hits in each of the ID sub-detectors [156]. Furthermore, the acceptances of the ID and MS are such that candidates can only be considered up to $|\eta| = 2.5$. The pair of tracks to be combined is chosen based on the minimisation of a χ^2 term, defined using the difference between the reconstructed track parameters in the ID and the MS [157]. The resulting objects are hence known as combined `Muid` muons.

Figure 3.5 displays the reconstruction efficiency for `Muid` muons measured in both

[2] For a description of prescaling, see Section 2.2.5.
[3] Referred to as e20_medium in Figure 3.4.

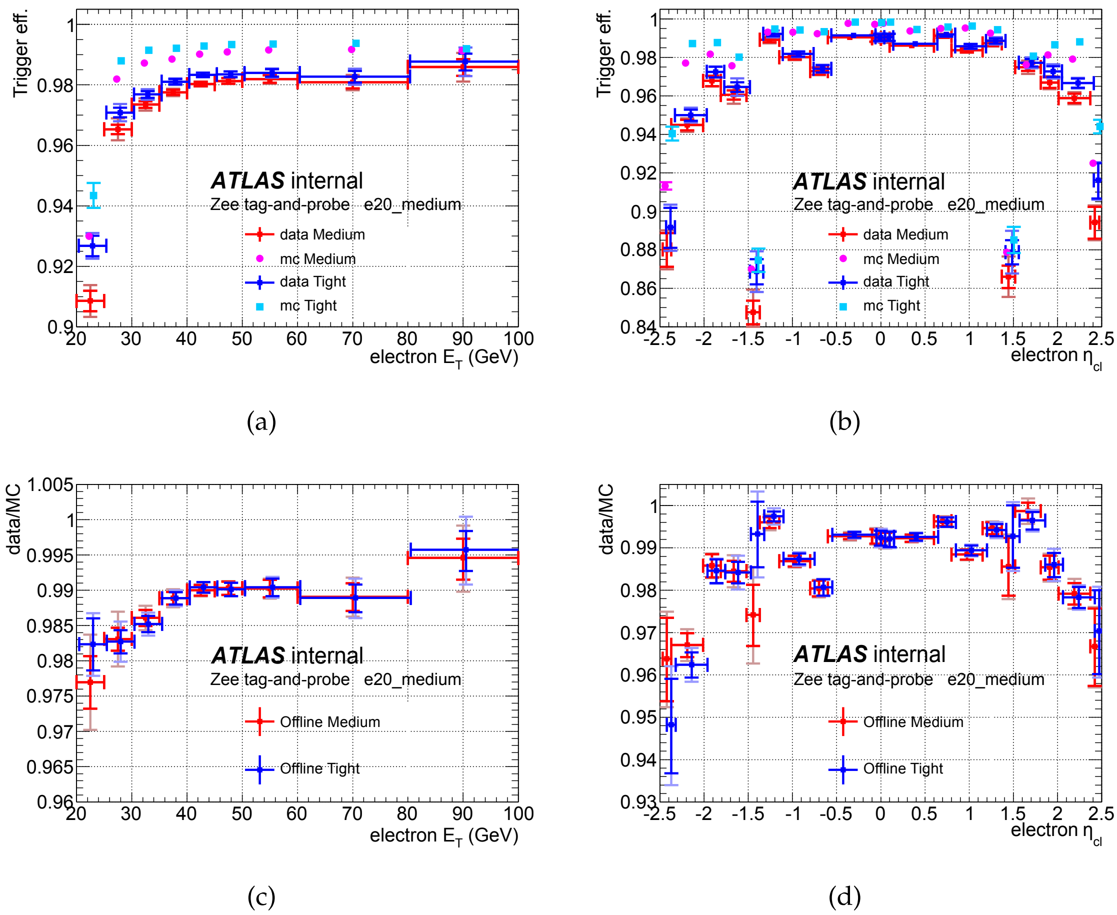

Figure 3.4: Efficiency ε for the electron trigger which is fired by an EM cluster with $E_T > 20$ GeV and is used to collect the first portion of data used in this thesis. The efficiency is measured in data and in MC simulation for both medium and tight electrons (the latter is used in this study). It is approximately stable for electrons with $E_T > 25$ GeV. The scale factors ($\varepsilon_{data}/\varepsilon_{MC}$) are within $2\ \%$ of unity for all tight electrons in the central region or having $E_T > 25$ GeV.

data and simulation, as a function of (a) the muon η and (b) the muon p_T. A tag-and-probe technique method is used as documented in [158]. The low efficiency for both data and MC simulation in the central region is due to the reduced number of muon chambers to make way for detector services and the muon system's support feet. The decrease in efficiency for data only, at $|\eta| \approx 1.2$, relates to the transition region between the barrel and end-caps of the MS. In this region, the magnetic field map used in the reconstruction of data has a reduced accuracy leading to a small mis-measurement of the muon momentum [158]. This leads to a decrease in the SF in this region, although the average SF across all regions in η is 0.995 ± 0.002 (statistical errors only).

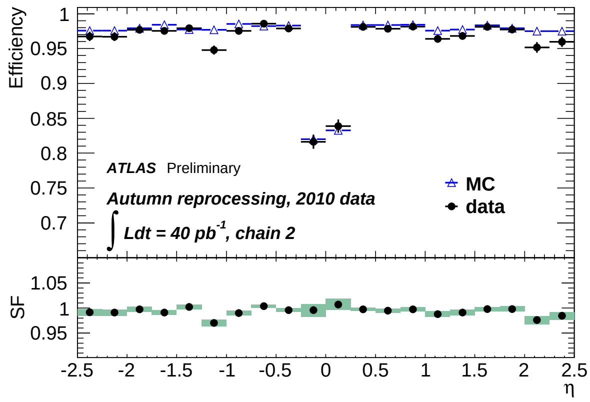

(a)

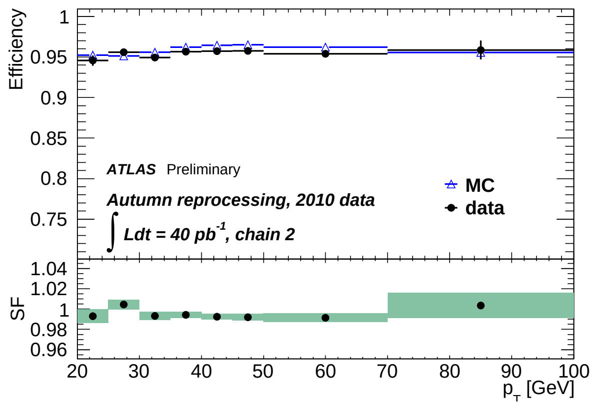

(b)

Figure 3.5: `Muid` muon reconstruction efficiency as a function of the muon (a) η and (b) p_T, measured in both data and MC simulation. The distinct drop in efficiency in the central region is due to the support feet of the muon system which necessitates removal of some of the active detector elements. The SFs are shown in the lower part of each subfigure and average 0.995 ± 0.002 across all regions. Taken from [158].

A number of systematic uncertainties in the tag-and-probe method are deemed to propagate to the SF estimation [156]: the estimation of background processes in the tag-and-probe selection, the choice of a certain di-muon invariant mass threshold, the mis-estimation of the muon momentum in the tag-and-probe selection, the choice of quality criteria in the selection and the effect of pile-up. The SFs are recalculated with relevant variations applied and the deviations from the nominal SFs are taken as the systematic uncertainty. The dominating systematic uncertainty is that associated with the background estimation.

The muon identification efficiency is also determined using a tag-and-probe method on $690\ \mathrm{pb}^{-1}$ of collision data at $\sqrt{s} = 7\ \mathrm{TeV}$ [156]. The efficiencies measured in data and

MC simulation are shown in Figure 3.6 as a function of muon η, p_T, ΔR to the closest jet, and number of primary vertices in the event (N_{PV})[4]. The efficiency is above $90\ \%$ for all muons having $\Delta R > 0.4$ to the closest jet, and in all events without a large amount of pile-up (i.e. if $N_{PV} < 11$). The SFs do not exhibit any significant dependence on any of the variables. Therefore flat SFs are applied to the MC simulation, with values of 1.008 ± 0.0003 (stat.) $\pm\ 0.0003$ (syst.) for the first $1.5\ \mathrm{fb}^{-1}$ of data and 1.0034 ± 0.0003 (stat.) $\pm\ 0.0002$ (syst.) thereafter. The same sources of systematic uncertainty are considered as for the reconstruction efficiency.

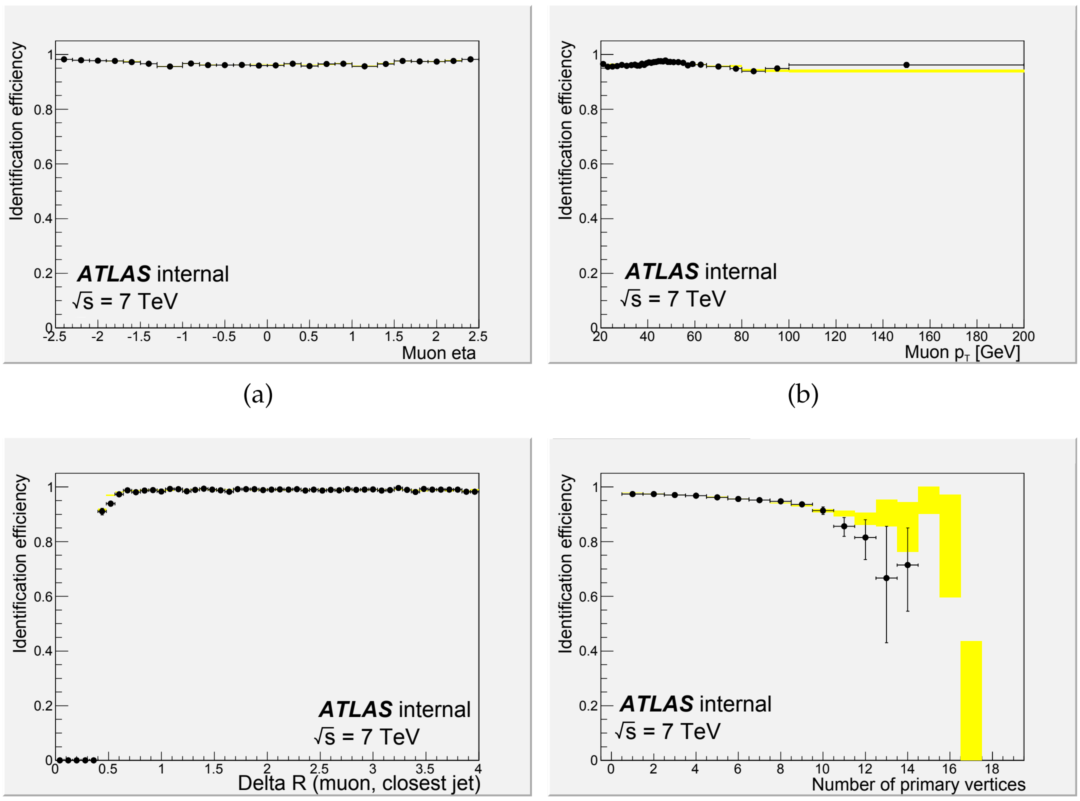

(a) (b)

(c) (d)

Figure 3.6: Muon identification efficiency measured in data (black circles) and MC simulation (yellow rectangles) using a tag-and-probe method. The efficiencies as a function of (a) muon η (b) muon p_T (c) ΔR from the muon to the closest jet (d) number of primary vertices in the event. The integrated luminosity of the dataset used was $690\ \mathrm{pb}^{-1}$.

The p_T resolution assumed in this thesis was determined for muons with $20 \lesssim p_T \lesssim 120$ GeV, using data collected in 2010. It ranges from $< 7\ \%$ for all muons reconstructed in the central region of the detector, up to $\approx\ 23\ \%$ for muons with $p_T > 60$ GeV and

[4] A primary vertex is one reconstructed from at least five tracks, each with $p_T > 150$ MeV.

$2.0 < |\eta| < 2.5$ [159]. The muon p_T measured in simulated events is corrected in order to reproduce these measurements.

Muons, like electrons, are required to be isolated to suppress those of non-prompt type. The scalar sum of the p_T of all tracks, and the scalar sum of the E_T measured by all calorimeter cells, in a cone of radius 0.3 surrounding the muon candidate, must each be less than 4 GeV. The muon track, and any energy deposited by the muon in the calorimeters, is excluded from the total p_T and E_T measurements respectively.

For further suppression of this "non-prompt background", reconstructed muons at a distance of less than 0.4 in η-ϕ space to a jet with $p_T > 20$ GeV cannot be considered as the lepton originating from the $t \to W$ decay chain. The jets referred to here are those reconstructed by the anti-k_T algorithm with $R = 0.4$ and calibrated using the EM+JES scheme.[5] This procedure is illustrated in Figure 3.11 (left) and described in more detail in [156].

3.2.2 Muon trigger

Two muon triggers are used for the data collected in this study, with the switchover occurring after ≈ 1.5 fb^{-1} of data were collected. To fire, both triggers required a single muon with $p_T > 18$ GeV. However, the second trigger had tightened level 1 criteria applied: all three layers of the muon trigger system were required to have fired, as opposed to only two for the first trigger.

The trigger efficiency is measured using the tag-and-probe technique in $Z \to \mu\mu$ events on both data and MC simulation; the event selection requirements are detailed in [156]. The efficiencies are presented in Figure 3.7 as functions of the probe muon η, ϕ and p_T, together with the number of reconstructed primary vertices N_{PV} in the event. The efficiency is lower in the barrel than in the endcaps due to the reduced geometrical coverage of the RPC detectors close to the support feet of the muon system [156].

[5] Jet calibration is introduced in Section 3.3.2.

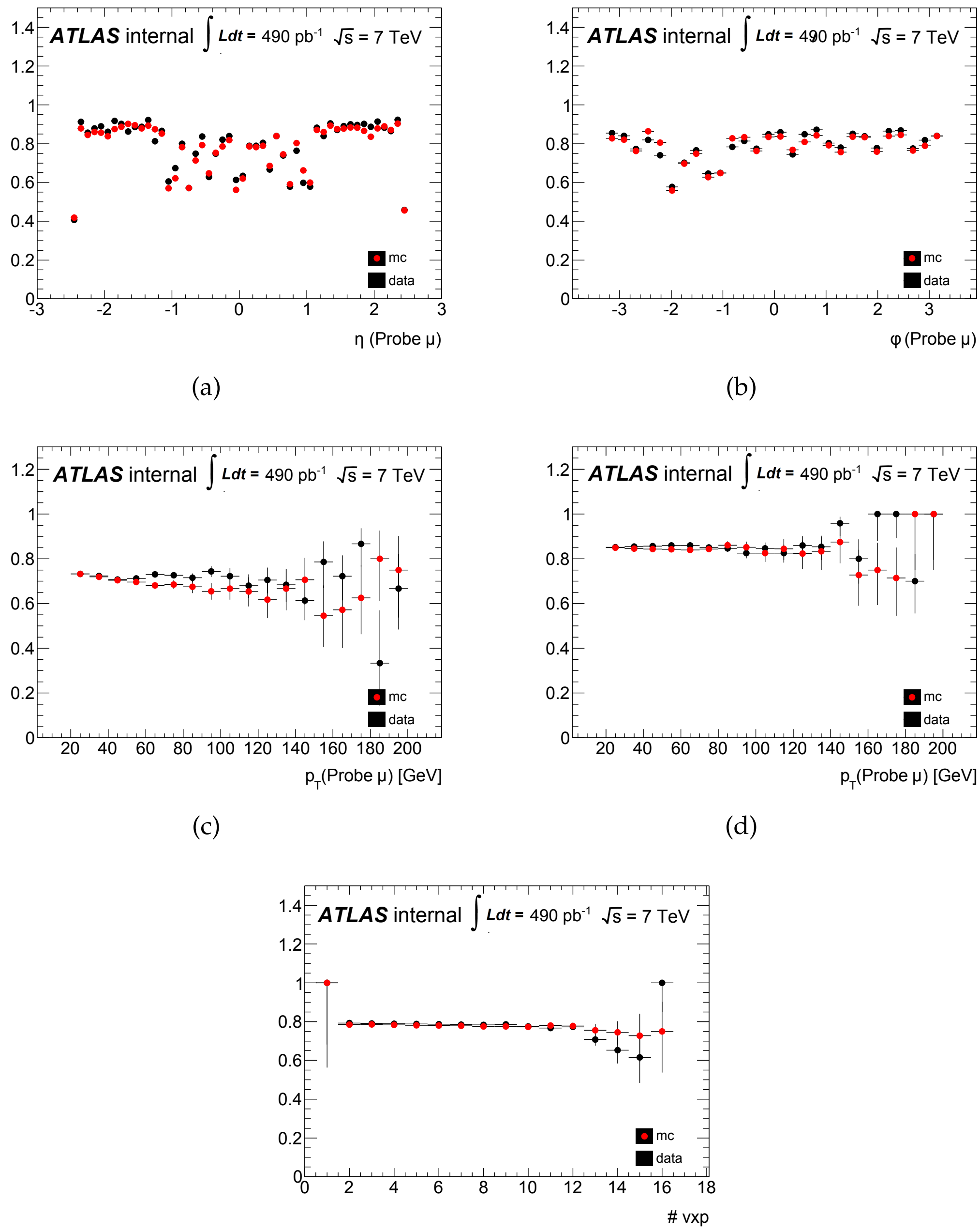

(a) (b) (c) (d) (e)

Figure 3.7: Efficiencies for the two (one) muon trigger(s) measured in events taken from the data (MC simulation) analysed in this thesis. The efficiencies are displayed as as function of (a) η (b) ϕ (c) p_T in the barrel of the muon system (d) p_T in the endcaps of the muon system (e) the number of reconstructed primary vertices in the event.

Figure 3.7(c) demonstrates that the SF in the *barrel* has a dependence on p_T. This is due to an error in the ATLAS simulation software which affected muons with large p_T in the barrel region $\eta < 1.2$ only. This dependence could not be investigated using the tag-and-probe technique due to the limited p_T range of muons from Z boson decays.

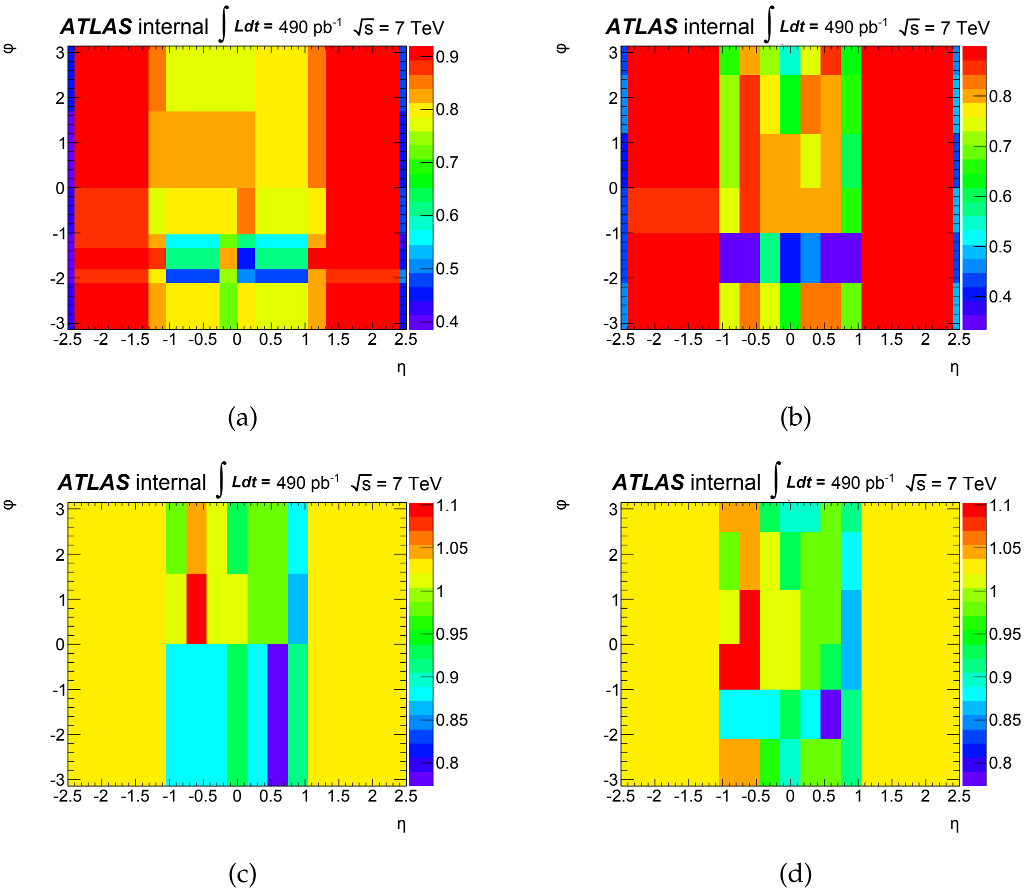

Figure 3.8: η-ϕ maps of the efficiency for (a) the first $1.5\ \mathrm{fb}^{-1}$ of data and (b) the second $\approx 0.5\ \mathrm{fb}^{-1}$. The lower efficiency in the barrel at $-1 < \phi < -2.2$ due to the muon system's support feet is apparent. The SFs for the same two triggers are shown in (c) and (d). The SF values are lower in the barrel due to an error in the ATLAS simulation software.

The recommendation provided by the ATLAS top group to account for this limitation is documented in the event selection description of Section 4.1.1.

The SFs for the two triggers are derived as functions of η and ϕ in three different p_T bins: $[20 - 60]$, $[60 - 120]$ and > 120 GeV. The efficiencies measured in data, together with the SFs, are displayed in the η-ϕ maps of Figure 3.8, for the lowest p_T bin only.

The systematic uncertainties on the trigger SFs are assumed to be due to a number of sources from the tag-and-probe method [156]: the choice of a certain di-muon invariant mass threshold, the choice of the trigger-matching threshold value for the tag muon and the isolation criteria applied to the tag muon. The first two thresholds were varied within

$1\ \sigma$ of their nominal values and the isolation criteria was removed altogether. The SFs were then recalculated, and the muon isolation was found to have the largest shift on the SF, of 0.0045 on average.

3.3 Jets

3.3.1 Reconstruction

All jets used in this study are reconstructed with the anti-k_T algorithm. Two collections of such jets are used, with different values for the radius parameter R, of 0.4 and 1.0; these will subsequently be referred to as AKT4 or AKT10 respectively. The substructure of the AKT10 jets, also known as *fat jets*, is determined through use of the k_T algorithm as detailed in Section 1.4.2. The four-momenta of *groups* of calorimeter cells are supplied as input to the jet algorithm. There are two possible definitions of these groups, known as topological clusters and towers.

Topological clusters, or *topo-clusters*, are collections of calorimeter cells whose size and shape is defined by a clustering algorithm. The basic requirement of such an algorithm is to group together neighbouring cells that have significant energy compared to the expected noise [160]. Hence, it is designed to suppress the clustering of cells which contain energy deposits resulting from low-level noise.

The specific algorithm used at ATLAS [161] takes as its input one or more neighbouring seed cells whose signal-to-noise ratio (SNR)[6] is greater than 4. Any cells which are adjacent to the seed and have an SNR of at least 2 are incorporated into the topo-cluster. When no further adjacent cells can be found with SNR ≥ 2, a ring comprising *all* adjacent cells is included in the topo-cluster. Figure 3.9 demonstrates the output from the clustering algorithm; in the top right, a topo-cluster has been formed around four neighbouring

[6] In this case, the noise is estimated as the absolute value of the energy deposited in the calorimeter cell, divided by the RMS of the energy distribution measured in events triggered at random bunch crossings.

seed cells all with SNR ≥ 4. No other topo-clusters are formed since there are no other cells with a sufficiently high SNR.

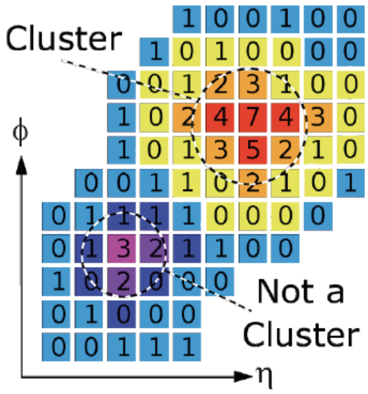

Figure 3.9: A demonstration of the output from the clustering algorithm described in the text. Topo-clusters can only be formed if there are one or more seed cells with SNR ≥ 4, such as in the top right of the figure. The squares represent calorimeter cells and the numbers denote the signal-to-noise ratio of each cell.

If two close-by particles produce adjoining showers in the calorimeter, the clustering algorithm may form a single topo-cluster which covers a large area of the calorimeter. The algorithm therefore involves a second procedure known as *splitting*, after the initial topo-cluster formation. The aim of this stage is to form separate topo-clusters if two particles are sufficiently far apart that the resulting single topo-cluster contains cells with local maxima of deposited energy. Specifically, the splitting procedure takes a single topo-cluster as input and searches for all contained cells having an energy content of greater than $500~\mathrm{MeV}$. Furthermore, these cells must have an energy content greater than that of all adjacent cells. The primary clustering procedure is then performed using these cells as seeds. The splitting procedure is described in detail in [160].

The energy of the topo-cluster is defined to be equal to the sum of the energies of all its constituent calorimeter cells. The direction is calculated from the weighted averages of the η and ϕ of the constituent cells, where the weight used is the absolute value of the cell energy. The mass of the topo-clusters is assumed to be zero.

The second type of grouping of calorimeter cells is called *towers*, detailed in section 6.1.2 of [161]. They are constructed from the cells in all longitudinal layers of the calorimeter which are projected into the elements of a grid in η-ϕ space. The chosen grid size for ATLAS analyses is $\Delta\eta \times \Delta\phi = 0.1 \times 0.1$. The benefit of using towers is that they are of fixed size, unlike topo-clusters whose size depends on the characteristics of the incident shower. However, all analyses involving top quarks at ATLAS are recommended to use jets formed from topo-clusters. A study was carried out in 2009 [93] in which a selection criteria relevant for $t\bar{t}$ pair production was applied to two samples of simulated events containing, respectively, the processes of SM $t\bar{t}$ pair production (the signal process, in this case) and W+jets production (the background process). The figure of merit used to compare the jets reconstructed from topo-clusters and from towers was the *signal significance* $F = S/\sqrt{S+B}$, where S (B) denotes the number of signal (background) events passing the selection criteria. The jets formed from topo-clusters resulted in a value of F approximately $4\ \%$ higher than that for jets formed from towers, for a jet p_T threshold of $20\ \mathrm{GeV}$.

3.3.2 Calibration

Energy deposits in the calorimeter are reconstructed at the EM-scale i.e. the scale at which the energy of a particle which interacts *electromagnetically* will be correctly reconstructed. This scale is obtained using test-beam measurements and the invariant mass of $Z \to ee$ events, as detailed in section three of [161].

Since the ATLAS calorimeters are non-compensating, an incident hadron with equivalent energy to an electron or photon will have a lower reconstructed energy. The presence of un-instrumented material in the detector also means that the hadron's reconstructed energy will be less than its incident energy [160]. The aim of jet calibration is to relate the *average* energy of a set of hadronic jets measured by the calorimeter to the energy of the incident particles which are the cause of each jet. Calibration to the *jet energy scale* is achieved using simulated data, by means of a comparison of the energy of a jet measured by the calorimeter to the energy of a nearby *truth jet*. Truth jets are reconstructed using only stable particles[7] which have not been passed through the detector simulation software. This stage of the calibration aims to correct for not only non-compensation and un-instrumented material, but also the following effects:

- Particles leaking from the detector, whose energy then goes (partially) undetected.
- The energy of some simulated particles failing to be included in the reconstructed jet but being included in its associated truth jet.
- The omission of energy deposits during the formation of topo-clusters and/or during jet reconstruction. The former may occur due to the noise threshold placed on candidates for topo-clusters; the latter, because jet algorithms are not guaranteed to recombine all energy deposits resulting from the decay of the originating parton, particularly if they fall beyond the scope of the chosen radius parameter used in the reconstruction.

The topo-clusters comprising the jet may contain energy resulting from pile-up. A correction is derived from minimum bias data, which accounts for the average additional energy deposited in a grid of 0.1×0.1 in the η-ϕ plane. It is applied to the EM-scale topoclusters, *before* the final correction to the jet energy scale.

The calibration scheme described above is known as EM+JES because it corrects the kinematic variables measured at the EM-scale directly to the jet energy scale, using multiplicative factors applied as a function of the jet E and η. The average energy correction under this scheme, as a function of jet p_T, is shown in Figure 3.10 for anti-k_T jets reconstructed with $R = 0.6$. It ranges from 1.2 for high p_T jets to 2.1 for low p_T jets, in the central region. The correction is larger for these softer jets because they have a smaller fraction of electromagnetically-interacting particles than harder jets [112]. The position of the jet is also corrected, but there is no correction for the mass. A comprehensive description of the calibration process for AKT4 jets, and estimation of the associated systematic uncertainties, can be found in [162].

[7]Stable particles are those having a lifetime longer than 10 ps and excluding muons and neutrinos

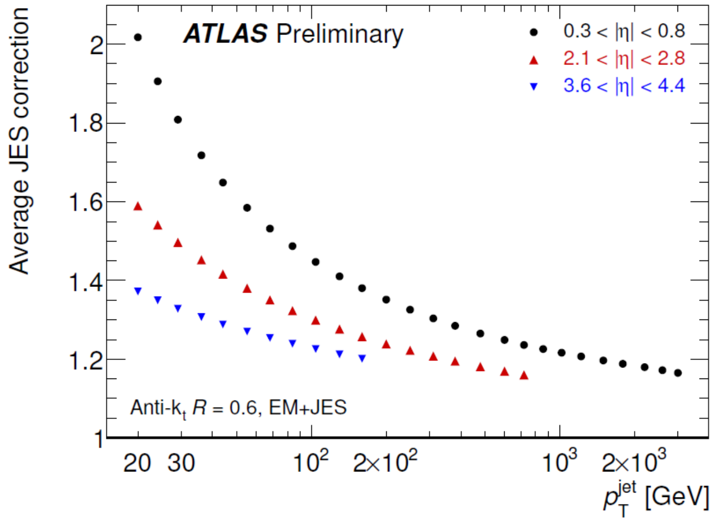

Figure 3.10: Average correction applied to anti-k_T EM+JES jets with $R = 0.6$ when calibrating to the jet energy scale (JES). Taken from [162].

However, the AKT10 jets used in this thesis have been calibrated under an alternative scheme, known as local cluster weighting (LCW, or LC) [163, 164]. In this procedure, the topo-clusters are first classified as either electromagnetic or hadronic in origin, according to the cluster topology measured in the calorimeter. A weight is then applied to each cell in the cluster according to the cluster energy and the cell energy density. These weights were derived from the simulation of single pions and verified in test-beam measurements. Further corrections are applied to account for the possibility of energy deposited (1) in the calorimeter but outside of the topo-cluster, (2) in material before the calorimeter and (3) in inactive regions of the calorimeter. These corrections are obtained from simulations of charged and neutral particles. Following jet reconstruction from the LC-scale topo-clusters, the JES calibration then proceeds as described above for EM-scale topo-clusters.

A first application of the LC+JES scheme on simulated ATLAS data [165] demonstrated its main advantages: an improved jet p_T resolution and a reduced difference between the response due to light-quark or gluon initiated jets, compared to jets at the EM+JES scale. These improvements are particularly beneficial when jet substructure is crucial to an analysis, as is the case here, since *individual* topo-clusters receive a specific calibration appropriate to their type, before the jets are reconstructed. Hence, the AKT10 jets used in this analysis have been calibrated using the LC+JES scheme, in a procedure detailed in [103]. A correction for the mass of these jets was also derived because this variable has a vital role in the identification of jets containing top quark decay products. The mass and energy are corrected by 10 – 20 % on average, and the jet η is corrected by ≈ 0.01.

At the time that this search for $t\bar{t}$ resonances was being formulated, the use of AKT4 jets at the EM+JES scale was highly recommended by the ATLAS jet performance group; the LC+JES calibration for these jets was still in the commissioning phase [162]. Hence, the EM+JES calibration is applied to the anti-k_T $R = 0.4$ jets used in this analysis.

3.3.3 Selection

Requirements are then imposed on both jet collections to determine whether they should receive further consideration. First, reconstructed jets with negative energy are discounted. Such jets occur mainly due to the treatment for pile-up effects [166], known as the *offset correction*. It is not the correction itself that produces the spurious negative energy, but a problem with its derivation in some cases [167]. However, this affects fewer than 0.01 % of the events in the dataset analysed for this search and therefore these objects are simply not deemed to be viable jet candidates.

A procedure is carried out to avoid inclusion of energy deposits which have already been assessed as contributing to the electron energy, in the jet reconstruction. The one jet from each collection that is closest, in η-ϕ space, to any of the electron candidates identified above, and having ΔR (jet, electron) ≤ 0.2 (for AKT4 jets) or ≤ 0.5 (for AKT10) is omitted from further consideration. This procedure is illustrated in Figure 3.11 (right).

General detector acceptance criteria are also applied: jets reconstructed with $|\eta| > 2.5$ (AKT4) or $|\eta| > 2.0$ (AKT10) are not considered as suitable candidates. For the smaller jets, this is motivated by the fact that the uncertainty on the jet energy scale for jets with $p_T = 20$ GeV in the very forward region ($3.6 < |\eta| < 4.5$) is over three times that in the central region [162]. For the larger jets, this *JES uncertainty* was not estimated for jets

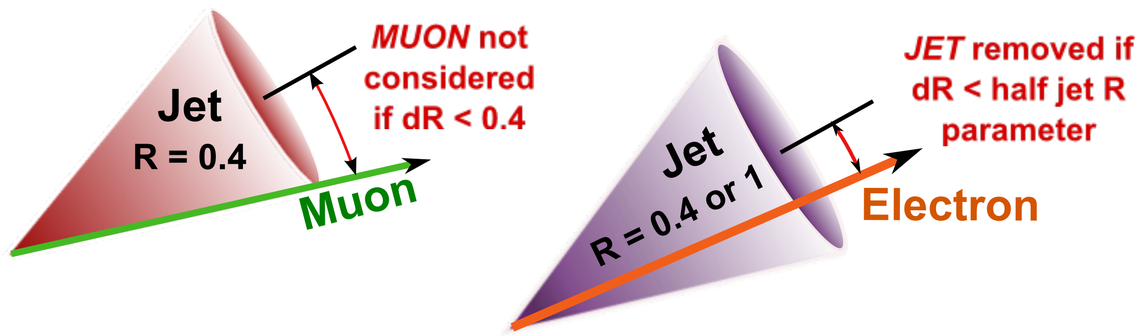

Figure 3.11: Visualisation of the procedure to treat closely-located jets and leptons. Left: any muon which has $\Delta R \leq 0.4$ to any anti-k_T $R = 0.4$ jet with $p_T > 20$ GeV cannot be considered to originate from the $t \to W$ decay chain. Right: removal of an anti-k_T $R = 0.4$ (1.0) *jet* with $\Delta R \leq 0.2$ (0.5) to an electron.

reconstructed beyond $|\eta| = 2.0$ [103].

The above requirements all apply to individual jets. However, there is an additional specification to reject entire events that contain any *fake jets*; that is, those deemed not to originate from the hard-scatter. Background processes resulting in these jets include interactions between protons and residual gas in the beam pipe, the incidence of cosmic-ray muons on the calorimeters, and noise in the calorimeters. The identification of these fake jets and the rejection of events in which they are contained is known as *jet cleaning*. There are different levels of cleaning depending on the required rejection power for the fake jets. The level used for this search has an efficiency[8] of over 99 %. The general cleaning process is described in section seven of [161] with details in [168]. The process was only carried out on events in real data, not in simulation, since the required variables are not well modelled in the latter. No correction was applied to the simulated events to account for this, since fewer than 1 % of events were affected by this cleaning.

The treatment of jets affected by the LAr hole problem, detailed in Section 2.2.3, is also applied on an event-level basis. That is, an event from data is removed from further consideration if any jet having $p_T > 20$ GeV is found with $\Delta R \leq 0.1$ to the hole. For simulated events, the same condition is applied, but for only the fraction of events corresponding to the fraction of luminosity for which the hole problem was present.

[8]The ratio of the number of jets passing the cleaning criteria to the total number of jets.

The application of techniques used to identify fat jets which are typical of those containing the decay products of top quarks is discussed in Section 4.1.4.

3.3.4 b-tagging

b-tagging is the common name for the identification of jets containing B-hadrons, through exploitation of the topologies of weak B- and D-hadron decays inside the jet. It therefore naturally assists in the identification of events containing top quarks. However the procedure is *not* deployed for the selection of potential signal events in this thesis due to concerns regarding the decrease in the fraction of jets tagged as the jet p_T increases. These concerns are particularly relevant since this search is tailored towards boosted top quarks which will result in jets having large p_T. The decrease in efficiency is demonstrated in Figure 3.12, for a high-performance multivariate algorithm [169] developed by ATLAS; the fraction of jets with $p_T = 480 – 500$ GeV that are tagged by the algorithm is approximately half that for jets having $p_T = 20 – 40$ GeV.

Although b-tagging is not used to select a potential signal, it *is* used in the validation of a data-driven normalisation for the W+jets production process. This is described comprehensively in Section 5.1.1.

3.4 Missing transverse energy

Missing transverse energy is the general signature of the production of "invisible" particles which do not interact with the detector material. These may be neutrinos, in SM processes, or something more exotic such as supersymmetric particles. The generic definition of E_T^{miss} was introduced in Section 2.2.1.

The E_T^{miss} reconstruction proceeds in two stages. The first stage uses calorimeter cells in which energy deposits have been recorded, resulting in the *calorimeter term*. The second stage uses reconstructed muon tracks, resulting in the *muon term*. In the calculation of

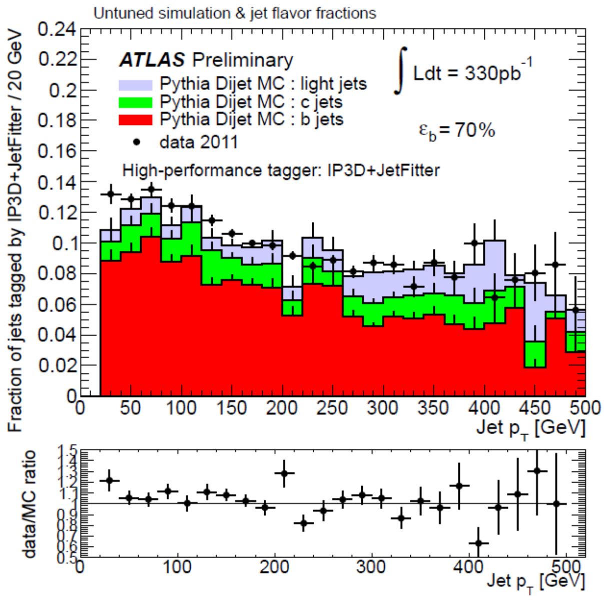

Figure 3.12: Fraction of jets tagged by a multivariate b-tagging algorithm [169] as a function of jet p_T, in a sample of simulated dijet events enriched in heavy-flavour hadrons.The algorithm is operating at a b-jet tagging efficiency of $70\ \%$, as measured in simulated $t\bar{t}$ events. The decrease in performance as the jet p_T increases can be seen clearly.

both terms, the respective cells and tracks are first associated to physics objects which have received the appropriate degree of calibration, as discussed in previous sections. The object definitions follow those specified by the ATLAS top working group above; details on the derivation of this specific form of E_T^{miss} can be found in [170].

For the calorimeter term, the cells are associated with, in order:

1. Electrons.
2. Photons.
3. τ-leptons.
4. Anti-k_T $R = 0.4$ jets with $p_T > 20$ GeV and calibrated to the EM+JES scale (`HardJets`).
5. Anti-k_T $R = 0.4$ jets with $20 > p_T \geq 7$ GeV and calibrated to the EM-scale only (`SoftJets`.).

The muon term is determined from the momenta of muon tracks reconstructed within $|\eta| < 2.7$ which is the acceptance region for the MS. This includes all combined `Muid` muons, in the region $|\eta| < 2.5$, which are reconstructed in both the ID and the MS.

The remaining energy from cells not associated with one of these objects is included as an additional term, `CellOut`. Any muon energy deposited in the calorimeters is included in either the `CellOut` term or the `HardJet` term depending on the degree of isolation from any anti-k_T $R = 0.4$ jet. This procedure is detailed in [171].

Overall, the E_T^{miss} components are calculated as follows:

$$E_{x(y)}^{miss} = E_{x(y)}^{El} + E_{x(y)}^{Photon} + E_{x(y)}^{Tau} + E_{x(y)}^{\texttt{HardJet}} + E_{x(y)}^{\texttt{SoftJet}} + E_{x(y)}^{Muon} + E_{x(y)}^{\texttt{CellOut}} \tag{3.1}$$

The values of E_T^{miss} and its azimuthal angle ϕ^{miss} are then formulated as:

$$E_T^{miss} = \sqrt{(E_x^{miss})^2 + (E_y^{miss})^2} \tag{3.2a}$$

$$\phi^{miss} = \arctan(E_y^{miss}/E_x^{miss}) \tag{3.2b}$$

The resolution of the E_T^{miss} is determined by the precision and the energy scales of the objects used in its reconstruction. It is therefore proportional to the square root of the total E_T deposited in the detector from one pp bunch crossing. The resolution is determined, using a method described in [170], by calculating the sum of the transverse energies of all objects (ΣE_T) in all events from the SM $t\bar{t}$ sample described in Section 2.4.2. A fit to the function $a \times \sqrt{\Sigma E_T}$ in the range $300 < \Sigma E_T < 1000$ GeV yields $a = 0.692 \pm 0.002$ (0.734 ± 0.002) in events where the leptonically decaying top quark produces an electron (muon).

Any possible dependence of the resolution on the level of in-time pile-up is also investigated by measuring the value of $\Delta a/\Delta(N_{PV})$. The dependence was found to be very weak in the electron channel ($\Delta a/\Delta(N_{PV}) = -0.37 \pm 0.25$) and no dependence was found in the muon channel ($\Delta a/\Delta(N_{PV}) = +0.20 \pm 0.24$). The results in the two channels are consistent at the level of one sigma.

Determination of all systematic uncertainties related to the physics objects discussed in this chapter, and their propagation to the final result, is discussed in Section 6.3.

3.5 Summary

The reconstruction and identification of leptons, jets and the missing transverse momentum forms the basis of this search. These procedures have been fully documented in this chapter, together with the lepton triggers applied to collect events of interest. The concept of scale factors is introduced, which are used to correct the reconstruction, identification and trigger efficiencies measured in simulated events to match those measured in data. The reconstruction, selection and calibration of jets is discussed in detail, since these objects play a crucial role in this thesis.

Chapter 4

Analysis strategy

Searches for new phenomena involve the selection of events produced by possible BSM *signal* processes amidst those produced by SM *background* processes. The general aim is to obtain a sample of events which is both enriched in the contribution from the signal and depleted in the contribution from the backgrounds. The enrichment is achieved by specifying a number of criteria which each event must pass in order to be entered into the final *signal sample*, also referred to as the *signal region*. Each criterium is composed of a variable and a corresponding threshold value. The choice of criteria is made based on the different characteristics of signal and background events, and of course optimised to favour selection of the former. The list of criteria, together with the rationale for the choices made, are detailed in this chapter.

The next stage in the search is the identification of any deviations from the background prediction demonstrated by the selected data events. The simplest method of identifying such deviations is known as “cut-and-count”. It involves simply counting the number of events from data, and from the SM prediction, in this signal region. This method has the benefit of not being tailored towards any particular signal model or mass.

This specific case of a search for resonant $t\bar{t}$ production in BSM processes is not so straightforward as the above procedure suggests. This is because there is no way to separate events containing $t\bar{t}$ pairs produced in these BSM processes from those produced within the standard model, without introducing specific criteria which may bias the selection towards a particular BSM model. Hence SM $t\bar{t}$ production is known as an *irreducible* background and the signal sample is composed mainly of SM $t\bar{t}$ events.

The cross-section for SM $t\bar{t}$ production is two orders of magnitude larger than the typical signal cross-section, as discussed in Section 2.4.2. This means that such a cut-and-count analysis would not be sufficiently sensitive to deviations caused by signal processes. A simple measure of sensitivity is $S/\sqrt{B}$, where S denotes the yield of signal events and $\sqrt{B}$ is the statistical uncertainty of the background yield, assuming that the latter follows a Poissonian distribution. The typical value of this ratio in the ATLAS resolved $t\bar{t}$ resonance search is < 0.01 for a Kaluza-Klein gluon of mass $1300\ \mathrm{GeV}$ [71].

A second stage is therefore required in order to identify the possible presence of resonant $t\bar{t}$ production. This uses the fact that distributions of certain *discriminating* variables will have different shapes depending on the physics process from which they are drawn. For this search, the discriminating variable is the invariant mass of the $t\bar{t}$ system, $m_{t\bar{t}}$, which is reconstructed from certain physics objects in the final state of the decay. This reconstruction is also described in this chapter.

Deviations from the background prediction are then searched for in windows of varying width across the $m_{t\bar{t}}$ distribution. This is essentially a cut-and-count in separate bins across the distribution of this discriminant, thereby enhancing the statistical significance of any possible signal. The description of the procedure for identifying the presence of a signal is the topic of Chapter 6.

This search has the following (reducible) background processes:

- Vector boson production with associated jets (W+jets and Z+jets).
- Electroweak single top quark production.
- Diboson production.
- QCD multijet production.

Although the SM $t\bar{t}$ background cannot be removed from the signal sample, it is still important to remove a significant number of events due to these other backgrounds. The reason can be seen when comparing the values for the production cross-sections for the backgrounds to that of SM $t\bar{t}$ production. For example, W or Z boson production has a cross-section which is $1-2$ orders of magnitude larger than that for SM $t\bar{t}$ production, as shown in Figure 4.1.

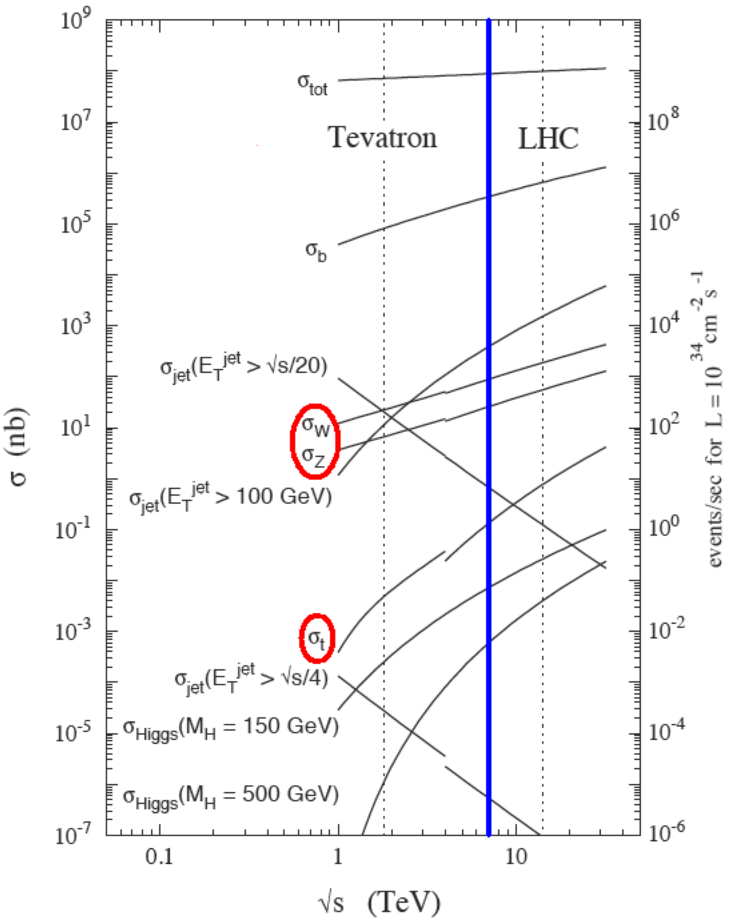

Figure 4.1: Cross-sections for SM processes in pp collisions, as a function of the centre-of-mass energy. The LHC operating at $\sqrt{s} = 7$ TeV is denoted with a blue vertical line. The production cross-sections for W bosons, Z bosons and SM $t\bar{t}$ pairs are indicated by the lines labelled with σ_W, σ_Z and σ_t respectively. Taken from [172].

4.1 Selection of $t\bar{t}$ events

4.1.1 Initial criteria

The first requirement of the signal selection is driven by the need for data of sufficiently high quality. Events must be in luminosity blocks contained in the good run list relevant to ATLAS analyses involving top quarks.

The event is then checked for having fired a certain trigger, indicating that it potentially contains an interaction which would be pertinent for this search. Since this analysis is performed on the lepton+jets final state, each event must fire *either* a single electron *or* a single muon trigger. These triggers were detailed in Sections 3.1 and 3.2 respectively. The separation of events into different channels by lepton flavour is retained throughout the event selection so that flavour-dependent criteria can be applied.

As introduced in Section 3.2, an error in the ATLAS simulation software resulted in a lower trigger efficiency in simulated events. However, the extent of this effect could not be measured with the tag-and-probe technique and therefore the muon trigger requirement is not applied to *simulated* events. Instead, these events are weighted by the muon trigger efficiency measured in data rather than by a scale factor, following a procedure described in [173].

Rejection of events not associated with a collision, such as those resulting from background radiation in the cavern or from cosmic rays, is achieved by requiring that the reconstructed primary vertex has at least five associated tracks each with $p_T > 400$ MeV.

Following these basic quality requirements, criteria more specific to the lepton+jets final state are employed. All physics objects referred to hereafter are required to have passed the object selection criteria specified in Chapter 3, unless otherwise stated.

In the electron channel, events must contain exactly one electron, with $E_T > 25$ GeV. The E_T variable is calculated using a combination of the energy measured in the calorimeter and the direction of the track recorded by the ID. For the muon channel, a single muon is required with $p_T > 20$ GeV, where the p_T is obtained from a combination of measurements taken by both the MS and the ID. The threshold placed on the electron (muon) E_T (p_T) ensures that the trigger used in each channel has a stable efficiency as measured in data with respect to the E_T (p_T) of the object firing the trigger. Therefore, the efficiency can be considered as constant for all selected events. The efficiencies for the electron and muon triggers as a function of E_T (p_T) are displayed in Figures 3.4 and 3.7 respectively.

The selected lepton must be matched to the object resulting from the positive trigger decision. That is to say, their separation in η-ϕ space must be < 0.15. The matching was not performed on simulated events in the muon channel because the trigger requirement was not applied, as described previously. An additional systematic uncertainty applied to cover this omission is described in Section 6.3.4.

To ensure that only one lepton of the required quality is produced in the interaction, events in the muon channel must not contain any electrons with $E_T > 25$ GeV. Likewise, in the electron channel events must not contain any muons with $p_T > 20$ GeV. Furthermore, there is the possibility that energy deposits may lead to the reconstruction of *both* an electron *and* a muon. To guard against this possibility, events are rejected in which the selected electron is made up of an ID track which is also used in the reconstruction of a muon. The muon candidate in this case does *not* have the hit multiplicity requirement placed on its associated ID track, nor is it checked for its proximity to a jet.

Suppression of non-prompt lepton and "fake" electron sources is achieved in two ways, additional to those described in Chapter 3. First, the E_T^{miss} must be greater than a certain threshold. Second, requirements are placed on a combination of the E_T^{miss} and the transverse mass of the selected charged lepton. This combined variable is known as the W transverse mass or $m_T(W)$ and is defined as:

$$m_T(W) = \sqrt{2p_T^l\, E_T^{miss}(1 - \cos(\Delta\phi))} \tag{4.1}$$

where p_T^l is the p_T of the selected charged lepton and $\Delta\phi$ is the azimuthal angle between this lepton and the E_T^{miss}.

In the muon channel, the criteria are: $E_T^{miss} > 20$ GeV and $E_T^{miss} + m_T(W) > 60$ GeV. The combined E_T^{miss} and $m_T(W)$ threshold exploits the fact that non-prompt lepton and fake electron production processes typically result in events with large E_T^{miss} but small $m_T(W)$, relative to those containing $W \rightarrow l\nu$ decays, where the W boson results directly from the hard-scatter or from a top quark decay. The thresholds in the electron channel are higher: $E_T^{miss} > 35$ GeV and $m_T(W) > 25$ GeV. This is because processes such as photon conversions or π^0 decays result in a larger overall contribution from these background processes in this channel [174].

It is at this stage that criteria related to jets are applied, which are disperse objects whose size is determined during their reconstruction. There are two approaches to this reconstruction. The first is to *separately* associate a jet to the hadrons resulting from each of the three hard partons from the $t \rightarrow bW \rightarrow bq\bar{q}'$ decay. This is referred to as the *resolved approach*.

The alternative strategy is to include the majority of the hadrons resulting from the decay in a single jet. This is known as the *boosted approach* and is tailored towards the reconstruction of top quarks with a higher p_T than in the resolved method. In this thesis, the boosted approach is applied for the first time on a search for $t\bar{t}$ resonances using ATLAS data. The resolved strategy is not used, but it is summarised below in order to highlight its shortcomings, and hence the need for a new "boosted strategy".

4.1.2 The resolved approach to top quark reconstruction

The resolved approach as used at ATLAS requires *four* jets in the final state, each having $p_T > 25$ GeV. Three of these are assumed to result from the decay of the hadronic top quark, which is illustrated in Figure 4.2 (a), although this quark is not specifically reconstructed. At least one of the four must be tagged as a b-jet, that is, originating from a

b-quark.

The standard value of R for jets used in ATLAS analyses involving top quarks, including this one, is 0.4. This is large enough to be reliably unaffected by the calorimeter granularity, yet, when compared to $R = 0.7$ jets, exhibits a smaller jet energy resolution and a higher efficiency for reconstructing W bosons in $t\bar{t}$ events using the resolved approach [175].

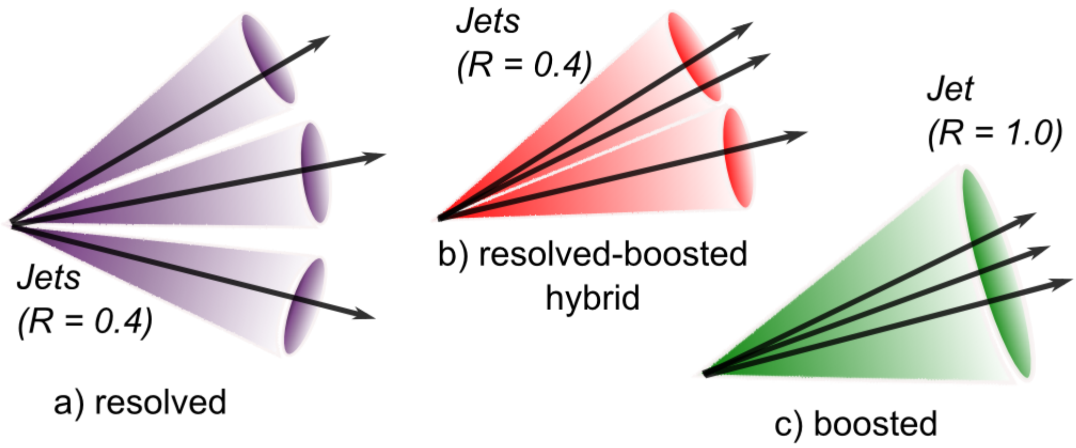

Figure 4.2: A basic representation of the strategies employed in the (a) resolved (b) resolved-boosted hybrid and (c) boosted approaches. The three hard partons resulting from the hadronic decay of a top quark are represented by black arrows, and the jets used to reconstruct the hadronic energy flow are represented by coloured cones. The p_T of the top quark increases from subfigures (a) to (c), therefore causing the partons to become increasingly collimated. The multiplicity and/or size of the jets is adapted accordingly in order that the top quark can still be identified.

The resolved approach is based on the assumption that three separate $R = 0.4$ jets are reconstructed from the decay products of the hadronic top quark. As the p_T of the top quark increases, these jets will become increasingly more collimated. This behaviour is approximately described through Equation 4.2 which relates the p_T of a decaying particle to the radius of the cone in which its decay products will be contained:

$$p_T \approx \frac{2m_t}{\Delta R} \tag{4.2}$$

One notable complication is that jets do not have a fixed and consistent size: as cautioned in Section 1.4.1, the R-parameter guides the reconstruction but does not define the exact radius of the cone of the final jet. However, the R-parameter can be used as an approximate measure for this radius in the case of the more regularly shaped anti-k_T jets. In this case, in order to have three anti-k_T jets reconstructed with $R = 0.4$ *just* separated in η-ϕ space, they must be contained in a cone having a radius of at least $0.4 \times 3 = 1.2$.

Through use of Equation 4.2, one can see that jets with such a spacing would result from the decay of a top quark with a p_T up to approximately $2m_t/1.2 = 300$ GeV. Over 85 % of the top quarks resulting from SM production have a p_T below this threshold, as illustrated in Figure 4.3. Therefore, the resolved approach is suitable for reconstructing the majority of top quark decays resulting from SM $t\bar{t}$ pair production.

ATLAS has released three results using a purely resolved approach, with $33\ \mathrm{pb}^{-1}$ [176], $204\ \mathrm{pb}^{-1}$ [177] and $2.05\ \mathrm{fb}^{-1}$ [71] of data analysed at $\sqrt{s} = 7$ TeV. However, there has been a programme to develop methods for boosted top quark reconstruction since the inception of the ATLAS experiment. This is required not only to carry out $t\bar{t}$ resonance searches, but also to study SM $t\bar{t}$ production during collisions with high Q^2 values. Such methods will be even more important when the centre-of-mass energy of the colliding protons is increased from 7 TeV to 14 TeV in 2014. In practice, a boosted strategy has been implemented in stages; the initial stage is now discussed.

4.1.3 The development of a resolved-boosted hybrid approach

A comprehensive study was carried out by ATLAS in 2010 [178] to enhance the sensitivity to $t\bar{t}$ resonances at the TeV-scale.[1] This included an adaption to the resolved approach, referred to in the original reference as the *minimal reconstruction* strategy and known in this thesis as the *resolved-boosted hybrid*. It was developed to handle events in which the p_T of the top quarks is so large that their decay products become collimated into a small

[1]Simulated data samples were used, with $\sqrt{s} = 10$ TeV since this was initially proposed as the centre-of-mass energy for the first stage of LHC data-taking. However, these results are expected to be applicable to a centre-of-mass energy of 7 TeV.

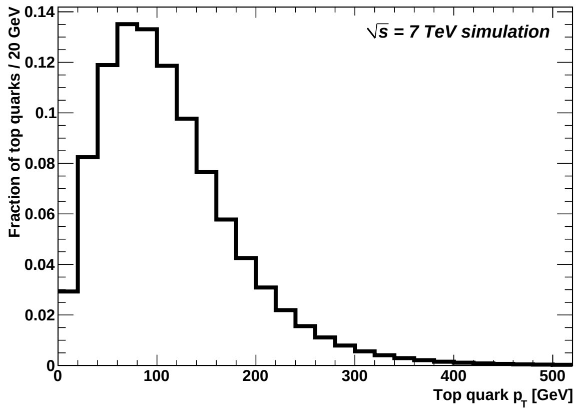

(a)

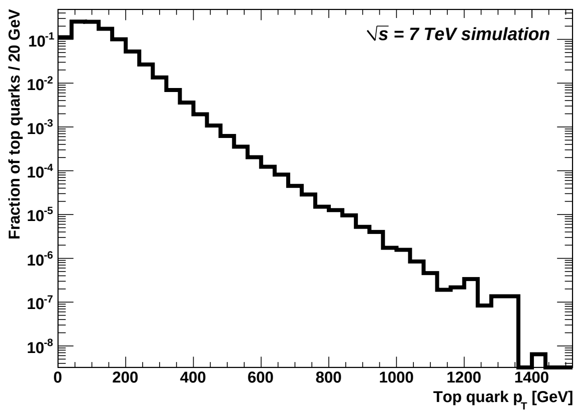

(b)

Figure 4.3: p_T of the top quarks resulting from SM $t\bar{t}$ production at $\sqrt{s} = 7$ TeV, with an (a) linear and (b) logarithmic scale for the x-axis. Over 85 % of the top quarks have $p_T \lesssim 300$ GeV and can therefore be reconstructed using the "resolved" topology. However, ≈ 1 % of top quarks are highly boosted, having a $p_T > 500$ GeV. The Monte Carlo sample for SM $t\bar{t}$ production obtained using the MC@NLO generator, detailed in Section 2.4.2, was used for the generation of these events. All distributions have been normalised to unit area.

region of the detector and the resolved approach is no longer valid. As demonstrated using Equation 4.2, this occurs when the top quark has $p_T \gtrsim 300$ GeV. This claim is supported by Figure 4.4(a), which reveals that events with $m_{t\bar{t}}$ from 500 to 1000 GeV have an increasing probability (from 5 to 70 %) for two of the three partons from the hadronic top quark decay to found within a cone of radius $\Delta R = 0.8$, i.e. to have *merged*.

At the reconstruction level, evidence of this merging manifests itself through the mass of the jets in the event. In Figure 4.4(b), one can see how the merging at *truth level*, that is before the generated event is passed through the detector simulation software, trans-

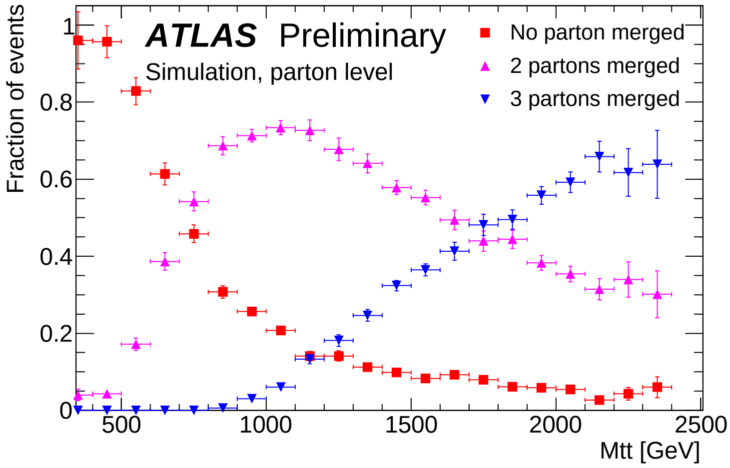

(a)

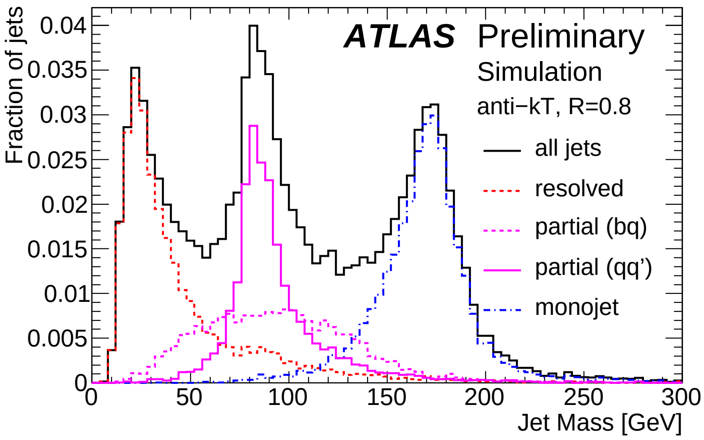

(b)

Figure 4.4: Fraction of events (a) with a certain reconstructed $t\bar{t}$ mass (Mtt) in which the three partons of a hadronic top quark decay are found within a cone of radius $\Delta R = 0.8$, or *merged*. The red squares indicate the fraction in which no partons merge. The pink triangles are the fraction in which two partons merge, with the third parton remaining well separated. The blue inverted triangles indicate the fraction of events in which all three partons merge. Reconstructed invariant mass (b) of the leading jet (with $R = 0.8$) in $pp \to X \to t\bar{t} \to$ lepton+jets events. The jet mass enables one to infer the degree of parton merging that has taken place. Taken from [178].

lates to reconstruction level. The distribution of the mass of the leading ($R = 0.8$) jet in categories of events with different degrees of parton merging is displayed. The red dashed line indicates events where *no* partons have merged; the pink solid and dashed lines represent events where two partons have merged; and the blue dot-dash line represents events where all three partons have merged. For events in which the leading jet has

$m \gtrsim 60$ GeV, the majority of jets have at least two partons which have merged.

This motivated an adaption to be made to the resolved approach used at ATLAS: rather than just requiring events to contain at least four $R = 0.4$ jets, a lower jet multiplicity of three can be permitted *if* one of the jets has $m > 60$ GeV. This situation is demonstrated in Figure 4.2(b), where the two jets with $R = 0.4$ are represented by red cones and, the partons from the hadronic top decay, by black arrows. ATLAS has previously produced an update of the search for $t\bar{t}$ resonances in the lepton+jets channel using this resolved-boosted hybrid [71].

However, it is clear that this adapted approach will also fail as the boost of the top quark increases further, similar to the situation of the purely resolved approach failing for top quarks with $p_T \gtrsim 300$ GeV. Specifically, the reconstruction will begin to fail when the two $R = 0.4$ jets overlap, that is, when they are contained in a cone of radius $\Delta R = 2 \times 0.4 = 0.8$ or smaller. This corresponds to a top quark with $p_T \gtrsim 450$ GeV. A fundamentally different reconstruction method is required in this case.

4.1.4 The boosted approach to top quark reconstruction

As the centre-of-mass energy of the $t\bar{t}$ production process increases, it is a natural progression to attempt to use a single object to reconstruct the top quark from its decay products. A preliminary investigation into such a method was carried out in 1999 (see section 18.1.3.4 of [172]). It involved a rather simple technique: the calculation of the invariant mass of all calorimeter cells contained within a cone of radius $\Delta R = 1.3$ and therefore the reconstruction of the hadronic top quark as a single object. The potential of this technique to reduce the overall systematic uncertainties was highlighted, since only one jet is used rather than several, which each have an uncertainty associated with their properties.

A more sophisticated technique was developed as part of the *mono-jet strategy* of [178]. Essentially, the vast majority of the decay products of the top quark are reconstructed into a single fat jet, as illustrated in Figure 4.2(c). A simplified version of this technique has been deployed on a search for $t\bar{t}$ resonances in this thesis.

A number of factors must be considered when selecting the radius parameter for the fat jets. One would like a suitably large jet so as to reconstruct top quarks with a *relatively* low $p_T \approx 300$ GeV. That is, in the kinematic region where the resolved approach begins to fail. However, the jet cannot be so large that its mass would be substantially affected by the presence of energy deposits from pile-up or that it would be restricted by the calorimeter acceptance.

To accommodate both considerations, a value of R equal to 1.0 was chosen for the analysis detailed in this thesis. Using Equation 4.2, one can see that such jets will enclose approximately all of the decay products from a top quark with p_T as low as 350 GeV. A lower p_T threshold of 250 GeV is actually used in this analysis, for reasons outlined in Section 4.2.1. This strategy of using a single fat jet has further benefits for the selection of events containing boosted top quarks because one automatically has a candidate for the hadronic top, and therefore can use its properties for event selection. This avoids the ambiguity associated with selecting two or three smaller jets.

It should be stressed that the value of R discussed so far is *fixed*, that is, all jets in all events are reconstructed with approximately the same size. However, the decay products of the top quark become increasingly more collimated as its p_T increases. The jets could therefore be permitted to decrease in size as the p_T increases, whilst still containing the majority of the top quark decay. This would also minimise the contribution from energy deposits due to pile-up and the underlying event. This idea is explored in Chapter 7, through the use of jets with a variable R value which decreases as the jet p_T increases.

The boosted approach would ideally be used to reconstruct both the hadronic *and* the leptonic top quark. However, the electron and muon definitions recommended by the ATLAS top working group at the time that this study was carried out both require a high degree of isolation in a *fixed* cone around the lepton (see Chapter 3). This is effective at rejecting events that result from QCD multijet production but is likely to have a detrimental effect[2] on the identification of boosted top quarks, as the lepton gets increasingly close to the jet and is eventually contained within it. Therefore, on the leptonic side of the decay the resolved strategy of using a separate $R = 0.4$ jet and lepton continue to be used in this thesis.

It is still necessary to apply certain requirements on the fat jet in order to reduce the contribution from background processes, namely W+jets and QCD multijet production. This is achieved by studying the properties of the fat jet to see if it more closely resembles a jet containing top quark decay products (a *top jet*), or one initiated by gluons or light quarks (a *QCD jet*). This process is known as *top-tagging*. In this thesis it is achieved with the use of two variables: the jet mass m_j and the first k_T-splitting scale $\sqrt{d_{12}}$, both introduced in Section 1.4. The distributions of these variables can be seen in Figure 4.5, for both top jets and QCD jets. These studies were performed in [178], where the top jets were taken from the simulated samples of $Z' \to t\bar{t}$ described in Section 2.4, with $m_{Z'} = 1$ TeV and 2 TeV. The QCD jets are from dijet samples generated using PYTHIA. Thresholds on both sets of jets were applied, of $p_T > 200$ GeV and $m_j > 100$ GeV. Both m_j and $\sqrt{d_{12}}$ have the capability to provide good discrimination between top and QCD jets.

Optimal discrimination for these events would be provided by using criteria of $m_j \gtrsim 160$ GeV and $\sqrt{d_{12}} \gtrsim 70$ GeV. However, Figure 4.6 illustrates the m_j and $\sqrt{d_{12}}$ distributions for all reconstructed fat jets with $p_T > 150$ GeV, in the sample of simulated $g_{KK} \to t\bar{t}$ events used in this thesis, where $m_{g_{KK}} = 1.6$ TeV. Only 30 ± 3.3 % of the jets would pass these m_j and $\sqrt{d_{12}}$ criteria, leading to the rejection of a similarly large proportion of *events* from the final signal sample. The thresholds on m_j and $\sqrt{d_{12}}$ in this thesis are therefore lowered to 40 GeV and 100 GeV respectively.

In summary, the list of event selection criteria based on jets, for the boosted approach is as follows. First, at least one $R = 0.4$ jet must be close to, but not overlapping with, the one lepton in the event i.e. $0.4 < \Delta R$ (jet, lepton) < 1.5. Of these, the one closest to the

[2] The extent of the effect is not investigated in this thesis. However, since the search detailed here was performed, ATLAS has subsequently released an updated search with the lepton isolation definition amended to incorporate a *variable* cone [179].

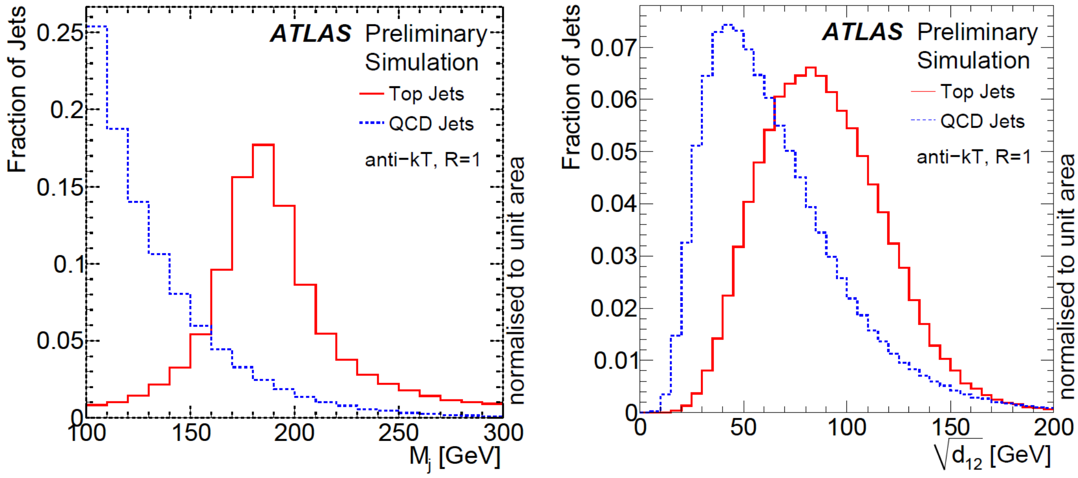

(a) (b)

Figure 4.5: Jet mass m_j (a) and first k_T-splitting scale $\sqrt{d_{12}}$ (b) distributions for fat jets containing top quark decays (*top jets*) and gluon / light-quark initiated decays (*QCD jets*). Good discrimination between the two types of jet is possible in this particular case by placing thresholds on the two variables of $m_j \gtrsim 160$ GeV and $\sqrt{d_{12}} \gtrsim 70$ GeV. All distributions normalised to unit area. Taken from [178].

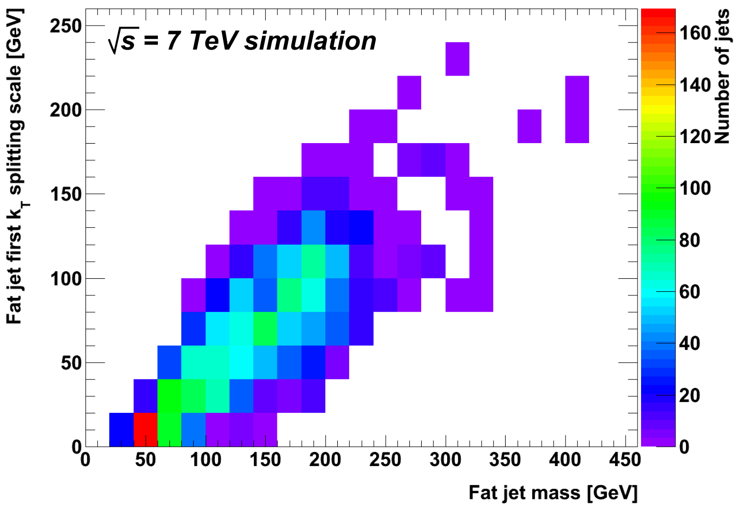

Figure 4.6: A 2-dimensional plot showing distributions for the mass and first k_T-splitting scale $\sqrt{d_{12}}$ for all anti-k_T $R = 1.0$ jets having $p_T > 150$ GeV. Only ≈ 30 % of the jets have $m_j \gtrsim 160$ GeV and $\sqrt{d_{12}} \gtrsim 70$ GeV. The jets are taken from the simulated sample of $g_{KK} \to t\bar{t}$ events with $m_{g_{KK}} = 1.6$ TeV, detailed in Section 2.4.1.

lepton is taken to be from the leptonic top decay, i.e. the *leptonic top jet*.

Following this, any fat jets that overlap with the leptonic top jet, i.e. with $\Delta R < 1.5$, are rejected from further consideration. This ensures that the same topo-cluster will not be used in the reconstruction of both the leptonic *and* hadronic top quarks, and therefore will not be double-counted in the reconstructed $t\bar{t}$ system. The justification for this particular value of ΔR can be seen in Figure 4.7. The ΔR between anti-k_T $R = 1.0$ and anti-k_T $R = 0.4$ jets is presented in a sample of simulated leptophobic $Z' \to t\bar{t}$ events with $m_{Z'} = 2$ TeV. The energy shared between a pair of jets is shown, as a fraction of the energy of the anti-k_T $R = 0.4$ jet in the pair measured at the EM-scale. There is no energy shared between the anti-k_T $R = 1.0$ and anti-k_T $R = 0.4$ jets if they are separated by a distance larger than $\Delta R = 1.5$.

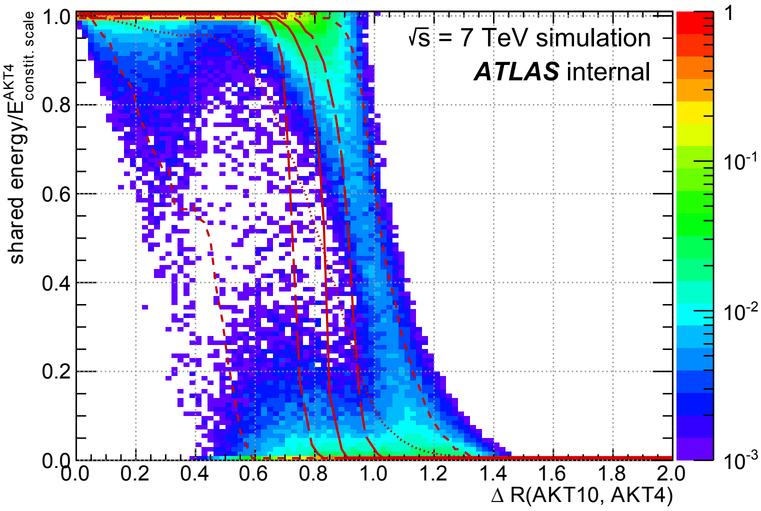

Figure 4.7: Energy sharing between anti-k_T $R = 1.0$ and anti-k_T $R = 0.4$ jets in a sample of simulated leptophobic $Z' \to t\bar{t}$ events with $m_{Z'} = 2$ TeV. There is no shared energy if the jets have $\Delta R > 1.5$. Taken from [2].

Finally, the top-tagging procedure requires there to be at least one fat jet with $p_T > 250$ GeV, $m_j > 100$ GeV and $\sqrt{d_{12}} > 40$ GeV. The hardest of these jets is known as the *hadronic top jet* and is designed to contain the *majority* of the hadronic top quark's decay products.

The resulting selection efficiency is displayed in Figure 4.8 for a range of $t\bar{t}$ masses at truth level. The selection efficiency is defined as the fraction of events selected, out of all those resulting from the process $Z' \to t\bar{t}$. A preliminary filter is applied, which requires the W boson from one of the top quarks to decay leptonically and the other to decay hadronically. Furthermore, the mass of the $t\bar{t}$ system, at truth level, has to be within $20\ \%$ of the nominal resonance mass to ensure that the inherent width of the resonance does not have an additional effect on the efficiency.

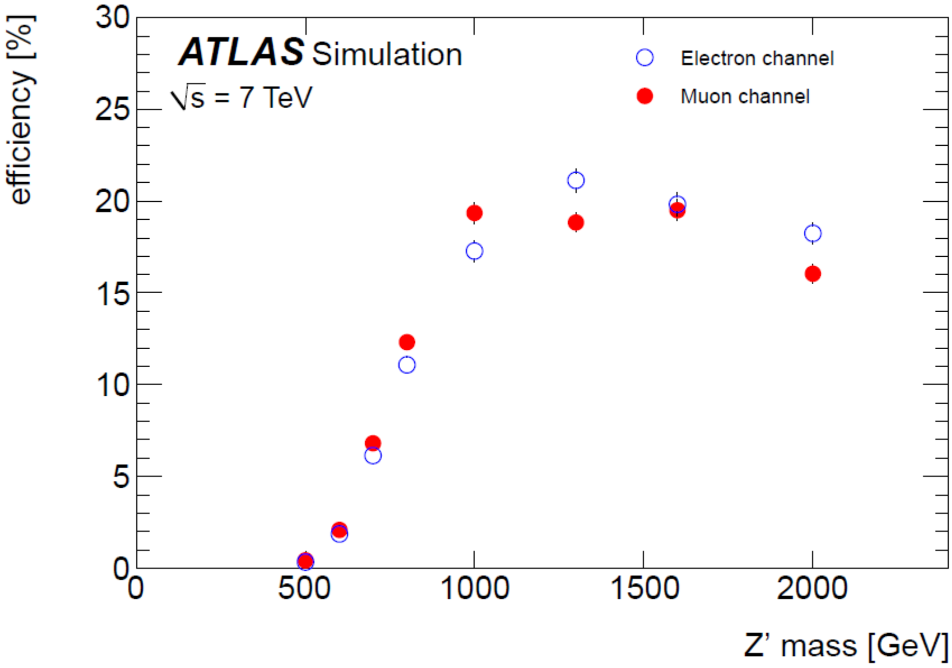

Figure 4.8: The selection efficiency for the leptophobic Z' benchmark model. The error bars represent the statistical uncertainty arising from the size of the simulated samples. The efficiency peaks for a $t\bar{t}$ invariant mass (at truth level) of approximately $1.3\ \mathrm{TeV}$.

The efficiency increases significantly until the resonance mass is just above $1\ \mathrm{TeV}$. The reason for this is as the boost of the hadronic top quark increases, an increasing proportion of its decay products are collected in the reconstruction of the fat jet. The jet p_T and mass therefore also increase, giving a greater probability for passing the top-tagging criteria.

The efficiency reaches a maximum of $\approx 20\ \%$ for a Z' mass of $1.3\ \mathrm{TeV}$, which is desirable in order to meet the original aim of increasing the sensitivity to TeV-scale resonances. The reason for the decrease in efficiency above this mass was not investigated further here, but it is likely to be due to the requirements of *isolated* leptons, the removal of jets that overlap with the electron within $\Delta R = 0.2$ and the rejection of muons that overlap with jets within $\Delta R = 0.4$. These all work to reject events containing boosted top quarks with highly collimated decay products. Indeed, in the previously mentioned successor to this analysis [179], it has been demonstrated that removing the separation requirement between the muon and anti-k_T $R = 0.4$ jets increases the efficiency for events with $m_{t\bar{t}} \gtrsim 1$ TeV (compare figures 11c and 11e in [179], for example).

A further point to note is that no events in the debug stream were selected using the criteria above. This check is required since, as highlighted in Section 2.2.5, events in the debug stream are not included in the main datasets.

4.2 Reconstruction of the top quark candidates and $t\bar{t}$ system

The discriminant used for this search is the invariant mass of the $t\bar{t}$ system. The method of reconstructing this system is discussed in the following sections, starting with the reconstruction of the individual top quark candidates.

4.2.1 Reconstruction of the hadronic top quark candidate

A major component of the event selection of the boosted approach is the top-tagging of one of the fat jets. The hadronic top quark candidate is then simply taken to be this tagged jet. The ambiguity of the reconstruction, which would arise in the resolved approach due to multiple smaller jets, is avoided.

Figure 4.9 displays the mass of the tagged fat jet, obtained from resonant and from background SM $t\bar{t}$ production. The signal chosen is a KK-gluon with a mass of 1.3 TeV. The lower mass threshold of 100 GeV is apparent, which was applied during the event selection process.

The distribution from signal events has a peak which is consistent with the top quark mass. However, there is no peak in the distribution arising from the SM $t\bar{t}$ background. This is because the hadronic top jet is taken from an $R = 1.0$ jet collection and the applied lower jet p_T threshold is 250 GeV. Only top quarks with $p_T \gtrsim 350$ GeV are expected to be sufficiently boosted that their decay products will fall into a cone with such a radius,

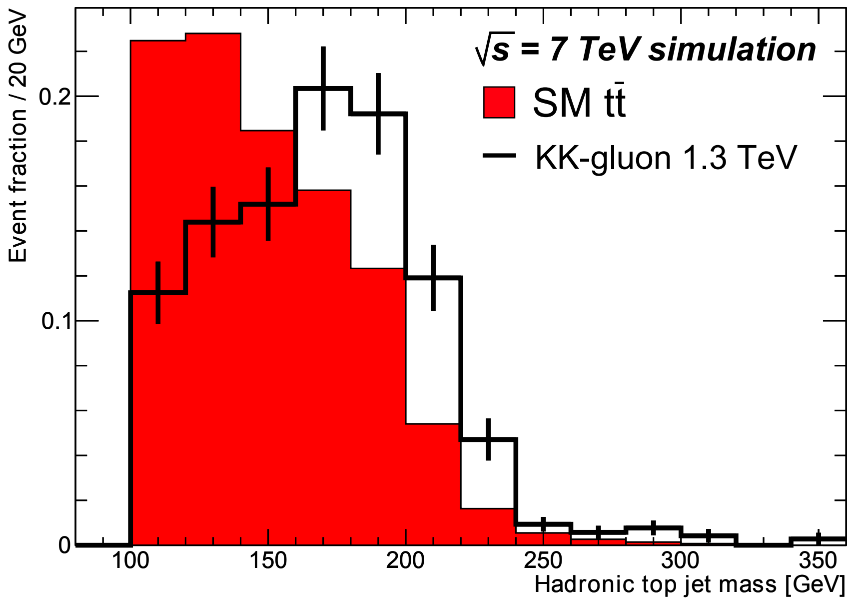

Figure 4.9: Mass of hadronic top quark candidate in simulated signal and SM $t\bar{t}$ background events. The signal is a KK-gluon with $m = 1.3$ TeV. There is a clear peak located at the top quark mass in the signal distribution. All distributions have been normalised to unit area.

as demonstrated using Equation 4.2. Therefore, this sample of fat jets tagged as hadronic top quarks will actually include a significant proportion that do not contain *all* the top quark decay products. If the lower p_T threshold on the hadronic top quark candidate is raised to 350 GeV, a peak emerges in the jet mass distribution as seen in Figure 4.10.

The rationale for retaining the lower jet p_T threshold of 250 GeV, in preference to 350 GeV, is driven by the $t\bar{t}$ reconstruction. This is discussed in Section 4.2.3 below.

4.2.2 Reconstruction of the leptonic top quark candidate

Criteria based on the leptonic top quark as a single entity do not form part of the event selection. However, its reconstruction serves as a useful investigation into whether the leptonic top jet has been correctly assigned.

In order to reconstruct this top quark candidate, the neutrino candidate must first be reconstructed. This neutrino results from the decay of the W boson in the leptonic top quark decay chain. It is assumed to dominate the E_T^{miss} in each event and therefore its p_T is

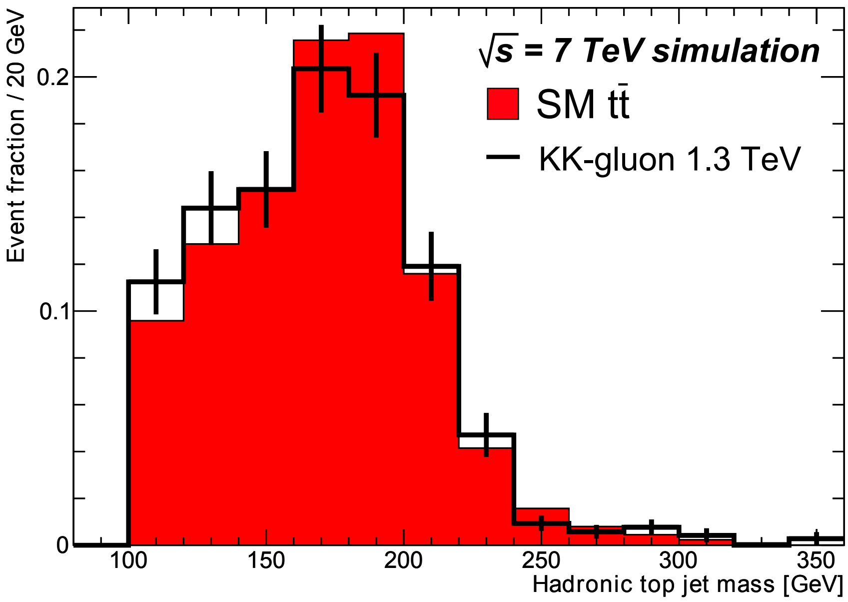

Figure 4.10: Mass of hadronic top quark candidate in simulated signal and SM $t\bar{t}$ background events when the lower p_T threshold on the associated fat jet is raised from 250 to 350 GeV. A peak at the top quark mass in the SM $t\bar{t}$ distribution becomes apparent as the threshold is raised, indicating that the majority of top quarks have their *entire* decay products contained within the $R = 1.0$ jet. The chosen signal is a KK-gluon with $m = 1.3$ TeV, as for Figure 4.9. All distributions have been normalised to unit area.

assumed to be equivalent to the E_T^{miss}. However, the neutrino p_z is not directly measured. Instead, it is inferred using the fact that the sum of the four-vectors of the lepton and the neutrino is equal to the four-vector of the W boson. Since the W boson is produced on-shell, its pole mass can be used to constrain the quadratic equation for the neutrino p_z. If only one real solution exists, this is used. If two real solutions exist, the solution with the smallest $|p_z|$ is chosen. A complex solution arises due to mismeasurement of the E_T^{miss}, as proposed in [180]. In that study, the x and y components of the E_T^{miss} are modified such that the solution for the neutrino p_z becomes real. This is also the approach used in this thesis.

The reconstruction then proceeds by adding the four-vectors of the lepton, the reconstructed neutrino and the leptonic top jet. The mass of the combined four-vector is displayed in Figure 4.11. The background and signal processes correspond to those displayed for the hadronic top quark candidate, in Figure 4.9 above.

A peak in the distribution from SM $t\bar{t}$ production, corresponding to the top quark mass, is clearly visible. The issue that affected the hadronic top, where some of the decay products of softer top quarks were not included in the reconstruction, does not come into play here. This is because the jet chosen in the leptonic top quark reconstruction can lie anywhere within an annulus around the lepton of upper radius equal to 1.5. If it is not present in this region, the reconstruction does not proceed and the event is discounted from the final selection.

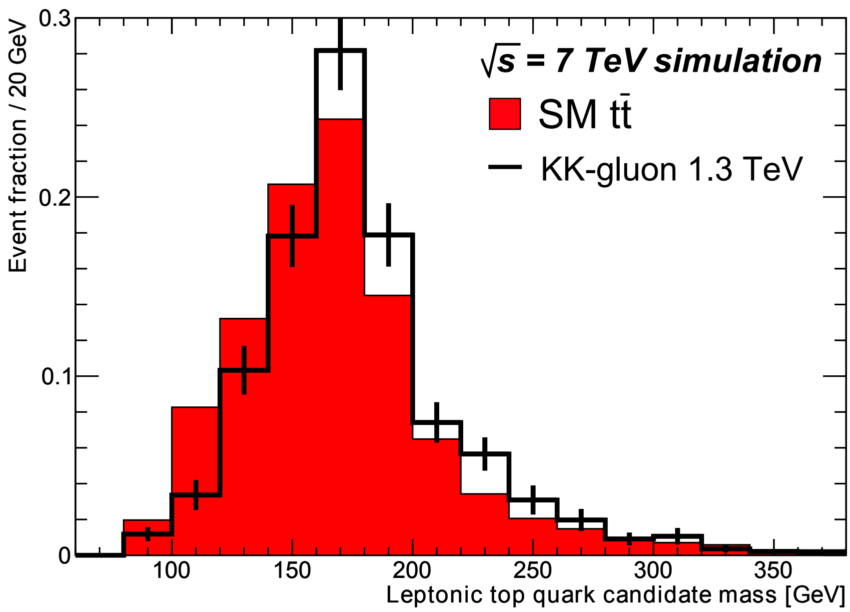

Figure 4.11: Mass of the leptonic top quark candidate in simulated signal and SM $t\bar{t}$ background events. The candidate has been reconstructed using the anti-k_T $R = 0.4$ jet chosen as the leptonic top jet, the single selected lepton, the E_T^{miss} and the neutrino p_z. There is a peak corresponding to the top quark mass for both the background and signal distributions. The chosen signal is a KK-gluon with $m = 1.3$ TeV, as for Figure 4.9. All distributions have been normalised to unit area.

4.2.3 Reconstruction of the $t\bar{t}$ system

The reconstruction of the $t\bar{t}$ candidate pair is achieved by adding the four-vectors of all the objects that compose the hadronic and leptonic top quark candidates. The mass of the resulting four-vector is taken to be the reconstructed $t\bar{t}$ invariant mass. Figure 4.12 displays this distribution for four different masses of each of the two benchmark signal models. The distributions for the KK-gluon are somewhat wider than for the leptophobic Z' boson. The difference is not particularly large for resonances with mass up to 1 TeV, although it increases for higher masses. Specifically, the full width at half maximum (FWHM) of the distributions for the resonances with $m = 1$ TeV is 150 GeV for both models. However, when resonances with $m = 1.6$ TeV are considered, the FWHM is 300 GeV for the leptophobic Z' boson but 825 GeV for the KK-gluon.

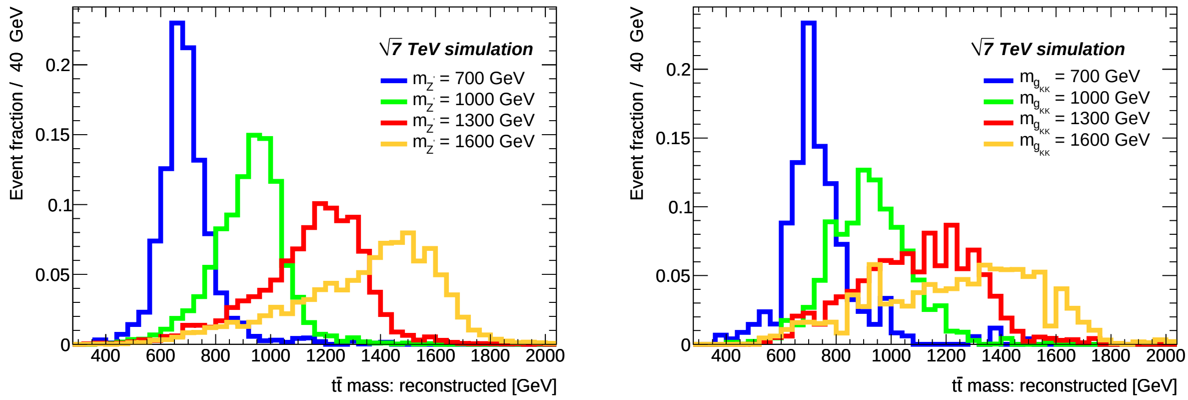

(a) (b)

Figure 4.12: Reconstruction level $t\bar{t}$ invariant mass distribution for benchmark signal models: (a) leptophobic Z' boson and (b) Kaluza-Klein gluon g_{KK}. All distributions have been normalised to unit area.

The width of the distributions arises from multiple sources. The predominate effect is the natural width of the resonances. Figure 4.13 shows the distributions for the $t\bar{t}$ invariant mass at truth level. The fact that the two models have different widths ($\Gamma/m \approx 1$ % for the Z' and ≈ 15 % for the KK-gluon) is clearly apparent. There is a tail in the lower half of the distribution for all samples, which becomes extremely pronounced as the mass of the resonance increases. This effect is due to the convolution of the resonances' Breit-Wigner line shape with the PDFs, which rapidly fall as the fraction of the parent hadron's momentum carried by the colliding parton increases.[3]

If the truth level distributions are subtracted from the reconstruction level distributions, it is clear that there are secondary effects which broaden the distributions at reconstruction level. Figure 4.14 displays these differential distributions; there are two main

[3]The PDFs are shown in Figure 1.4(a).

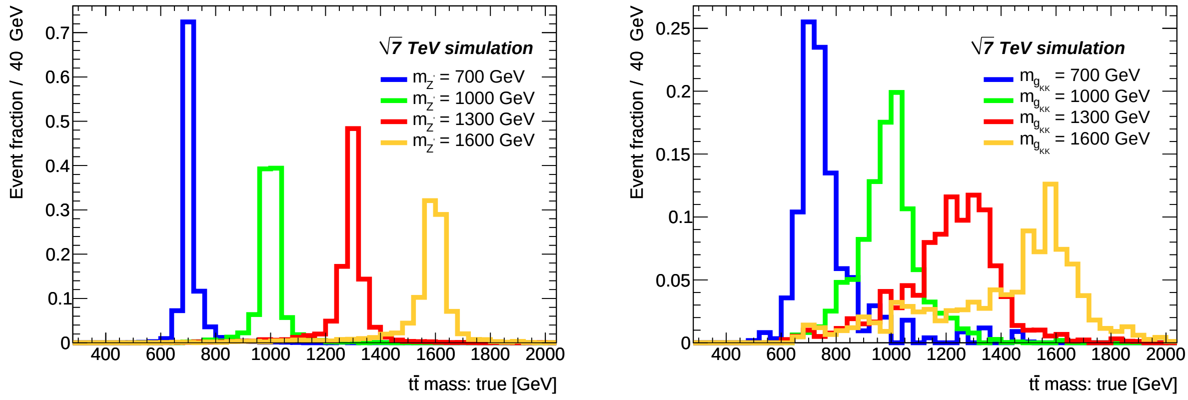

(a) (b)

Figure 4.13: Truth level $t\bar{t}$ invariant mass distributions for benchmark signal models: (a) leptophobic Z' boson (b) Kaluza-Klein gluon g_{KK}. All distributions have been normalised to unit area.

reasons why they diverge from zero. First, each sub-detector has a finite resolution associated to the measurements it takes; this results in a finite resolution on the kinematic and spatial variables of the physics objects which compose the reconstructed $t\bar{t}$ system. Second, the assignment of objects to the $t\bar{t}$ system may not always be the correct choice, particularly for top quarks produced with low transverse momentum whose decay products are more uniformly distributed throughout the detector. Both effects will cause a spread in the distribution at reconstruction level relative to that at truth level. Furthermore, these effects are expected to be random processes and therefore the reconstruction level distribution will effectively be the truth distribution convoluted with a number of Gaussian distributions of different widths. As expected, the width of this differential distribution does not depend on the model under consideration: for either model with $m = 1.6$ TeV, the FWHM is ≈ 300 GeV.

The differential distribution can be well approximated by a Crystal Ball function [181], which is a Gaussian function with a power-law tail. This tail is required to account for the effect of high momentum top quarks which radiate gluons [178]. The differential distribution for the KK-gluon of $m = 1300$ GeV is shown in Figure 4.14(c) with a Crystal ball function fitted to it.

A comparison of the differential distributions obtained using the boosted and resolved approaches demonstrates further benefits of using the boosted approach. The $m_{t\bar{t}}$ distribution for the Z' boson with $m = 1$ TeV using the two approaches is represented by the green line in Figures 4.14(a) and 4.14(d). The FWHM of this distribution is around 15 % narrower using the boosted approach, demonstrating that the reconstructed $t\bar{t}$ mass distribution is closer to the true distribution of the resonance mass.

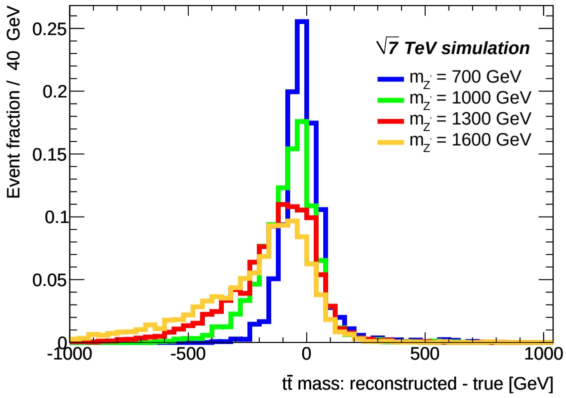

(a)

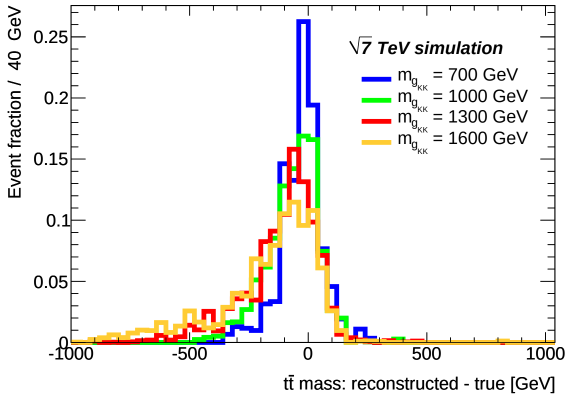

(b)

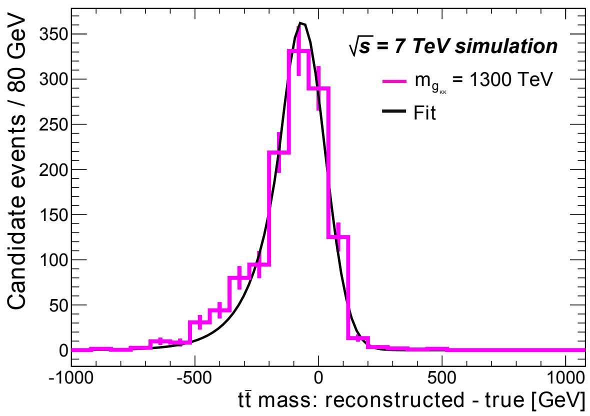

(c)

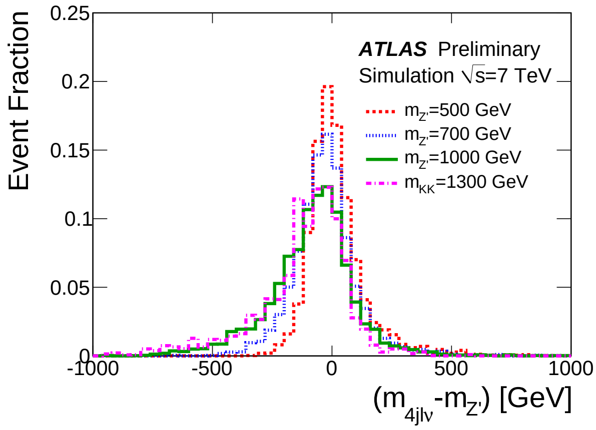

(d)

Figure 4.14: Difference between the reconstructed and truth level $t\bar{t}$ invariant mass distribution for benchmark signal models: (a) leptophobic Z' boson, (b) g_{KK}. A Crystal ball function provides a good fit to the distribution for the KK-gluon of $m = 1300$ GeV in (c). In (d), the differential distributions obtained from the ATLAS search using the resolved approach [71] are displayed. The width of the distribution for the 1 TeV Z' is narrower using the boosted approach (shown in (a)) than the resolved approach. All distributions except that in subfigure (c) have been normalised to unit area.

The rationale for retaining a lower p_T threshold of 250 GeV on the hadronic top jet, rather than 350 GeV, is evident when investigating the effect of raising the threshold on the $t\bar{t}$ invariant mass distribution. Figure 4.15 illustrates the distribution taken from

SM $t\bar{t}$ events and from the decay of a KK-gluon with $m = 1$ TeV. In subfigure (a), the p_T threshold on the hadronic top jet is 250 GeV and the peaks in the two distributions are well separated. This enables the identification of $t\bar{t}$ resonances at the TeV-scale and above. However, if the p_T threshold on the hadronic top jet is raised to 350 GeV, the peaks in the distributions from the SM and BSM processes become almost coincident. This situation is displayed in Figure 4.15(b). This would severely restrict the ability to identify any such BSM processes.

In Chapter 6, the use of the $t\bar{t}$ invariant mass distribution to identify the possible presence of BSM processes is described. Prior to that, the procedure for estimating the W+jets and QCD multijet backgrounds must be described, which is the subject of the next chapter.

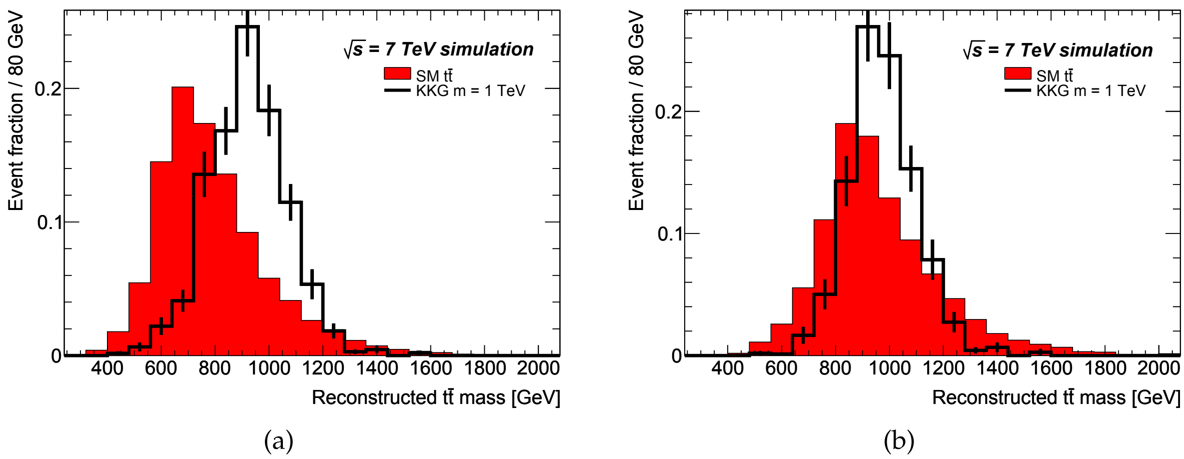

Figure 4.15: Distributions for the reconstructed $t\bar{t}$ invariant mass in resonant and SM $t\bar{t}$ production. The signal is a KK-gluon resonance with $m = 1$ TeV. In (a), the p_T threshold on the hadronic top jet is 250 GeV, as used in the search described in this thesis. In (b), the threshold has been raised to 350 GeV which causes the peaks in the two distributions to overlap. This would restrict the identification of such $t\bar{t}$ resonances at the TeV-scale and above. All distributions have been normalised to unit area.

4.3 Summary

Analyses involving pairs of top and antitop quarks which result in a lepton+jets final state are particularly challenging due to there being many background processes. The chosen strategy to select events due to signal processes, whilst rejecting those from background processes, is highly dependent on the transverse momentum of the top quarks. A method for selecting highly-boosted top quarks, which would result from TeV-scale $t\bar{t}$ resonances, has been developed in this chapter. This method relies on the use of large jets, with an investigation of their substructure, in order to identify the hadronically decaying top quark. This thesis represents the first application of jet substructure techniques to a search for $t\bar{t}$ resonances at the ATLAS experiment. The procedure for reconstructing the invariant mass of the $t\bar{t}$ pair in all selected events has also been comprehensively detailed. The resulting distributions for BSM signal processes, reconstructed using this boosted strategy, are compared to those from previous ATLAS analyses tailored towards less highly-boosted top quarks. The ability to reduce the resolution of this distribution, using the boosted strategy, has been demonstrated.

Chapter 5

Estimation of background processes

Monte Carlo techniques have a great deal of predictive power. However, it is preferable to estimate background processes from data where possible, since the dependence on knowledge of the detector simulation and the nature of the initial processes is vastly reduced. For the analysis presented here, a fully data-driven estimation is provided for the QCD multijet background. The shape of the W+jets background is predicted using Monte Carlo simulation and then the distributions are *normalised* using data. These data-driven procedures are the subject of this chapter.

5.1 Data-driven estimation of backgrounds

5.1.1 $W+$jets production

The ALPGEN LO simulation with cross-section normalised to the NNLO prediction has been shown to provide an adequate description of the event yield and kinematics at the lower end of the kinematic region [182]. Low in this context means for $H_T < 700$ GeV, where H_T is the scalar sum of the p_T of all partons and of the lepton and neutrino from the W boson decay. However, the aim of this thesis is to improve the sensitivity to $t\bar{t}$ resonances at the TeV-*scale*.

The yield predicted by MC simulation is normalised using scale factors (SFs) derived from data. These SFs are obtained by exploiting the fact that the rate of $W^+ +$ jets production is larger than that of $W^- +$ jets production at the LHC pp collider, due to the dominance of u quarks over d quarks in the proton. W+jets production is hence known as a *charge asymmetric* process. This method to calculate the SFs relies on the fact that the ratio of $\sigma(pp \to W^+)$ to $\sigma(pp \to W^-)$ is relatively well understood [183], and to a greater degree than the overall cross-section $\sigma(pp \to W)$ whose major theoretical uncertainty is associated with the PDFs. The charge asymmetry method has also been considered by the CMS collaboration [184].

The following formula is used to obtain the normalisation SFs:

$$N_{W^+} + N_{W^-} = \left(\frac{r_{MC} + 1}{r_{MC} - 1}\right)(D^+ - D^-) \tag{5.1}$$

where r_{MC} is the ratio of the yields from W^+ and W^- production, estimated using the MC simulation. The charge of the W boson is inferred from the charge of the single hard lepton in the event. D^+ (D^-) represents the yield of data events when the selected lepton is of positive (negative) charge; the contributions from charge asymmetric processes are subtracted using their estimation from MC simulation. Therefore $N_{W^+} + N_{W^-}$ is the total estimated yield due to W+jets production, derived using data. This is divided by the total yield for W+jets production, estimated using MC simulation, to obtain the normalisation SFs. This procedure is carried out separately in the electron and in the muon channels.

The region in which these yields are obtained does not necessarily need to be the signal region. Indeed, in order to reduce the statistical uncertainties on the yields and hence on the final SFs, a so-called *normalisation region (NR)* was used. The statistics in the NR are increased relative to those in the signal region (SR) by removing or loosening some of the criteria of the SR. Specifically, the fat jet criteria of $m_j > 250$ GeV and $\sqrt{d_{12}} > 40$ GeV are removed completely and the minimum fat jet p_T requirement is lowered from 250 GeV to 150 GeV. This is a valid procedure only if these variables are well modelled in MC simulation, which is investigated in Section 5.2 below. The definition of the NR is summarised in Table 5.1.

Table 5.1: Criteria placed on the fat jet collection in order to define the normalisation region (NR) used to derive the scale factors for the W+jets background normalisation. "VR" denotes the validation regions used to validate the scale factors, in a procedure described below. "SR" denotes the signal region used in the main search. All other SR criteria apart from those related to the fat jets are applied to the normalisation and validation regions.

Region	Fat jet criteria
NR	$p_T > 150$ GeV only
VR1	$p_T > 250$ GeV only
VR2	$p_T > 150$ GeV and $m_j > 100$ GeV only
VR3	$p_T > 150$ GeV and $\sqrt{d_{12}} > 40$ GeV only
SR	$p_T > 250$ GeV, $m_j > 250$ GeV, $\sqrt{d_{12}} > 40$ GeV

The yields of events with a positive or with a negative lepton, as measured in data and simulated samples for all backgrounds, are shown in Table 5.2. These yields are derived in the normalisation region. No correction is made for the probability of lepton charge mis-identification. However, this probability has been found to be in the range 0 – 0.003 % for muons and 0.2 – 3 % for electrons [185], with the measurements made in data agreeing well with those taken from MC simulation. Therefore, the effect of this mis-identification on the data-driven yield of W+jets events is deemed to be negligible.

As shown in Table 5.2 the other background with a large degree of charge asymmetry, besides W+jets production, is single top quark production. This is because it involves the exchange of a W boson as demonstrated in the Feynman diagrams of Figure 1.6. The degree of asymmetry is ≈ 40 %. Its contribution is subtracted using the estimation given by MC simulation. Although this introduces an additional uncertainty due to the simulation processes, estimated in Section 6.3, this is preferable to having an additional contribution to the asymmetry which is not from W+jets production.

The contribution due to diboson production is expected to have a small degree of asymmetry because it is a mixture of WW, WZ and ZZ production. Table 5.2 shows that the asymmetry is at the level of ≈ 10 %. The production of Z+jets and multijets in purely QCD processes was also subtracted using their estimation from MC simulation, although they are expected to be approximately charge *symmetric*. The measured asymmetry is ≈ 5 %, as seen in Table 5.2. Pair production of $t\bar{t}$ pairs in the standard model is expected to be overwhelmingly charge symmetric and is therefore *not* subtracted, in order to minimise the uncertainty due to MC simulation.

Table 5.2: Yields of events in the normalisation region for which the selected lepton is positive (+) or negative (-). The ratio of the positive and negative yields is also shown, denoted by (+/-). This ratio indicates the degree of charge asymmetry that each process exhibits. Entries for the data and for each of the background processes are shown separately. The displayed uncertainties are due to statistical effects only. The yields have not been corrected for the probability of charge mis-identification, although this is at the level of below 3 (0.003) $\%$ for electrons (muons).

	Channel	
	Electron	Muon
Data (+) [D^+]	6931 $\pm$ 83	10051 $\pm$ 100
Data (-) [D^-]	5392 $\pm$ 73	7507 $\pm$ 87
W+jets (+) [W^+]	5000 $\pm$ 61	7793 $\pm$ 75
W+jets (-) [W^-]	3060 $\pm$ 53	4555 $\pm$ 58
W+jets (+/-) [r_{MC}]	1.63 $\pm$ 0.02	1.71 $\pm$ 0.02
Single top (+)	194 $\pm$ 6.2	263 $\pm$ 6.5
Single top (-)	136 $\pm$ 4.7	182 $\pm$ 5.0
Single top (+/-)	1.43 $\pm$ 0.05	1.44 $\pm$ 0.04
QCD multijet (+)	662 $\pm$ 7.8	475 $\pm$ 1.3
QCD multijet (-)	623 $\pm$ 7.5	460 $\pm$ 1.2
QCD multijet (+/-)	1.06 $\pm$ 0.01	1.03 $\pm$ 0.00
Diboson (+)	27.9 $\pm$ 1.2	39.6 $\pm$ 1.4
Diboson (-)	26.7 $\pm$ 1.2	33.8 $\pm$ 1.1
Diboson (+/-)	1.05 $\pm$ 0.05	1.17 $\pm$ 0.04
Z+jets (+)	439 $\pm$ 16.7	558 $\pm$ 16.6
Z+jets (-)	463 $\pm$ 17.0	605 $\pm$ 17.7
Z+jets (+/-)	0.95 $\pm$ 0.04	0.92 $\pm$ 0.03

The SFs in each channel are derived by first inserting the values for D^+, D^- and r_{MC} from Table 5.2 into Equation 5.1. This gives the yield due to W+jets production estimated from *data*. The estimation from MC simulation is obtained from the addition of the values for [W^+] and [W^-] in Table 5.2. The SFs are the ratios of the yield from data to the yields in simulation. The NR SFs are displayed in the first row of Table 5.3, separately for the two channels.

As shown in the last line of this table, the SFs calculated in the signal region do indeed have a large statistical uncertainty, of $50\ \%$ in the muon channel. The final SFs used to normalise the W+jets background are calcuated in the NR but applied in the SR. A check was carried out to ensure that the two sets of SFs are consistent. This was achieved by *individual* application, on top of the NR definition, of the three fat jet criteria: $p_T > 250$ GeV, $m_j > 250$ GeV, $\sqrt{d_{12}} > 40$ GeV. This resulted in three *validation regions* (VR1, VR2, VR3), which are defined in Table 5.1. They are essentially intermediaries between the NR and the SR.

The resulting SFs in all three validation regions and in the signal region are shown in Table 5.3. They are compatible with the final SF in the normalisation region, within the stated uncertainties. The estimation of the systematic uncertainties associated with these SFs is provided in Section 6.3.

Table 5.3: Scale factors derived for the data-driven normalisation of the W+jets background, in the "normalisation region" (NR). The calculation performed in the intermediate validation regions, VRX, and the signal region, SR, are also shown. The first uncertainty is statistical and the second is due to systematic uncertainties associated with the measurement of the SF. The methods for estimating these systematic uncertainties is described in Section 6.3. The SFs calculated in the SR have a large statistical uncertainty of up to $50\ \%$.

Region	Electron channel	Muon channel
NR	$0.75 \pm 0.06 \pm 0.11$	$0.79 \pm 0.05 \pm 0.11$
VR1	$0.67 \pm 0.12 \pm 0.03$	$0.68 \pm 0.09 \pm 0.01$
VR2	$0.79 \pm 0.20 \pm 0.24$	$0.53 \pm 0.15 \pm 0.16$
VR3	$0.74 \pm 0.26 \pm 0.32$	$0.58 \pm 0.16 \pm 0.06$
SR	$0.88 \pm 0.34 \pm 0.27$	$0.48 \pm 0.27 \pm 0.18$

Since W+jets production is one of the major background processes in this analysis, a further check is carried out to ensure that its prediction is in good agreement with the data *after* the application of the SFs. This was achieved by constructing a *control region* in which W+jets production is the dominant process. The mass and $\sqrt{d_{12}}$ criteria applied to the fat jet, which are part of the signal region, are removed. However, the lower p_T threshold of 250 GeV on this jet collection is retained. Events containing any b-jets are rejected, in order to suppress the contribution due to $t\bar{t}$ pair production, in both SM and BSM

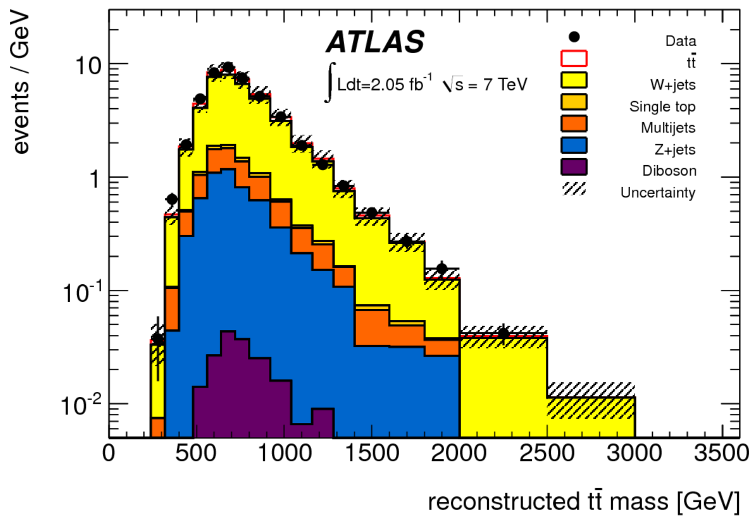

(a)

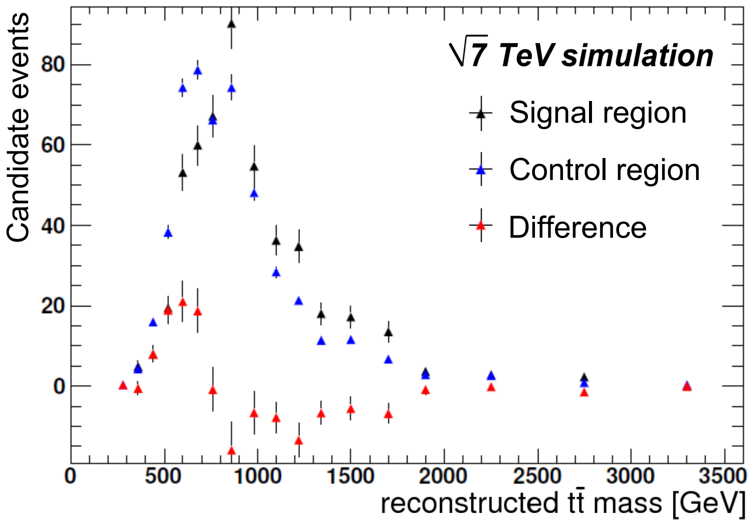

(b)

Figure 5.1: Reconstructed $t\bar{t}$ invariant mass distribution in the W+jets-enriched control region (a), for both channels combined. The scale factors derived in this section have been applied. The displayed uncertainty relates to the normalisation uncertainty on the scale factors, estimated in Section 6.3. The distributions *for simulated W+jets events*, in this control region and in the signal region, are displayed in (b) The difference between the two distributions is also shown, demonstrating that the two regions are kinematically similar.

processes. This veto requires that none of the anti-k_T $R = 0.4$ jets give a positive result when a multivariate b-tagging algorithm [169] is applied. The chosen operating point of the algorithm gives an average b-tagging efficiency of $60\ \%$ in simulated $t\bar{t}$ events and a light-quark rejection factor[1] of 345.

The resulting proportion of W+jets events in this control region is just over $70\ \%$, with the next largest contribution (Z+jets) reduced to $12\ \%$. The presence of signal events is at the level of $6\ \%$ compared to the total yield from background sources, where the signal referred to here is a KK-gluon with $m = 700$ GeV. This particular mass point is conservatively chosen because it results in the maximum yield from all mass points, for both benchmark models. This level of W+jets enrichment and signal suppression is judged to be sufficient to assess the validation of the SFs derived above.

The reconstructed $t\bar{t}$ invariant mass distribution in this control region is shown in Figure 5.1(a), for both the data and the background prediction. The observed and predicted yields agree to within $3\ \%$ in the electron and muon channels combined; this is well within the total uncertainty associated with the W+jets SFs. The predicted shape of the distribution also describes the data well.

An additional check on this validation procedure was performed to ensure that this control region had sufficiently similar kinematic properties to the signal region. This was carried out solely with the use of the ALPGEN W+jets simulated samples; no data was used. The results are shown in Figure 5.1(b), by means of a comparison of the reconstructed $t\bar{t}$ invariant mass distribution obtained in the two regions. The control region results in a slightly softer distribution which is to be expected since the mass and $\sqrt{d_{12}}$ lower thresholds on the hadronic top quark candidate are removed. However the retention of the lower p_T threshold of 250 GeV on the fat jet acts to minimise this difference to an acceptable level.

[1]The reciprocal of the fraction of light-quark initiated jets that are incorrectly labelled as b-jets, based on MC simulation.

5.1.2 QCD multijet production

A diverse range of processes result in the production of multijets, where one or more of the jets are mis-identified as leptons, thereby constituting a background to searches in the *lepton*+jets channel. The sources of such non-prompt leptons and fake electrons were identified in Section 3, together with techniques used for their suppression, such as "tight" identification requirements and a certain degree of isolation from other energy deposits in the calorimeter.

These techniques do not reject the multijet contribution entirely, since the production cross-section for multijet events can be up to 10^6 times that for SM $t\bar{t}$ production. However, it *is* reduced to the level of a relatively minor background, making up ≈ 5 % of the total background as demonstrated in Section 5.2.

The accurate MC simulation of these processes is particularly challenging and results in large systematic and statistical uncertainties. Their behaviour is also highly detector-dependent. Therefore data-driven methods are most appropriate for the estimation of the multijet contribution to the background. Both the normalisation *and* the shape of the $t\bar{t}$ invariant mass distribution are estimated from data, as described below.

The estimation is carried out using the *matrix-method*, a general description of which can be found in [186]. The method essentially relies on the ability to estimate the number of leptons which have passed the tight identification requirements but are actually of non-prompt type and therefore result from multijet production processes.

A data sample is collected which is enriched in the multijet background. This is achieved by using loosened identification criteria, as follows:

- The *Loose1* definition for electrons is made up of the medium criteria of Section 3.1, together with at least one hit in the pixel B-layer. The isolation requirement of Section 3.1 is loosened from 3.5 to 6 GeV.
- The *Loose2* definition for electrons is equivalent to *Loose1* but the pixel hit require-

ment and isolation requirement are removed.

- The *Loose1* definition for muons is that described in Section 3.2 *except* the isolation requirements are also completely removed.

- The *Loose2* definition for muons has, additionally, the muon-jet overlap check removed (i.e. muons are allowed to overlap with jets).

All other event selection criteria, listed in Chapter 4, are otherwise applied for the collection of the data sample. Therefore it is of equivalent luminosity to the main sample which is used for the $t\bar{t}$ resonances search.

Two loose definitions are used in order to make two separate estimations of the multijet background. This enables estimation of the uncertainty on the *shape* as well as on the normalisation of the $t\bar{t}$ invariant mass distribution from the multijet background. The estimation of this shape uncertainty, as well as all other systematic uncertainties associated with the multijet estimation, is discussed in Section 6.3.2.

The aim of the matrix-method is to determine the number of events in this data sample which contains a tight lepton that actually arises from (non-prompt) multijet production processes ($N_{non-prompt}$). In order to estimate this number, first consider that the number of events in the sample which contain a lepton passing one of the loose criteria above is:

$$N_L = N_{prompt} + N_{non-prompt} \tag{5.2}$$

where N_{prompt} is the number of events containing a lepton from prompt sources.

Secondly, consider that the number of events containing containing a tight lepton from *any* source is:

$$N_T = \varepsilon \times N_{prompt} + f \times N_{non-prompt} \tag{5.3}$$

where the efficiency ε and false-identification rate f are the probabilities that a lepton passing the loose criteria will also pass the tight criteria, for the prompt and for the (non-prompt) multijet processes respectively. These probabilities are estimated using data, as described below.

The value of $N_{non-prompt}$ is finally determined by combining the above two equations and eliminating the other unknown variable, N_{prompt}. The value of $N_{non-prompt}$ is therefore given by:

$$f \times N_{non-prompt} = \left[\frac{\varepsilon - 1}{\varepsilon - f}\right] N_T + \left[\frac{\varepsilon f}{\varepsilon - f}\right] N_A \tag{5.4}$$

Here, N_A is simply the number of events with a lepton which passes the loose criteria but failed the tight criteria (i.e. "anti-tight"). Both N_T and N_A can simply be counted using the observed data.

False-identification rate

The false-identification rate f is estimated by collecting a data sample composed mainly of multijet events, with the loose lepton definitions applied. The number of events is then counted in which a lepton that is classified as loose is also classified as tight. The suppression of events other than those from multijet processes is achieved in the following ways, resulting in a region called *control region 0* (CR0).

1. The contribution from SM $t\bar{t}$ production is suppressed by reversing the mass and $\sqrt{d_{12}}$ criteria on the fat jet collection. That is, the jets are required to have mass *less than* 100 GeV and $\sqrt{d_{12}}$ *less than* 40 GeV.

2. W+jets production is suppressed using the method for SM $t\bar{t}$ production above. Furthermore, the E_T^{miss} in the events is required to be less than 35 GeV and the W transverse mass to be less than 25 GeV.

3. Finally, the Z+jets production is suppressed by vetoing any event containing a Z boson candidate. The details of this are provided in [2].

Furthermore, the lower p_T threshold on the hadronic top jet is loosened from 250 to 150 GeV to increase the number of events in the sample and therefore lower the statistical uncertainty on f.

The data sample collected in CR0 contains events with loose leptons. Some of these leptons will have failed the tight criteria and those events will be dominated by multijet processes, as desired. However, the events with leptons which also pass the tight criteria will have a considerable fraction from prompt sources. This contribution is estimated using MC-simulated samples by counting the number of events in CR0 containing a *tight* lepton. The resulting distributions for the hadronic top jet p_T, obtained from both data and from the background prediction, are demonstrated in Figure 5.2. The distributions are shown for the electron channel only; the equivalent figure for the muon channel is available in [2].

The final values for f using the *Loose1* (*Loose2*) definition are 0.209 ± 0.021 (0.066 ± 0.010) in the electron channel and 0.258 ± 0.056 (0.00395 ± 0.00161) in the muon channel. The combined statistical and systematic uncertainty is quoted. The estimation of the uncertainty is discussed in Section 6.3.2.

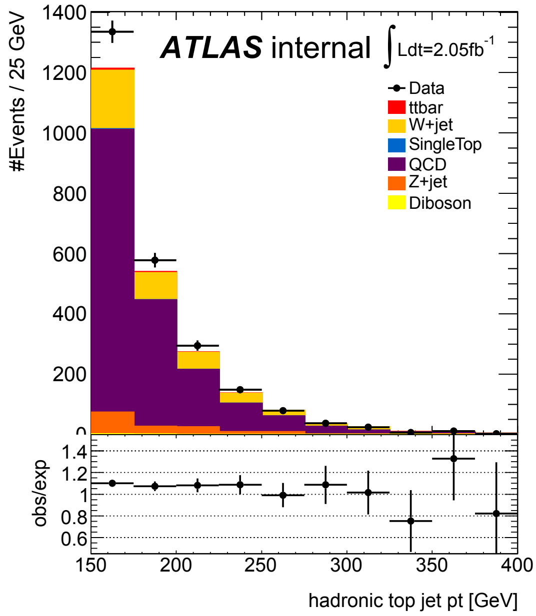

Figure 5.2: Events from data and the background estimations in control region 0 (CR0), for *only* those events containing a *tight* lepton. This result is used in the measurement of the false-identification rate, to estimate and subtract the contribution from prompt lepton sources (i.e. all except "QCD") in CR0. The "QCD" contribution has been estimated using the matrix-method.

Efficiency

The efficiency ε is the probability that a *prompt* lepton passing the loose criteria will also pass the tight criteria. It is estimated for both loose lepton definitions using a tag-and-probe technique on a sample of predominantly $Z \to ll$ data events, which is of course a source of prompt leptons. These events are collected by requiring each event to have exactly two loose leptons of the same flavour. At least one of these must also pass the tight selection. The invariant mass of the two leptons is required to be between 86 and $96\ \mathrm{GeV}$. The efficiency is then estimated by:

$$\varepsilon = \frac{1}{\frac{N_{TA}/2}{N_{TT}} + 1} \tag{5.5}$$

where N_{TA} is the number of events with one tight and one anti-tight lepton and N_{TT} is the number of events with two tight leptons.

The measured values of ε using the *Loose1* (*Loose2*) definitions are 0.884 (0.853) and 0.992 (0.969) in the electron and muon channels respectively. The total uncertainty on each value is less than $0.3\ \%$. As for the false-identification rate, the estimation of this uncertainty is discussed in Section 6.3.2.

A check is carried out to ensure that the efficiency measured using the tag-and-probe technique is applicable to events in the signal region. Simulated samples of SM $t\bar{t}$, W+jets and Z+jets are used with the signal selection criteria applied and the efficiency is recalculated; the values are shown in Table 5.4, labelled as "SR". They are compared to the efficiencies measured in simulated Z+jets events with the tag-and-probe selection applied; good consistency is found for all lepton definitions *except* the *Loose2* muons. This is thought to be because this lepton definition does not require muons that overlap with jets to be rejected (i.e. leptons are allowed to be in the jets) [2].

The measured efficiency is expected to be lower in events with $m_{t\bar{t}}$ at the TeV-scale. This is because the leptons are expected to fail the tight isolation criteria as $m_{t\bar{t}}$, and hence the degree of collimation of the top quark decay products, increases. The efficiency is therefore also estimated in the simulated sample of leptophobic Z' boson events with $m = 1.6$ TeV, with the signal selection criteria applied. The shifts in the yields of multijet events when using these alternative values of ε are shown in the last line of Table 5.4 and are indeed considerable downward shifts. This is taken into account in the estimation of the systematic uncertainty associated with ε, discussed in Section 6.3.2. It is specifically labelled as Z' in Table 5.5 and is the dominant source of uncertainty for the *Loose2* definition in the electron channel.

Table 5.4: Matrix-method efficiency ε estimated using both data and simulated samples. The "Tag-and-probe (Data)" values are used for the final multijet estimation. The values measured in the SM samples in the signal region (SR) are consistent with those having the tag-and-probe selection applied, for all except the *Loose2* definition. The efficiencies in high-mass Z' samples are considerably lower than for other simulated samples; this is considered as a source of the systematic uncertainty on ε.

Sources	*Loose1* electron	*Loose2* electron	*Loose1* muon	*Loose2* muon
Tag-and-probe (Data)	0.884 ± 0.002	0.853 ± 0.002	0.992 ± 0.001	0.969 ± 0.001
Tag-and-probe (MC Z)	0.847 ± 0.001	0.813 ± 0.001	0.992 ± 0.001	0.965 ± 0.001
MC $t\bar{t}$ SR	0.851 ± 0.008	0.815 ± 0.008	0.957 ± 0.007	0.758 ± 0.006
MC W+jets SR	0.850 ± 0.046	0.814 ± 0.043	0.965 ± 0.036	0.725 ± 0.026
MC Z+jets SR	0.862 ± 0.125	0.806 ± 0.121	0.972 ± 0.132	0.631 ± 0.095
MC Z' 1.6 TeV SR	0.814 ± 0.032	0.700 ± 0.027	0.828 ± 0.030	0.459 ± 0.016

Yield of events due to QCD multijet production

The estimated yields ($N_{non-prompt}$) due to multijet processes are obtained using Equation 5.4 and displayed in Table 5.5. The methods for estimating the associated systematic uncertainties are discussed in Section 6.3.2. The *Loose2* definition is used to provide the final estimation because the associated statistical and systematic uncertainties are lower than for the *Loose1* definition.

Table 5.5: The yield of multijet events in the signal region, estimated using the data-driven matrix-method. The yield for the *Loose2* definition is used in the final search due to the lower associated uncertainties. Both statistical and systematic uncertainties are displayed.

	electron	muon
Loose1	34.7 ± 4.8 (stat.) $\pm$ 7.3 (sys.) $^{+0.0}_{-29.5}$ (Z')	33.8 ± 3.4 (stat.) $\pm$ 7.9 (sys.) $^{+0.0}_{-33.8}(Z')$
Loose2	49.1 ± 2.3 (stat.) $\pm$ 7.1 (sys.) $^{+0.0}_{-18.0}$ (Z')	29.7 ± 0.3 (stat.) $\pm$ 7.9 (sys.) $^{+0.0}_{-2.0}(Z')$

5.2 Comparison of data with the background prediction

5.2.1 Total yield

The application of the selection criteria detailed in Section 4.1 gives a yield of 1837 events from data, across both channels. This is found to be in good agreement with the SM prediction of 1840 ± 130, obtained using the simulated samples and data-driven techniques described above. The specific contribution from each background is displayed in Table 5.6, for the electron and muon channels separately, and then both combined. The yields given by the two benchmark signal models, at a number of mass points, are displayed in Table 5.7.

SM $t\bar{t}$ production is found to be the dominant background at a level of just over 60 % of the total; W+jets is approximately 25 % of the total. Smaller backgrounds include the production of multijets and of Z+jets, each at a level of just under 5 % of the total. Single top quark and diboson production together make up the remaining 5 % of the total background yield.

5.2.2 Distributions of variables

It is necessary to inspect the composite background estimation to verify if it compares well with the observed data. Ideally, this would be carried out in a control region which contains no events due to possible signal processes, or at the very least, is substantially depleted in signal events. This is not possible in this particular analysis since the SM $t\bar{t}$ back-

Table 5.6: Selected data events and expected background yields after the full selection. The displayed uncertainties are those due to the normalisation of the expected background yield from each contribution; estimation of these uncertainties is described in Section 6.3.2.

Type	e+jets	μ+jets	Sum
$t\bar{t}$	510 ± 40	620 ± 50	1130 ± 90
$W+$ jets	200 ± 34	300 ± 50	500 ± 80
Multijets	45 ± 23	30 ± 15	75 ± 38
Z+jets	41 ± 20	34 ± 16	75 ± 36
Single top	21 ± 2	27 ± 3	48 ± 5
Dibosons	3.4 ± 0.2	4.3 ± 0.2	7.7 ± 0.4
Total	830 ± 60	1010 ± 70	1840 ± 130
Data	803	1034	1837

Table 5.7: Expected yields in the signal region for the two benchmark signal models, at a number of mass points. The uncertainties are statistical only.

Model and mass [GeV]	e+jets	μ+jets	Sum
Z' $m = 700$	27 ± 1.4	32 ± 1.3	59 ± 2.7
Z' $m = 800$	31 ± 1.1	36 ± 1.1	67 ± 2.2
Z' $m = 1000$	18.7 ± 0.4	21.4 ± 0.4	40.1 ± 0.8
Z' $m = 1300$	6.4 ± 0.2	5.9 ± 0.1	12.3 ± 0.3
Z' $m = 1600$	1.96 ± 0.06	1.99 ± 0.05	3.95 ± 0.11
Z' $m = 2000$	0.42 ± 0.02	0.39 ± 0.01	0.81 ± 0.03
g_{KK} $m = 700$	490 ± 55	473 ± 49	963 ± 104
g_{KK} $m = 800$	400 ± 36	509 ± 38	909 ± 74
g_{KK} $m = 1000$	242 ± 17	336 ± 19	578 ± 36
g_{KK} $m = 1300$	76 ± 5	92 ± 5	168 ± 10
g_{KK} $m = 1600$	30 ± 1.9	28 ± 1.6	58 ± 3.5
g_{KK} $m = 2000$	4.3 ± 0.3	4.4 ± 0.3	8.7 ± 0.6

ground is irreducible: rejection of events due to this background would also reject signal events. Therefore the comparison of the background prediction and the data is performed in the signal region, but using distributions of variables which are *not* used to identify BSM processes.

The distributions of such variables are displayed in this section. The contributions from the two lepton channels have been added together and the individual processes contributing to the prediction are shown separately, stacked on top of each other. The hashed region shows the systematic uncertainty associated with the data-driven normalisation of the W+jets contribution. This sole systematic is displayed because it is has one of the largest effects on the background yield, as discussed in Section 6.3.

The statistical uncertainty is displayed for data, but not for the background. However, the lower part of each figure shows the ratio of the data yield to predicted yield in each bin. In the calculation of this ratio, the statistical uncertainties on both data and the prediction have been taken into account. The level of agreement between data and the background can be assessed using the value of this ratio in each bin.

The hadronic top jet

The first set of distributions is related to the fat jet selected as the hadronic top quark candidate. The process of this selection was detailed in Section 4.2.1. Good agreement can be seen between the data and the background prediction for all variables. The lower kinematic thresholds of $p_T > 250$ GeV, $m_j > 100$ GeV and $\sqrt{d_{12}} > 40$ GeV are apparent by the absence of events in the lower bins of Figures 5.3(a), 5.3(c) and 5.3(d) respectively.

Distributions for the distance in η-ϕ space between the hadronic top jet and 1) the lepton, 2) the leptonic top jet, are also shown in Figures 5.3(e) and 5.3(f) respectively. Both distributions peak at $\Delta R = 3$, giving clear evidence for the back-to-back topology of the majority of events. There are no events in the region $\Delta R < 1.2$ of Figure 5.3(f) due to the event selection criteria of Section 4.1.4. Part of these criteria is the rejection of any fat jets which lie within $\Delta R = 1.5$ of the leptonic top jet.

Leptonic top quark decay objects

This set of distributions is related to the individual objects which comprise the leptonic top quark candidate. The lepton p_T and η are displayed in Figures 5.4(a) and 5.4(b) respectively. The data to background ratio demonstrates that the prediction describes the data well, across the full range of both variables. The marked reduction in events having a lepton in the very central region is driven by the low muon reconstruction efficiency,

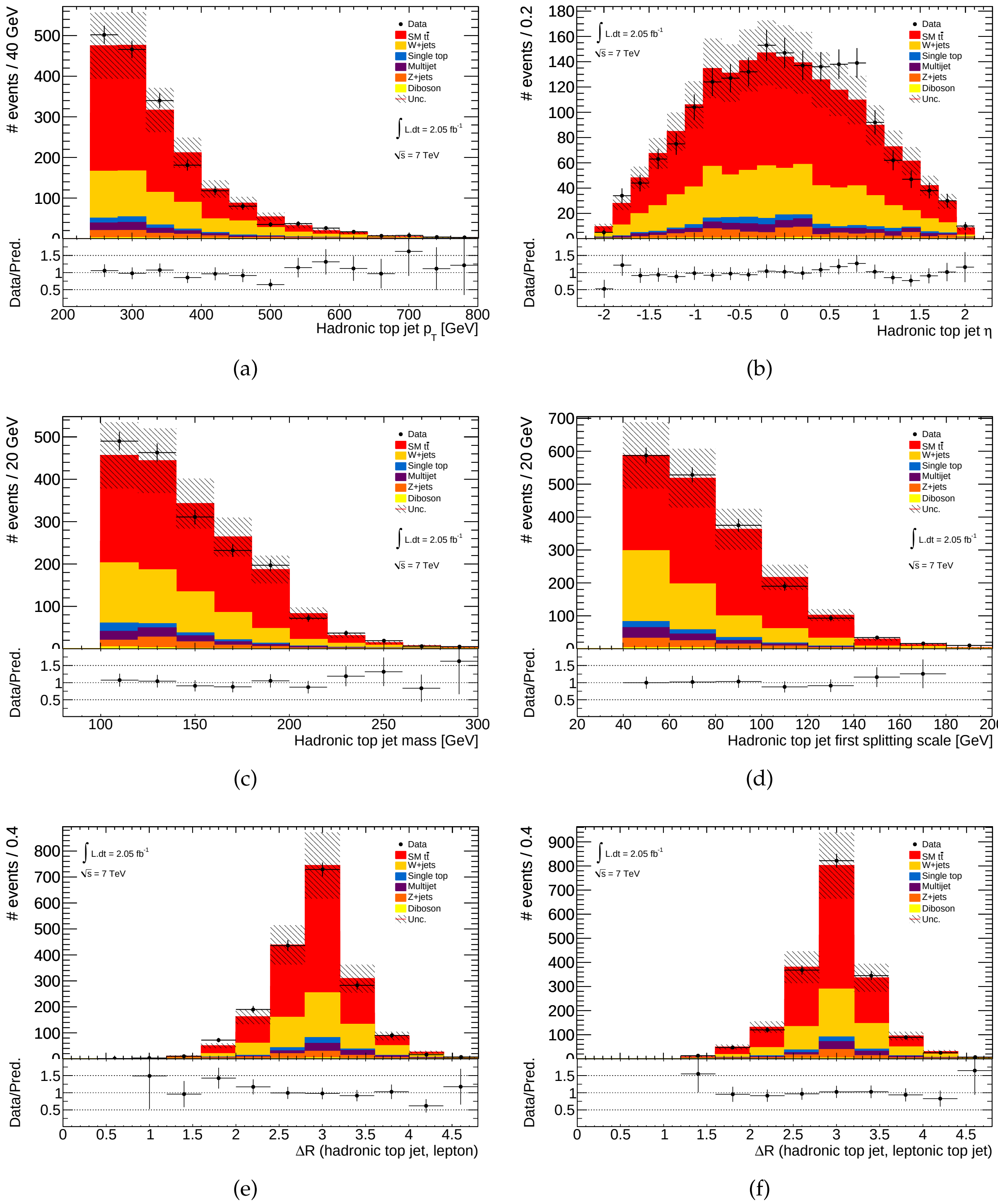

Figure 5.3: Comparison of the data and background prediction for key kinematic and spatial variables related to the fat jet selected as the hadronic top quark candidate. The prediction is found to provide a very good description of the data, for all distributions.

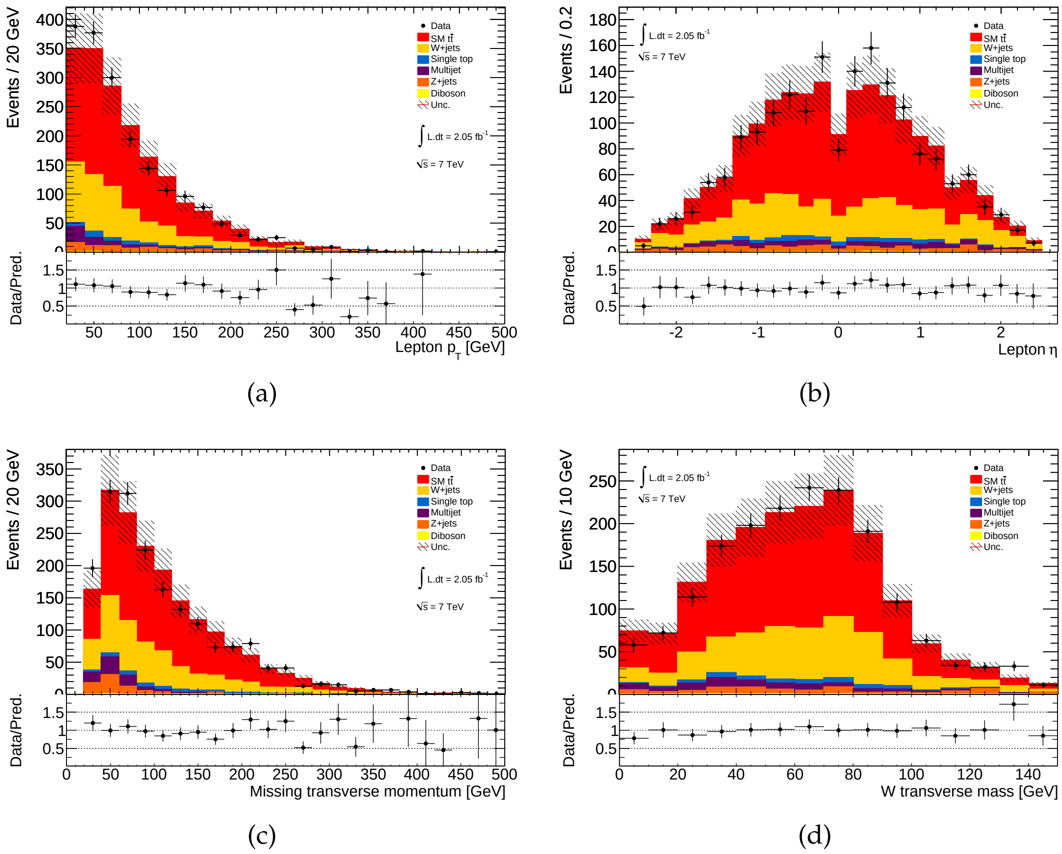

Figure 5.4: Data and background model comparison for distributions related to the single selected lepton, the E_T^{miss} and the W transverse mass. Good agreement is seen between the background model and the observation.

illustrated in Figure 3.5(a). The lepton p_T exhibits a gradually falling distribution, as expected from the dependence of the cross-section for SM $t\bar{t}$ production [51], for example, on the centre-of-mass of the colliding partons.

The distribution for the E_T^{miss} is displayed in Figure 5.4(c). It exhibits the same shape as the lepton p_T distribution. The second bin, between 20 and 40 GeV, has a reduced number of counts due to the E_T^{miss} threshold in the electron channel of 35 GeV. The distribution for the W transverse mass is shown in Figure 5.4(d). A peak with an upper edge at $\approx M_W$ is apparent, which occurs when the lepton lies in the transverse plane. Approximately 70 % of events lie below this upper edge, primarily due to leptons having some momentum in the longitudinal direction. The tail of events with $M_T(W) > M_W$ arises due to the finite width of the W boson.

Distributions related to the leptonic top jet, which is part of the leptonic top quark

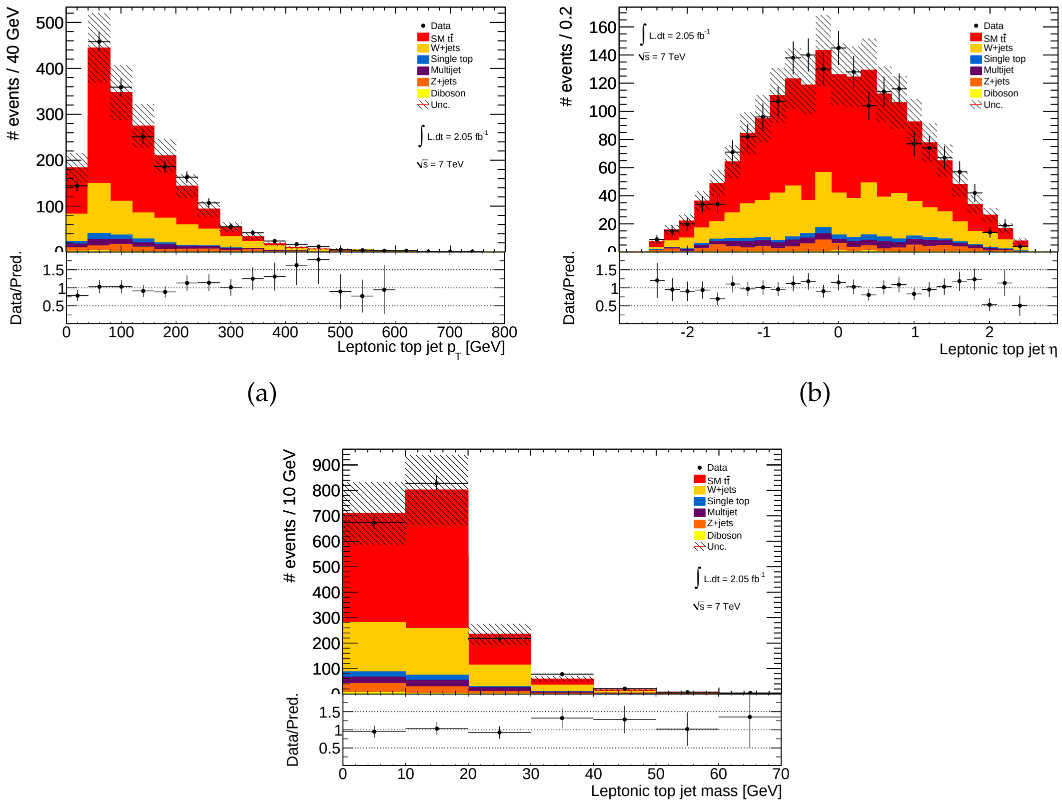

(a) (b)

(c)

Figure 5.5: Data and background comparisons for distributions related to the *jet* which is part of the leptonic top system: a) p_T b) η and c) mass. This jet is part of the reconstructed leptonic top quark, the mass of which is displayed in Figure 5.6. Good agreement is once again observed between the data and the background prediction.

reconstruction, are displayed in Figure 5.5. Good agreement is observed for all variables, within the level of the statistical uncertainties.

The reconstructed leptonic top quark candidate

The mass of the reconstructed leptonic top quark candidate is displayed in Figure 5.6 for both the data and the background prediction. This candidate has been reconstructed from the selected lepton, the E_T^{miss}, the neutrino p_z and the leptonic top jet discussed above. A peak in the contribution from SM $t\bar{t}$ production, corresponding to the top quark mass, is clearly visible. The background estimation provides a good prediction of the distribution drawn from data. The discrepancy centred on $m \approx 330$ GeV is at the level of only $1.5\ \sigma$ if statistical uncertainties are considered. A rigorous comparison of the data with the standard model prediction is presented in the next chapter.

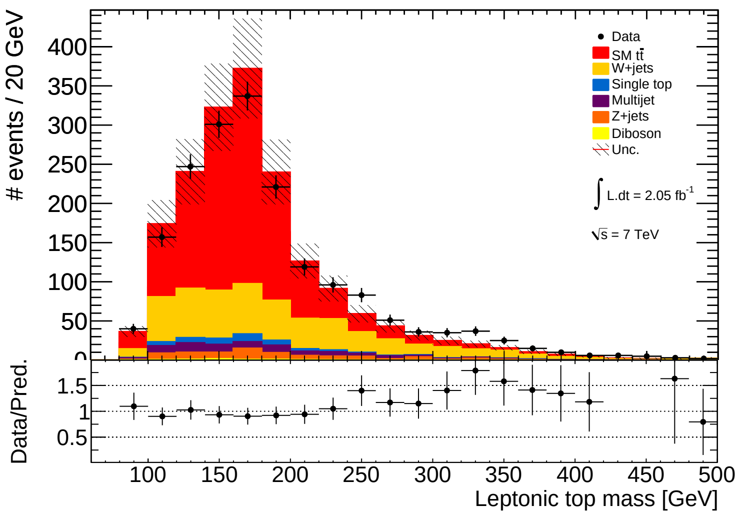

Figure 5.6: Data and background model comparison for the mass distribution of the leptonic top quark candidate. There is a peak in the distribution for SM $t\bar{t}$ production at the position expected for a decaying top quark.

5.3 Summary

Estimation of the two primary reducible backgrounds, W+jets and QCD multijet production, has been presented in this chapter. The pp collision data is used to improve the estimation in both cases. For W+jets, data is used to *normalise* the estimated yield taken from MC simulation; excellent agreement is obtained between the yields from data and from the normalised simulation, as assessed in a control region dominated by W+jets production. The QCD multijet background involves a number of processes which are extremely challenging to simulate. A fully data-driven method is therefore used, to obtain the normalisation *and* the shape of distributions due to this background.

The observed number of data events is then compared to the predicted number of events, taking into account *all* background processes. The predicted shapes of distributions for a number of key variables used in the analysis are found to agree extremely well with the distributions obtained using data. This demonstrates that the background modelling provides a good description of the data.

Chapter 6

Results

The invariant mass of the $t\bar{t}$ system is reconstructed in all selected events in the signal region, defined in Chapter 4. This forms the discriminant by which deviations from the SM prediction are identified. The distributions are shown, for the data and for the background prediction, in Figure 6.1 (electron channel) and Figure 6.2 (muon channel). Any deviations of the data from the prediction are investigated in this chapter.

The strategy for setting the bin widths for the x-axis was developed prior to this thesis [70]. For the low-mass region ($m_{t\bar{t}} \lesssim 1400$ GeV), the bin widths are no wider than half the experimental resolution[1]. Above this region, the widths were increased to reduce the sensitivity to statistical fluctuations. As shown in Section 6.2 below, the effect of using this configuration of bins as opposed to those of constant width across the distribution is small compared to the effect of statistical fluctuations.

The event containing the $t\bar{t}$ candidate with the largest invariant mass in this dataset, of 2.6 TeV, is illustrated in Figure 6. In the x-y plane, used here, the back-to-back topology of the event is clearly evident. The hadronic top jet candidate has $p_T = 1.0$ TeV and is centered on the ID tracks and calorimeter deposits recorded at $\phi = 0.4$. The leptonic top quark candidate is composed of a jet at $\phi = -2.6$ with $p_T = 730$ GeV, an electron with

[1] The experimental resolution is approximately 6 – 12 % of the resonance mass, as discussed in Section 1.3.1.

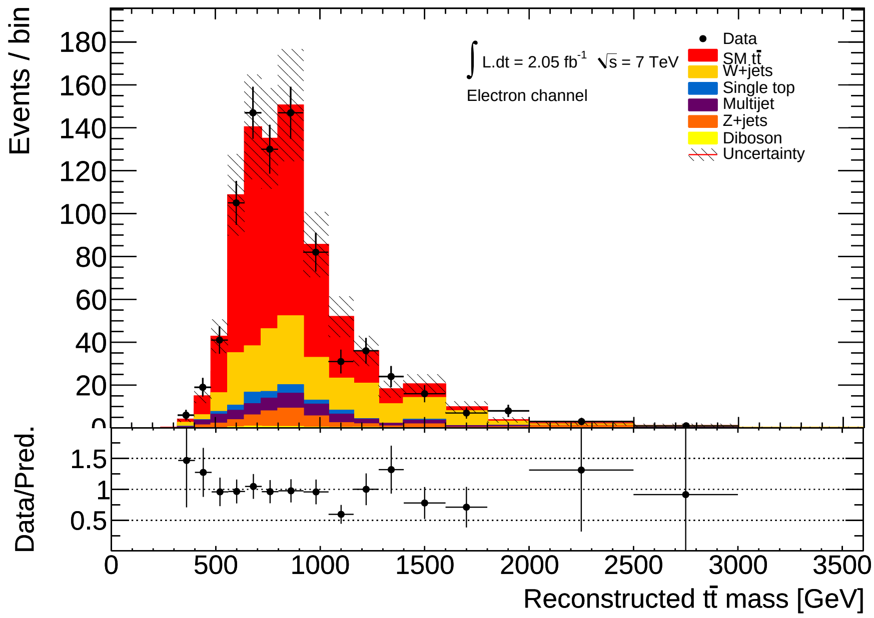

(a)

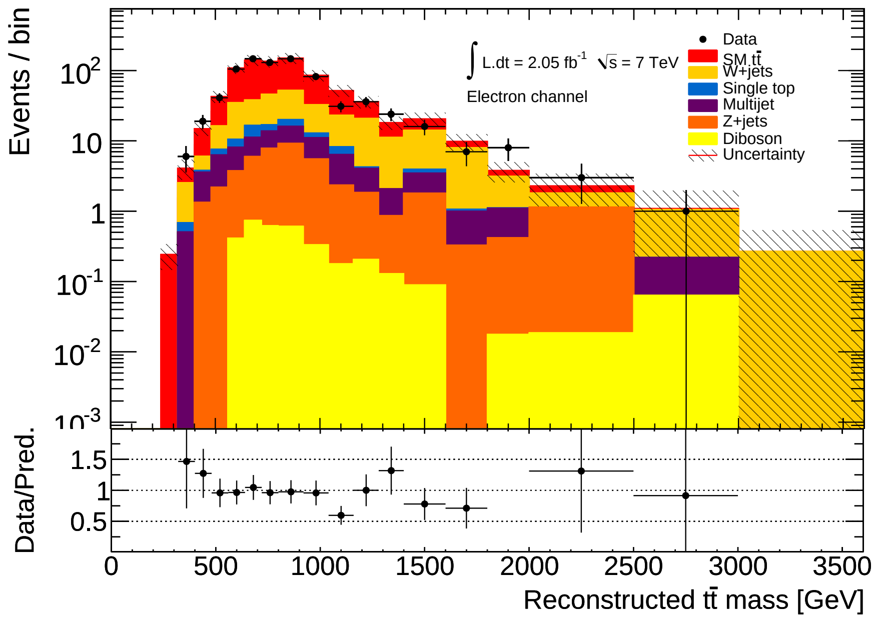

(b)

Figure 6.1: Invariant mass of the reconstructed $t\bar{t}$ system for all events in the signal region of the *electron channel*. The distribution derived from data events is compared to that from the background prediction. The shaded band indicates the systematic uncertainty associated with the W+jets data-driven normalisation only, since the level of this uncertainty is comparable with the observed differences between the yields given by data and by simulation. The distribution with a linear scale for the y-axis is shown in (a) and with a logarithmic scale in (b). This figure is used to identify deviations from the background prediction in the search for $t\bar{t}$ resonances.

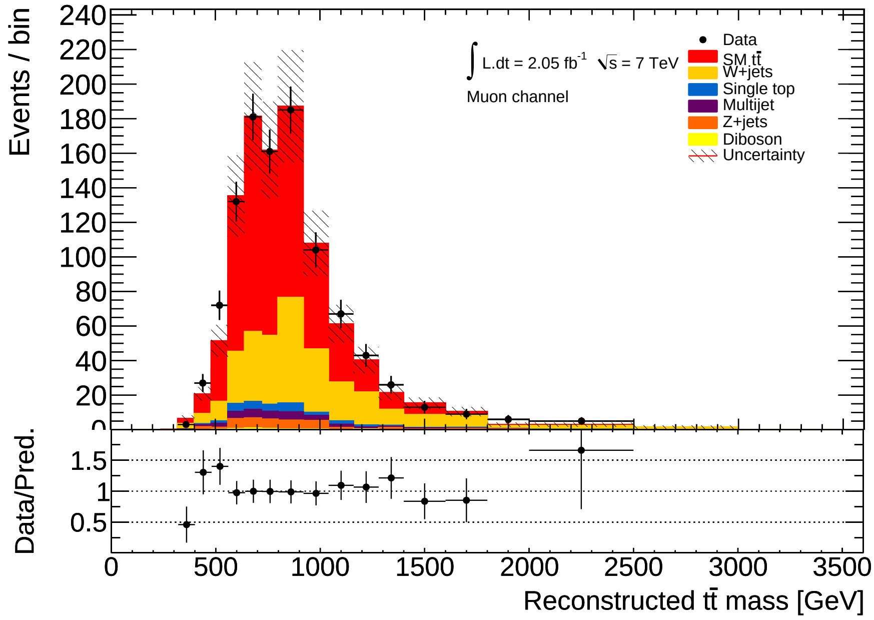

(a)

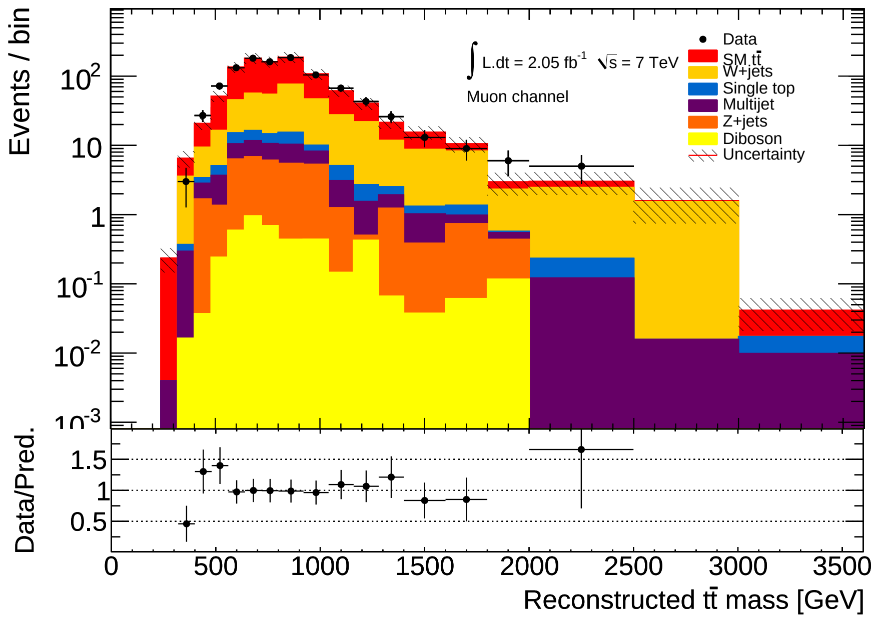

(b)

Figure 6.2: Invariant mass of the reconstructed $t\bar{t}$ system for all events in the signal region of the *muon channel*. This figure is used to identify deviations from the background prediction in the search for $t\bar{t}$ resonances. Other details as for Figure 6.1.

$p_T = 230$ GeV and $E_T^{miss} = 110$ GeV. The p_z of the neutrino is reconstructed following the procedure described in Section 4.2.2. There are two reasons why this event would not have been selected if the resolved criteria of Section 4.1.2 had been applied. First, only one anti-k_T $R = 0.4$ jet was reconstructed from the calorimeter deposits of the hadronic top quark candidate, indicating that the three partons from the decay of the candidate top quark are highly collimated. Secondly, none of the anti-k_T $R = 0.4$ jets in the event were b-tagged.

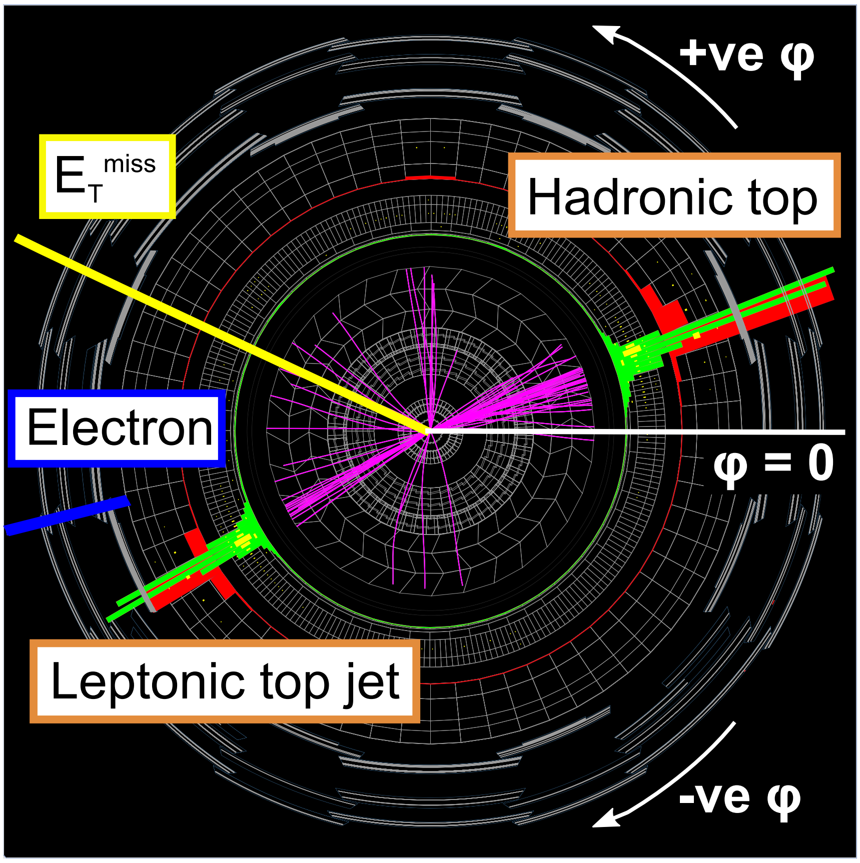

Figure 6.3: Event display of the $t\bar{t}$ candidate with the largest reconstructed invariant mass (2.6 TeV) from all events analysed in this dataset. The display is shown in the x-y plane, with $\phi = 0$ at "three o'clock". The locations of the reconstructed physics objects are denoted.

6.1 Compatibility with the null hypothesis

The reconstructed $t\bar{t}$ invariant mass distributions from data and from the background prediction are systematically compared using the BUMPHUNTER [187]. This is a tool widely used at both the Tevatron and the LHC to indicate the presence of observed deviations from the prediction of a certain hypothesis H.

In most searches for BSM phenomena, including this one, the chosen hypothesis is the *null hypothesis* H_0 i.e. the standard model. This is because the initial aim is to identify the possible existence of *any* new phenomena rather than to focus on one particular model. The reconstructed $t\bar{t}$ invariant mass distribution given by H_0 is obtained using the MC simulations and data-driven estimations of background processes described in Chapters 2 and 5.

Deviations from the null hypothesis may be caused by the presence of BSM phenomena. The prediction, assuming the null hypothesis, is also subject to statistical fluctuations however. The aim of hypothesis-testing tools such as the BUMPHUNTER is to determine the probability that an observed deviation would result simply from a statistical fluctuation, under the assumption that the standard model is valid and no BSM process have occurred. This probability is known as the *p-value*. A small p-value indicates a greater degree of inconsistency with the standard model, or in other words, a more *statistically significant* deviation.

p-values are also converted to *significance*, denoted by σ. This is the number of standard deviations of a normal distribution away from its mean, which, when integrated over the remaining tail of the distribution corresponds to the same probability as the p-value.[2] It is standard practice in particle physics to declare a discovery if a deviation is found with $\sigma \geq 5$. This corresponds to a p-value of $\lesssim 3 \times 10^{-7}$. A significance level of $\sigma \geq 2$ (corresponding to a p-value of $\lesssim 4 \times 10^{-2}$) is an unofficial but commonly used threshold for the triggering of interest in a deviation.

There are two stages in the calculation of the p-value. First, the reconstructed $t\bar{t}$ invariant mass distribution obtained from the background prediction is used to generate N pseudo-datasets. The yield b in each bin of this distribution is assumed to be the mean value of a Poission distribution, which therefore also has a variance equal to b. The pseudo-datasets are generated in line with this Poisson distribution. In this case, $10,000$ pseudo-datasets are generated.

The second stage is to quantify the deviation between the data and H_0 using a *test*

[2]Specifically, the conversion is $\sigma = \sqrt{2}\,\mathrm{erf}^{-1(1-2p)}$ [188] where erf is the inverse error function [189].

statistic, t. The test statistic is formulated so that the greater the difference between the compared distributions, the greater the value of the test statistic. For a general hypothesis test, the p-value would then be calculated as:

$$p = \frac{\int_{t_{obs}}^{\infty} f_0(t)\,dt}{\int_0^{\infty} f_0(t)\,dt} \tag{6.1}$$

where t_{obs} is the observed value of the test statistic and $f_0(t)$ is the probability density of t if the hypothesis H_0 is true.

However, a particularly important consideration in the formulation of a p-value is the *trials factor* or *look-elsewhere effect*. This arises because the reconstructed $t\bar{t}$ invariant mass distribution has multiple bins. The larger the number of bins, the greater the probability that at least one bin will contain a deviation in the data that will be classed as statistically significant. This probability is known as the *local probability* and the BUMPHUNTER uses a test statistic that combines these local probabilities. The bins are first combined into windows, with index i, which vary in width for each iteration of the BUMPHUNTER: the first iteration combines two neighbouring bins into single windows, across the entire distribution. Each subsequent iteration adds one additional neighbouring bin to each window and continues in this way until the window width is half of the entire distribution. The windows are not fixed in position, but slide across the entire distribution. The BUMPHUNTER calculates a test statistic which is the minimum of the local probabilities from all i windows. It has the specific form:

$$t = -\log(\min_i \{p\text{-value}_i\}) \tag{6.2}$$

where the negative log function ensures that t increases monotonically as this minimum local probability increases.

The test statistic is first derived using the $m_{t\bar{t}}$ distributions in the electron and muon channels added together and then separately in the two channels. The p-value in each case is calculated as the number of pseudo-datasets which have a value of the test statistic larger than that observed in the data, divided by the total number of pseudo-datasets ($10,000$ in this case). The resulting p-values are displayed in Table 6.1; the upper (lower) part represents deviations which are excesses (deficits) of the data compared to the background prediction.

All systematic uncertainties have been taken into account by increasing the expected background yield in each bin. This increase is calculated by applying a particular systematic uncertainty to the distribution taken from background, finding the maximum shift from the shift up and shift down and then halving this shift. In this way, there is full correlation between the shift across all the bins. The individual systematic uncertainties are assumed to be uncorrelated with each other and are therefore combined by adding the shifts due to each uncertainty in quadrature. The estimation of each uncertainty is discussed in Section 6.3.

Table 6.1: p-values for the most significant deviations found in the reconstructed $t\bar{t}$ invariant mass distribution. The two channels are initially added together ("add"), then considered separately ("electron" and "muon") and finally the combined p-values are computed for deviations that are in the same position in the two channels ("overlap"). None of the deviations are considered to be statistically significant. The uncertainty on the p-value and its effect on the significance are both quoted, and statistical and systematic uncertainties have been considered.

Excesses			
Channel	p-value	σ (low, high)	Mass range [GeV]
add	0.0799 ± 0.0027	1.4057 (1.3877, 1.4242)	$1800 - 2500$
electron	0.2863 ± 0.0045	0.5642 (0.05510, 0.5576)	$1800 - 2500$
muon	1.0000 ± 0.0000	–	–
overlap	1.0000 ± 0.0000	–	–

Deficits			
Channel	p-value	σ (low, high)	Mass range [GeV]
add	0.1985 ± 0.0040	0.8470 (0.8328, 0.8614)	$1400 - 1800$
electron	0.1849 ± 0.0039	0.8968 (0.8824, 0.9115)	$1040 - 1280$
muon	0.1686 ± 0.0037	0.9597 (0.9449, 0.9747)	$2500 - 3600$
overlap	1.0000 ± 0.0000	–	–

The uncertainty on the p-value is $\delta p = \sqrt{p(1-p)}/N$ [187] where N is the number of pseudo-datasets. The values of δp are stated in Table 6.1 and are propagated to the significance to give the stated "low" and "high" values.

The largest deviation from the SM expectation is an excess in the region $m_{t\bar{t}} = 1800$ – 2500 GeV. The p-value of the excess is 0.08, corresponding to a significance of 1.4. If the distributions are separated out into the two channels, one can see from the second row of Table 6.1 that this excess is in the electron channel only.

One would expect resonant $t\bar{t}$ production to result in deviations at the same mass position in the two lepton channels. This is because any possible signal is not expected to be biased towards the flavour of the lepton from the top quark decay. This feature can be exploited in the hypothesis-testing procedure. The position of the largest deviation in each channel is found; if this is at the same position in both channels, the "overlap" p-value is taken to be the product of the individual local probabilities for the deviation. If they are at different positions, the result is assumed to be compatible with H_0 and the p-value is set to unity. As shown in Table 6.1, the overlap p-value for any possible excess is indeed equal to one. It is therefore concluded that there is no evidence in this dataset for a statistically significant excess over the background prediction due to BSM resonant $t\bar{t}$ production.

The p-values for possible deficits, shown in the lower part of Table 6.1, demonstrate that there are again no significant deviations. The most significant deficit when both channels are added together is at the level of only $\sigma = 0.85$. Furthermore, the small deviations in the separate channels are not found in the same mass region.

6.2 Determination of upper limits on the production cross-section

Following the assessment that the data is compatible with the SM, one can set upper limits on the cross-section for production, times branching ratio for decay to a $t\bar{t}$ pair ($\sigma \times BR(\rightarrow t\bar{t})$), for the two benchmark models described in Section 1.3. These upper limits can be transformed into the exclusion of the models within certain mass ranges.

6.2.1 The Bayesian approach

The limit-setting procedure is carried out by assuming either a frequentist or a Bayesian interpretation of probability. Searches for $t\bar{t}$ resonances at both the LHC and Tevatron experiments have traditionally applied a Bayesian approach.[3] The analysis presented here continues that strategy, which has been documented by the D0 collaboration [190] and is described below.

The two interpretations provide answers to different questions. In the frequentist case, it is possible to determine the probability to observe a certain dataset given a specific signal. However, this is usually *not* the aim of the study; rather, the intention is to find the probability that a certain signal exists, given an observed dataset. This is provided by a Bayesian interpretation and hence this approach is taken in this case.

6.2.2 Choice of prior

Practically, the Bayesian implementation requires an initial degree of belief that the signal hypothesis is true, known as the *prior* or $P(theory)$. The prior is then updated using the data, to obtain the degree of belief that the hypothesis is true given the observed data. This is known as the *posterior probability* or $P(theory \mid data)$. The concept is summarised as:

$$P(theory \mid data) \propto P(data \mid theory)P(theory) \tag{6.3}$$

where $P(data \mid theory)$ is known as the *likelihood* i.e. the probability of obtaining the observed data, given the hypothesis.

The choice of prior is the most contested part of Bayesian inference since it represents a subjective degree of belief about the signal cross-section, before the incorporation of the results of the data analysis. Historically, priors judged to be "non-informative", relative to the information contained in the data, were preferred since the influence of the experi-

[3]Recent results from the CMS experiment [74, 87] use a frequentist interpretation.

menters' initial degree of belief would be minimised. However, it is very difficult to reach consensus on the form of such a prior, as discussed in [191].

The form of the prior, $P(theory)$, chosen in this study is as follows, where σ is the cross-section for production of the signal model and mass point in question:

$$\pi(\sigma) = \frac{1}{\sigma_{\text{max}}} \tag{6.4a}$$

if $0 < \sigma < \sigma_{\text{max}}$;[4] otherwise

$$\pi(\sigma) = 0 \tag{6.4b}$$

This is a particularly simple "flat" prior. However, it was *not* chosen for being non-informative. Indeed it could not be considered as representing a degree of belief because it is not properly normalisable (i.e. it is improper). The choice is actually made because, for this particular analysis, a flat prior is a good approximation to the *reference prior*. These reference priors are designed to maximise the amount of missing information but are not considered to represent a degree of belief. In the wider context of reference analysis, discussed in [192], an improper prior is permissible as long as the resulting reference posterior is normalisable. This is indeed the case here.

To validate the claim that a flat prior is a good approximation to the reference prior, it is noted from section 4 of [192] that the formulation of the reference prior depends on two parameters α and β. Both parameters depend on the background yield b and its variance V, specifically: $\alpha = b^2/V$ and $\beta = b/V$. Using the values of $b = 1840$ and $\sqrt{V} = 130$ from Table 5.6, leads to values of α and β of approximately 200 and 0.1 respectively. Figure 6.2.2 demonstrates that if $\alpha = 10$ and $\beta = 0.1$, a flat prior is obtained. This is also the case for $\alpha > 10$ and $\beta < 0.1$ [192], which are the parameter values relevant to the analysis presented here.

[4]The strategy for setting σ_{max} is discussed in relation to Equation 6.9 below.

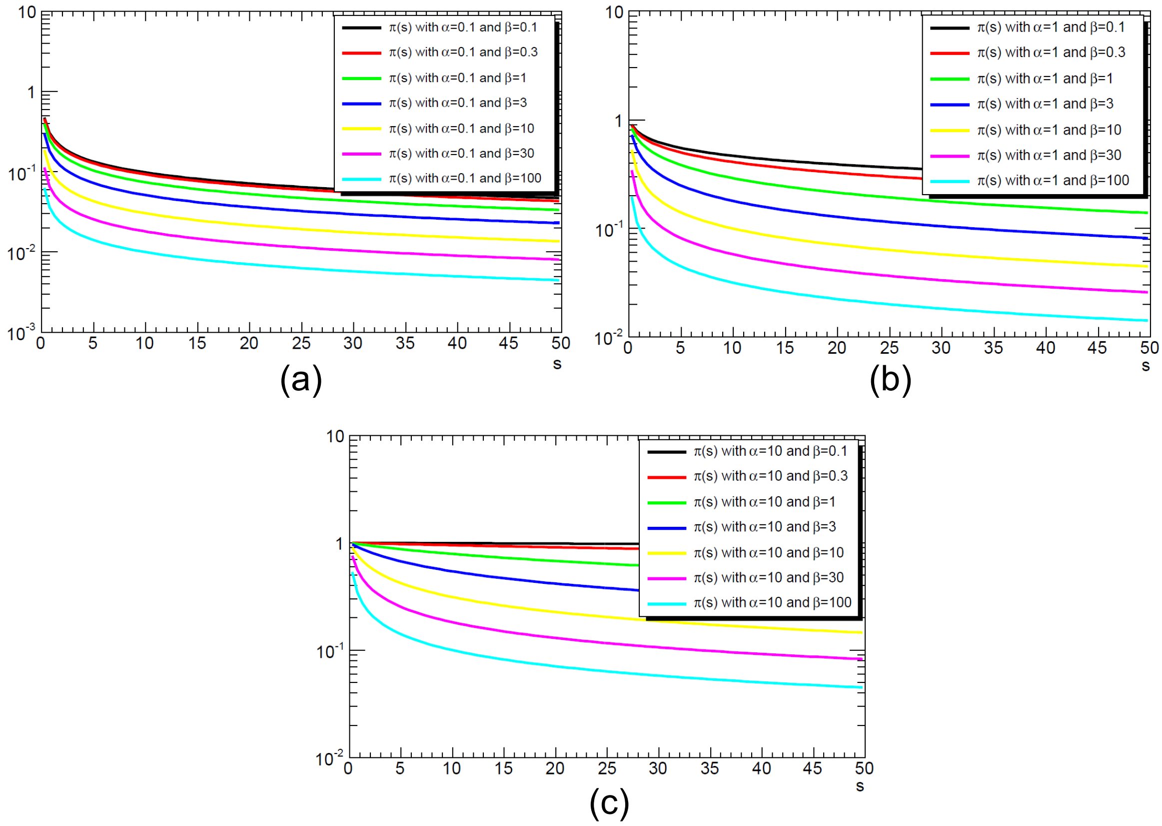

Figure 6.4: Reference priors for the signal parameter s obtained with the parameter α set equal to (a) 0.1 (b) 1 and (c) 10, and different values for the parameter β. The prior is flat if $\alpha = 10$ and $\beta = 0.1$. Taken from [192].

6.2.3 Obtaining the posterior probability

The first stage for obtaining a posterior probability density, given a prior, is to select a form for the likelihood, L. In the case of analyses involving counting experiments, such as this one, the basic form of L is a Poisson distribution with expectation value μ:

$$L(D \mid \mu, I) = \frac{e^{-\mu}\mu^{D}}{D!} \tag{6.5}$$

where D is the number of events observed in the data and I represents all the information used to calculate μ, together with the validity of assuming a Poisson distribution for L. μ is given by the sum of the expected background yield b and the proposed signal yield $a_r\sigma_r$ due to a particular signal model and mass point r:

$$\mu = b + a_r\sigma_r \tag{6.6}$$

where σ_r is the cross-section for a resonance of mass r and a_r is the product of the following factors:

- the detector acceptance;
- the integrated luminosity of the data sample;
- and, the selection efficiency for the same signal model and mass point.

The yields resulting from the two benchmark signal models considered in this thesis were displayed in Table 5.7, for a number of mass points.

Equations 6.5 and 6.6 are combined to give the final likelihood function of Equation 6.7. The likelihood functions calculated in each bin can be multiplied together in this way because the probability to observe a count in a given bin or channel is independent of the counts observed in other bins/channels.

$$L(D \mid \sigma_r, a_r, b) = \prod_{i=1}^{N} \frac{e^{-(a_{r,i}\sigma_r + b_i)}(a_{r,i}\sigma_r + b_i)^{D_i}}{D_i!} \tag{6.7}$$

Incorporation of this likelihood function and the prior $\pi(\sigma)$ of Equation 6.4, into Bayes theorem given by Equation 6.3, results in the following form for the posterior probability density:

$$P(\sigma, a_r, b \mid D) = \frac{1}{N} \int_0^\infty da_r \int_0^\infty db\, L(D \mid \sigma_r, a_r, b)\, \pi(\sigma) \tag{6.8}$$

Integration is performed over the so-called *nuisance parameters* a_r and b, since their determination is not the aim of the analysis. Any dependence on them is thereby removed. The normalising constant N is determined from the axiom that the probability over the entire sample space is one:

$$\int_0^\infty d\sigma \int_0^{\sigma_{\max}} da_r \int_0^\infty db P(\sigma, a_r, b \mid D) = 1 \tag{6.9}$$

where $\sigma_{\max}$ was used in the definition of the prior of Equation 6.4. The value is chosen so that the integration over σ is performed up to an upper bound where the posterior probability density becomes sufficiently close to zero.

The posterior represents the final result: the probability density for the signal cross-section, using the information gained from analysis of the data. However, since the data have already been judged to be consistent with the standard model, only the upper limit on the cross-section is needed, rather than determination of the entire probability density. The posterior is therefore integrated up to a certain level, to give a value β, resulting in an upper limit on the cross-section σ_{UL} at the $(100 \times \beta)$ % credibility level (C.L.). Specifically:

$$\beta = \int_0^{\sigma_{UL}} d\sigma P(\sigma \mid D) \tag{6.10}$$

The posterior is computed using a package developed by the D0 collaboration, called `top_statistics` [193]. Each systematic uncertainty is considered as follows. A shift factor $g(0,1)_{isys}$ is computed by sampling a random number from a Gaussian distribution which has a mean of zero and a width of one.[5]. The nominal yield y in each bin of the $m_{t\bar{t}}$ distribution is shifted by an amount Δ_{isys} due to the systematic uncertainty $isys$ as follows:

$$\Delta_{isys} = s^{+}_{tot} \times g(0,1)_{isys} \times (y^{+}_{isys} - y), \tag{6.11a}$$

if $g(0,1)_{isys}$ is a positive number; otherwise

$$\Delta_{isys} = s^{-}_{tot} \times g(0,1)_{isys} \times (y - y^{-}_{isys}). \tag{6.11b}$$

$y^{+(-)}_{isys}$ is the yield in each bin following application of the systematic uncertainty $isys$ at the level of one sigma, when the factor $g(0,1)_{isys}$ is positive (negative). $s^{+(-)}_{tot}$ is a multiplicative scale factor which ensures that, if the systematic uncertainty should only affect the shape rather than the normalisation of the distribution, then the overall normalisation

[5]The size and method of estimation of all systematic uncertainties is discussed in the next section.

can be corrected.

Integration over the sampled Gaussian is performed by drawing random numbers from its distribution many times and computing a likelihood each time. The final posterior, with all systematic effects combined, is derived from the sum of the individual likelihoods. In this calculation, the integral of each posterior is preserved in the calculation, which means that those individual likelihoods with a large integral will be the main contributions to the final posterior. To reduce the frequency with which the systematic shifts create a negative yield in a particular bin, if the level of systematic uncertainty is larger than $20\ \%$ [70], a log-normal distribution, rather than a Gaussian, is sampled.

A number of cross-checks were carried out to ensure the stability of the calculated limits. The first considered the effect of using the chosen binning strategy for the reconstructed $t\bar{t}$ invariant mass distribution, rather than constant bin widths of $80\ \mathrm{GeV}$. The limit was found to vary between only 5 and $15\ \%$, which is less than half of the $1\ \sigma$ shift due to statistical fluctuations (30 – $50\ \%$). The second cross-check considered the choice of random seed used in the sampling of the Gaussian distribution which propagates the systematic uncertainties to the upper limit. The seed was varied twenty times and the upper limits were found to vary by only 1 – $2\ \%$, resulting in the conclusion that the limit-setting procedure is also stable with respect to the choice of seed.

The resulting upper limits on the cross-section times $t\bar{t}$ branching ratio are detailed in Table 6.2. The results for the two models, Z' and g_{KK}, are shown separately.

The observed upper limits for the narrow leptophobic topcolor Z' boson range from $7.7\ \mathrm{pb}$ for a mass of $600\ \mathrm{GeV}$ to $0.27\ \mathrm{pb}$ for a mass of $3\ \mathrm{TeV}$. For the same mass points, the wider KK-gluon has an observed upper limit of $2.8\ \mathrm{pb}$ and $0.61\ \mathrm{pb}$ respectively. The expected upper limits, computed using the SM prediction in place of the data, are in good agreement with the observed upper limits for both models.

The limits for this particular topcolor Z' boson are applicable to *any* resonance whose width is narrow compared to the experimental resolution. This is because all such res-

Table 6.2: Upper limits on the cross-section times $t\bar{t}$ branching ratio for the leptophobic Z' boson and the KK-gluon, at the 95 % credibility level. Systematic and statistical uncertainties have been included. The expected variation in the expected limits due to statistical fluctuations is also given, at the $1\ \sigma$ level.

$Z' \to t\bar{t}$ limits				
Z' mass [GeV]	Observed [pb]	Expected [pb]	-1σ [pb]	$+1\sigma$[pb]
600	7.7	10.4	7.0	15.6
700	2.2	2.7	1.8	4.0
800	1.4	1.6	1.0	2.3
1000	0.61	0.72	0.49	1.0
1300	0.56	0.39	0.27	0.57
1600	0.22	0.25	0.17	0.36
2000	0.34	0.18	0.12	0.25
3000	0.27	0.27	0.19	0.41
$g_{\mathrm{KK}} \to t\bar{t}$ limits				
g_{KK} mass [GeV]	Observed [pb]	Expected [pb]	-1σ [pb]	$+1\sigma$[pb]
700	2.8	2.9	2.0	4.2
800	2.3	2.1	1.4	3.0
900	1.0	1.5	0.97	2.2
1000	0.65	0.99	0.69	1.4
1150	0.53	0.64	0.45	0.94
1300	0.80	0.60	0.42	0.87
1600	0.37	0.40	0.28	0.58
1800	0.49	0.38	0.26	0.55
2000	0.61	0.38	0.26	0.55

onances would yield a similar distribution of the reconstructed $t\bar{t}$ invariant mass. However, the results for the KK-gluon are specific to this particular model because of the assumptions made about its couplings to light quarks, discussed in Chapter 1.

For heavy resonances, with a mass greater than $700\ \mathrm{GeV}$, the limits represent a significant improvement on the ATLAS search for $t\bar{t}$ resonances in the lepton+jets channel using the *resolved* approach with the same $2\ \mathrm{fb}^{-1}$ of data [71]. Specifically, the observed upper limits for the topcolor Z' boson using the resolved approach were 2.5, 2.4 and $0.76\ \mathrm{pb}^{-1}$ for $m_{Z'} = 700$, 1000 and $1600\ \mathrm{GeV}$ respectively. For the KK-gluon, the upper limits were 3.1, 2.9 and $1.4\ \mathrm{pb}$ for the same mass points.

The upper limits derived from this search are shown in graphical format in Figure 6.5, together with the predicted $\sigma \times BR(\to t\bar{t})$ values for the two models, as a red band. The

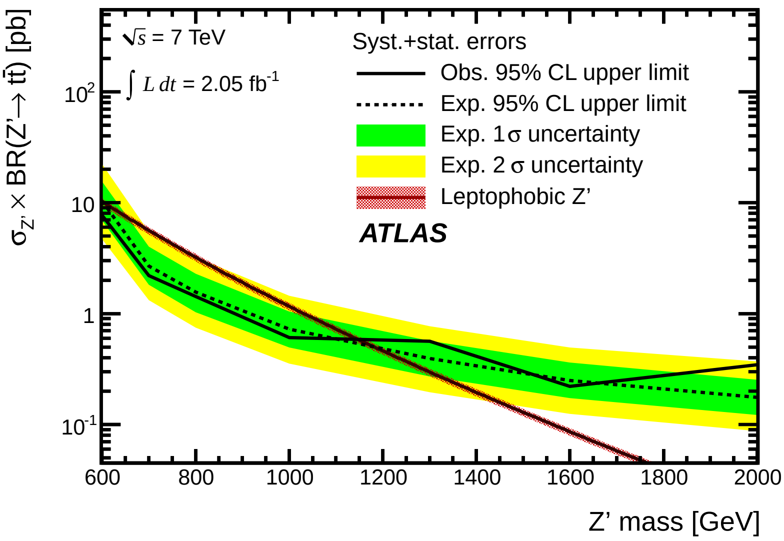

(a)

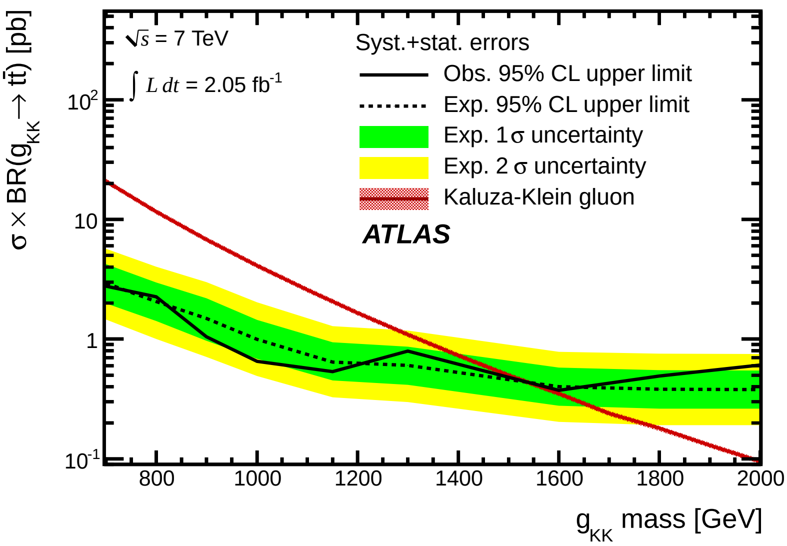

(b)

Figure 6.5: Upper limits on the production cross-section times $t\bar{t}$ branching ratio for (a) the topcolor leptophobic Z' boson and (b) the Kaluza-Klein gluon g_{KK}. The expected and observed limits are given by the dashed and solid lines respectively; the smooth (red) line represents the predicted cross-section times branching ratio for the signal in question. Both statistical and systematic uncertainties have been incorporated.

finite width of this band represents the effect due to the systematic uncertainty associated with the determination of the PDFs. Certain mass regions of the two models can be excluded, at the $95\ \%$ C.L. If the observed limits are considered, the topcolor Z' boson is excluded in the mass region $0.6 < m_{Z'} < 1.15$ TeV. The KK-gluon with a mass of lower than 1.5 TeV is also excluded. The excluded regions when using the expected limits are in agreement with the "observed exclusion". The green (dark) and yellow (light) represent the expected limits from 68 % and 95 % of pseudo-experiments respectively.

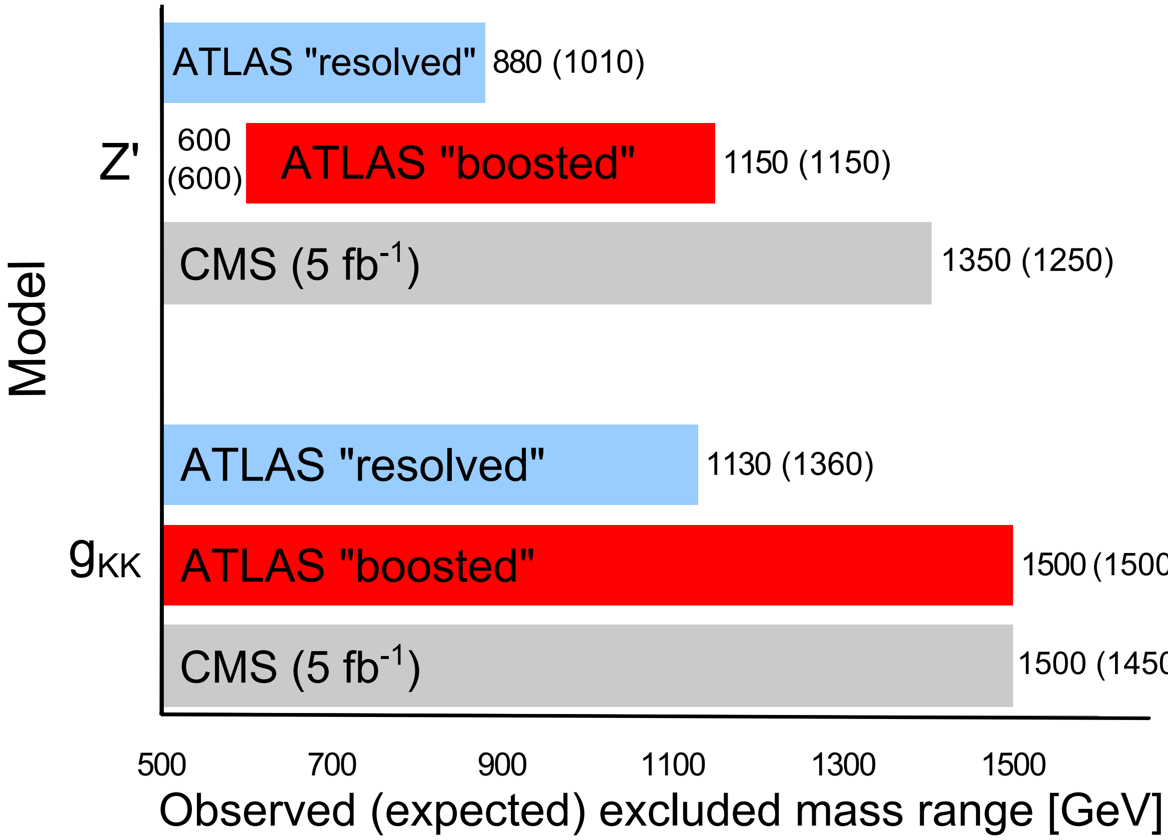

Figure 6.6: Observed and expected excluded mass ranges for the Kaluza-Klein (g_{KK}) and leptophobic Z' models. The results displayed are taken from the ATLAS search presented in this thesis (*ATLAS "boosted"*), from the previous ATLAS search using the resolved strategy (*ATLAS "resolved"*) and from a contemporary CMS result, also in the lepton+jets channel [87]. Both ATLAS searches analysed $2.05\ \text{fb}^{-1}$ of data whereas the CMS search analysed almost $5\ \text{fb}^{-1}$; the centre-of-mass energy was $\sqrt{s} = 7\ \text{TeV}$ for all. The ATLAS search using the boosted approach represents a great improvement on the resolved approach and is very competitive with the CMS result.

These results for the mass exclusion can also be compared to those from the previous ATLAS search in the lepton+jets channel using the resolved approach, as demonstrated in Figure 6.5. The search presented in this thesis extends the excluded region for both models by $\approx 300\ \text{GeV}$ over the results from the resolved analysis. This demonstrates the reason for developing a boosted strategy. A comparison with a contemporary result from March 2012 in the same channel from the CMS experiment [87] is also presented. The results shown in this thesis are also extremely competitive with these released by CMS, particularly considering that the latter was performed on a dataset of more than double the size used in the ATLAS searches.

Both the ATLAS and CMS experiments have produced updated results for $t\bar{t}$ resonances searches in the lepton+jets channel, superseding the above results from the summer of 2012. The latest result from the ATLAS experiment excludes the leptophobic topcolor Z' boson (Kaluza-Klein gluon) with mass below 1.7 TeV (1.9 TeV) at the 95 % C.L. [179]. The most recent result from the CMS experiment excludes the same two benchmark models with mass below 1.49 and 1.82 TeV respectively [74], at the 95 % confidence level. All results use the full 2011 dataset recorded at $\sqrt{s} = 7$ TeV and feature "boosted" techniques, specifically tailored to the reconstruction of events with $m_{t\bar{t}}$ at the TeV scale.

6.3 Systematic uncertainties

There are a number of systematic uncertainties associated with the physics objects used in this analysis, with the background estimations, with the luminosity measurement and with the estimation of the PDFs. Each systematic uncertainty can affect the reconstructed $t\bar{t}$ invariant mass distribution in two ways. It can alter the total number of events which make up the distribution, that is, the *normalisation*. It can alter the *shape* of the distribution but leave the normalisation the same. However, all systematic uncertainties except for those connected with the luminosity, or specifically referred to below as shape-changing only, affect both the shape *and* the normalisation.

There are three measures of each systematic effect: the impact on the expected yield[6] from the background processes (*background yield*); the impact on the expected yield from a particular signal model (*signal yield*); and the impact on the expected upper limit for $\sigma \times BR(\rightarrow t\bar{t})$ for the same signal model. The latter gives what is known as the *impact on the sensitivity*. Notably, "shape-changing" systematic uncertainties may have negligible impact on the signal or background yields but a large impact on the sensitivity.

The impact of a particular systematic uncertainty is assessed by computing the ex-

[6] All yields are relevant to the signal region.

pected yield, background yield and expected upper limit with the level of uncertainty set to zero. The three measures are then recomputed with the uncertainty returned to its estimated value. A comparison of the two sets of measures results in the levels of impact quoted in Table 6.3. Methods for determining the level of each systematic uncertainty are discussed in turn below.

The chosen signal model for determining the impact on the sensitivity is a leptophobic Z' boson with a mass of $1.3\ \mathrm{TeV}$, since the existence of lower mass points has been excluded by previous experiments.[7] Only systematic uncertainties which have at least a $2\ \%$ impact on the background yield or a $1\ \%$ impact on the sensitivity are included. Although some systematic uncertainties are therefore not displayed, they have all been taken into account in the limit-setting procedure.

6.3.1 Related to the luminosity determination and PDFs

The method of determining the luminosity at ATLAS was summarised in Section 2.2.7. The relative uncertainty on this measurement is primarily due to the Van der Meer scan and was determined to be $3.7\ \%$ [194]. This systematic uncertainty affects only the normalisation of the reconstructed $t\bar{t}$ invariant mass distribution i.e. it is a normalisation uncertainty. It has a relatively large effect on the yields of both the signal and the background. However, because the effect on these two yields is the same, there is a rather small impact ($0.4\ \%$) on the sensitivity, for this particular signal model and mass point.

The determination of the PDFs has an associated systematic uncertainty which affects both the normalisation and the shape of the reconstructed $t\bar{t}$ invariant mass distribution. It is due to a large number of effects [45], including: the systematic and statistical uncertainties of the data used to determine the PDFs; the choice of parameterisation for the initial PDFs before evolution to higher Q^2 scales. The PDF uncertainty propagates to an uncertainty on the estimation of the yields due to signal processes and due to background

[7] At the $95\ \%$ confidence level.

Table 6.3: Systematic uncertainties and their impact on the sensitivity. All uncertainties except "luminosity" and those labelled *norm* affect both the yield and the shape of the reconstructed $t\bar{t}$ mass distribution. In the first two columns the relative impact (in percent) is shown on the total expected background yield (nominally 1840 events) and on the number of selected signal events due to the topcolor Z' boson with mass 1.3 TeV. The final column lists the relative variation of the expected limit for the cross-section times branching ratio of this benchmark, if the corresponding systematic effect is ignored. Only those systematic uncertainties which have at least either a 2 % effect on the background yield or a 1 % effect on the sensitivity are shown.

Systematic effect	Impact on yield [%]		Impact on
	Background	Z' (1.3 TeV)	sensitivity [%]
Luminosity	2.5	3.7	0.4
PDF uncertainty	3.1	1.0	0.2
$t\bar{t}$ normalisation	4.9	−−	0.7
$t\bar{t}$ ISR, FSR	6.3	−−	0.7
$t\bar{t}$ fragmentation & parton shower	3.4	−−	0.9
$t\bar{t}$ generator for hard-scatter	2.8	−−	2.2
W+jets normalisation	4.3	−−	1.4
W+jets shape	*norm.*	−−	0.1
Multijets normalisation	2.1	−−	0.2
Multijets shape	*norm.*	−−	1.1
Z+jets normalisation	2.0	−−	0.5
Jet energy and mass scale	6.7	2.0	5.2
Jet energy and mass resolution	4.7	4.0	1.2
Electron-related	1.1	1.3	1.0
Muon-related	2.2	2.1	4.8

processes which have been simulated using Monte Carlo methods.

Three NLO PDF sets are used to estimate the total PDF uncertainty: CTEQ66[142], MSTW2008nlo68cl[195] and NNPDF20[196]. These are chosen because they are determined using data from the Tevatron, from fixed target experiments, and from HERA. Each set has an associated *error set* which is obtained by varying certain parameters and recalculating the PDFs. When estimating the effect of the overall PDF uncertainty on the search presented here, both the uncertainty within each PDF set (*intra-PDF uncertainty*), and the uncertainty arising from using the different PDF sets (*inter-PDF uncertainty*), is considered.

The method for obtaining the intra-PDF uncertainty involves reweighting each event according to:

$$w = \frac{\mathrm{PDF}_a(x_1, f_1, Q) \times \mathrm{PDF}_a(x_2, f_2, Q)}{\mathrm{PDF}_0(x_1, f_1, Q) \times \mathrm{PDF}_0(x_2, f_2, Q)} \tag{6.12}$$

where x_i is the fraction of the hadron's momentum carried by the i^{th} parton and Q^2 is the momentum transfer scale at which this parton is probed, as defined in Section 1.2.1. PDF_0 is the nominal PDF set and PDF_a is the PDF set obtained after the particular parameter variation has been applied. For each one of the three PDF sets, the reconstructed $t\bar{t}$ invariant mass distributions are obtained with each of the parameter variations applied. The final intra-PDF uncertainty is the $1\ \sigma$ band resulting from all variations.

To obtain the inter-PDF uncertainty, the intra-PDF uncertainties from each PDF set are combined in a linear way. That is, an envelope between the maximum and minimum of all the variations is obtained. This process is illustrated in Figure 6.7. Half of the width of this envelope is assigned to be the inter-PDF uncertainty, which is taken as the overall PDF uncertainty. Details of the prescription are provided in [197, 198].

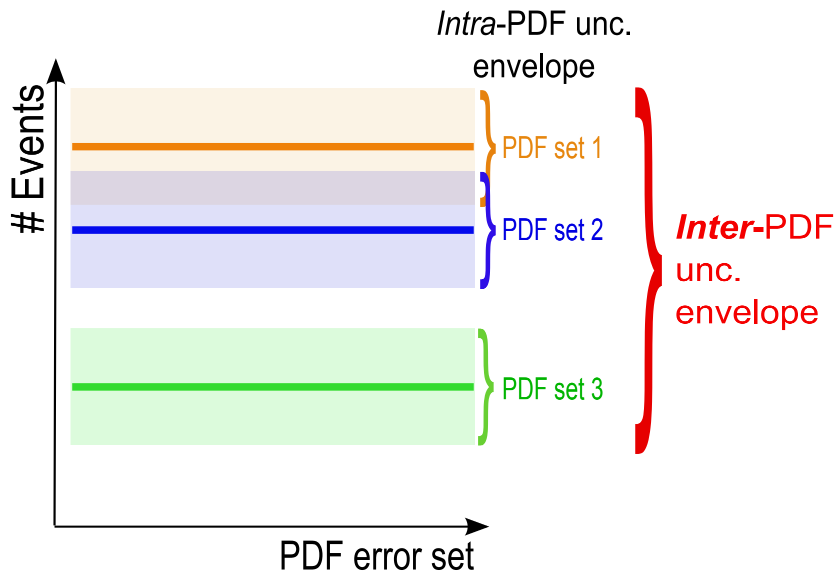

Figure 6.7: A simple illustration to demonstrate how the inter-PDF uncertainty is obtained from intra-PDF uncertainties from the three PDF sets. Half of the width of the inter-PDF uncertainty envelope is assigned as the final inter-PDF uncertainty.

The variation of the PDFs is carried out for every background prediction derived from simulation and for the chosen signal prediction. When the results from all background processes are combined, this PDF uncertainty affects both the shape and the normalisation of the reconstructed $t\bar{t}$ mass distribution. However, for certain processes listed below, only the *shape* of the distribution is permitted to change. The reasons for this are as follows:

- The W+jets background has a data-driven normalisation applied, as discussed in Section 5.1.1. This normalisation has an associated uncertainty which was specifically derived and is also discussed in the next section. Therefore, only the effect of the PDF uncertainty on the *shape* of the distribution, which is estimated using MC simulation, is considered here. This is done by applying the PDF variations, as described above, and then normalising the resulting distribution to the nominal expected yield after the data-driven normalisation has been applied.

- For the SM $t\bar{t}$ background, the PDF uncertainty is considered separately in the estimation of the effect on the SM $t\bar{t}$ production (NNLO) cross-section uncertainty, discussed in the next section. Like all cross-section uncertainties, this affects only the normalisation and not the shape of the distribution. Together with the standard procedure described above, the effect of the PDF uncertainty on *both* the shape and the normalisation of the distribution is accounted for. It is necessary to consider the effect of the uncertainty in two stages in this way because the normalisation uncertainty uses an NLO calculation whereas the shape uncertainty uses an NNLO calculation. The former would dominate the latter if both uncertainties were estimated simultaneously [199].

The overall PDF uncertainty affects the background yield by $3.1\ \%$, the signal yield by $1\ \%$ and the upper limit by a relatively small $0.2\ \%$.

6.3.2 Related to background determination

The background processes are determined via a mixture of MC simulation and data-driven techniques, depending on the particular process. Therefore, specific methods are required to estimate the systematic uncertainties associated with each background. These methods are detailed below. It is important to note that the uncertainties associated with a production cross-section affect only the normalisation of the distribution, whereas all other uncertainties can affect both the normalisation and the shape.

SM $t\bar{t}$ production

SM $t\bar{t}$ production has the largest contribution to the total background yield, at a level of just over $60\ \%$ as shown previously in Table 5.6. Hence, systematic uncertainties associated with a wide range of steps in the modelling process must be estimated.

The uncertainty on the production cross-section arises due to two classes of effects: first, due to the uncertainty on the PDFs. The level of this particular uncertainty is estimated according to the general procedure discussed above. In this case, the contribution due to the uncertainty on the coupling constant α_s of the strong interaction is not considered since it is considered to be sufficiently small relative to the PDF uncertainties [200]. The effect of the second contribution, due to the uncertainties on the renormalisation μ_r and factorisation scales μ_f, is estimated by independently varying each scale between $0.5\ m_t$ and $2\ m_t$, with the constraint of $0.5 < \mu_f/\mu_r < 2$. The envelope of the resulting cross-section is taken to be the total uncertainty due to the systematic effect from these scales. In this procedure, the uncertainty on the top quark mass is not considered.

The overall uncertainty on the $t\bar{t}$ normalisation is determined to be $^{+7.0\%}_{-9.6}$. This has a $4.9\ \%$ effect on the total background yield but a small ($0.7\ \%$) impact on the upper limit. Therefore, the current level of the uncertainty on the SM $t\bar{t}$ cross-section does not have a dominant impact on this search, compared to other sources of uncertainty.

The uncertainty on the fragmentation and parton shower procedures used by the default generator (HERWIG) is estimated by comparing to the results when using PYTHIA. In this case, both HERWIG and PYTHIA are interfaced to POWHEG [201], instead of to the default generator MC@NLO. The uncertainty on the generator used for the hard-scatting process is determined through comparison of the results using MC@NLO with an alternative (POWHEG). In both cases, HERWIG is used for the parton shower and fragmentation. All uncertainties associated with the parton shower, fragmentation and hard-scattering processes affect both the normalisation and the shape of the distribution. The largest impact on the sensitivity is due to the hard-scattering process and is relatively large (2.2 %).

The systematic uncertainty associated with the modelling of initial and final state radiation (ISR and FSR) has a relatively small impact (0.7 %) on the sensitivity. It is estimated by considering SM $t\bar{t}$ samples generated using ACERMC [202], with PYTHIA for the hadronisation. The amounts of ISR and FSR are varied by altering a number of the parameters of PYTHIA related to the Q^2 scale of the hard-scatter and to the α_s coupling constant. Details are provided in section 2.1.3 of [128].

W+jets production

The W+jets background contributes around 25 % of the total background yield across the entire $m_{t\bar{t}}$ region and 35 % for $m_{t\bar{t}} > 1$ TeV. Therefore the systematic uncertainties associated with its prediction must be estimated in detail.

The shape of this background is predicted using the ALPGEN generator but a data-driven normalisation is then applied to the yield. Therefore, the uncertainties associated with the generator are only permitted to affect the shape of the distribution and the uncertainties associated with the data affect only the normalisation of the distribution. Both are discussed in turn below, starting with the normalisation uncertainty.

The normalisation is performed by applying a multiplicative factor, known as the normalisation scale factor (SF), to the yield. These SFs were derived following a method described in Section 5.1.1. The nominal values of the SFs, together with the associated systematic and statistical uncertainties, are shown again in Table 6.4 for convenience.

The SFs derived in the normalisation region (NR) are the ones applied to normalise the W+jets yield. There are two sets of systematic uncertainties associated with these SFs.

Table 6.4: Scale factors derived for the data-driven normalisation of the W+jets background, denoted as NR, for "normalisation region". The calculation performed in the intermediate validation regions, VRX, and in the signal region, SR, are also shown. The first uncertainty is statistical and the second is due to systematic effects associated with the measurement of the particular SF.

Region	Electron channel	Muon channel
NR	$0.75 \pm 0.06 \pm 0.11$	$0.79 \pm 0.05 \pm 0.11$
VR1	$0.67 \pm 0.12 \pm 0.03$	$0.68 \pm 0.09 \pm 0.01$
VR2	$0.79 \pm 0.20 \pm 0.24$	$0.53 \pm 0.15 \pm 0.16$
VR3	$0.74 \pm 0.26 \pm 0.32$	$0.58 \pm 0.16 \pm 0.06$
SR	$0.88 \pm 0.34 \pm 0.27$	$0.48 \pm 0.27 \pm 0.18$

The first is the systematic uncertainty on the SF itself. The major sources of this uncertainty, together with the methods of estimation, are:

- The contributions from charge asymmetric processes to the yield measured in data. These contributions are subtracted using their estimation taken from MC simulation, or in the case of the QCD multijet background, using the data-driven estimation. For this purpose, a conservative $100\ \%$ uncertainty is assigned to the yields from each of these contributions. The SFs were then recalculated with this uncertainty applied. The resulting systematic uncertainty on the NR SF is 5.2 (2.2) $\%$ in the electron (muon) channel.

- The effect of the systematic uncertainty associated with the PDFs is propagated to the NR SF result by varying the PDFs as described in Section 6.3.1. This results in a systematic uncertainty on the SF of $5.2\ \%$ in both channels.

- The definition of the NR, given in Table 5.1, involves criteria placed on the p_T of the $R = 0.4$ and $R = 1.0$ jets. The values of these p_T thresholds are affected by the jet energy scale uncertainties. The thresholds are varied according to these uncertainties and the NR SF is recalculated. The SF uncertainty is found to be 7.9 (10.1) $\%$ in the electron (muon) channel.

- There is a final systematic uncertainty associated with the modelling of the W+jets production process performed by the ALPGEN generator. This is described below, together with the method of its estimation. It is found to have an effect on the ratio of positively to negatively charged leptons arising from W+jets production, of $+9$ ($+8$) $\%$ and -5 (-6) $\%$ in the electron (muon) channel.

All the above sources of systematic uncertainties were assumed to be uncorrelated. They are therefore added in quadrature to obtain the first part of the systematic uncertainty on the normalisation region SF.

The second part of the NR SF systematic arises from the fact that the SFs are applied to the yield calculated in the signal region, but derived in the normalisation region. To account for this, a "transfer" uncertainty is derived. As shown in Table 5.1, the definitions of the NR and SR differ in terms of the criteria applied to the fat jets: for the NR, the mass and $\sqrt{d_{12}}$ criteria are removed and the p_T threshold is lowered from 250 to 150 GeV. The transfer uncertainty is estimated by varying the fat jet p_T, mass and $\sqrt{d_{12}}$ variables within the levels of their uncertainties. The SFs are derived in the signal region with these variations applied and compared to the nominal SFs in the signal region. The SFs are found to vary by $\pm$ 0.27 ($\pm$ 0.18) in the electron (muon) channel as shown in the final row of Table 6.4.

The two parts of the systematic uncertainty associated with the NR SF, estimated above, are assumed to be uncorrelated. They are therefore added in quadrature, resulting in a final estimate of the SFs in the normalisation region of $0.75 \pm 0.06 \pm 0.11$ (17 $\%$ total uncertainty) in the electron channel and $0.79 \pm 0.05 \pm 0.11$ (15 $\%$ total uncertainty) in the muon channel.

The shape uncertainty associated with the W+jets' background is taken to be due to the uncertainty on the chosen values of the MC generator parameters. In Section 5.1.1 it was demonstrated that the ALPGEN MC simulation provides a good prediction of the shape of the reconstructed $t\bar{t}$ invariant mass distribution in the W+jets-dominated control region. This confirms what was found to be the case in a measurement of the pair production cross-section at ATLAS, which uses the same generator [203]. However, it is necessary to estimate the uncertainties surrounding the simulation of events with large invariant mass of the reconstructed $t\bar{t}$ pair. This is because such events are characteristic of those in the signal region of this search. Specifically, the effect on the shape of the reconstructed $t\bar{t}$ invariant mass distribution in the region $m_{t\bar{t}} > 2$ TeV must be studied.

The study is performed by mimicking the variation of key parameters in the ALPGEN generator, through modification of the relative contributions of the W+light-jets simulated sub-samples listed in Table 2.2. This method was originally proposed in [204], which also provides the correspondence between the parameter variations and the sub-samples' cross-sections. The parameters that are varied are listed below, together with their default and shifted values. Further details regarding these parameters can be found in the manual for the ALPGEN generator [146].

- `iqopt`, which is the functional form of the factorisation scale. The default form is $m_W^2 + \sum_{partons}(m^2 + p_T^2)$, where the sum is over all final state partons, including heavy quarks but excluding W boson decay products. It is varied "down", to m_W^2, and "up" to $m_W^2 + p_{T_W}^2$.
- `qfac` is a multiplicative factor applied to the factorisation scale. The default value is 1 and it is varied to 0.5 and to 2.
- `ktfac` is a multiplicative factor applied to the renormalisation scale. The default and varied values are as for the `qfac` parameter.
- `ptmin` is the minimum p_T of partons generated in the simulation of the matrix element process. This threshold is required so that the phase space region of jets generated by the matrix element does not overlap with those generated in the parton shower. The default is 15 GeV which is varied down to 10 GeV and up to 20 GeV.

Figure 6.8 shows the effect of the parameter variations on the reconstructed $t\bar{t}$ invariant mass distribution. The ratio of the distribution *with* a particular variation applied, to that with the default values of the parameters, are displayed. The distributions of all

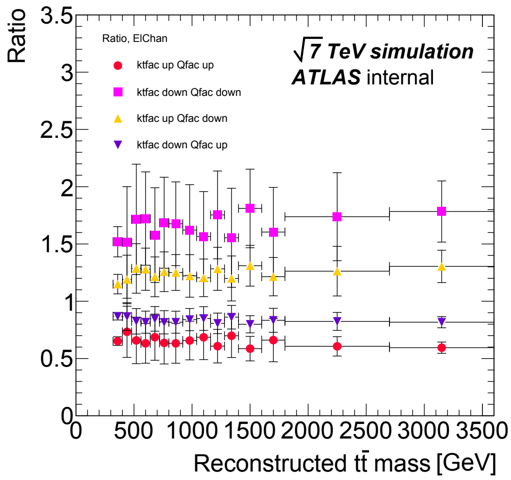

(a) Variations in `ktfac` and `qfac` (electron channel).

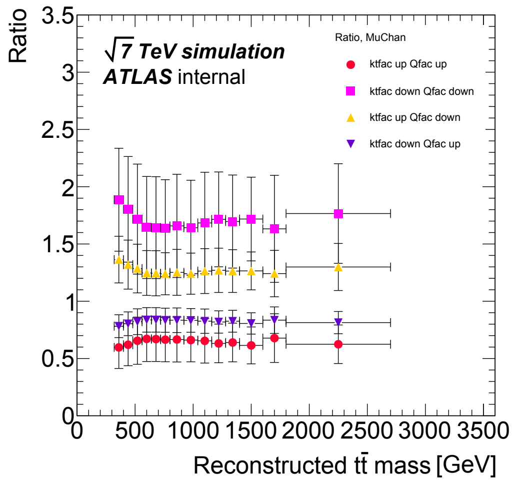

(b) Variations in `ktfac` and `qfac` (muon channel).

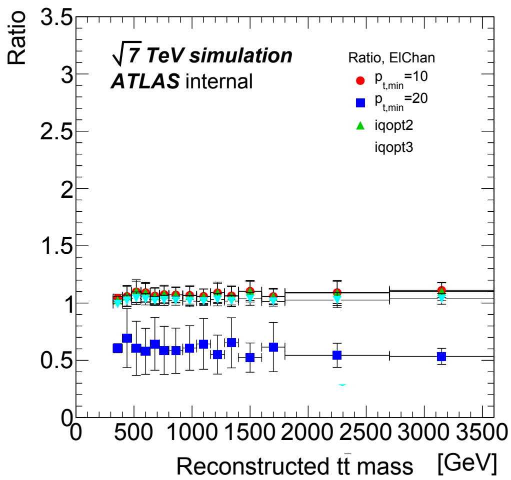

(c) Variations in `iqopt` and `ptmin` (electron channel).

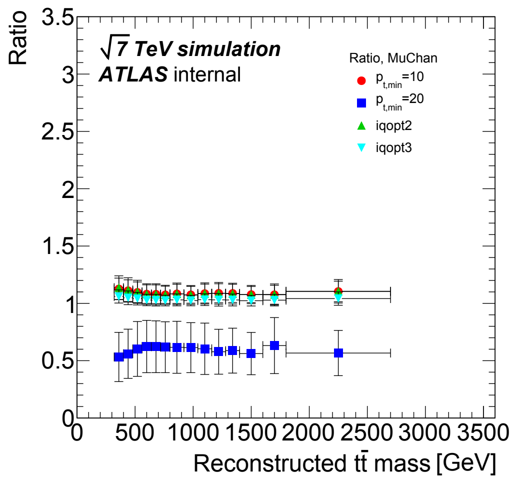

(d) Variations in `iqopt` and `ptmin` (muon channel).

Figure 6.8: Ratio of the reconstructed $t\bar{t}$ invariant mass distribution with key ALPGEN parameters varied, to that with default values of the parameters.

ratios are approximately flat, particularly in the region $m_{t\bar{t}} > 2$ TeV. An increase in the statistics would be needed in order to make a conclusive assessment. Many of the variations have a large effect on the normalisation of the $m_{t\bar{t}}$ distribution; that is, the values of the ratios are above 1.5 or below 0.7 in many cases. However, the normalisation uncertainty, detailed above, takes into account the uncertainty on the SFs due to this generator uncertainty.

The systematic effect associated with shape of the W+jets prediction is propagated to the final result by deriving a new reconstructed $t\bar{t}$ invariant mass distribution with each parameter varied as specified. Each distribution is normalised to the nominal distribution, with no variation applied, so that the uncertainty affects only the shape. The shape uncertainty is listed in Table 6.3 as "W+jets shape". "*norm.*" denotes the fact that this uncertainty has no effect on the normalisation and hence no effect on the background yield. The impact on the cross-section upper limit is very small (0.1 %).

QCD multijet production

The QCD multijet production background is derived using data-driven techniques as discussed in Section 5.1.2. Both the normalisation and the shape, together with their associated uncertainties, are estimated from data. The estimated yield due to the multijet production processes are again displayed in Table 6.5 for convenience. Both loose lepton definitions are also given in Section 5.1.2. The *Loose2* lepton definition was used to estimate the multijet yield because the associated systematic and statistical uncertainties are lower than for the *Loose1* definition. The method of estimating the uncertainties is detailed in this section.

Table 6.5: The yield of multijet events in the signal region, estimated using the data-driven matrix-method. Both statistical and systematic uncertainties are displayed. The yields with the *Loose2* definition are the ones used for the final estimation; the *Loose1* definition is used to estimate the resulting shape uncertainty associated with the matrix-method.

	electron	muon
Loose1	34.7 ± 4.8 (stat.) $\pm$ 7.3 (sys.) ${}^{+0.0}_{-29.5}$ (Z')	33.8 ± 3.4 (stat.) $\pm$ 7.9 (sys.) ${}^{+0.0}_{-33.8}$ (Z')
Loose2	49.1 ± 2.3 (stat.) $\pm$ 7.1 (sys.) ${}^{+0.0}_{-18.0}$ (Z')	29.7 ± 0.3 (stat.) $\pm$ 7.9 (sys.) ${}^{+0.0}_{-2.0}$ (Z')

The normalisation uncertainty results from the uncertainty on the yield. The *statistical* uncertainty is estimated by propagating the statistical fluctuations on the number of events with a tight lepton N_{tight} and the number of events with a loose, but not tight, lepton ($N_{anti-tight}$) through to the yield. The *systematic* uncertainty is estimated by propagation of the uncertainties on the false-identification rate f and the efficiency ε. The two parameters are randomly sampled around their measured values, in line with a Gaussian distribution whose width is given by the level of uncertainty on the parameter. Measurement of f and ε was discussed in Section 5.1.2; estimation of their systematic uncertainties is detailed below.

The systematic associated with f is estimated in two ways. First, by studying the precision of the simulated samples which are used in the subtraction procedure to obtain a multijet-dominated sample.[8] To do this, the following additional control regions (CR) are defined in which the contributions from each of the respective samples is dominant:

- The *top-CR* is equivalent to the first and third criteria from CR0. That is, the E_T^{miss} and $M_T(W)$ thresholds are recovered to be the same as in the signal region. Additionally, a b-tagged $R = 0.4$ jet is required in the event.
- The *W-CR* is equivalent to the top-CR above, except that a b-jet *veto* is now applied i.e. no events to contain a b-tagged $R = 0.4$ jet.
- The *Z-CR* is equivalent to the first and second criteria from CR0. However, the Z+jets veto from the third criterium is *inverted*.

Figures 6.9 demonstrate the consistency between data and simulation in the (a) top, (b) W and (c) Z control regions. This is for the muon channel only; the complementary figures for the electron channel can be found in [2]. Based on the observed level of consistency, a $20\ \%$ uncertainty is assumed on all of the simulated samples used in the subtraction from CR0.

The second source of systematic on f is due to the uncertainties associated with the variables used to define CR0. These are: the fat jet variables (p_T, mass and $\sqrt{d_{12}}$), the E_T^{miss} and the W transverse mass, $m_T(W)$. The thresholds on these variables are varied *exclusively* as follows, compared to the thresholds applied for CR0. f is recalculated with each variation applied and the resulting values of f are displayed in Table 6.6.

1. The fat jet p_T threshold is raised from 150 to $200\ \mathrm{GeV}$.

[8]This sample is obtained in "control region 0" (CR0), defined in Section 5.1.2.

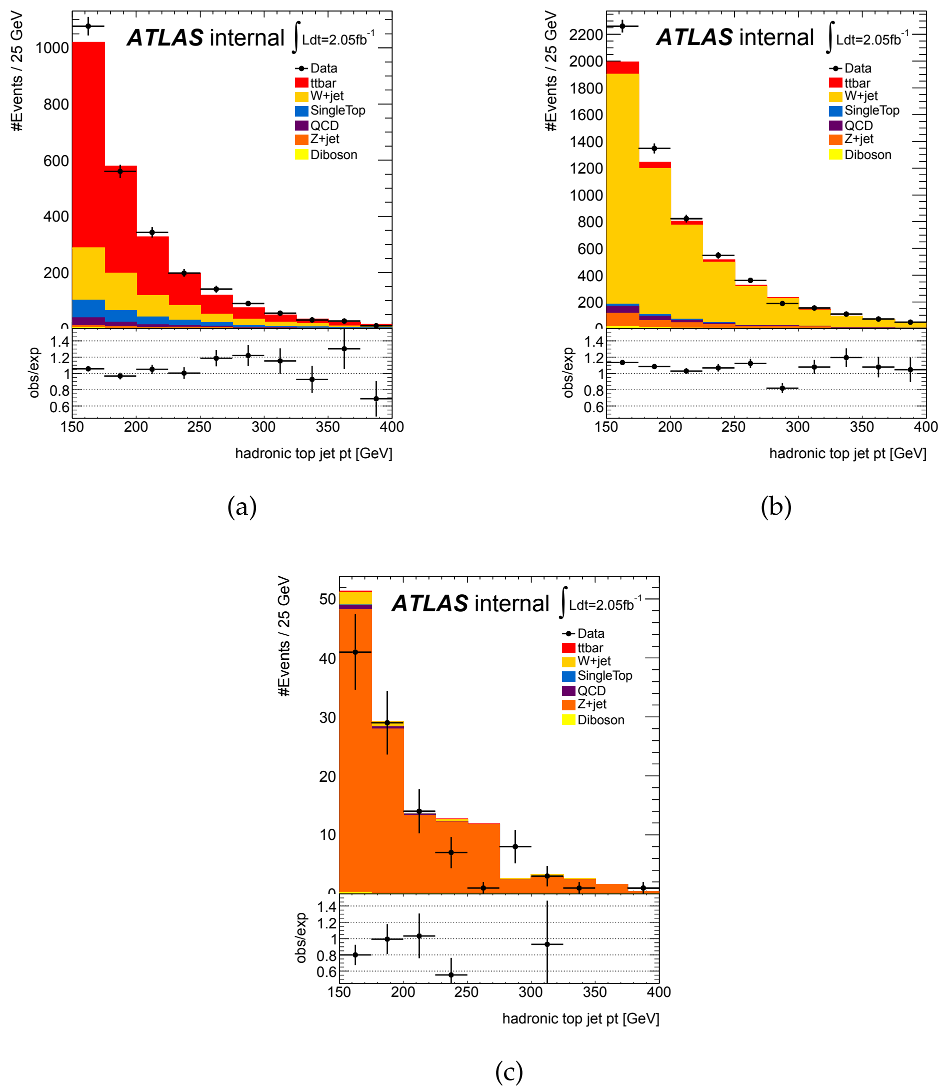

Figure 6.9: Comparison of events from data and from simulated estimations of backgrounds, in the control regions where the following prompt lepton sources are enhanced: (a) SM $t\bar{t}$ production, (b) W+jets production, (c) Z+jets production. The consistency between data and simulation supports the subtraction procedure used in the false-ID rate estimation. The consistency between data and simulation leads to the assignment of a $20\ \%$ uncertainty on the simulated samples used to estimate the false-identification rate systematic uncertainty.

2. A lower threshold on the fat jet mass is applied, resulting in the criteria: $100 > m_j > 50$ GeV.

3. A lower threshold on the fat jet $\sqrt{d_{12}}$ variable is applied, i.e. $40 > \sqrt{d_{12}} > 20$ GeV.

4. A lower threshold on E_T^{miss} variable is applied, resulting in $35 > E_T^{miss} > 17.5$ GeV.

5. A lower threshold on the W transverse mass is applied, i.e. $25 > M_T(W) > 12.5$ GeV.

Table 6.6: The false-identification rates measured in CR0 (column 2) and then with the thresholds on a particular variable adjusted as stated in the text (columns 3 – 7). The differences between the rates calculated in CR0 and the alternative regions are taken as part of the systematic uncertainty on the false-identification rate in CR0, whose total value is given in brackets. The first three criteria in the table are placed on the anti-k_T $R = 1.0$ jet collection.

	CR0 (syst.)	$p_T > 200$ GeV	$100 > m_j > 50$ GeV	$40 > \sqrt{d_{12}} > 20$ GeV	$35 > E_T^{miss} > 17.5$ GeV	$25 > M_T(W) > 12.5$ GeV
Loose1 e	0.209 (0.021)	0.210	0.202	0.208	0.197	0.211
Loose2 e	0.066 (0.010)	0.061	0.063	0.063	0.061	0.066
Loose1 μ	0.258 (0.056)	0.228	0.253	0.249	0.235	0.260
Loose2 μ	0.00395 (0.00161)	0.00264	0.00366	0.00374	0.00382	0.00373

The systematic uncertainty on f due to the application of each threshold is taken to be the difference between the f estimation in CR0 and with the amended threshold on that variable applied. These uncertainties are then combined into the final systematic uncertainty on the false-identification rates, which are listed in column 2 of Table 6.6 in brackets.

In Section 5.1.2, the nominal value of the efficiency ε was measured in collision data using a sample of well-reconstructed $Z \to ll$ events. It was also calculated using the simulated samples for SM $t\bar{t}$ production, W+jets production and Z+jets production. The maximum variation of ε between all these samples is taken as the first part of the systematic uncertainty on ε.

The fact that the value of ε as measured using a sample of 1.6 TeV leptophobic $Z' \to t\bar{t}$ events is much lower than that measured in the collision data[9] must also be taken into account. This is achieved by rederiving the multijet estimation using these lower values of ε; the variations in the yields are stated in Table 6.5 as a second systematic uncertainty, with the label Z'. An alternative method is also possible, whereby the nominal value of ε is shifted down to take account of the lower value in the BSM process compared to the SM processes. This requires the assumption of a certain cross-section for the BSM process. However, this strategy was not pursued because the search must remain

[9] Compare the first and final rows of Table 5.4.

model-independent and therefore a certain value for the cross-section cannot be assumed without biasing the multijet estimation towards a particular model.

To obtain the overall normalisation uncertainty on the final multijet estimation (using the *loose2* definition), the three separate uncertainties quoted in Table 6.5 are added in quadrature. It is therefore $40\ \%$ in the electron channel and $27\ \%$ in the muon channel, but a total uncertainty of $50\ \%$ for each channel is used for simplicity. There is a relatively small impact on the sensitivity ($0.2\ \%$) compared to the impact of the other systematic uncertainties.

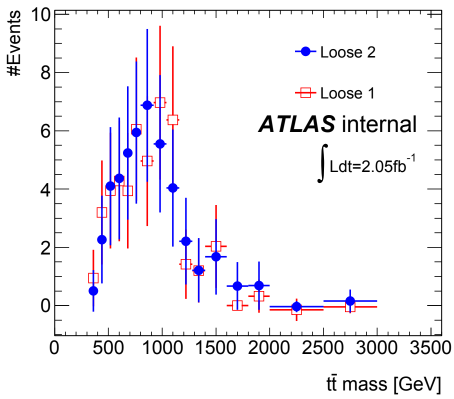

(a)

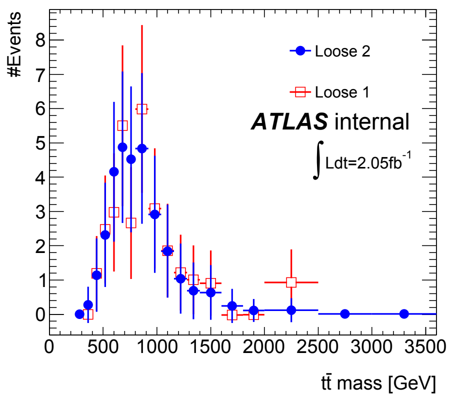

(b)

Figure 6.10: The reconstructed $t\bar{t}$ invariant mass distributions for the multijet background processes, derived from the data sample which is analysed in this thesis, using the matrix-method. Distributions are shown separately for the electron (a) and muon (b) channels. *Loose2* is the main definition used in the matrix-method. *Loose1* is an alternative definition used to derive the shape uncertainty associated with the multijet estimation. The distribution given by *Loose1* has been normalised to that of *Loose2*.

There is a systematic uncertainty associated with the shape of the reconstructed $t\bar{t}$ mass distribution due to the multijet estimation. It is estimated by considering the difference between the distributions when using the two loose lepton definitions, *Loose1* and *Loose2*; the two distributions are shown in Figure 6.10. Since this uncertainty affects only the shape, the distribution using the alternative *Loose1* definition is normalised to that obtained using the main *Loose2* definition. It can be seen from Figure 6.10 that the two definitions give distributions of equivalent shapes within the level of the statistical uncertainties. The resulting effect of the shape uncertainty on the upper limit for the cross-section is relatively small ($1.1\ \%$) compared to that for other systematic uncertainties, since the multijet-production background gives a relatively small yield.

6.3.3 Related to the minor backgrounds

The other backgrounds of Z+jets, single top quark and diboson production together contribute less than $10\ \%$ of the total background yield. Their yield is determined entirely from simulation and the associated systematic uncertainties are assumed to be due to the cross-section uncertainties only. Hence, there is only a normalisation uncertainty associated with these backgrounds, and no shape uncertainty.

The cross-section uncertainties are $\pm\ 48\ \%$, $\pm\ 10\ \%$ and $\pm\ 5\ \%$ for Z+jets [150], single top quark [145] and diboson production [145], respectively. As shown in Table 6.3, the uncertainty due to the Z+jets production has the largest impact on the background yield and sensitivity, at a level of $2\ \%$ and $0.5\ \%$ respectively. The cross-section uncertainties on the other two processes have a negligible effect on the background yield and sensitivity and they are therefore not included in Table 6.3. However, their cross-section uncertainties have been accounted for in the limit-setting procedure.

6.3.4 Related to the physics objects

There are almost fifteen systematic uncertainties associated with various properties of the physics objects used to reconstruct the $t\bar{t}$ system. These properties include the energy scale, energy resolution, identification efficiency and reconstruction efficiencies of the objects. The effects of each systematic uncertainty on the background yield, the signal yield and the upper limit are estimated. This is achieved by applying a $\pm\ 1\ \sigma$ variation to each property, then reapplying the entire event selection and obtaining a new reconstructed $t\bar{t}$ invariant mass distribution. The methods of estimation for these systematic uncertainties are now discussed in detail.

Jets are the physics objects whose systematic uncertainties have the largest effect on the background yield, signal yield and sensitivity. This is because they usually contain the majority of energy in the final state. In this analysis there are two jet collections; the leptonic top jet is taken from the anti-k_T $R = 0.4$ collection and the hadronic top jet is taken from the anti-k_T $R = 1.0$ collection. The following subsection is related to the collection of smaller jets; the larger jets are considered after that, together with a summary of the impact of all jet-related systematic uncertainties on the sensitivity.

Jets: anti-k_T $R = 0.4$

These jets are reconstructed from EM-scale topo-clusters and the jet is then calibrated to the jet energy scale, as described in Section 3.3.2. The *JES uncertainty* associated with this calibration is derived by combining information from in-situ measurements of the single-particle response and from single-pion test-beam measurements. Sets of simulated samples are also used that have variations applied to the material budget of the detector, to the electronic noise and to the MC modelling used for event generation. Finally, uncertainties due to the presence of "close-by" jets and knowledge of the jets' flavour composition are applied. A comprehensive explanation is given in [162].

Figure 6.3.4 displays the fractional JES uncertainty in a central region of $0.3 \leq |\eta| < 0.8$. The relative contributions of each component are also shown. The larger uncertainty for jets with $p_T < 50$ GeV is driven by the uncertainties in the modelling of soft physics processes by the MC generators (denoted by "ALPGEN + HERWIG + JIMMY" and "PYTHIA Perugia2010"). For high p_T jets, the increase is driven by the uncertainty associated with the single-particle calorimeter response studies. An absence of test-beam data for pions with $p_T > 350$ GeV means that a conservative uncertainty of 10 % was assigned to the energy measurement of these particles [162].

The uncertainties in *all* $|\eta|$ regions are summarised in Table 6.7. Soft jets in the region beyond $|\eta| = 2.8$ have a JES uncertainty of larger than 10 % and therefore no jets with $|\eta| > 2.5$ are used in this analysis. Approximately 75 % of the $R = 0.4$ jets present in the

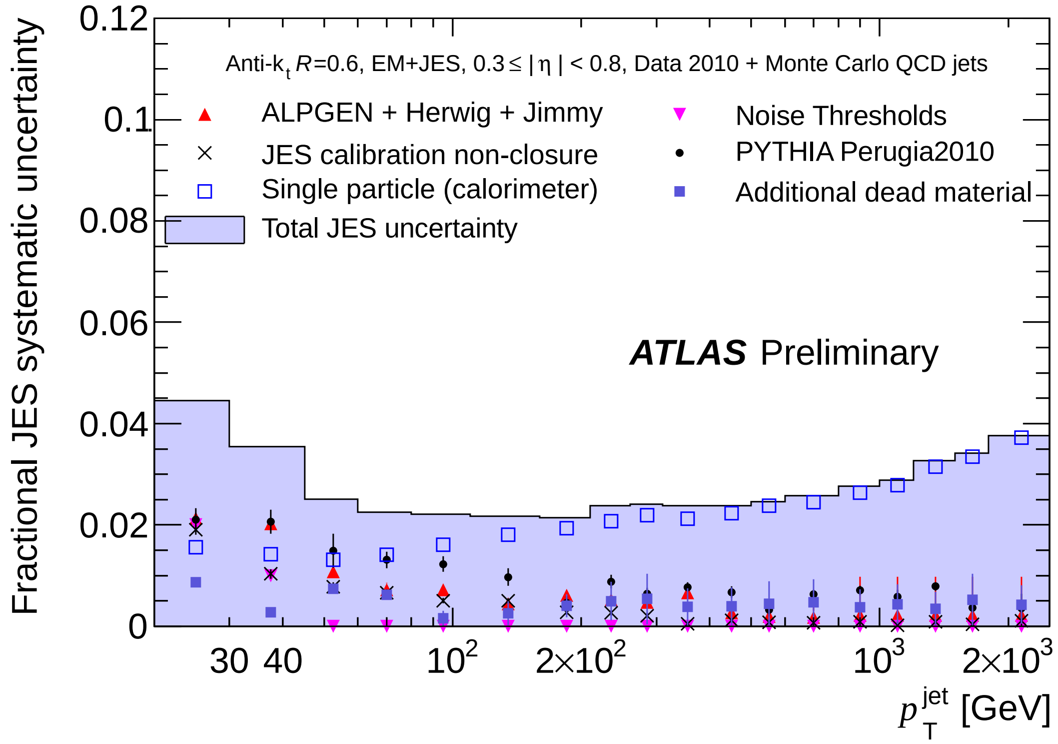

Figure 6.11: Fractional jet energy scale systematic uncertainty as a function of p_T for anti-k_T $R = 0.4$ jets in the region $0.3 < |\eta| < 0.8$. The shaded area represents the total uncertainty. Taken from [162].

signal region for this analysis have $|\eta| < 1.3$ and $p_T < 180$ GeV. Therefore, most $R = 0.4$ jets used in this analysis have a JES uncertainty of 4.3 % or less.

Jets that have been b-tagged are used in the definition of control regions for the data-driven background estimations. An additional JES uncertainty for these jets is estimated by considering effects due to the MC generator modelling, b-quark fragmentation, distortions in the calorimeter geometry and the calorimeter response. In the estimation of this uncertainty, a jet is assigned as a b-jet if it is within $\Delta R = 0.4$ of a B-hadron at truth level. The uncertainties are stated in Table 6.8. They are assumed to be uncorrelated with the main JES uncertainty and are therefore added in quadrature to it.

The jet energy resolution (JER) for anti-k_T $R = 0.4$ jets was measured using the first $1\ \text{fb}^{-1}$ of data collected in 2011. Two in-situ techniques were used, which are sensitive to different sources of systematic uncertainty. The JER measurement in data was found to match that in simulation to within 10 % for jets with $|y| < 2.8$. A description of the

Table 6.7: Summary of the maximum jet energy scale uncertainty for anti-k_T $R = 0.4$ jets at the EM+JES scale, in different p_T and η regions. Taken from [162]. This is added in quadrature to the main JES uncertainty, given in Table 6.3.4.

η region	Maximum fractional JES uncertainty (%)		
	$p_T^{jet} = 20$ GeV	$p_T^{jet} = 200$ GeV	$p_T^{jet} = 1.5$ TeV
$0 \leq \lvert\eta\rvert < 0.3$	4.1	2.3	3.1
$0.3 \leq \lvert\eta\rvert < 0.8$	4.3	2.4	3.3
$0.8 \leq \lvert\eta\rvert < 1.2$	4.3	2.5	3.5
$1.2 \leq \lvert\eta\rvert < 2.1$	5.2	2.6	3.6
$2.1 \leq \lvert\eta\rvert < 2.8$	8.2	2.9	
$2.8 \leq \lvert\eta\rvert < 3.2$	10.1	3.5	
$3.2 \leq \lvert\eta\rvert < 3.6$	10.3	3.7	
$3.6 \leq \lvert\eta\rvert < 4.5$	13.8	5.3	

Table 6.8: The b-jet energy scale uncertainty for a number of jet p_T bins. Taken from [205]. This is added in quadrature to the main JES uncertainty, given in Table 6.7.

p_T range [GeV]	b-JES uncertainty %
20 – 40	2.5
40 – 80	2.0
80 – 210	1.7
210 – 600	1.1
> 600	0.76

techniques can be found in [206], although the *values* from that study have been superceded by those in [207]. The latter values are used in the search presented here.

The JER obtained from simulated samples is corrected (or *smeared*) to match the value of the JER measured in data, which is $\approx 25\ (12)\ \%$ for jets with $p_T = 30\ (100)\ \mathrm{GeV}$ [208]. However, following a subsequent prescription from the ATLAS top working group, no smearing was performed on jets with $p_T < 15\ \mathrm{GeV}$ and it was reduced for jets having $15 < p_T < 70\ \mathrm{GeV}$; details of the implementation can be found in [209]. The resulting systematic uncertainty associated with the JER measurement is $\approx 8\ \%$ for jets with a p_T of $30\ \mathrm{GeV}$ and $4\ \%$ for jets with a p_T of $500\ \mathrm{GeV}$ [206].

The final systematic considered for these jets is that associated with the reconstruction efficiency. The central value is estimated from simulation by using a tag-and-probe technique in dijet events. In this method, *track jets* are formed by supplying reconstructed ID tracks to a jet algorithm. The hardest track jet is defined as the tag object and a second track jet, pointing in the opposite ϕ direction, is assigned to be the probe jet. The reconstruction efficiency is defined as the fraction of probe jets which are matched to a calorimeter jet[10], within a distance of $R = 0.4$. The systematic associated with this efficiency is estimated by varying the following event selection requirements: the minimum p_T of the tag object, the $\Delta\phi$ window in which the probe jet can be identified, and the matching distance between the probe jet and calorimeter jet. Details of this method are given in [113]. The systematic uncertainty is very small: 2% for jets with $p_T < 30\ \mathrm{GeV}$ and negligible for harder jets.

Jets: anti-k_T $R = 1.0$

These jets are formed from topo-clusters which have been locally calibrated as described in Section 3.3.2. The energy, η *and the mass* of the jets are all corrected back to the jet energy scale, as described in Section 3.3.2. The previously-described method to estimate the jet uncertainties are applicable only to anti-k_T $R = 0.4$ and 0.6 jets. In particular, it did not

[10] A calorimeter jet is formed from topo-clusters of energy deposited in the calorimeter.

encompass a correction to the jet mass. Hence, an alternative method is used to estimate all the systematic uncertainties associated with the jet energy scale and the jet mass scale (JMS) for these fat jets. The method used exploits the fact that the ID and calorimeter have mainly uncorrelated systematic effects. Therefore the contribution to the systematic uncertainties from detector effects can be separated out from that due to the modelling of hard physics processes.

The details of the method are as follows. Track jets are matched to calorimeter jets if they are within a distance of $\Delta R = 0.3$ of each other. The ratio r of a particular property related to a calorimeter jet to that of its matched track jet is formed:

$$r^X = \frac{X_{calorimeter-jet}}{X_{track-jet}} \tag{6.13}$$

where X denotes the property in question: jet p_T, jet mass m or jet $\sqrt{d_{12}}$. A *double ratio* ρ is then calculated for each variable, using r^X measured in data and r^X measured using MC simulation, as shown in Equations 6.14. The MC generator used in this case is PYTHIA v6.423 [131], with the Perugia2010 PYTHIA tune [210] since it has been found to describe jet shapes more accurately within the ATLAS experiment [211].

$$\rho^{p_T} = \frac{r^{p_T}_{data}}{r^{p_T}_{MC}} \tag{6.14a}$$

$$\rho^{m} = \frac{r^{m}_{data}}{r^{m}_{MC}} \tag{6.14b}$$

$$\rho^{\sqrt{d_{12}}} = \frac{r^{\sqrt{d_{12}}}_{data}}{r^{\sqrt{d_{12}}}_{MC}} \tag{6.14c}$$

The p_T, mass and $\sqrt{d_{12}}$ distributions are not expected to be perfectly modelled by the simulation. However, any difference in the modelling of hard physics processes are expected to approximately cancel in these ratios. Any deviation of ρ from unity therefore represents a mis-modelling in the simulation arising from *detector* effects only. The double ratios for jet mass and $\sqrt{d_{12}}$ are displayed in Figure 6.12 for a number of different generators. All anti-k_T $R = 1.0$ jets with p_T in the range 300 – 400 GeV have been considered. The double ratio obtained using PYTHIA is within 1 % of unity indicating that the detector effects have been well modelled by the simulation. This deviation is added in quadrature to the estimated 3 – 5 % systematic uncertainty on the ID measurements, to obtain the final uncertainties on the scale of energy, mass and $\sqrt{d_{12}}$. These uncertainties are stated in Table 6.9.

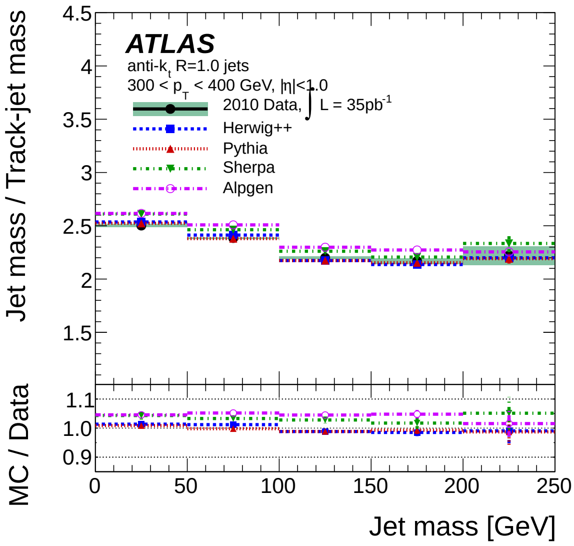

(a)

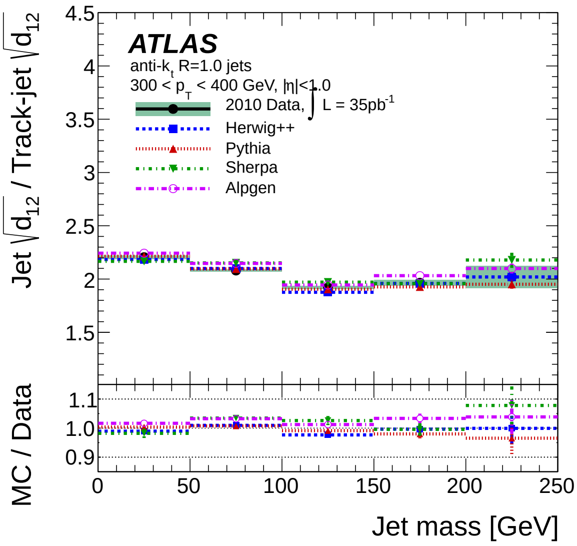

(b)

Figure 6.12: The ratio of (a) jet mass and (b) first k_T-splitting scale determined using the calorimeter to that determined using the inner detector. All jets with $300 < p_T < 400$ GeV have been considered. Ratios obtained from data and from a variety of MC generators are shown. The lower part of each subfigure provides a comparison between each MC generator and the data. Taken from [103].

Possible uncertainties due to different fragmentation and hadronisation models, are estimated by calculating the double ratios using the alternative generators HERWIG++ [212], SHERPA 1.2.3 [213] and ALPGEN 2.13 [146]. The double ratios obtained using all generators are also shown in Figure 6.12. ALPGEN and SHERPA exhibit the largest deviations of the ratio from unity and hence a poorer modelling of the detector effects. However, the discrepancy from unity is generally below the level of 5 %.

The uncertainties associated with the JER, JMR and $\sqrt{d_{12}}$ resolution are estimated using simulation only, primarily because the mass and substructure variable resolutions were difficult to validate in-situ with the dataset used [103]. The method uses simulated samples from the different generators listed above, together with a set of samples containing variations in the amount of detector dead material, in the hadronic shower model, in the fragmentation model and in the underlying event model. In general, the maximum deviations across all the samples is $20\ \%$, with a $30\ \%$ deviation when the ALPGEN samples are included. The JER for these larger jets as measured in the simulation is assumed to match that measured in data to within $10\ \%$, as for the smaller jets described above. The systematic uncertainties due to the variation in the simulations, and the difference between data and simulation, are added in quadrature to give the uncertainty on all resolution measurements as $\approx 20\ \%$. The specific values are listed in Table 6.9. Full details on the estimation of the fat jet systematic uncertainties can be found in [103, 104].

The method for determining these jet-related systematic uncertainties did not consider the effect of pile-up, which produces a background of relatively soft, dispersed energy deposits. The dependence of jet mass on the amount of *in-time* pile-up can be ascertained from studying the relationship between the average jet mass and the number of reconstructed primary vertices (N_{PV}).

As shown in Figure 6.3.4, the mass of *large* jets is particularly affected by in-time pile-up: a straight line fitted to the data points for each R value has a gradient of 3.0 ± 0.1 for large jets and less than a tenth of that value for $R = 0.4$ jets. The ratio of the slopes is in fact equal to the ratios of the jet R values to the third power, which is predicted by non-perturbative QCD (see section 2.3 of [214]).

Jet mass is a key variable used in the top-tagging procedure described in Section 4.1.4. Therefore, it should be corrected to account for the additional energy deposits due to pile-up. If this is not possible, an additional systematic uncertainty can be applied to the JMS in order to account for any potential mis-modelling of the pile-up. The former approach was chosen for anti-k_T $R = 0.4$ jets and is known as the offset correction, described in

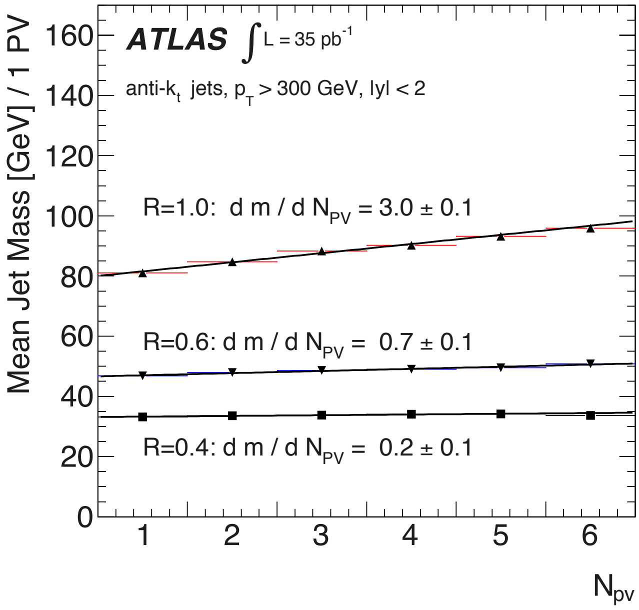

Figure 6.13: Mean mass of anti-k_T jets, having different radius parameters, as a function of the number of primary vertices. Taken from [103].

Table 6.9: Systematic uncertainties associated with kinematic quantities for the anti-k_T $R = 1.0$ jets, expressed as a percentage of the central value. Taken from [103].

Uncertainty	$200-300$ GeV	$300-400$ GeV	$400-500$ GeV	$500-600$ GeV
JES	4.0	5.2	6.0	3.9
JMS	4.5	4.5	6.0	6.0
JER	20.0	20.0	20.0	20.0
JMR	20.0	20.0	20.0	20.0
$\sqrt{d_{12}}$ scale	4.4	3.8	6.0	6.8
$\sqrt{d_{12}}$ resolution	21.0	22.0	28.0	31.0

Section 3.3.3. This was not possible for fat jets in the time available.

The method of estimating this additional pile-up uncertainty involved varying the average number of pp interactions, up one and then down one, for the SM $t\bar{t}$ simulated sample. The nominal value of $\langle\mu\rangle$ has been adjusted to closely match that in data, using the reweighting procedure described in Chapter 2. The effect on the yield of SM $t\bar{t}$ events was found to be ≈ 5 %, which is around half that due to the JMS uncertainty. Hence, the JMS uncertainty described above was augmented by 5 % to account for this additional pile-up uncertainty. Full details can be found in appendix A of [2].

The sample of jets, both simulated and collected from data, used in these studies is an *inclusive* dijet sample. That is, the resulting jets were initiated by gluons, light quarks, b-quarks but *not* top quarks. It is *assumed* that the uncertainties can be applied to jets containing the decay products of top quarks. However, the estimation of systematic uncertainties specific to these top jets is recommended for future analyses.

Summary of the impact of all jet systematics

The systematic uncertainties associated with the JES and JMS for both jet collections combined has a very large combined impact on the background yield (6.7 %) and on the sensitivity (5.2 %). In fact, this is the largest impact of all systematic uncertainties. The systematic associated with the jet energy and mass resolution also has a large impact on the background and signal yields (4.7 and 4.0 % respectively), although a moderate (≈ 1 %) impact on the sensitivity.

Leptons

All systematic uncertainties related to the leptons (energy scale, energy resolution, identification, reconstruction, isolation and triggering) are combined together when displayed in Table 6.3. The procedures for lepton reconstruction, identification, isolation and triggering were discussed in Chapter 3, together with the associated systematic uncertainties on the efficiencies, energy scales and energy resolutions.

The impact of the electron-related systematic uncertainties is rather moderate, at the level of around 1 % on both the background yield and the sensitivity. However, the muon-related systematic uncertainties have almost a 5 % effect on the sensitivity. This is driven by the systematic uncertainties related to muon reconstruction, identification and triggering which have impacts of 2.6, 2.2 and 2.1 % respectively [215]. The latter included a systematic uncertainty of 1.8 % to account for the fact that the object which fired the trigger could not be matched with the selected lepton in simulated events in the muon channel, as discussed in Section 4.1.1. This was added in quadrature to the systematic uncertainty associated with the muon trigger efficiency.

Missing transverse momentum

The systematic uncertainties associated with the E_T^{miss} are due to a number of sources. First, the uncertainties on the energy scale of energy deposits not associated with a physics object. These are the so-called `CellOut` and `SoftJet` terms described in Section 3.4. They arise due to discrepancies between the simulation and the processes occurring in the detector; for instance, the showering in the detector material, and the underlying event process.

Secondly, there is an uncertainty on the topo-cluster energy scale which directly forms the energy scale of the `CellOut` and `SoftJet` terms. The uncertainties on both terms are estimated in [170] to be at the level of $13.2\ \%$ and $10.5\ \%$ respectively. The two systematic uncertainties are assumed to be fully correlated since they arise from the same sources, and are therefore added linearly.

There is a third source of uncertainty due to the effect of pile-up modelling on the E_T^{miss}. The effect arising due to jets is included in the JES uncertainties above. For the `CellOut` and `SoftJet` terms, both the x and y components of the E_T^{miss} are shifted by $\pm 10\ \%$ to account for any mis-modelling.

The final uncertainty arising due to the E_T^{miss} estimation is associated with the LAr hole treatment. As described in Section 3.3.3, events with any anti-k_T $R = 0.4$ jet having $p_T > 20$ GeV and falling near the hole are rejected. This procedure contributes to the E_T^{miss} uncertainty since the energy of these jets cannot be measured neither accurately nor precisely. The degree of the effect is estimated by applying the JES uncertainty to the these jets and rerunning the procedure. A detailed discussion on the estimation of these systematic uncertainties can be found in [170]; their combined effect on the background yield and on the sensitivity is less than $2\ \%$ and $1\ \%$ respectively.

A final point to note is that the E_T^{miss} was recalculated after the application of the above systematic shifts which affected the energy of the physics objects, to take into account the uncertainties associated with these objects.

6.4 Summary

The final results of this search for $t\bar{t}$ resonances have been presented in this chapter, achieved through a comparison of the distributions for the invariant mass of the reconstructed $t\bar{t}$ pair taken from the background prediction and from data. The data is found to be in agreement with the standard model prediction and hence there is no evidence for BSM resonant $t\bar{t}$ production in this dataset. Upper limits are set on the cross-section times branching ratio for $t\bar{t}$ production for the two benchmark signal models: one wide and one narrow resonance. The strategy to reconstruct highly boosted top quarks, developed in this thesis, results in a significant improvement in the limits compared to those from previous ATLAS analyses in the lepton+jets channel. The observed limits are used to exclude the topcolor leptophobic Z' boson with mass between $600\ \mathrm{GeV}$ and $1.15\ \mathrm{TeV}$, and the Kaluza-Klein gluon with mass lower than $1.5\ \mathrm{TeV}$. The estimation of all associated systematic uncertainties has been presented, together with the method for their incorporation into the limit-setting procedure.

Chapter 7

Top quark reconstruction with jets of variable radius

7.1 Motivation

The main motivation for the introduction of jets with a *variable* value for the R parameter is to have a more flexible approach where, with the use of a single type of jet, the efficiency for selection of $t\bar{t}$ events can be maintained across a wide range of values of $m_{t\bar{t}}$. These jets are known as *variable-R* or *VR* jets.

The current strategy at ATLAS employs two different approaches: resolved and boosted, both introduced in Chapter 4. Each is tailored to the reconstruction and identification of events only within a particular range of $m_{t\bar{t}}$. To illustrate this, first consider the boosted approach which has been used for the search described in this thesis. The hadronic top quark is reconstructed using a large jet with $R = 1.0$. This assumes that the quark is sufficiently boosted that most of its decay products can be contained within a cone of radius 1.0. However, this will *not* be the case for top quarks produced with a p_T lower than 350 GeV: they will fail to meet the identification criteria and therefore the entire event will also fail to be selected.

The resolved topology is a more appropriate assumption for events containing these softer top quarks. This approach has been applied, using jets with a fixed value of the radius ($R = 0.4$), for all previous ATLAS $t\bar{t}$ resonance searches. A review of this "resolved-FR4" method was presented in Section 4.1.2, however, a crucial problem was highlighted there. That is, when the p_T of the hadronic top quark reaches approximately 300 GeV, its decay products become so collimated that three separate FR4 jets can no longer be reconstructed from these decay products. Since this situation is caused by an increasingly energetic parent top quark, the use of jets which decrease in size as the top quark becomes harder may enable the resolved topology to be preserved for top quarks with $p_T > 300$ GeV. This is the principle behind VR jets. The hypothesis is explored in Section 7.4 through comparison of the efficiency for selecting signal events using the resolved event selection with 1) $R = 0.4$ jets (resolved-FR4) and 2) VR jets (resolved-VR).

There is a region of phase space when the top quark has $300 < p_T < 350$ GeV in which neither the boosted nor the resolved-FR4 approaches are suitable for its reconstruction. The resolved-VR approach should be of particular use in this "transition region". Furthermore, the use of VR as opposed to FR4 jets should enable the reconstruction of top quarks with $p_T \gtrsim 350$ GeV: the VR jets decrease in size as the top quark p_T increases and hence can become closer together before merging into a single jet. There is, however, a limiting lower bound on the value of R due to the finite granularity of the calorimeter cells. This, in turn, places an upper limit on the p_T of the top quarks which can be reconstructed using resolved-VR.

Variable-R jets could also be used in conjunction with the boosted approach by reconstructing the top quark decay using a *single* VR jet. The parameters of the jet recombination would be such that a low p_T top quark would be reconstructed with a single large jet, rather than three jets. This jet would then reduce in size as the p_T of the top quark increases, down to the level that all the decay products are contained within a spatial region equivalent in scale to the calorimeter granularity. This strategy is not pursued in this thesis, but is recommended for further investigation since it has the potential to reduce additional energy deposits in the jet due to pile-up.

In this chapter, an investigation is carried out on the feasibility of the resolved-VR approach to improve the efficiency for selecting $t\bar{t}$ events. An increase in the efficiency would rely on the fact a greater proportion of events when using VR jets as opposed to FR jets contain the required number of jets to pass the event selection[1]. The subsequent *reconstruction* of the candidate top quarks and the $t\bar{t}$ system is also investigated across a wide kinematic range, to investigate if the use of VR jets could have additional benefits such as a reduction in the mass resolution of the reconstructed $t\bar{t}$ pair.

7.2 Variable radius jets

Jet reconstruction algorithms aim to combine energy deposits in the detector, to represent the flow of the energy carried by hadrons emerging from a collision. A detailed description was presented in Section 3.3. Therein, Equation 1.5a defines the size of the resulting jets through the value chosen for the radius parameter R. This is because the recombination of a particular jet ceases when the distance d_{iX} (which is proportional to R^2) becomes greater than the jet-jet distance d_{ij}.

In the vast majority of cases of jet reconstruction, and for all instances discussed in this thesis so far, R is a fixed number. Hence, jets with the same value of R are reconstructed with approximately the same size in η-ϕ space, regardless of their kinematic properties. VR jets, with a value of R that is inversely proportional to their p_T, arise by modifying Equation 1.5b to read as follows:

$$d_{iX} = p_{T_i}^{2n} R_{eff}(P_{T_i})^2 \tag{7.1a}$$

where

$$R_{eff} = \frac{\rho}{p_{T_i}} \tag{7.1b}$$

[1]Three or four jets are required for an event to pass the resolved selection, detailed in Section 4.1.2.

This causes the recombination for a particular jet to cease at a stage inversely proportional to the p_T of the i^{th} intermediate jet being considered at that particular stage of the recombination. Since the intermediate jet at the final stage of recombination then becomes the final jet, the p_T of the intermediate jet becomes the p_T of the resulting jet. Hence, the value of R_{eff} is inversely proportional to the p_T *of this final jet*. The choice of p_T, rather than some other kinematic measure such as the energy of the jet, is meaningful. It arises due to the environment of a hadron-hadron collider, where the partonic centre-of-mass frame is not equivalent to the laboratory frame hence requiring the use of boost invariant quantities such as p_T or η. In the following sections, the tailoring of VR jets to the reconstruction of high p_T top quarks is investigated. A full description of the VR approach is provided in [216].

It is important to note that the original motivation for VR jets was due to their property of having a uniform *angular* size (i.e. in θ-ϕ space) across all regions of the detector. While FR jets are indeed of constant radius in η-ϕ space, the nature of the η variable, defined in Equation 2.1, means that the angular size of these jets shrinks towards the forward region. However, one cannot simply define jets in θ-ϕ space since $\Delta S^2 = \sqrt{(\Delta\theta)^2 + (\sin\theta\Delta\phi)^2}$ is not boost invariant. The VR approach therefore maintains operation in η-ϕ space, but modifies the radius parameter of the jet recombination algorithm so that jets in the central region aren't inflated relative to their true physical size.

A considerable caveat to the applicability of VR jets is that the assumption of R scaling with the inverse of p_T is only valid for jets which originate from the same resonant state, such as the leptophobic Z' boson featured in these studies. This is because the value of $R_{eff} \times p_{T_i}$ for each jet is equivalent to $\Delta S \times E_i$ and the latter only holds for jets originating from the same resonance[2]. Hence the VR algorithm is not appropriate for the reconstruction of jets from ISR/FSR. The possibility of using a hybrid VR/FR algorithm in this case is discussed in [216]. It is not explored further here but it should be noted that VR jets

[2] $\Delta S \approx \Delta R/\cosh(\eta)$, and $E \approx p_T \cosh(\eta)$ for jets of low mass.

from ISR/FSR are present in the studies described here.

Implementation of VR jet reconstruction is via a `FastJet` plug-in, introduced in general terms in Section 2.3. Use of the term plug-in refers to the fact that VR is not a jet algorithm in itself, but an adaption that can be made to *any* of the three sequential recombination algorithms described in Section 1.4.1. The underlying algorithm used for these studies is anti-k_T, for consistency with previous studies. Furthermore, only jets with a lower p_T threshold of $7\ \mathrm{GeV}$ are produced by this `FastJet` implementation, which is well below the lower threshold applied to jets in $t\bar{t}$ resonance searches.

7.2.1 Choice of parameter values

The user must have control over the reconstruction of VR jets in two ways. First, in terms of setting an upper limit on the jet size. The reason for this is that the softer the jet constituents, the larger the resulting VR jet. Very soft constituents could lead to jets which encompass vast portions of the calorimeter, including un-instrumented areas. This is likely to result in a degraded jet energy resolution, together with a large dependence of the jets' kinematic variables on pile-up. Hence, the maximum possible value of the radius parameter (R_{max}) must be specified. The particular value chosen for R_{max} depends on whether top quark reconstruction with a single fat jet is required (the boosted approach), or several smaller resolved jets. As outlined above, the strategy explored here aims to retain the latter topology. Therefore, $R_{max} = 0.6$ is chosen for these studies.

The second user-defined parameter is ρ, which determines the *scale* of the dependence of R on p_T. Very hard constituents could result in *small* jets whose size may actually approach that of the constituents. The p_T of the jets which would be affected, is crucially dependent on the value of ρ and also on the size of the constituents.

In order to propose a reasonable value for ρ, the typical values of two key properties must be understood. First, the size of the inputs to the jet reconstruction. For these studies, jets are built from topo-clusters, described in Section 3.3. The advantage of using topo-clusters lies in the ability of the clustering algorithm to suppress the inclusion of calorimeter cells with significant noise. However, the size of some topo-clusters will be rather large compared to the granularity of the calorimeter cells.

To put this on a more quantitative basis, consider the granularity of the hadronic calorimeter and the current method of topo-cluster formation used at ATLAS. The typical calorimeter cell size is $\Delta\eta \times \Delta\phi = 0.1 \times 0.1$, as outlined in Section 2.2.3. However, topo-clusters can never be formed from a single cell: the clustering algorithm is seeded by cells with a signal to noise ratio (SNR) of 4, adds adjacent cells with SNR $= 2$ and then adds a ring of "guard" cells with SNR $= 0$. This leads to topo-clusters with a minimum size of $\Delta\eta \times \Delta\phi = 0.3 \times 0.3$, for a seed cell surrounded by a single layer of guard cells.

However, the third longitudinal layer of the central region in the hadronic (tile) calorimeter, is composed of cells with a coarser granularity of $\Delta\eta \times \Delta\phi = 0.2 \times 0.1$. Their inclusion would lead to topo-clusters with a minimum size $\Delta\eta \times \Delta\phi = 0.6 \times 0.3$. The effect of the "splitting" of cells which contain a number of local maxima, outlined in Section 3.3.1, will not be considered here since the simple discussion above gives an adequate guide to the minimum topo-cluster size, or "topo-cluster granularity", resulting from deposits in the *hadronic* calorimeter.

The finest topo-cluster granularity of $\Delta\eta \times \Delta\phi = 0.3 \times 0.3$ indicates that jets should not be reconstructed with $R < 0.2$. This of course is accompanied by the considerable caveats that a significant number of topo-clusters will be found in the third layer of the tile calorimeter and/or be composed of more cells than the nine proposed above. It is strongly recommended that further investigation of VR jets prioritises the study of such "small" jets.

This minimum R value of 0.2 sets an upper limit on the top quark p_T that could currently be reconstructed with the resolved-VR approach. To illustrate this, consider three adjacent jets having $R = 0.2$, such as might result from a hadronic top quark decay. For the resolved assumption to be valid, all of the decay products of the top quark should fall into a cone with a radius no smaller than approximately $0.2 \times 3 = 0.6$. If the decay

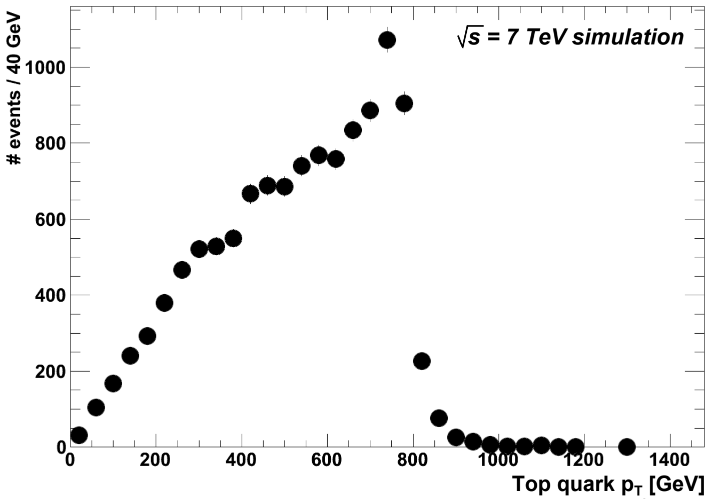

(a)

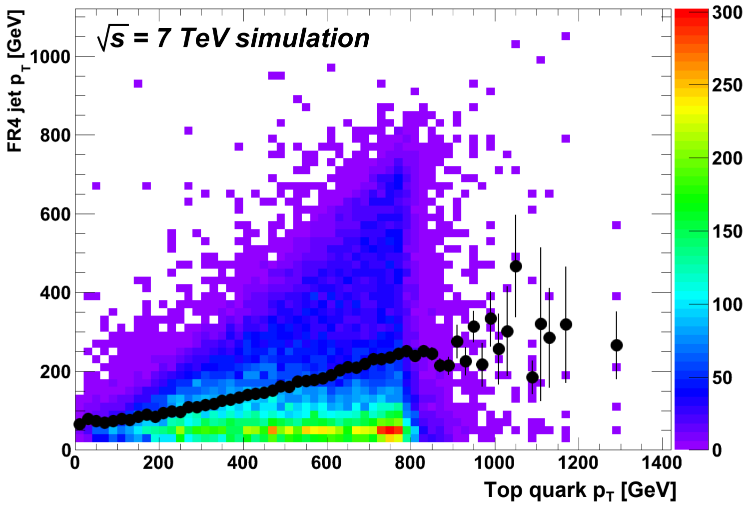

(b)

Figure 7.1: p_T of the top quarks, at truth level, in a sample of 1.6 TeV $Z' \rightarrow t\bar{t}$ events (a); and (b) the *relationship* between the top quark p_T at truth level and the p_T of the reconstructed FR4 jets. The resolved selection was applied, up to and including application of the E_T^{miss} and W transverse mass thresholds (i.e. no criteria involving jets were applied). However, the individual jets have a lower threshold of $p_T = 25$ GeV. The number of top quarks at each p_T value has an approximately linear dependence on the top quark p_T, up to the maximum defined by the kinematic threshold for top quark pair production. The mean p_T of all FR4 jets in the event is approximately one third of the top quark p_T, with the maximum being just under this value.

products are more collimated than this, a jet algorithm may fail to reconstruct three jets and hence the event would fail selection criteria. Using Equation 4.2, the upper limit on the hadronic top quark p_T is therefore ≈ 600 GeV. A $t\bar{t}$ resonance, such as a leptophobic Z' boson with a mass of 1.6 TeV, would decay to top quarks with p_T up to and beyond this value, as illustrated in Figure 7.1(a). This mass point lies just above the excluded region of the Z' mass obtained in the main search detailed in this thesis and therefore the 1.6 TeV $pp \rightarrow Z' \rightarrow t\bar{t}$ MC simulated sample described in Section 2.4.1 is used as the basis for these studies.

The second factor influencing the chosen value of ρ is the typical p_T range of the jets to be reconstructed. Bearing in mind the topo-cluster granularity outlined above, it is desirable for the hardest jets to be reconstructed with a size at least commensurate with this granularity, and no smaller. Figure 7.1(b) demonstrates the typical p_T range of jets versus the p_T of the parent top quark in the event. Although FR4, not VR jets, are displayed here, the results serve as a guide to the order of magnitude of the typical jet p_T. For the targeted events, with top quark p_T up to 600 GeV, the majority of FR4 jets have p_T up to 300 GeV. For VR jets having a p_T at this limit, Equation 7.1b determines that a ρ value of 60 GeV would result in jets being reconstructed with radius parameter 0.2. Hence $\rho = 60$ GeV is chosen for these studies.

7.2.2 Structure of variable radius jets

An η-ϕ map of the constituent topo-clusters for a set of VR jets is shown in Figure 7.2, together with that for FR4 jets. The jets are taken from the sample of leptophobic $Z' \rightarrow t\bar{t}$ events with $m_{Z'} = 1.6$ TeV. The distances in η-ϕ space between the topo-clusters and the jet axis are displayed and the distance to the peripheral topo-clusters indicates the size of the jet in η-ϕ space. Both maps are composed from the *four hardest* jets of each type in the event; the jet selection criteria, outlined in Section 3.3, have not been applied. The sample contains those events satisfying all criteria, up to and including the W transverse mass and E_T^{miss} criteria, of the resolved selection which was described in Section 4.1.2.

The expected decrease in size of the VR jets with p_T can be clearly seen in Figure 7.2(a) for jets with $p_T \gtrsim 100$ GeV; the chosen R_{max} value of 0.6 constrains the size of softer jets. The use of a value for R_{max} which is larger than the value of R for the FR jets results in the

VR jets having a minimum p_T of 20 GeV, whereas FR4 jets can be found with p_T as low as 7 GeV, the threshold for production by `FastJet`. At the upper end of the p_T distribution, VR jets with a $p_T \gtrsim 300$ GeV will have a size approaching the topo-cluster granularity. However, as shown from the maps, fewer than 1 $\%$ of the topo-clusters are affected by this. The lack of a dependence of jet size on jet p_T for the FR4 jets (Figure 7.2(b)) verifies that the recombination is working as expected.

The existence of a small proportion of clusters (< 1 $\%$, for either jet collection.) lying further from the jet axis than the value of the radius parameter, indicated by the black line, is to be expected: the radius parameter *does not* define the size of the jets in sequential recombination algorithms. Rather, it is used at each recombination stage to determine whether a constituent should be combined with another, or "set aside" as a final jet. At each step, the axis of the resulting jet will move and some of the peripheral constituents of the final jets may indeed be more distant from the jet axis than the scale of the radius parameter.

It is illuminating to investigate specific examples of this effect. Figure 7.3(a) shows an example of a jet ("Jet 1") which has three clusters with ΔR (cluster, jet axis) $> R_{max}$, shown enclosed by the brown ellipse. "Jet 2" by comparison, has all constituent clusters with $\Delta R < R_{max}$. In Figure 7.3(b), a similar situation for *FR* jets is demonstrated: "Jet" "1" contains three clusters having $0.50 < \Delta R$ (cluster, jet axis) < 0.55, i.e. more distant than the value of R of 0.4. "Jet 2" has all constituents lying closer to the jet axis than this. These peripheral constituents in Jet 1 are included at some stage of the recombination because they have neighbouring clusters within a ΔR distance of R_{max} (0.4) for the VR (FR) example.

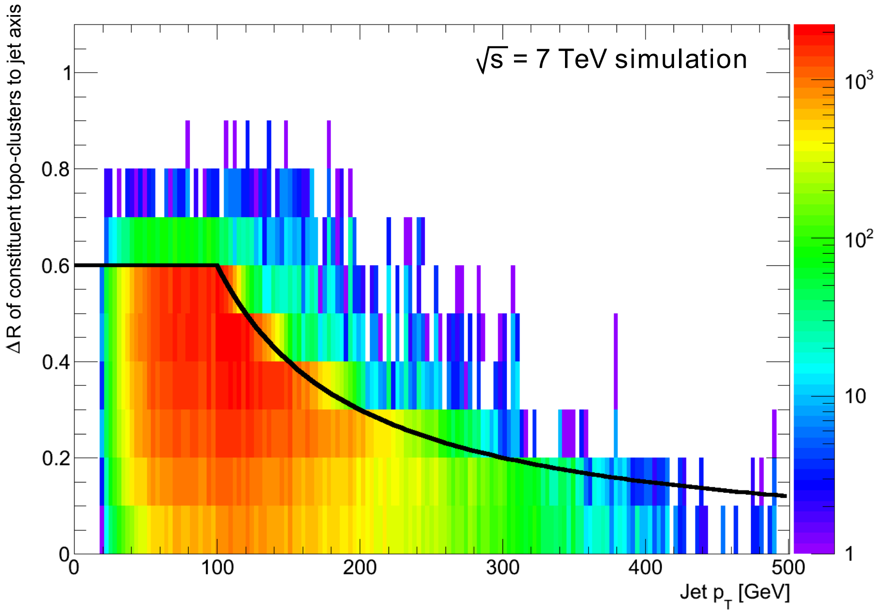

(a)

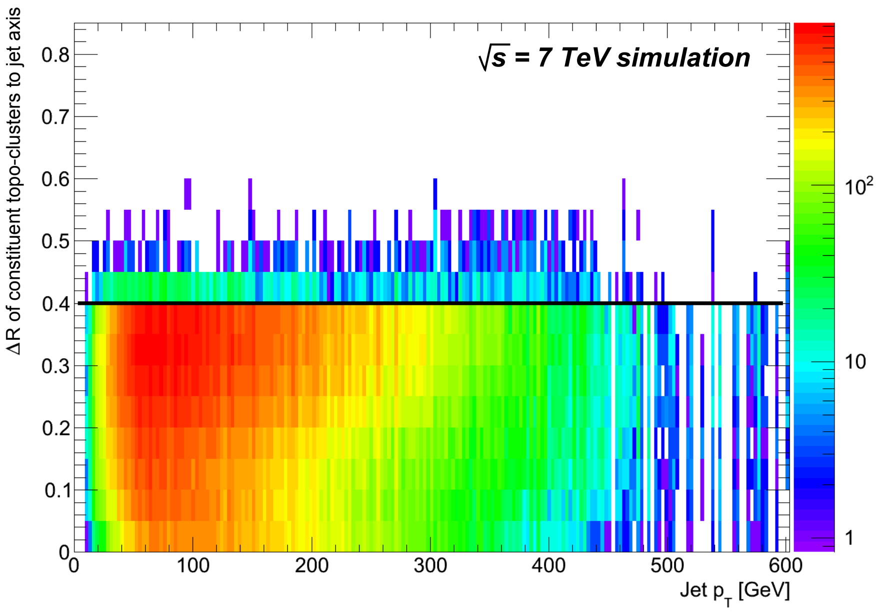

(b)

Figure 7.2: ΔR of constituent topo-clusters to jet axis, for (a) variable radius (VR) and (b) fixed radius (FR) jets as a function of the jet p_T. The colour scale represents the number of clusters in each bin. The black lines represent the radius parameter for the jet algorithm used, with settings of $\rho = 60$ GeV and $R_{max} = 0.6$ for VR jets. For both jet collections, the expected dependence of ΔR on p_T is observed. For either type of jet, a small proportion (< 1 %) of the constituent topo-clusters have ΔR greater than the value of R (i.e. they lie above the black line), as discussed in the text.

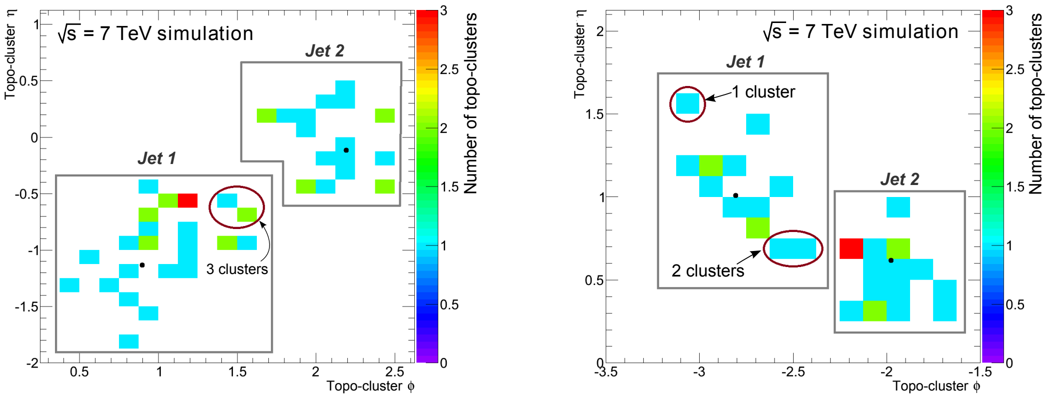

(a) (b)

Figure 7.3: Maps of constituent clusters, in η-ϕ space, for (a) VR and (b) FR jets which contain clusters with ΔR (cluster, jet axis) $> R_{max}$ (for the VR jets) or ΔR (cluster, jet axis) > 0.4 (for the FR jets). In both cases, these jets are labelled "Jet 1" and the peripheral clusters have been enclosed by ellipses. A second jet ("Jet 2") is included for comparison in both cases, which has *all* constituents within these circular boundaries defined by R_{max} or 0.4 respectively.

7.3 Application of variable radius jets to top quark reconstruction

This is the first documented use of VR jets for top quark reconstruction, to the best of the author's knowledge. Therefore the process used is thoroughly documented below.

The VR jets are produced specifically for these studies, using the `FastJet` plug-in outlined above. It is essential to validate this standalone implementation of `FastJet`: the jets reconstructed using this method must have the same properties as those reconstructed using the ATLAS software framework (the "ATLAS" jets). However in order to make a fair comparison, the two sets of jets must have the same level of calibration applied. There is currently no calibration procedure applied to the VR jets, therefore the effect of calibration must be *removed* from the "ATLAS" jets. This was only possible for the anti-k_T jet collection with $R = 1.0$.

Excellent agreement is observed between the p_T distributions for the "ATLAS" anti-k_T $R = 1.0$ jets and the corresponding ones made for these studies ("standalone"). The figure comparing the p_T distributions can be found in Appendix A and serves as a validation of this standalone implementation of `FastJet`. For this, and all subsequent instances of the standalone implementation, the jets are recombined from topo-clusters at the LC-scale with *positive* energy, to reduce the contribution from noisy cells.

7.4 Comparison of VR and fixed radius jets

The viability of using VR jets for $t\bar{t}$ reconstruction is assessed by comparing their performance relative to the most common jet collection used in ATLAS: anti-k_T $R = 0.4$ jets, previously introduced as FR4 [3]. There are a number of metrics that could be used for this comparison, such as the jet energy resolution or susceptibility to pile-up. It is important to study those comparisons before any jet collection can be used in an analysis of data. However, the studies conducted here instead seek specifically to understand if VR jets can improve the sensitivity to searches for high mass $t\bar{t}$ resonances. Hence, the metrics used are:

- The selection efficiency for signal events due to resonant $p\bar{p} \to Z' \to t\bar{t}$ production.
- The resolution of the mass of the reconstructed hadronic and leptonic top quark candidates in these events.
- The separation in $\eta - \phi$ space between the top quarks at truth level and the reconstructed candidates.
- The resolution of the invariant mass of the reconstructed $t\bar{t}$ pair. This is a particularly important metric since the hypothesis testing procedure described in Chapter 6 investigates the statistical significance of deviations in the $m_{t\bar{t}}$ distribution, from the SM prediction. Therefore, a particular deviation should have as small a width as possible.

[3] These jets were also made in the standalone `FastJet` implementation, so that the VR jets could be compared to *uncalibrated* FR jets.

The results of each comparison are presented in the following sections.

7.4.1 Selection efficiency for $Z' \to t\bar{t}$ events

To achieve this comparison, the event selection of the resolved approach is applied to the sample of $1.6\ \mathrm{TeV}$ leptophobic Z' bosons decaying to $t\bar{t}$, referred to in Section 7.2.1. Events containing fully hadronic or fully leptonic decays of the $t\bar{t}$ pair were rejected using information about the types of particles at truth level. The event selection was applied in the electron channel only.[4] A full description of the selection is given in Chapter 4 and the object selection criteria are detailed in Chapter 3. The "jet cleaning" of Section 3.3 was not applied here since the jet properties required to perform the cleaning have not yet been studied for VR jets.

Figure 7.4 shows the reconstructed $t\bar{t}$ invariant mass distributions, at truth level. In the upper part of the figure, the solid black line represents the distribution before the criteria involving jets are applied (hence the distribution is the same for both VR and FR jets). The dashed orange line and dotted blue line represent the distributions in the signal region using VR jets and FR jets respectively. In the lower part of the figure, the fractional change in selection efficiency when VR jets are used as opposed to FR jets is shown.[5] The use of VR jets is found to increase the selection efficiency, within the level of the statistical uncertainties, for all $t\bar{t}$ masses. Any possible dependence on $m_{t\bar{t}}$ would need a reduction of the uncertainties in order to investigate it further.

7.4.2 Top quark reconstruction and jet kinematic properties

To investigate the effect on the second metric, both the leptonic and hadronic top quark candidates must be reconstructed. This involves making a choice as to which jets to use in the reconstruction, from all those in the final state. As can be seen in Figure 7.5(a), there

[4] The studies were not performed in the muon channel due to time constraints. However, the results of the studies presented here are expected to be equally valid in the muon channel.

[5] The fractional change in efficiency is calculated as $\frac{\text{Efficiency using VR jets} - \text{Efficiency using FR jets}}{\text{Efficiency using FR jets}}$.

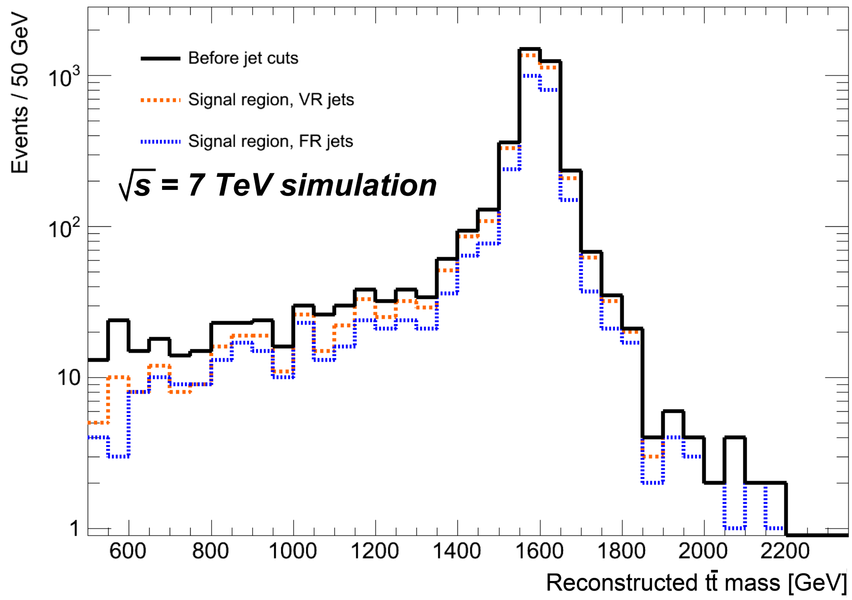

(a)

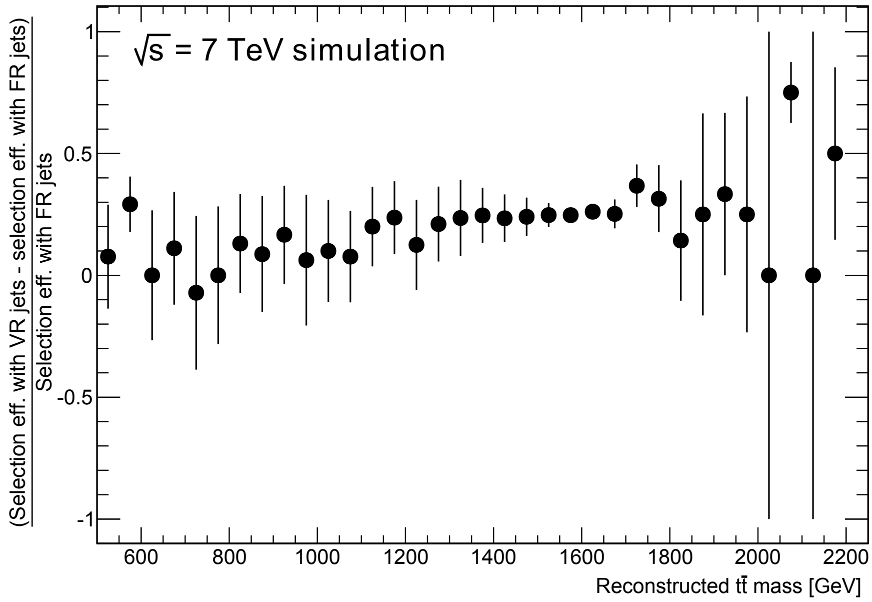

(b)

Figure 7.4: Reconstructed $t\bar{t}$ invariant mass distributions for 1.6 TeV $Z' \to t\bar{t}$ events (a) before application of the criteria involving jets (black line), and then in the signal region, using either VR (orange dashed line) or FR (blue dotted line) jets for the selection. The *change* in selection efficiency (b) when using VR jets compared to FR jets. The error bars represent the statistical uncertainty only. At the region centered around $m_{t\bar{t}} = 1.6$ TeV, the use of VR jets increases the selection efficiency by 20 % relative to the efficiency when using FR jets.

is a higher multiplicity of VR jets in each event, than FR jets. However, for *either* type of jet, approximately 50 (20) % of events in the signal region have more than four (five) jets in the final state. These can arise from a variety of sources such as ISR, FSR and the underlying event. In the published ATLAS search for $t\bar{t}$ resonances using the resolved approach [71], the contamination from such jets is reduced by rejecting jets which are "well-separated from the rest of the activity in the event". In this case of a high mass (1.6 TeV) resonance, one can assume a back-to-back topology for the decay products of the $t\bar{t}$ pair to a sufficient extent that: 1) the one jet from the leptonic top quark can be assumed to be that *closest* to the selected lepton,[6] and, 2) the jets from the hadronic top quark can be taken as those *furthest* from this lepton, with the additional requirements that they must have ΔR (lepton, jet) > 2.0 and must not already have been used in the leptonic top quark reconstruction.

Up to three jets can be proposed to constitute the hadronic top quark, although if three cannot be found, just the one or two jets satisfying the above conditions are used. This allows for the possibility of jet-merging amongst the hadronic top quark decay products, an issue first identified in the context of the resolved-FR4 in Section 4.1.2. There, it was proposed that the presence of a jet with mass greater than 60 GeV indicated that merging had taken place. In the case now under consideration, one can see from Figure 7.5(d) that there is a larger fraction (7.8 ± 0.2 %) of FR jets having $m_j > 60$ GeV compared to VR ($\lesssim 0.5$ %), with a peak in the FR distribution at approximately the W boson mass. This indicates that FR jets have indeed merged but VR jets have remained well separated.

Figure 7.6 shows the number of VR/FR jets constituting the hadronic top quark, versus the mass of the heaviest of these subjets. Indeed, the mass of the VR subjets is approximately stable with respect to the number of subjets used. However, if one or two FR jets are used to reconstruct the hadronic top quark, the heaviest of these has a mass indicative of the reconstruction of a W boson decay.

The resulting mass distributions for the reconstructed hadronic and leptonic top quark candidates can be seen in Figure 7.7, using either VR or FR jets in the reconstruction. For the hadronic top quark, there is a clear peak at ≈ 150 GeV when using either type of jet.

[6]The standard removal of the jet closest to the selected electron, and with ΔR (electron, jet) < 0.2, is still applied here. Details in Section 3.3.

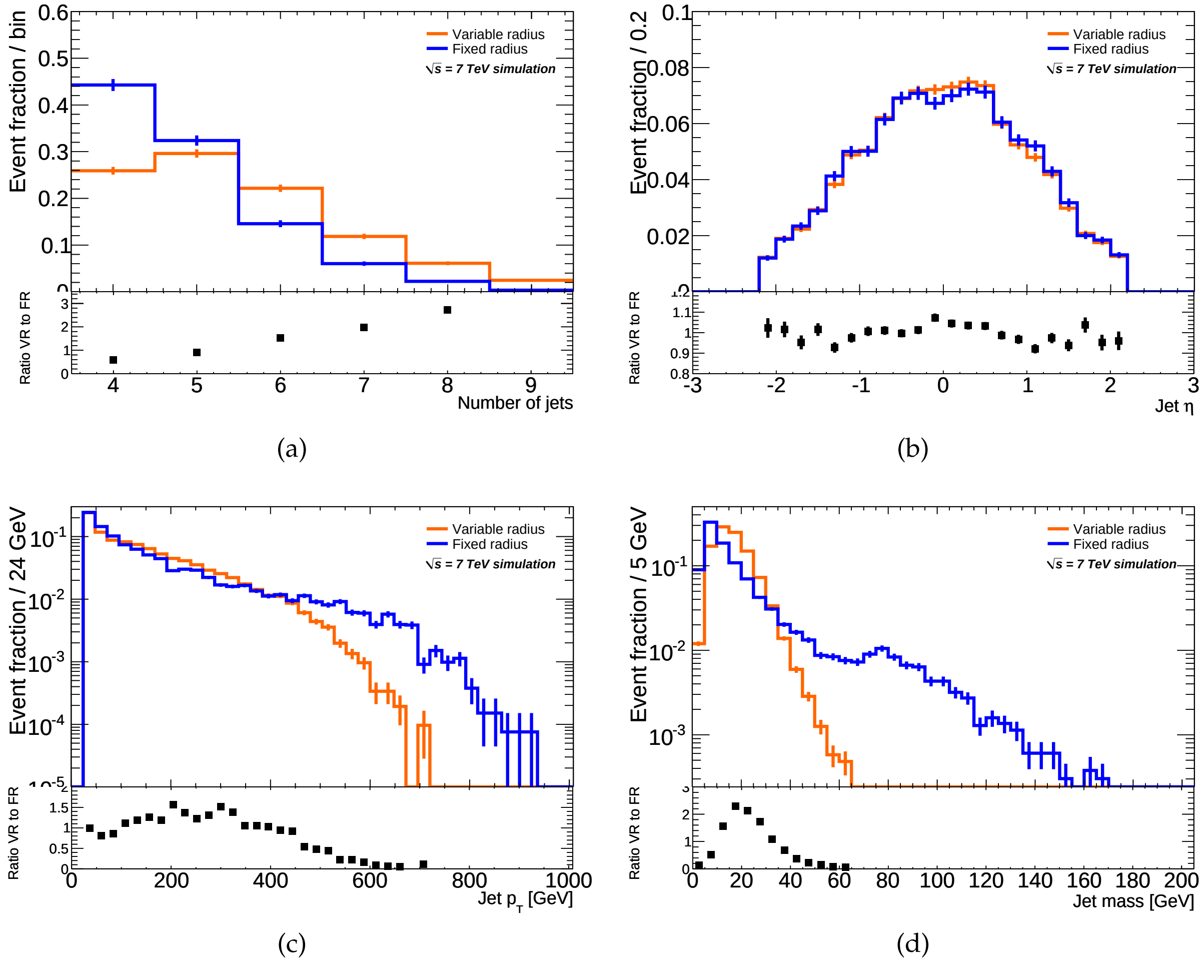

Figure 7.5: A comparison of the properties of VR (orange squares) and FR (blue circles) jets in the signal regions when using each type of jet (with $p_T > 25$ GeV). The mean jet multiplicity per event (a) is higher for VR than for FR jets. In (b) it is demonstrated that the η distributions for the two types of jet are approximately equal. The p_T distribution of VR jets (c) is somewhat harder than FR jets resulting in a smaller average jet size for VR jets. The largest difference in the distributions occurs for jet *mass* (d): 7.8 ± 0.2 % of FR jets have $m_j > 60$ GeV compared to $\lesssim 0.5$ % of VR jets. All histograms have been normalised to unit area and produced using the simulated sample of 1.6 TeV $Z' \to t\bar{t}$ events.

This falls short of that expected, given the top quark mass. However, it must be noted that neither the VR nor the FR jets have been calibrated to the jet energy scale.

Use of FR jets gives a more prominent tail at the high mass end of the distribution for the hadronic top quark mass. When reconstructed with FR jets, 44.5 ± 0.4 % of hadronic tops have $m_j > 200$ GeV, compared to only 29.0 ± 0.4 % when using VR jets. This is most likely due to the fact that more than a third[7] of VR jets are reconstructed with a radius

[7] 38 ± 0.1 % of VR jets have $p_T > 150$ GeV (Figure 7.5(c)) and hence are reconstructed with a radius

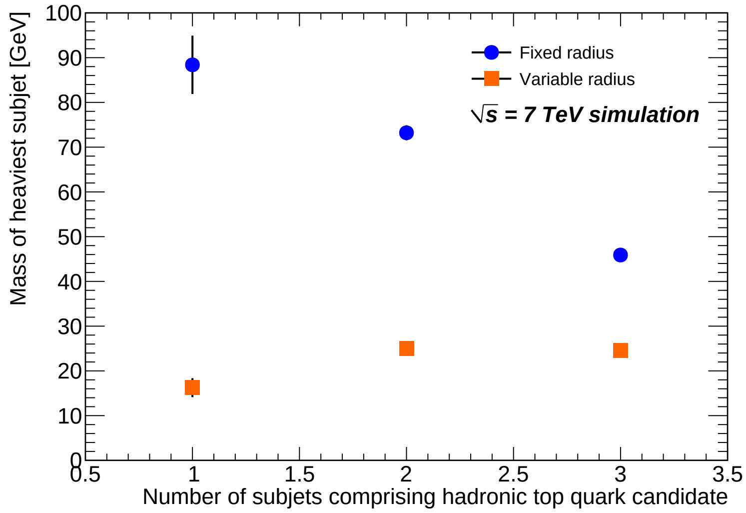

Figure 7.6: The number of constituent subjets of the reconstructed hadronic top quark candidates, versus the mass of the heaviest of these subjets, using both VR and FR jets. The presence of a high mass ($m_j > 80$ GeV) FR subjet, when fewer than three jets are used in the reconstruction, indicates that the hadronically decaying W boson is being reconstructed as a single jet. Produced using the simulated sample of 1.6 TeV $Z' \rightarrow t\bar{t}$ events.

parameter smaller than the 0.4 used for the FR jets. There are two main consequences of this. First, smaller jets have lower contamination by energy deposits due to pile-up. Second, they are also less subject to jet merging as shown above. However, caution must be exercised when using such small jets, to ensure that a sufficient proportion of the top quark decay products are being included in the jet recombination and therefore that the reconstructed top quark will pass any top-tagging criteria. This would require calibration of the VR jets to enable comparison of the reconstructed mass with the top quark mass.

Leptonic top quark reconstruction also results in a peak in the distribution at approximately the same mass as for the hadronic top quark mass distribution. However in this case the choice of jet collection appears to have a much smaller effect on the distribution. This is to be expected since the leptonic side of the $t\bar{t}$ decay has far less hadronic activity than the hadronic side, resulting in a much lower probability of the single leptonic top jet merging with other jets either from the decaying $t\bar{t}$ system or otherwise.

A further measure that can be used to assess the suitability of each jet collection for

parameter smaller than 0.4, if $\rho = 60$ GeV is used, as in this case.

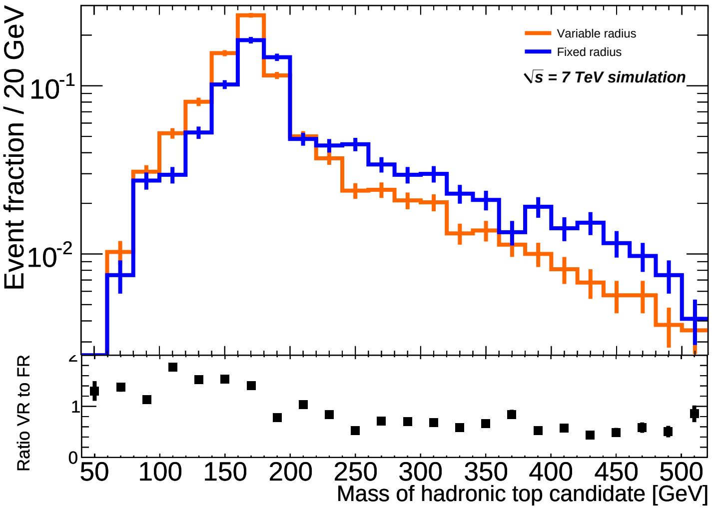

(a)

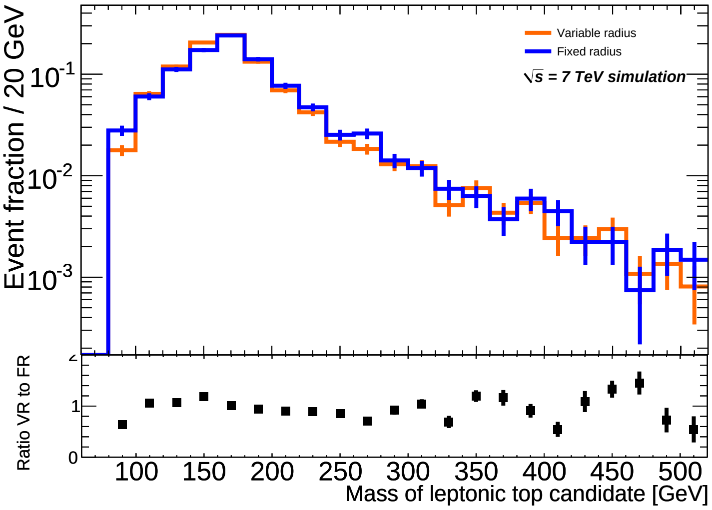

(b)

Figure 7.7: Reconstructed invariant mass distribution for (a) the hadronic and (b) the leptonic top quark candidates. In both cases there is a clear peak corresponding to the top quark. The distribution in the leptonic case is not affected by the type of jet used. However in the more challenging case of hadronic top quark reconstruction, where there are more constituent jets, the use of VR jets results in fewer tops in the high mass tail of the distribution (29.0 ± 0.4 %, compared to 44.4 ± 0.4 % for FR jets). All histograms have been normalised to unit area and produced using the simulated sample of 1.6 TeV $Z' \rightarrow t\bar{t}$ events.

top quark reconstruction, is the separation in η-ϕ space between the reconstructed top quark candidate and the true top quark at truth level. Figure 7.8 shows the distribution of ΔR between the reconstructed top quark candidate and the true top quark against the p_T of the true top quark. The performance is similar using either type of jet. There are indications that the use of VR jets may improve this “matching” between reconstructed

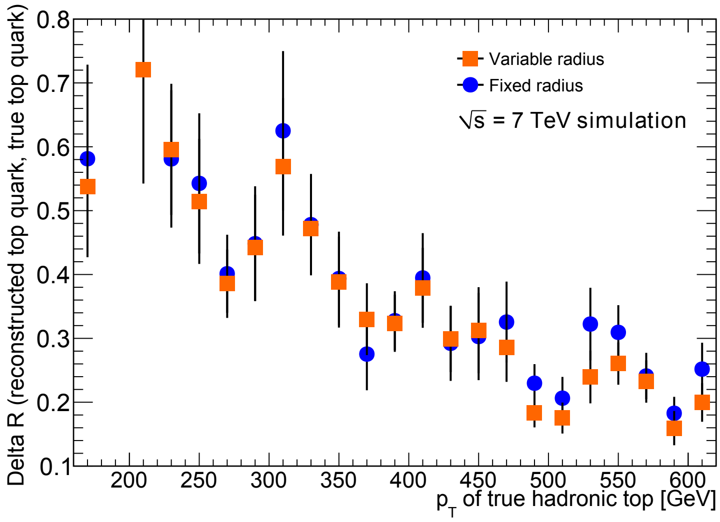

(a)

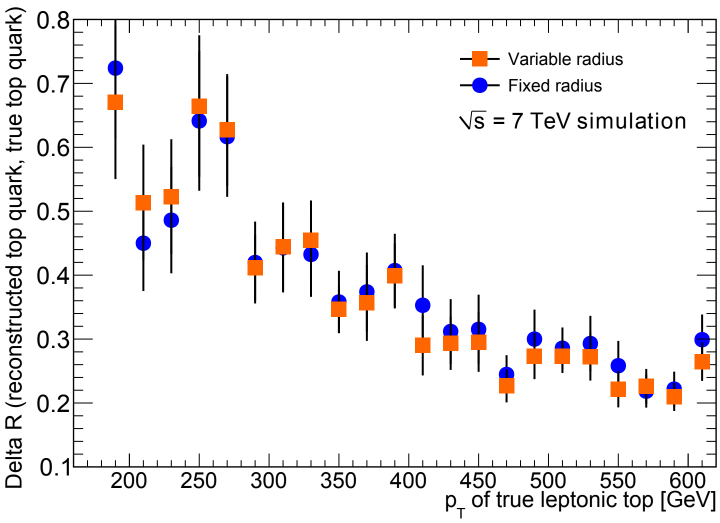

(b)

Figure 7.8: ΔR between the reconstructed top quark candidate and the true top quark for the (a) hadronic and (b) leptonic top quark candidates, as a function of the top quark p_T at truth level. The results using VR and FR jets are shown together for comparison, and indicate a slight improvement in performance when using VR jets, for top quarks with $p_T > 450$ GeV. For both types of top quark, and of jets, this "matching" of reconstructed to true top quark improves as the top quark becomes harder. Produced using the simulated sample of 1.6 TeV $Z' \to t\bar{t}$ events.

and true top quarks with $p_T \gtrsim 450$ GeV, although statistical uncertainties are dominating in this case. For both the leptonic and hadronic top quarks, and using either jet collection, the matching improves significantly as the top quark becomes harder. This is expected since the selection of jets for each top quark candidate inherently assumes a back-to-back event topology, which is more typical of boosted top quark pairs.

7.4.3 $t\bar{t}$ invariant mass reconstruction

The final test in the comparison of $t\bar{t}$ resonance searches using either VR or FR jets is the reconstruction of the $t\bar{t}$ system, in terms of the resolution of the invariant mass distribution. Figure 7.9 shows the results using both types of jets, in their respective signal regions. The upper part of the figure displays the mass distribution for the reconstructed $t\bar{t}$ pair. The peak in the distribution falls in approximately the same place using either type of jet. This is somewhat lower than that observed in the ATLAS $t\bar{t}$ resonance using the resolved approach [71], although it should be stressed that the jets used in these VR/FR studies are *not* calibrated to the jet energy scale.

The lower part of Figure 7.9 illustrates the fractional difference between the mass distributions at reconstruction level and at truth level. For both types of jets, a Gaussian distribution has been fitted to the upper part of the distribution; the tail of the lower half is not expected to be Gaussian in shape due to radiative losses from lower energy events. It is found that the width of the distribution using VR jets is 0.087 ± 0.004 and the width using FR jets is 0.105 ± 0.005. Therefore the width when using VR jets is 83 ± 6 % of that when using FR jets. This demonstrates that a significant improvement in the mass resolution of the reconstructed $t\bar{t}$ system is possible when using variable-R jets.

7.5 Summary

The use of jets which decrease in size as their transverse momentum increases has been investigated in this chapter. The potential of using these variable-R jets in $t\bar{t}$ resonance searches is highlighted, by means of a number of metrics. The efficiency for selecting signal events is found to increase by up to ≈ 20 % when using variable-R jets as opposed to the standard jets of fixed R value. Furthermore, the mass distribution for the reconstructed hadronic top quark candidate demonstrates a significant reduction in the fraction of candidates with $m > 200$ GeV. The final, key metric used is the resolution of the

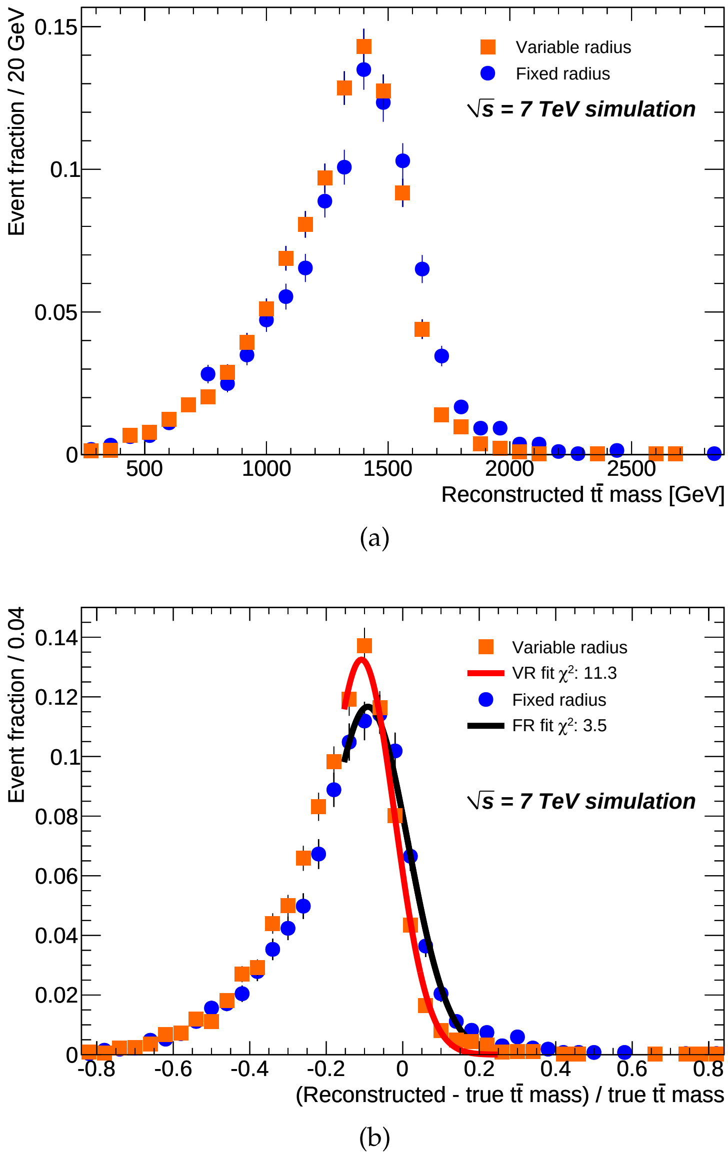

Figure 7.9: The invariant mass of the reconstructed $t\bar{t}$ system (a), using both VR and FR jets, together with (b) the difference between the reconstruction and truth level distributions. With a fit of a partial Gaussian to the latter, the width of the distribution using VR jets is $83 \pm 6\ \%$ of that using FR jets. This indicates an improvement in the resolution of the reconstructed $t\bar{t}$ mass through the use of VR jets. All histograms have been normalised to unit area and produced using the simulated sample of $1.6\ \mathrm{TeV}\ Z' \rightarrow t\bar{t}$ events.

reconstructed $t\bar{t}$ invariant mass. Variable-R jets enable a improvement in the resolution, which is almost $80\ \%$ of the resolution when using fixed-R jets.

The parameters of the variable-R jet reconstruction have been tailored towards the use of the resolved approach to top reconstruction, with a consideration of the finite granularity of the ATLAS calorimeters. However, variable-R jets could also be used in conjunction with the boosted approach i.e. a single variable-R jet to reconstruct the top quark candidates. Further investigation of this, together with the calibration of these jets, is recommended for future studies.

Chapter 8

Conclusions and outlook

The standard model encompasses all matter and interactions in our known universe and has proved robust against decades of stringent testing. However, it has a number of shortcomings. Of primary concern is a lack of explanation for the hierarchy of fermion masses, which is dominated by the top quark. In spite of this, the mystery of the top quark can be turned to our advantage; if the standard model provides no explanation for the mass hierarchy, then the top quark could be intimately connected to previously undiscovered, beyond standard model, processes.

There are a variety of studies which seek to probe this connection; the approach of this thesis is to search for proposed new particles which predominantly decay to a top and an antitop quark ($t\bar{t}$) pair. Searches at the Tevatron collider did not find evidence for such $t\bar{t}$ resonant states. However, the Large Hadron Collider at CERN provides a long-awaited opportunity to extend this search, at a centre-of-mass energy and luminosity far in-excess of anything previously achieved. This study uses the first $2.05\ \mathrm{fb}^{-1}$ of pp collision data collected at $\sqrt{s} = 7\ \mathrm{TeV}$ with the ATLAS detector. The search is carried out in the lepton+jets final state of the $t\bar{t}$ decay.

The invariant mass of the reconstructed $t\bar{t}$ pair in all selected data events was compared to the standard model prediction. There was no evidence for any statistically significant deviations of the data from the background prediction, in this particular dataset.

Upper limits were set on the production cross-section times branching ratio to $t\bar{t}$ pairs, at the $95\ \%$ credibility level, for two specific models of new physics: the narrow leptophobic topcolor Z' boson and the wide Kaluza-Klein gluon. The observed upper limits for the Z' (g_{KK}) with $m = 1$ TeV were 0.61 (0.65) pb^{-1}. This represents a great improvement on the previous ATLAS search for $t\bar{t}$ resonances in the lepton+jets channel, using the same dataset: the observed upper limits in that search were 2.4 and $2.9\ \mathrm{pb}^{-1}$ for the two models, respectively, at the same mass point.

The results of this search enabled the exclusion of the leptophobic Z' boson with mass in the range $0.6 < m_{Z'} < 1.15$ TeV and of the KK-gluon with $m_{g_{KK}} < 1.5$ TeV. The result for the KK-gluon is equivalent to a contemporaneous result from the CMS experiment, which analysed over twice the amount of data compared to this search. The previous result from the ATLAS experiment excluded substantially smaller mass regions:
$m_{Z'} < 880$ GeV and $m_{g_{KK}} < 1.13$ TeV.

Such an improvement was made possible by the development of a strategy to identify and reconstruct highly boosted top quarks. A *single large jet* was used for the reconstruction of the hadronically decaying top quark; the presence of a top quark was then determined by investigation of the mass and internal substructure of this jet. This enabled the reconstruction of highly boosted top quarks, which could not be reliably reconstructed using previous methods. This thesis documents the first application of jet substructure techniques in $t\bar{t}$ resonance searches using collision data. The approach could be yet further improved by also reconstructing the *leptonically* decaying top quark using a single large jet which has a lepton embedded in it. This will require improvements to the treatment of such non-isolated leptons, and is left to future studies.

An alternative strategy for reconstructing and identifying highly boosted top quarks has been developed in this thesis. This involves the use of a completely different type of jet which decreases in size as its transverse momentum increases, as opposed to standard jets which are fixed in size. This is the first documented use of these variable-R jets for analyses involving top quarks. The aim is to maintain the association of a jet to each of the partons resulting from the top quark decay as the transverse momentum of the top quark increases. This is achieved by allowing the jets to shrink in size and hence become closer together. The kinematic and spatial properties of the variable-R jets was studied in a sample of simulated $t\bar{t}$ events. This demonstrated that these jets are less subject to merging together than jets which are fixed in size and therefore indicated their potential for the reconstruction of highly energetic top quarks. The efficiency for selecting $t\bar{t}$ events and the resulting mass resolution of the reconstructed $t\bar{t}$ system were also studied. The use of variable-R jets was shown to be beneficial on both counts: in particular, the mass resolution was improved by almost $20\ \%$ compared to when using fixed-size jets.

An extension of the study of variable-R jets is recommended on a larger sample of $t\bar{t}$ events, in order to reduce the statistical uncertainties. A detailed understanding of the jet properties is also recommended so that the jets can be calibrated and any effects of pile-up can be determined and mitigated for. The effect of the finite granularity of the calorimeter on the properties of small jets is also recommended for further study. The variable-R jets could be combined with the strategy of jet substructure analysis, leading to the reconstruction and identification of the top quark decay using a single variable-R jet with an investigation of its substructure.

In summary, this thesis represents a range of work carried out to increase the sensitivity to new physics processes which result in massive top quark resonances. This improvement has been demonstrated using the first set of data collected by the ATLAS detector at $\sqrt{s} = 7\ \mathrm{TeV}$. The potential of a new type of variable-sized jet has also been illustrated, which could open up a rich new branch of strategies for the identification and reconstruction of highly energetic top quarks.

Appendix A

Standalone FastJet implementation

The figure below serves as a demonstration that the standalone implementation of `FastJet`, used in the variable-R jet studies of Chapter 7, reproduces an equivalent jet collection for anti-k_T $R = 1.0$ jets as does the ATLAS central-production.

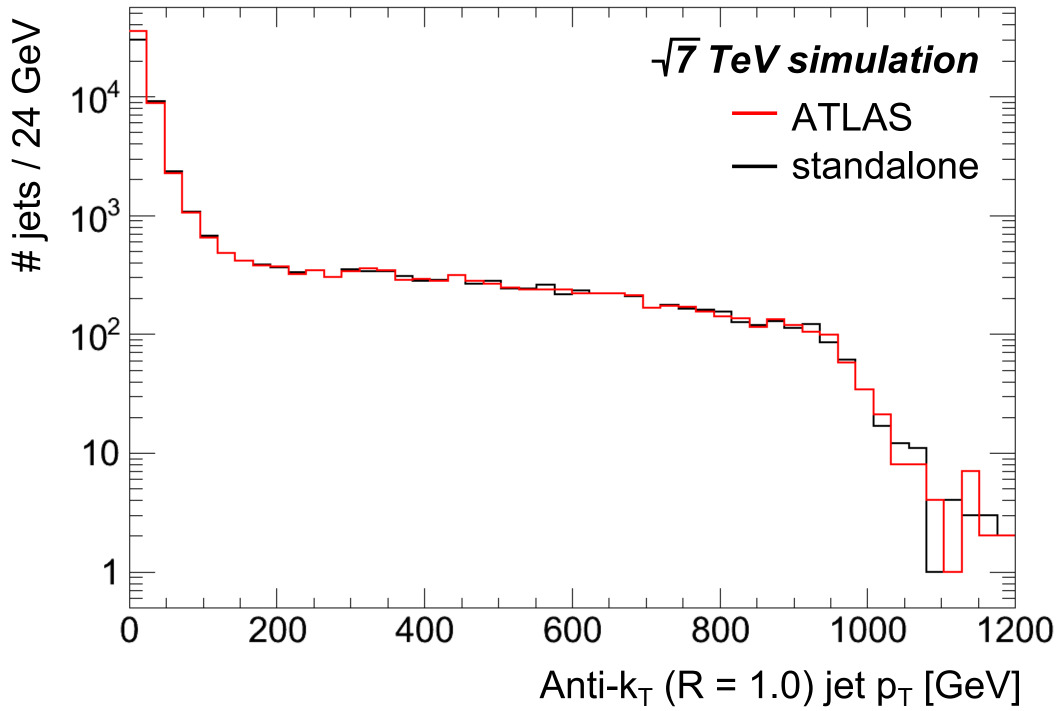

Figure A.1: A comparison of the p_T distributions for anti-k_T $R = 1.0$ jets made by ATLAS central-production to the same jet collection produced with a standalone `FastJet` implementation. The distribution for the standalone jets agrees very well with that for the ATLAS-jets.

Bibliography

[1] ATLAS collaboration. "A search for $t\bar{t}$ resonances in lepton+jets events with highly boosted top quarks in $2\ \text{fb}^{-1}$ of pp collisions at $\sqrt{s} = 7$ TeV with the ATLAS detector". JHEP **1209** (2012) 041. arXiv:1207.2409v1 [hep-ex].

[2] ATLAS collaboration. "A search for $t\bar{t}$ resonances in lepton+jets events with highly boosted top quarks in $2\ \text{fb}^{-1}$ of pp collisions at $\sqrt{s} = 7$ TeV". ATL-COM-PHYS-2011-1692. [Internal note], CERN, Geneva, Jun. 2012.

[3] J. Dalton. "On the absorption of gases by water and other liquids". Memoirs of the literary and philosophical society of Manchester, second series. **1** (1805) 271.

[4] E. Rutherford. "The Scattering of α and β particles by matter and the structure of the atom". Philosophical magazine **21** (1911) 669.

[5] N. Bohr. "On the constitution of atoms and molecules, part II: systems containing only a single nucleus". Philosophical magazine **26** (1913) 476.

[6] C. D. Anderson. "The positive electron". Phys. Rev. **43** (1933) 491.

[7] J. Chadwick. "Possible existence of a neutron". Nature **129** (1932) 312.

[8] P. A. M. Dirac. "The quantum theory of the electron". Proc. R. Soc. Lond. **A117** (1928) 610-624.

[9] E. Fermi. "Fermi's theory of beta decay (English translation by F. L. Wilson)". American Journal of Physics **36** (1968) 1150.

[10] D. H. Perkins. "Introduction to high energy physics". 4th ed. Cambridge: Cambridge University press; 2012.

[11] G. D. Rochester & C. C. Butler. "Evidence for the existence of new unstable elementary particles". Nature **160** (1947) 855.

[12] W. B. Fowler et al. "Production of heavy unstable particles by negative pions". Phys. Rev. **93** (1954) 861.

[13] M. Gell-Mann. "A schematic model of baryons and mesons". Phys. Lett. **8** (1964) 214-215.

[14] G. Zweig. "An $SU(3)$ model for strong interaction symmetry and its breaking". CERN-TH-401. CERN, Geneva, Jan. 1964.

[15] G. Zweig. "An $SU(3)$ model for strong interaction symmetry and its breaking II". CERN-TH-412. CERN, Geneva, Feb. 1964.

[16] D. Griffiths. "Introduction to elementary particles". 2nd ed. Weinheim: WILEY-VCH Verlag GmbH and co.; 2008.

[17] S. L. Glashow. "Partial-symmetries of weak interactions". Nucl. Phys. **22** (1961) 579-588.

[18] A. Salam & J. C. Ward. "Electromagnetic and weak interactions". Phys. Rev. Lett. **13** (1964) 168-171.

[19] S. Weinberg. "A model of leptons". Phys. Rev. Lett. **19** (1967) 1264-1266.

[20] UA1 collaboration. "Experimental observation of isolated large transverse energy electrons with associated missing energy at 540 GeV". Phys. Lett. **B122** (1983) 103-116.

[21] UA2 collaboration. "Observation of single isolated electrons of high transverse momentum in events with missing transverse energy at the CERN $\bar{p}p$ collider". Phys. Lett. **B122** (1983) 476-485.

[22] UA1 collaboration. "Experimental observation of lepton pairs of invariant mass around 95 GeV/c^2 at the CERN SPS collider". Phys. Lett. **B126** (1983) 398-410.

[23] UA2 collaboration. "Evidence for $Z^0 \to e^+e^-$ at the CERN $\bar{p}p$ collider". Phys. Lett. **B129** (1983) 130-140.

[24] F. Englert & R. Brout. "Broken symmetry and the mass of gauge vector mesons". Phys. Lett. **13** (1964) 321-323.

[25] P. W. Higgs. "Broken symmetries, massless particles and gauge fields". Phys. Lett. **12** (1964) 132-133.

[26] P. W. Higgs. "Broken symmetries and the masses of gauge bosons". Phys. Rev. Lett **13** (1964) 508-509.

[27] G. Guralnik, C. Hagen & T. Kibble. "Global conservation laws and massless particles". Phys. Rev. Lett **13** (1964) 585-587.

[28] C. T. Hill & E. H. Simmons. “Strong dynamics and electroweak symmetry breaking”. Phys.Rept. **381** (2003) 235-402; Erratum-ibid. **390** (2004) 553-554. arXiv:hep-ph/0203079.

[29] ATLAS collaboration. “Observation of a new particle in the search for the standard model Higgs boson with the ATLAS detector at the LHC”. Phys. Lett. **B716** (2012) 1. arXiv:1207.7214 [hep-ex].

[30] CMS collaboration. “Observation of a new boson at a mass of 125 GeV with the CMS experiment at the LHC”. Phys. Lett. **B716** (2012) 30. arXiv:1207.7235 [hep-ex].

[31] ATLAS collaboration. “An update of combined measurements of the new Higgs-like boson with high mass resolution channels”. ATLAS-CONF-2012-170. CERN, Geneva, Dec. 2012.

[32] ATLAS collaboration. “Coupling properties of the new Higgs-like boson observed with the ATLAS detector at the LHC”. ATLAS-CONF-2012-127. CERN, Geneva, Sep. 2012.

[33] H. Backe et. al. “Improved limit on the electron-antineutrino rest mass from tritium β-decay”. Phys. Lett. **B300** (1993) 210-216.

[34] S. A. Thomas, F. B. Abdalla & O. Lahav. “Upper bound of 0.28 eV on neutrino masses from the largest photometric redshift survey”. Phys. Lett. **105** (2010) 031301.

[35] S. L. Glashow, J. Iliopoulos & L. Maiani. “Weak interactions with lepton-hadron symmetry”. Phys. Rev. **D2** (1970) 1285.

[36] J. J. Aubert et al. “Experimental observation of a heavy particle J”. Phys. Rev. Lett. **33** (1974) 1404-1406.

[37] J. E. Augustin et al. “Discovery of a narrow resonance in e^+e^- annihilation”. Phys. Rev. Lett. **33** (1974) 1406-1408.

[38] J. A. Appel et. al. “Observation of a dimuon resonance at 9.5 GeV in 400 GeV proton-nucleus collisions”. Phys. Rev. Lett. **39** (1977) 252-255.

[39] J. Beringer et al. (Particle Data Group). “Review of particle physics”. Phys. Rev. **D86** (2012) 010001.

[40] CDF collaboration. “Observation of top quark production in $\bar{p}p$ collisions with the collider detector at Fermilab”. Phys. Rev. Lett. **74** (1995) 2626-2631.

[41] D0 collaboration. “Observation of the top quark”. Phys. Rev. Lett. **74** (1995) 2632-2637.

[42] C. Quigg. “Unanswered questions in the electroweak theory”. Ann.Rev.Nucl.Part.Sci. **59** (2009) 505-555. arXiv:0905.3187 [hep-ph].

[43] Göckeler et al. "A determination of the lambda parameter from full lattice QCD". Phys. Rev. **D73** (2006) 014513. arXiv:hep-ph/0502212.

[44] American linear collider working group. "Linear collider physics resource book for Snowmass 2001. Chapter 6: Top quark physics". BNL-52627.

[45] R. Devenish & A. Cooper-Sarkar. "Deep inelastic scattering". 1st ed. Oxford: Oxford University press; 2011.

[46] The Durham HEP data project. "[Online PDF plotting and calculation]". http://hepdata.cedar.ac.uk/pdf/pdf3.html. Durham, UK. Retrieved on 7 October 2012 from.

[47] W.J. Stirling. "Private communication". Available from: `http://www.hep.phy.cam.ac.uk/~wjs/plots/plots.html`.

[48] P. Nason & S. Dawson. "The total cross-section for the production of heavy quarks in hadronic collisions". Nucl. Phys. **B303** (1988) 607.

[49] ATLAS collaboration. "Combination of ATLAS and CMS top-quark pair cross-section measurements using up to $1.1\ \mathrm{fb}^{-1}$ of data at $7\ \mathrm{TeV}$". ATLAS-CONF-2012-134.

[50] M. Cacciari et. al. "Top-pair production at hadron colliders with next-to-next-to-leading logarithmic soft-gluon resummation". arXiv:1111.5869 [hep-ph]. CERN, Geneva, Nov. 2011.

[51] M. Aliev et al. "HATHOR: HAdronic Top and Heavy quarks crOss section calculatoR". Comput. Phys. Commun. **182** (2011) 1034. arXiv:1007.1327v1 [hep-ph].

[52] J. Sterman et al. "Handbook of perturbative QCD". Rev. Mod. Phys. **67** (1995) 157.

[53] T. M. P. Tait & C. P. Yuan. "Single top quark production as a window to physics beyond the standard model". Phys. Rev. **D63** (2000) 014018. arXiv:hep-ph/0007298v2.

[54] J. R. Incandela et. al. "Status and prospects for top-quark physics". Prog.Part.Nucl.Phys. **63** (2009) 239-292. arXiv:0904.2499v3 [hep-ex].

[55] P. B. Renton. "Precision electroweak tests of the standard model". Rep. Prog. Phys. **65** (2002) 1271. arXiv:hep-ph/0206231v2.

[56] V. C. Rubin & W. K. Ford Jr. "Rotation of the andromeda nebula from a spectroscopic survey of emission regions". Ap. J. **159** (1970) 379.

[57] D. Clowe et al. "A direct empirical proof of the existence of dark matter". Astrophys. J. **648** (2006) 109-113. arXiv:astro-ph/0608407.

[58] G. Bertone, D. Hooper & J. Silk. "Particle dark matter: evidence, candidates and constraints". Phys. Rept. **405** (2005) 279. arXiv:hep-ph/0404175.

[59] A. G. Cohen, D. B. Kaplan & A. E. Nelson. "Progress in electroweak baryogenesis". Ann. Rev. Nucl. Part. Sci. **V43** (1993) 27. arXiv:hep-ph/9302210v1.

[60] A. D. Sakharov. "Violation of CP invariance, C asymmetry, and baryon asymmetry of the universe". Sov. Phys. Usp. **34** (1991) 392.

[61] ALEPH collaboration, DELPHI collaboration, L3 collaboration, OPAL collaboration & SLD collaboration. "Precision electroweak measurements on the Z resonance". Phys. Rept. **427** (2006) 257-454. arXiv:hep-ex/0509008.

[62] D. Wicke. "Properties of the top quark". Eur.Phys.J.C **71** (2011) 1627. arXiv:1005.2460 [hep-ex].

[63] ATLAS experiment. "Top public results". Available from: `https://twiki.cern.ch/twiki/bin/view/AtlasPublic/TopPublicResults`. [Accessed 27 November 2011].

[64] CMS experiment. "Top public results". Available from: `https://twiki.cern.ch/twiki/bin/view/CMSPublic/PhysicsResultsTOP`. [Accessed 27 November 2011].

[65] J. H. Kühn & G. Rodrigo. "Charge asymmetry in hadroproduction of heavy quarks". Phys. Rev. Lett. **81** (1998) 49. arXiv:hep-ph/9802268.

[66] CDF collaboration. "Measurement of the top quark forward-backward production asymmetry and its dependence on event kinematic properties". Accepted by Phys. Rev. **D**. arXiv:1211.1003 [hep-ex].

[67] D0 collaboration. "Forward-backward asymmetry in top quark-antiquark production". Phys. Rev. **D84** (2011) 112005. arXiv:1107.4995v2 [hep-ex].

[68] ATLAS collaboration. "Measurement of the charge asymmetry in top quark pair production in pp collisions at $\sqrt{s} = 7$ TeV using the ATLAS detector". Eur.Phys.J.C **72** (2012) 2039. arXiv:1203.4211 [hep-ex].

[69] CMS collaboration. "Inclusive and differential measurements of the $t\bar{t}$ charge asymmetry in pp collisions at 7 TeV". Phys. Lett. **B717** (2012) 129. arXiv:1207.0065 [hep-ex].

[70] G. Brooijmans. "Re: Two questions on binning and systematics for ttbar resonances (r16)". E-mail to Sarah Livermore, 13 Dec. 2012.

[71] ATLAS collaboration. "A search for $t\bar{t}$ resonances with the ATLAS detector in 2.05 fb^{-1} of proton-proton collisions at $\sqrt{s} = 7\mathrm{TeV}$". Eur. Phys. J. **C72** (2012) 2083. arXiv:1205.5371v1 [hep-ex].

[72] CDF collaboration. "Search for resonant $t\bar{t}$ production in the semi-leptonic decay mode using the full CDF data set". Phys. Rev. Lett. **110** (2013) 121802. arXiv:1211.5363v1 [hep-ex].

[73] D0 collaboration. "Search for a narrow $t\bar{t}$ resonance in $p\bar{p}$ collisions at $\sqrt{s} = 1.96$ TeV". Phys. Rev. **D85** (2012) 051101. arXiv:1111.1271 [hep-ex].

[74] CMS collaboration. "Search for resonant $t\bar{t}$ production in lepton+jets events in pp collisions at $\sqrt{s} = 7$ TeV". arXiv:1209.4397 [hep-ex]. CMS-TOP-12-017.

[75] C. T. Hill. "Topcolor assisted technicolor". Phys. Lett. **B345** (1995) 483-489. arXiv:hep-ph/9411426.

[76] S. Weinberg. "Implications of dynamical symmetry breaking". Phys. Rev. **D13** (1976) 974-996.

[77] L. Susskind. "Dynamics of spontaneous symmetry breaking in the Weinberg-Salam theory". Phys. Rev. **D20** (1979) 2619-2625.

[78] R. Foadi, M. T. Frandsen & F. Sannino. "125 GeV Higgs from a not so light Technicolor scalar". arXiv:1211.1083v2 [hep-ph].

[79] R. M. Harris, C. T. Hill & S. J. Parke. "Cross-section for topcolor Z' decaying to top-antitop". arXiv:hep-ph/9911288v1.

[80] N. Arkani-Hamed, S. Dimopoulos & G. Dvali. "The hierarchy problem and new dimensions at a millimeter". Phys. Lett. **B429** (1998) 263-272. arXiv:hep-ph/9803315.

[81] L. Randall & R. Sundrum. "A large mass hierarchy from a small extra dimension". Phys. Rev. Lett. **83** (1999) 3370-3373. arXiv:hep-ph/9905221.

[82] L. Randall & R. Sundrum. "An alternative to compactification". Phys. Rev. Lett. **83** (1999) 4690-4693. arXiv:hep-th/9906064.

[83] B. Lillie, L. Randall & L. T. Wang. "The bulk RS KK-gluon at the LHC". JHEP **09** (2007) 074. arXiv:hep-ph/0701166.

[84] G. Brooijmans et al. "New physics at the LHC: a Les Houches report". arXiv:1005.1229 [hep-ph].

[85] F. Maltoni & T. Stelzer. "MadEvent: automatic event generation with MadGraph". JHEP **02** (2003) 027. arXiv:hep-ph/0208156v1.

[86] CDF collaboration. "A search for resonant production of $t\bar{t}$ pairs in $4.8~\mathrm{fb}^{-1}$ of integrated luminosity of $p\bar{p}$ collisions at $\sqrt{s} = 1.96~\mathrm{TeV}$". Phys. Rev. **D84** (2010) 072004. arXiv:1107.5063v3 [hep-ex].

[87] CMS collaboration. "A search for resonances in semileptonic top pair production at $\sqrt{s} = 7~\mathrm{TeV}$". CMS-PAS-TOP-11-009. CERN, Geneva, Mar. 2012.

[88] S. Bethke. "The 2009 world average of α_s". Eur.Phys.J.C **64** (2009) 689. arXiv:0908.1135v2 [hep-ph].

[89] J. E. Huth et al. "Toward a standardization of jet definitions". FNAL-C-90-249-E.

[90] G.P. Salam. "Towards jetography". Eur. Phys. J. **C67** (2010) 637. arXiv:0906.1833v2 [hep-ph].

[91] G.P. Salam & G. Soyez. "A practical seedless infrared-safe cone jet algorithm". JHEP **05** (2007) 086. arXiv:0704.0292 [hep-ph].

[92] M. Cacciari, G. P. Salam & G. Soyez. "The anti-k_T jet clustering algorithm". JHEP **04** (2008) 063. arXiv:0802.1189.

[93] ATLAS top reconstruction group. "Study on reconstructed object definition and selection for top physics". ATL-COM-PHYS-2009-633. [Internal note], CERN, Geneva, Dec. 2009.

[94] ATLAS collaboration. "Performance of jet algorithms in the ATLAS detector". ATLAS-PHYS-INT-129. [Internal note], CERN, Geneva, Dec. 2010.

[95] K. Agashe et al. "LHC signals from warped extra dimensions". Phys. Rev. **D77** (2008) 015003. arXiv:hep-ph/0612015.

[96] J. M. Butterworth, J. R. Ellis & A. R. Raklev. "Reconstructing sparticle mass spectra using hadronic decays". JHEP **07** (2007) 033. arXiv:hep-ph/0702150.

[97] J. Thaler & L. T. Wang. "Strategies to identify boosted tops". JHEP **07** (2008) 092. arXiv:0806.0023[hep-ph].

[98] U. Baur & L. H. Orr. "High p_T top quarks at the CERN Large Hadron Collider". Phys. Rev. **D76** (2007) 094012. arXiv:0707.2066[hep-ph].

[99] B. Tweedie. "Re: Illustrations of energy deposits inside jets". E-mail to Sarah Livermore, 20 Nov. 2012.

[100] M. H. Seymour. "Searches for new particles using cone and cluster jet algorithms: a comparative study". Z. Phys. **C62** (1994) 127-138 .

[101] J. M. Butterworth, B. E. Cox & J. R. Forshaw. "WW scattering at the LHC". Phys. Rev. **D65** (2002) 096014. arXiv:hep-ph/0201098.

[102] G. Brooijmans. "High p_T hadronic top quark identification part I: jet mass and the YSplitter". ATL-PHYS-CONF-2008-008. CERN, Geneva, Jan. 2008.

[103] ATLAS collaboration. "Jet mass and substructure of inclusive jets in $\sqrt{s} = 7$ TeV $p\bar{p}$ collisions with the ATLAS experiment". JHEP **05** (2012) 128. arXiv:1203.4606v2 [hep-ex].

[104] ATLAS collaboration. "Backup note for measurement of jet mass and substructure in QCD with the ATLAS experiment". ATL-COM-PHYS-2011-401. [Internal note], CERN, Geneva, Apr. 2011.

[105] "LHC commissioning with beam, 2012 - progress". Available from: `http://lhc-commissioning.web.cern.ch`. [Accessed 03 July 2012].

[106] R. Bailey. "Stages of LHC operation from first collisions to 25 ns operation". LHC-OP-BCP-0001. [Internal note], CERN, Geneva, Dec. 2004.

[107] ATLAS experiment. "Luminosity public results". Available from: `https://twiki.cern.ch/twiki/bin/view/AtlasPublic/LuminosityPublicResults`. [Accessed 29 November 2011].

[108] ATLAS collaboration. "The ATLAS experiment at the Large Hadron Collider". JINST **3** (2008) S08003.

[109] ATLAS collaboration. "Electron performance measurements with the ATLAS detector using the 2010 LHC proton-proton collision data". Eur. Phys. J. **C72** (2012) 1909. arXiv:1110.3174v2 [hep-ex].

[110] ATLAS collaboration. "Tile calorimeter technical design report". CERN-LHCC-96-42.

[111] J. Beringer et al. (Particle Data Group). "Review of particle physics: section 31.9.2, hadronic calorimeters". Phys. Rev. **D86** (2012) 010001.

[112] R. Wigmans. "Advances in hadron calorimetry". Annu. Rev. Nucl. Part. Sci. **41** (1991) 133.

[113] ATLAS collaboration. "Jet energy resolution and selection efficiency relative to track jets from in-situ techniques with the ATLAS detector using pp collisions at $\sqrt{s} = 7$ TeV". ATLAS-CONF-2010-054. CERN, Geneva, Jul. 2010.

[114] C. Grupen & B. A. Shwartz. "Particle detectors. 2nd ed. Cambridge University Press; 2008. p. 255-257".

[115] E. Fullana Torregrosa. "Re: Question about why the tile is non-compensating". E-mail to Sarah Livermore, 20 Sep. 2012.

[116] B. Abou-Donia et al. "Depleted and natural uranium: chemistry and toxicological effects". Journal of toxicology and environmental health, part B: critical reviews.

[117] ATLAS collaboration. "Performance of the ATLAS electron and photon trigger in pp collisions at $\sqrt{s} = 7$ TeV in 2011". ATL-COM-DAQ-2012-017. [Internal note], CERN, Geneva, May 2012.

[118] S. van der Meer. "Calibration of the effective beam height in the ISR". CERN-ISR-PO-68-31. CERN, Geneva, Jun. 1968.

[119] ATLAS collaboration. "Luminosity determination in pp collisions at $\sqrt{s} = 7$ TeV using the ATLAS detector at the LHC". Eur. Phys. J. **C71** (2011) 1630. arXiv:1101.2185 [hep-ex].

[120] ATLAS collaboration. "Final report of the ATLAS AOD/ESD definition task force". ATL-SOFT-2004-006. [Internal note], CERN, Geneva, Dec. 2004.

[121] G. Barrand et al. "GAUDI - A software architecture and framework for building HEP data processing applications". Comput. Phys. Commun. **140** (2001) 45.

[122] F. Brun & F. Rademakers. "ROOT: An object oriented data analysis framework". Nucl. Instrum. Meth. **A389** (1997) 81-86.

[123] ATLAS collaboration. "ATLAS Computing: technical design report". CERN-LHCC-2005-022.

[124] CERN. "Worldwide LHC computing grid". Available from: `http://wlcg.web.cern.ch/`. [Accessed 03 July 2012].

[125] M. Cacciari, G. P. Salam & G. Soyez. "`FastJet` user manual". Eur. Phys. J. **C72** (2012) 1896. arXiv:1111.6097v1 [hep-ph].

[126] M. Cacciari & G. P. Salam. "Dispelling the N^3 myth for the k_t jet-finder". Phys. Lett. **B641** (2006) 57-61. arXiv:hep-ph/0512210v2.

[127] J. Beringer et al. (Particle Data Group). "Review of particle physics: section 38, Monte Carlo event generators". Phys. Rev. **D86** (2012) 010001.

[128] ATLAS collaboration. "Monte Carlo samples used for top physics". ATL-COM-PHYS-2010-836. [Internal note], CERN, Geneva, Oct. 2010.

[129] GEANT4 collaboration. "GEANT4: a simulation toolkit". Nucl. Instrum. Meth. A **506** (2003) 250.

[130] ATLAS Collaboration. "The ATLAS simulation infrastructure". Eur. Phys. J. **C70** (2010) 823-874. arXiv:1005.4568 [physics.ins-det].

[131] T. Sjostrand, S. Mrenna & P.Z. Skands. "PYTHIA 6.4 physics and manual". JHEP **05** (2006) 026. arXiv:hep-ph/0603175v2.

[132] J. Pumplin et al. "New generation of parton distributions with uncertainties from global QCD analysis". JHEP **07** (2002) 012. arXiv:hep-ph/0201195v3.

[133] R.M. Harris & S. Jain. "Cross-sections for leptophobic topcolor Z' decaying to top-antitop". Eur. Phys. J. **C72** (2012) 2072. arXiv:1112.4928v2 [hep-ph].

[134] J. Gao et al. "Next-to-leading order QCD corrections to the heavy resonance production and decay into top quark pair at the LHC". Phys. Rev. **D82** (2010) 014020. arXiv:1004.0876v4 [hep-ph].

[135] T. Sjostrand, S. Mrenna & P. Z. Skands. "A brief introduction to PYTHIA 8.1". Comput. Phys. Commun. **178** (2008) 852-867. arXiv:0710.3820v1 [hep-ph].

[136] S. Frixione & B.R. Webber. "Matching NLO QCD computations and parton shower simulations". JHEP **06** (2002) 029. arXiv:hep-ph/0204244v2.

[137] S.Frixione, P. Nason & B.R. Webber. "Matching NLO QCD computations and parton shower in heavy flavour production". JHEP **08** (2003) 007. arXiv:hep-ph/0305252v2.

[138] S. Frixione et al. "Single-top production in MC@NLO". JHEP **03** (2006) 092. arXiv:hep-ph/0512250v2.

[139] G. Corcella et al. "HERWIG 6: An event generator for hadron emission reactions with interfering gluons (including supersymmetric processes)". JHEP **01** (2001) 010. arXiv:hep-ph/0011363v3.

[140] G. Corcella et al. "HERWIG 6.5 release note". arXiv:hep-ph/0210213v2.

[141] J. M. Butterworth, J. R. Forshaw & M. H. Seymour. "Multiparton interactions in photoproduction at HERA". Z. Phys. **C72** (1996) 637. arXiv:hep-ph/9601371v1.

[142] P. M. Nadolsky et al. "Implications of CTEQ global analysis for collider observables". Phys. Rev. **D78** (2008) 013004. arXiv:0802.0007v3 [hep-ph].

[143] S. Moch & P. Uwer. "Theoretical status and prospects for top-quark pair production at hadron colliders". Phys. Rev. **D78** (2008) 034003. arXiv:0804.1476v2 [hep-ph].

[144] M. Beneke et al. "Threshold expansion of the $gg(q\bar{q}) \to Q\bar{Q} + X$ cross-section at $O(\alpha(s)^4)$". arXiv:0911.5166v1 [hep-ph].

[145] ATLAS collaboration. "Measurement of the top quark-pair production cross-section with ATLAS in pp collisions at $\sqrt{s} = 7$ TeV". Eur. Phys. J. **C71** (2011) 1577. arXiv:1012.1792 [hep-ex].

[146] M.L. Mangano et al. "ALPGEN, a generator for hard multiparton processes in hadronic collisions". JHEP **07** (2003) 001. arXiv:hep-ph/0206293v2.

[147] J. Alwall et al. "Comparative study of various algorithms for the merging of parton showers and matrix elements in hadronic collisions". Eur. Phys. J. **C53** (2008) 473. arXiv:0706.2569v2 [hep-ph].

[148] C. Anastasiou et al. "High precision QCD at hadron colliders: electroweak gauge boson rapidity distributions at NNLO". Phys. Rev. **D69** (2004) 094008. arXiv:hep-ph/0312266v2.

[149] L. Mijovic. "Re: Quick question about Alpgen Z+jets in mc10b". E-mail to Sarah Livermore, 02 Dec. 2012.

[150] ATLAS collaboration. "Estimation of the W+jets background for top quark re-discovery in the single lepton+jets channel". ATL-COM-PHYS-2010-834. [Internal note], CERN, Geneva, Oct. 2010.

[151] J. M. Butterworth et al. "Single boson and diboson production cross-sections in pp collisions at $\sqrt{s} = 7$ TeV". ATL-COM-PHYS-2010-695. [Internal note], CERN, Geneva, Oct. 2010.

[152] ATLAS collaboration. "ATLAS pixel detector electronics and sensors". JINST **3** (2008) P07007.

[153] ATLAS collaboration. "Expected electron performance in the ATLAS experiment". ATL-PHYS-PUB-2011-006.

[154] ATLAS collaboration. "Performance studies for e/gamma calorimeter isolation". ATL-COM-PHYS-2011-1186.

[155] ATLAS collaboration. "$pp \to \gamma/Z \to \mu^+\mu^-$ and $pp \to W \to \mu\nu$ inclusive cross-section measurement in early data with the ATLAS detector". ATL-COM-PHYS-2010-124. [Internal note], CERN, Geneva, Mar. 2010.

[156] ATLAS collaboration. "Lepton trigger and identification for the winter 2011 top quark analyses". ATL-COM-PHYS-2011-123. [Internal note], CERN, Geneva, Feb. 2011.

[157] ATLAS collaboration. "Identification of muon candidates in pp collisions at $\sqrt{s} = 900$ GeV with the ATLAS detector". ATLAS-CONF-2010-015. CERN, Geneva, Apr. 2010.

[158] ATLAS collaboration. "Muon reconstruction efficiency in reprocessed 2010 LHC proton-proton collision data recorded with the ATLAS detector". ATLAS-CONF-2011-063. CERN, Geneva, Apr. 2011.

[159] ATLAS collaboration. "Muon momentum resolution in the first pass reconstruction of the 2010 pp collision data at $\sqrt{s} = 7$ TeV". ATLAS-CONF-2011-046. CERN, Geneva, Mar. 2011.

[160] W. Lampl et al. "Calorimeter clustering algorithms: description and performance". ATL-LARG-PUB-2008-002. CERN, Geneva, May 2008.

[161] ATLAS collaboration. "Jet energy measurement with the ATLAS detector in proton-proton collisions at $\sqrt{s} = 7$ TeV taken in 2010". arXiv:1112.6426v1 [hep-ex].

[162] ATLAS collaboration. "Jet energy scale and its systematic uncertainty in proton-proton collisions at $\sqrt{s} = 7$ TeV in ATLAS 2010 data". ATLAS-CONF-2011-032.

[163] K. Borras, Ç. İşsever & D. Wegener. "An improved weighting algorithm to achieve software compensation in a fine grained LAr calorimeter". Nucl.Instrum.Meth. **A545** (2005) 803-812. arXiv:physics/0408129 [physics.ins-det].

[164] T. Barilliari. "Local hadronic calibration". ATL-LARG-PUB-2009-001. CERN, Geneva, Jan. 2009.

[165] ATLAS collaboration. "Inputs to jet reconstruction and calibration with the ATLAS detector using proton-proton collisions at $\sqrt{s} = 900$ GeV". ATLAS-CONF-2010-016.

[166] C. Doglioni. Private communication. 31 Aug. 2012.

[167] C. Doglioni. "Pile-up offset correction (r16) in the transition/forward region". `https://indico.cern.ch/getFile.py/access?contribId=2\&resId=1\&materialId=slides\&confId=90833`. [Internal talk], CERN, Geneva, Dec. 2010.

[168] ATLAS twiki. "How to clean jets". Available from: `https://twiki.cern.ch/twiki/bin/viewauth/AtlasProtected/HowToCleanJets`. [Accessed 31 October 2011].

[169] ATLAS collaboration. "Commissioning of the ATLAS high-performance b-tagging algorithms in the 7 TeV collision data". ATLAS-CONF-2011-102.

[170] ATLAS collaboration. "Missing transverse energy for top physics analyses in release 16.6.5.5.1 with the 2011 dataset". ATL-PHYS-INT-2011-092. [Internal note], CERN, Geneva, Nov. 2011.

[171] ATLAS collaboration. "Missing transverse energy for top physics analyses with early ATLAS data at $\sqrt{s} = 7$ TeV". ATL-COM-PHYS-2010-821. [Internal note], CERN, Geneva, Oct. 2010.

[172] ATLAS collaboration. "ATLAS detector and physics performance: technical design report". CERN-LHCC-99-014.

[173] ATLAS experiment. "Top common objects 2011 rel16: muons". Available from: `https://twiki.cern.ch/twiki/bin/viewauth/AtlasProtected/TopCommonObjects2011rel16#Muons`. [Accessed 29 August 2011].

[174] ATLAS collaboration. "Top quark pair production cross-section measurement in ATLAS in the single lepton+jets channel without b-tagging". ATLAS-CONF-2011-023. CERN, Geneva, Mar. 2011.

[175] ATLAS collaboration. "Expected performance of the ATLAS experiment - detector, trigger and physics. Section: jets from light quarks in $t\bar{t}$ events". arXiv:0901.0512v4. CERN-OPEN-2008-020.

[176] ATLAS collaboration. "A search for new high mass phenomena producing top quarks with the ATLAS experiment". ATLAS-CONF-2011-070. CERN, Geneva, May 2011.

[177] ATLAS collaboration. "A search for $t\bar{t}$ resonances in the lepton plus jets channel using $200\ \mathrm{pb}^{-1}$ of pp collisions at $\sqrt{s} = 7\ \mathrm{TeV}$". ATLAS-CONF-2011-087. CERN, Geneva, Jun. 2011.

[178] ATLAS collaboration. "Prospects for top anti-top resonance searches using early ATLAS data". ATL-PHYS-PUB-2010-008. CERN, Geneva, Jul. 2010.

[179] ATLAS collaboration. "A search for $t\bar{t}$ resonances in the lepton plus jets final state using $4.66\ \mathrm{fb}^{-1}$ of pp collisions at $\sqrt{s} = 7\ \mathrm{TeV}$". ATLAS-CONF-2012-136. CERN, Geneva, Sep. 2012.

[180] T. Chwalek. "Ph.D. thesis (pp. 81-85)". IEKP-KA/2010-5. KIT Karlsruhe, Feb. 2010.

[181] J. E. Gaiser. "Charmonium spectroscopy from radiative decays of the J/ψ and ψ', appendix F1". SLAC-R-255. Ph.D. thesis, SLAC, Stanford, Aug. 1982.

[182] ATLAS collaboration. "Study of jets produced in association with a W boson in pp collisions at $\sqrt{s} = 7\ \mathrm{TeV}$ with the ATLAS detector". Phys. Rev. **D85** (2012) 092002. arXiv:1201.1276v3 [hep-ex].

[183] C. H. Kom & W.J. Stirling. "Charge asymmetry in W+jets production at the LHC". Eur. Phys. J. **C69** (2010) 67-73. arXiv:1004.3404v3 [hep-ph].

[184] CMS collaboration. "Expectations for observation of top quark pair production in the dilepton final state with the first $10\ \mathrm{pb}^{-1}$ of CMS data". CMS-PAS-TOP-08-001.

[185] ATLAS collaboration. "Cut-and-count measurement of the top quark pair production in the semileptonic decay channel at $\sqrt{s} = 7\ \mathrm{TeV}$ with the ATLAS detector". ATL-PHYS-INT-2011-048. [Internal note], CERN, Geneva, May 2011.

[186] ATLAS collaboration. "Mis-identified lepton backgrounds in top quark pair production studies for EPS 2011 analyses". ATL-COM-PHYS-2011-768. [Internal note], CERN, Geneva, Jun. 2011.

[187] G. Choudalakis. "On hypothesis testing, trials factor, hypertests and the BUMPHUNTER". arXiv:1101.0390v2 [physics.data-an].

[188] D. Casadei. "Proceedings of the PHYSTAT 2011 workshop on statistical issues related to discovery claims in search experiments and unfolding: statistical methods used in ATLAS for exclusion and discovery". CERN-2011-006. arXiv:1108.2288v1 [physics.data-an].

[189] Eric W. Weisstein. "Inverse erf". From MathWorld – A Wolfram web resource. `http://mathworld.wolfram.com/InverseErf.html`. [Accessed 23 May 2012].

[190] D0 Collaboration (I. Bertram et al.). "A Recipe for the construction of confidence limits". FERMILAB-TM-2104. Fermilab, Apr. 2000.

[191] J. O. Berger, J. M. Bernardo & D. Sun. "The formal definition of reference priors". Ann. Statist. **37** (2009) 905-938.

[192] D. Casadei. "Reference analysis of the signal + background model in counting experiments". JINST **7** (2012) 01012. arXiv:1108.4270 [physics.data-an].

[193] D0 Collaboration (S. Jain et al.). "Statistical methods implemented in the package top_statistics". D0 note 5817, Feb. 2011.

[194] ATLAS collaboration. "Luminosity determination in pp collisions at $\sqrt{s} = 7$ TeV using the ATLAS detector in 2011". ATLAS-CONF-2011-116. CERN, Geneva, Aug. 2011.

[195] A. D. Martin et. al. "Parton distributions for the LHC". Eur. Phys. J. **C63** (2009) 189-285. arXiv:0901.0002v3.

[196] The NNPDF collaboration. "A first unbiased global NLO determination of parton distributions and their uncertainties". arXiv:1002.4407 [hep-ph].

[197] ATLAS experiment. "Top PDF uncertainty". Available from: `https://twiki.cern.ch/twiki/bin/viewauth/AtlasProtected/TopPdfUncertainty`. [Accessed 16 April 2012].

[198] M. Botje et al. "The PDF4LHC Working Group". arXiv:1101.0538.

[199] J. Ferrando. "final final question (PDF uncertainty for ttbar - r16". E-mail to Sarah Livermore, 29 Apr. 2013.

[200] F. Demartin et al. "The impact of PDF and α_s uncertainties on Higgs production in gluon fusion at hadron colliders". arXiv:1004.0962 [hep-ph].

[201] S. Frixione, P. Nason & C. Oleari. "Matching NLO QCD computations with parton shower simulations: the POWHEG method". JHEP **11** (2007) 070. arXiv:0709.2092v1 [hep-ph].

[202] B.P. Kersevan & E. Richter-Was. "The Monte Carlo event generator AcerMC version 2.0 with interfaces to PYTHIA 6.2 and HERWIG 6.5". arXiv:hep-ph/0405247v2.

[203] ATLAS collaboration. "Measurement of the top quark pair production cross-section with ATLAS in the single lepton channel". Phys. Lett. **B711** (2012) 244-263. arXiv:1201.1889v2 [hep-ex].

[204] ATLAS collaboration. "Estimating theory uncertainties in W/Z+jets and $t\bar{t}$+jets events using the ALPGEN generator". ATL-COM-PHYS-2012-070. [Internal note], CERN, Geneva, Jan. 2012.

[205] ATLAS experiment. "Top jet liaison R16 recommendations: b-jets JES uncertainty". Available from: https://twiki.cern.ch/twiki/bin/viewauth/AtlasProtected/TopJetLiaisonR16Recommendations#b_jets_JES_uncertainty. [Accessed 2 June 2012].

[206] ATLAS collaboration. "Jet energy resolution from in-situ techniques with the ATLAS detector using proton-proton collisions at a center of mass energy $\sqrt{s} = 7$ TeV". ATLAS-COM-PHYS-2011-240. CERN, Geneva, Mar. 2011.

[207] ATLAS experiment. "R16.6 final recommendations". Available from: https://twiki.cern.ch/twiki/bin/viewauth/AtlasProtected/JERProviderTop#R16_6_final_recommendations. [Accessed 24 December 2011].

[208] C. Doglioni. "JER smearing in R16". Available from: https://indico.cern.ch/getFile.py/access?contribId=4&resId=0&materialId=slides&confId=178111 [page 8]. [Internal talk], CERN, Geneva, Feb. 2012.

[209] ATLAS experiment. "R16.6 recommendations updated February 2012". Available from: https://twiki.cern.ch/twiki/bin/viewauth/AtlasProtected/JERProviderTop#R16_6_recommendations_updated_Fe. [Accessed 24 December 2011].

[210] P. Z. Skands. "Tuning Monte Carlo generators: the Perugia tunes". Phys. Rev. **D82** (2010) 074018. arXiv:hep-ph/1005.3457.

[211] ATLAS collaboration. "Study of jet shapes in inclusive jet production in pp collisions at $\sqrt{s} = 7$ TeV using the ATLAS detector". Phys. Rev. **D83** (2011) 052003. arXiv:1101.0070 [hep-ex].

[212] M. Bahr et. al. "HERWIG++ physics and manual". Eur. Phys. J. **C58** (2008) 639. arXiv:0803.0883v3 [hep-ph].

[213] T. Gleisberg et al. "Event generation with SHERPA 1.1". JHEP **02** (2009) 007. arXiv:hep-ph/0811.4622.

[214] ATLAS collaboration. "Jet substructure at the Tevatron and LHC (Proceedings of the Boost 2011 workshop)". J. Phys. **G39** (2012) 063001. arXiv:1201.0008v2 [hep-ph].

[215] E. Bergeaas Kuutmann. "Re: Bayesian vs Frequentist and topStats vs RooStats". E-mail to Sarah Livermore, 02 Dec. 2012.

[216] D. Krohn, J. Thaler & L. T. Wang. "Jets with variable R". JHEP **06** (2008) 063. arXiv:0903.0392v1 [hep-ph].